Characterization of Halogen Bonds with Different Solid-State Nuclear Magnetic Resonance Methods

Yijue Xu

A thesis submitted in partial fulfillment of the requirements for the
Doctorate in Philosophy degree in Chemistry

Ottawa-Carleton Chemistry Institute

Department of Chemistry and Biomolecular Sciences
Faculty of Science
University of Ottawa

Abstract

The nature and potential application of halogen bonding are currently topics of great interest among various research fields, including biochemistry, functional materials, organocatalysis, etc. Solid-state nuclear magnetic resonance (SSNMR) has been recognized as one of the important tools for characterizing different types of non-covalent interactions. This dissertation demonstrates how different SSNMR methods can be used to characterize the changes in electronic structure associated with halogen bonding interactions and investigates the processes leading to the formation of halogen bonds.

A series of cocrystals featuring halogen bonds between phosphine oxides and different diiodoperfluorobenzenes (1,4-diiodotetrafluorobenzene, 1,2-diiodotetrafluorobenzene, and 1,3,5-trifluoro-2,4,6-triiodobenzene) have been synthesized through slow evaporation from solvent or by mechanochemistry. We began by characterizing the naturally abundant and ^{17}O-labeled phosphine oxides and their halogen-bonded cocrystals by a combination of theoretical and experimental multinuclear magnetic resonance spectroscopy (^{31}P and ^{17}O), and X-ray diffraction (XRD) methods. This first study of ^{17}O NMR parameters in halogen-bonded solids has provided key insights into the correlation between NMR observables and the nature of the halogen bond.

Then a rare example of a cocrystal featuring a phosphine as a halogen bond acceptor was synthesized and characterized by both solution and solid-state NMR experiments, and the ^{31}P NMR experiment acted as a direct probe for the formation of halogen bonds in both solution and solid states.

In addition to the conventional polycrystalline solid-state NMR experiments, single-crystal NMR studies were performed on ^{17}O labeled triphenylphosphine oxide and its halogen-bonded cocrystals with diiodoperfluorobenzenes, which allowed for the measurement of not only the magnitude but also the orientation of the NMR tensors. The work helped investigate the changes in NMR tensor orientation

caused by the formation of halogen bonds and thereby provides a novel connection between the electronic structure and the NMR interactions. Novel single-crystal NMR analysis software was developed to fit the data in two ways: either through an unconstrained fitting process or through a constrained fitting process, which can improve the precision of the resulting tensor orientations in some cases.

The mechanochemical production of halogen bonds inspired us to investigate the mechanism and kinetics behind this solid-state reaction process in situ. In situ ^{31}P solid-state NMR studies of halogen bond formation between triphenylphosphine oxide and 1,4-diiodotetrafluorobenzene were carried out under different conditions (temperature, spinning speed, and different amounts of liquid added) to provide insight into the crystallization process and provide an estimation of the activation energy.

Overall, this thesis provides several new applications of NMR spectroscopy to the study of halogen bonds and provides various novel insights into the connection between the NMR observables and the nature of this non-covalent interaction.

Acknowledgements

The past nine-year experience at the University of Ottawa has been a challenging but rewarding journey. First of all, I would like to thank all the services and staff for their help. In particular, the International Office offered me an opportunity to participate in a Summer Undergraduate International Research Internship and join Dr. Paul-Fleurat Lessard's group in Lyon, France. I would also like to thank the Department of Chemistry and Biomolecular Sciences for always being there to answer my questions and solve my problems, and for offering me an International Doctoral Scholarship to reduce my financial burden. I also thank the Office of Graduate and Postdoctoral Studies for awarding me an Ontario Graduate Scholarship.

My deepest appreciation is of course given to my supervisor, Dr. David Bryce, for initially giving me an opportunity to work in his lab during my undergraduate studies, then accepting me as a graduate student. Now I have been working in the lab for almost seven years, and Dave has always been there for any help and support throughout my entire research. Thank you, Dave, for your patience while I was stuck at my single-crystal NMR project, and thank you for all your guidance, discussion and comments that you provided for all my manuscripts. I would also like to thank you for offering me many opportunities to attend multiple Canadian and global conferences over the past years, in which I have got a chance to know other experts and present my research to other groups. It has been my greatest honor of working with you.

I am also very thankful to the past and current members in the NMR and X-ray facilities. Dr. Eric Ye, Dr. Glenn Facey and Dr. Peter Pallister, thank you all for coming all the way from the top floor of D'lorio to the basement of STEM/MacDonald building and trying to help me fix the spectrometer or set up the experiments (especially for staying late on Friday afternoons). Glenn, I really appreciate your help with the single-crystal NMR probe. Without you none of this work would have been possible. Dr. Jeffrey

Ovens, Dr. Bulat Gabidullin, Dr. Ilia Korobkov, and Dr. Tara Kell, I thank you all for your time to explain the basics of X-ray diffraction and train me to perform the experiments on my own. Bulat, thank you for your patience and kindness. You have always arranged some time slots for me when I rushed to get some works done, and you have always been there to help me out, even on Saturdays.

I would also like to express my gratitude to all the current and past members of the Bryce lab. It has been a greatest pleasure to work with them. Dr. Frédéric Perras, Dr. Kevin Burgess, and Dr Jasmine Viger-Gravel have always been my models in the lab. Your work attitudes are always inspiring. Thank you all for bringing the entire lab to a Korean BBQ restaurant on my birthday; that was a special birthday party. Fred, you are the person who explained all the foundations of the solid-state NMR spectroscopy, and you are the first person who showed me how to set up the NMR experiments. Jasmine, you are the person who opened up the halogen bonding interaction world to me, and thank you for mentoring me during my honor's project. Kevin, even though we did not work together, your comments and edits on my poster presentation and manuscripts are greatly appreciated.

My work has also been greatly influenced by the past postdoctoral fellows: Dr. Libor Kobera, Dr. César Leroy, and Dr. Vijith Kumar. Libor, thank you for teaching me various practical aspect of solid-state NMR experiments. César, thank you for helping me set up DFS experiments, which significantly reduced my single-crystal NMR experimental time. Also, I really appreciate you for introducing me to your French NMR community. Vijith, I am very thankful for your guidance in the synthetic chemistry, and it has been a great experience to work with you and publish several papers together.

I would also like to acknowledge all the past and current graduate students in Bryce lab: Dr. Patrick Szell, Scott Southern, Peter Werhun, Angel Wong, Vincent Morin, Shubha Gunaga, Tamali Nag, Christelle Hajjar. Pat, your patience and time to answer my questions, your suggestions and comments on

my presentation and manuscripts are greatly appreciated. Also, I am very thankful for the advice and experience that you gave to me to prepare for my comprehensive exam and research proposal. Scott, I thank you for your valuable help with my computational studies, and your punctuality has been truly motivating. Peter and Angel, we started our graduate studies together. All the time that we spent on surviving all the scientific obstacles, TA workload, graduate courses is extremely valuable to me. Thank you all for still keeping check up on me even after you left the lab. Vincent, Shubha, Tamali and Christelle, I want to thank you for all your comments and suggestions on my manuscripts, oral presentations, and also this dissertation. Good luck in your graduate studies.

Many undergraduate students have helped me a lot in my various projects: Lysiane Champion, Jasmine Huang, and Maressa Bradshaw. Lysiane, your time management kept our project moving efficiently. Jasmine, I am very impressed by your drive and organization skills. I value the friendship that we built during that time. Also, thank you for bringing me your homemade rice cake on Chinese New Year. That was a huge surprise for me after working overnight on New Year's Eve. Maressa, I am thankful to work with you this past year. Your corrections to my grammar in our last paper are very valuable.

I would also like to acknowledge my committee members for taking the time to review this dissertation.

Finally, I would like thank my friends and my family for their continuous support. I wish to express my deepest gratitude to my parents for their love and encouragement throughout my long studies. No matter what decision I made, they have always supported me with no doubt, and always been there for me whenever I needed them. I would not be where I am without them. Love you!

Statement of Authenticity

I hereby certify that the results presented in this dissertation are my own work. All ideas and references to other work are fully acknowledged. I acknowledge my supervisor Dr. David L. Bryce for his guidance in the research projects as well as being invaluable in the writing and editing of all the manuscripts. Dr. Jasmine Viger-Gravel is acknowledged for her guidance at the beginning of this halogen bonding project. Dr. Ilia Korobkov and Dr. Bulat Gabidullin are acknowledged for solving the single-crystal X-ray diffraction structures. I also acknowledge Ms. Lysiane Champion and Ms. Jasmine Huang in their assistance with the synthesis of some halogen bonded compounds as well as for the acquisition of routine ^{31}P NMR spectra. The following Chapters of this dissertation are based on published work in peer-reviewed journals:

Chapter 2-section 2.4: Xu, Y.; Gabidullin, B.; Bryce, D. L. Single-Crystal NMR Characterization of Halogen Bonds. *J. Phys. Chem. A* **2019**, *123*, 6194-6209.

Chapter 3: Xu, Y.; Viger-Gravel, J.; Bryce, D. L. Mechanochemical Production of Halogen-Bonded Solids Featuring P=O···I-C Motifs and Characterization via X-ray Diffraction, Solid-State Multinuclear Magnetic Resonance, and Density Functional Theory. *J. Phys. Chem. C* **2015**, *119*, 27104-27117.

Chapter 4: Xu, Y.; Huang, J.; Gabidullin, B.; Bryce, D. L. A Rare Example of a Phosphine as a Halogen Bond Acceptor. *Chem. Commun.* **2018**, *54*, 11041-11043.

Chapter 5: Xu, Y.; Gabidullin, B.; Bryce, D. L. Single-Crystal NMR Characterization of Halogen Bonds. *J. Phys. Chem. A* **2019**, *123*, 6194-6209.

Chapter 6: Xu, Y.; Bryce, D. L. SCFit: Software for Single-Crystal NMR Analysis. Free vs Constrained Fitting. *Solid State Nucl. Magn. Reson.* **2019**, *102*, 53-62.

Chapter 7: Xu, Y.; Champion, L.; Gabidullin, B.; Bryce, D. L. A Kinetic Study of Mechanochemical Halogen Bond Formation by In-situ ^{31}P Solid-State NMR Spectroscopy. *Chem. Commun.* **2017**, *53*, 9930-9933.

Table of Contents

List of Tables

List of Figures

List of Abbreviations

ADF	Amsterdam Density Functional
ALMO	absolutely localized molecular orbitals
a.u.	atomic units
B3LYP	Becke 3-parameter Lee Yang Parr
CASTEP	Cambridge Serial Total Energy Package
CCDC	Cambridge Crystallographic Data Centre
CP	cross polarization
CS	chemical shift
CSA	chemical shift anisotropy
CSD	Cambridge Structural Database
CT	central transition
DAS	dynamic angle spinning
DFS	double frequency sweep
DFT	density functional theory
DSO	diamagnetic spin orbital
DOR	double rotation
DZP	double zeta basis set with 1 polarization function
EFG	electric field gradient
FC	Fermi contact
FID	free induction decay
GGA	generalized gradient approximation
GIPAW	gauge-including projector-augmented wave
HB	hydrogen bond
HOMO	highest occupied molecular orbital
HPCVL	High Performance Computing Virtual Laboratory
IUPAC	International Union of Pure and Applied Chemistry
LDA	local density approximation
LUMO	lowest unoccupied molecular orbital

MAS	magic angle spinning
MO	molecular orbital
MQMAS	multiple quantum magic angle spinning
NBO	natural bond orbital
NLMO	natural localized molecular orbital
NMR	nuclear magnetic resonance
NOE	nuclear Overhauser effect
NQR	nuclear quadrupole resonance
PAS	principal axis system
PBE	Perdew Burke Ernzerhof
ppm	parts per million
PSO	paramagnetic spin orbital
PXRD	powder X-ray diffraction
rf	radiofrequency
revPBE	revised Perdew Burke Ernzerhof
SAPT	symmetry-adapted perturbation theory
SCXRD	single crystal X-ray diffraction
SD	spin dipolar coupling
SH	Sharp-Hancock
SSNMR	solid-state nuclear magnetic resonance
ST	satellite transition
TPSS	Tao Perdew Staroverov Scuseria
TZP	triple-zeta basis set with 1 polarization function
XB	halogen bond
ZORA	zeroth-order regular approximation

List of Symbols

a, b, c	unit cell dimensions
B_0	magnetic field strength
$\mathbf{B}_0$	magnetic field vector
B_1	radiofrequency magnetic field strength
B_{eff}	effective magnetic field
C_i	atomic orbital mixing coefficient
C_{Q}	quadrupolar coupling constant
D	dipolar coupling interaction
$\mathbf{D}$	dipolar coupling tensor
$d_{\text{X}\cdots\text{Y}}$	distance between the halogen bond donor and acceptor atoms
$\sum d_{vdW}$	sum of the van der Waals radii
e	fundamental charge
h	Planck's constant (6.62607×10^{-34} J·s).
$\hbar$	reduced Planck's constant
$\widehat{H}$	general Hamiltonian operator
$\widehat{H}_D$	direct dipolar coupling Hamiltonian
$\widehat{H}_J$	indirect nuclear spin-spin coupling Hamiltonian
$\widehat{H}_Q$	quadrupolar interaction Hamiltonian
$\widehat{H}_Q{}^{(1)}$, $\widehat{H}_Q{}^{(2)}$	the first, second order term of quadrupolar interaction Hamiltonian
$\widehat{H}_Z$	Zeeman interaction Hamiltonian
$\widehat{H}_\sigma$	magnetic shielding Hamiltonian
k	Boltzmann constant (1.3806×10^{-23} J·K^{-1})
k	rate constant
I	spin quantum number
I_0, I_t, I_{max}	normalized NMR peak integral
$\mathbf{I}$	spin angular momentum
$\hat{I}$, $\hat{I}_x, \hat{I}_y, \hat{I}_z$	angular momentum operator

J	indirect nuclear spin-spin coupling interaction
$\mathbf{J}$	J coupling tensor
J_{11}, J_{22}, J_{33}	principal components of the J coupling tensor
J_{iso}	isotropic J coupling constant
J_{xx}, J_{yy}, J_{zz}	Cartesian components of the J coupling tensor
m	magnetic quantum number
m_0, m_t	initial mass, mass at time t
$\mathbf{M}$	bulk magnetization vector
M_x, M_y, M_z	net magnetization along x, y, z axes
n	Avrami exponent
N	number of data points
N_{var}	number of optimized variables during fitting
N_α, N_β	Boltzmann population at lower or higher energy states
Q	nuclear electric quadrupole moment
$\boldsymbol{Q}$	intermediate nuclear quadrupole coupling tensor
Q_{xx}, $Q_{yy,}$ Q_{zz}	Cartesian components of the intermediate Q tensor
Q_{11}, $Q_{22,}$ Q_{33}	principal components of the intermediate Q tensor
r	internuclear distance
R_{DD}	dipolar coupling constant
R_{eff}	effective dipolar coupling constant
R_{XB}	normalized distance parameter
$R(\alpha, \beta, \gamma)$	rotation matrix
T_1, T_2	spin-lattice and spin-spin relaxation time constant
$\mathbf{V}$	EFG tensor
$V(r)$	electrostatic potential
$V_s(r)$	surface potential
$V_{S,max}$	maximum electrostatic potential
V_{xx}, $V_{yy,}$ V_{zz}	Cartesian components of the EFG tensor
V_{11}, $V_{22,}$ V_{33}	principal components of the EFG tensor

W_{jj}	coefficients of localized NBOs associated to the Lewis structures
α, β, γ	Euler angles
χ_i	atomic orbital
χ^2	reduced chi-square goodness-of-fit value
δ_{iso}	isotropic chemical shift
$\delta_{11}, \delta_{22}, \delta_{33}$	principal components of the chemical shift tensor
ΔB	reduced field
$\Delta\delta$	chemical shift difference
ΔJ	anisotropy of the *J* coupling tensor
$\Delta\nu$	difference in the splitting
ϕ_j^{NLMO}	NLMO orbital
γ	gyromagnetic ratio
η_Q	asymmetry parameter of the EFG tensor
η_J	asymmetry parameter of the *J* coupling tensor
$\vartheta, \phi, \vartheta', \phi'$	polar angles
κ	chemical shift tensor skew
$\boldsymbol{\mu}$	magnetic moment
μ_0	permeability constant
v_i^{exp}, v_i^{calc}	experimental and calculated data points
ν_0	Larmor frequency in Hz
ν_{MAS}	MAS spinning frequency
$\upsilon_{\frac{1}{2}\leftrightarrow-\frac{1}{2}}$	resonance frequency for the central transition
θ	rotation angles in the single-crystal NMR probe
θ_R	MAS rotation angle
$\theta_{R\text{-}X\ldots Y}$	R-X⋯Y halogen bond angle
$\rho(r)$	electronic density
σ	magnetic shielding

$\boldsymbol{\sigma}$	magnetic shielding tensor
σ_i	uncertainty in the measurement
$\boldsymbol{\sigma}_{Lab}$	magnetic shielding tensor in the laboratory frame
$\boldsymbol{\sigma}_{G}$	magnetic shielding tensor in the orthogonal goniometer system
$\sigma_{iso,ref}$	isotropic shielding constant of a reference sample
σ_{xx}, σ_{yy}, σ_{zz}	Cartesian components of the magnetic shielding tensor
σ_{11}, σ_{22}, σ_{33}	principal components of the magnetic shielding tensor
Ω	chemical shift tensor span
Ωn	a set of strongly localized NBOs that closely associate to the Lewis structure of the molecule
Ω_{off}	offset
ω_0	Larmor frequency in rad·s^{-1}
$\omega_{rot,frame}$	angular frequency in rotating frame
Ψ	wavefunction

PART 1 : OBJECTIVES AND INTRODUCTION

Objectives

The importance of halogen bonding continues to be demonstrated in a variety of research areas, in large part due to its directionality, tunability, and strength. Diverse applications include those found in the fields of crystal engineering, functional materials, organocatalysis, and biological systems. Therefore, Chapter 1 includes the classification of chemical bonds and non-covalent interactions followed by an introduction of the halogen bond. The history and the nature of halogen bonding will be provided along with a focus on its diverse applications.

NMR is increasingly used to probe the formation of halogen bonds in solution and in the solid state. Due to the orientation dependence of the NMR interactions in polycrystalline samples, the NMR observables in the solid state can yield a wealth of information about the local electronic structure relative to the halogen bond. Chapter 2 will cover the basic theory of NMR and the experimental methods applied to characterize halogen-bonded compounds. In this thesis, density functional theory (DFT) calculations were also used to complement the experimental NMR results; therefore, an introduction of the relevant DFT methods will also be provided.

The overall objective of this dissertation is to investigate the halogen bonding interaction from three perspectives: changes in (1) the magnitude and (2) the orientation of various NMR tensors relative to the local geometry of the halogen bonding interaction, and (3) the crystallization process associated with halogen bond formation.

Following the Part 1 of Introduction, the goal of Part 2 is to perform polycrystalline solid-state NMR experiments to observe the changes in the magnitude of various NMR

tensors, caused by the formation of halogen bonds, and to understand the correlation between the electronic structure of halogen bond and the resulting NMR properties. Chapter 3 will focus on the characterization of mechanochemically synthesized cocrystals featuring halogen bonds between phosphine oxides and a series of diiodoperfluorobenzene derivatives. Multinuclear magnetic resonance spectroscopy (^{31}P and ^{17}O) will provide both indirect and direct insights into the correlation between the several NMR observables (chemical shift, quadrupolar interaction, and *J* coupling) and the geometry of the halogen bond. Quantum chemical calculations can provide a great understanding of the origins of the NMR interactions and the electronic structures of the halogen bonds. In Chapter 3, the influence of halogen bonding interaction on ^{31}P chemical shifts is not clear since the phosphorus is only indirectly involved in the halogen bond when phosphine oxide acts as a halogen bond acceptor. ^{31}P, a spin-1/2 nucleus with a 100% natural abundance and a broad chemical shift range, motivated us to design cocrystals featuring phosphorus as a halogen bond acceptor so that ^{31}P NMR can be used as a direct probe for the formation of halogen bond. Chapter 4 will describe a rare halogen-bonded cocrystal featuring a phosphorus-iodine halogen bond. Halogen bonding can be characterized by single-crystal X ray diffraction as well as both solution and solid-state NMR experiments.

The goal of Part 3 is to investigate the changes in not only the magnitude but also the orientations of NMR tensor as a result of halogen bonding interaction, which can provide a novel connection between the electronic structure and the halogen bonding interaction. Chapter 5 provides the first single-crystal NMR studies of halogen bonds. We apply ^{31}P and ^{17}O single-crystal NMR experiments to the ^{17}O-labeled halogen bond acceptor triphenylphosphine oxide ($Ph_3P^{17}O$) and its halogen-bonded cocrystals featuring

two different iodoperfluorobenzene compounds: 1,4-diiodotetrafluorobenzene and 1,3,5-trifluoro-2,4,6-triiodobenzene. By rotating a large (on the order of mm) single crystal stepwise about three orthogonal axes perpendicular to the magnetic field and fitting the plots of the frequency as a function of rotation angles, the orientation of several anisotropic NMR tensors (^{31}P chemical shift, ^{17}O chemical shift, and quadrupolar coupling tensor) in the crystal frame can be obtained. Anisotropy of *J* coupling between ^{31}P and ^{17}O can also be measured experimentally. Gauge-including projector-augmented wave (GIPAW) calculations will validate the experimental findings. Chapter 6 introduces single-crystal NMR analysis software, SCFit, which includes the analysis of dipolar and indirect spin-spin coupling, chemical shift, and quadrupolar coupling interaction. Two fitting strategies are explored to provide an extra check on the quality and consistency of the NMR results obtained from both polycrystalline and single-crystal NMR experiments.

The objective of Part 4 is to study the reaction mechanism behind the mechanochemical formation of halogen bond and to estimate the activation energy. In Chapter 7, we develop an in situ ^{31}P solid-state NMR study of halogen bonds between triphenylphosphine oxide and 1,4-diiodotetrafluorobenzene. By varying the temperature inside the NMR probe, the spinning speed of the sample, and different amounts of liquid to initiate the reaction, ^{31}P in situ SSNMR can provide an opportunity to observe the different formation rates of two cocrystals, to determine the mechanism of the halogen bond formation, and to observe the effect of different conditions on monitoring the halogen bond formation. The temperature dependence of the reaction rate is used to estimate the activation energy.

Chapter 1. Introduction to σ-Hole Interaction

1.1 Chemical Bonds

The behaviour of matter really depends on how atoms and/or ions bond. Chemical bond is the general term used to describe the forces that hold atoms together to form ions and molecules. If we look at the periodic table, across a period and up a group, there is a gradual transition from more metallic elements to more nonmetallic elements. There are three types of bonding resulting from the three ways these two types of atoms can combine: covalent bond (nonmetal with nonmetal), ionic bond (nonmetal with metal), and metallic bond (metal with metal).[1] The covalent bond results from the sharing of the electrons between the two atoms. Based on quantum mechanics, this can also be described as a pair of electrons occupying the overlap region of the orbitals of two atoms to give a molecular orbital. The ionic bond involves the transfer of valence electrons from metal to nonmetal and results in the attraction between two oppositely charged ions. Metals have low ionization energies. As a result, the valence electrons can be delocalized throughout the metal. The delocalized electrons are not only associated with one particular nucleus of the metal; instead, they freely move throughout the entire crystalline structures to form an "electron sea".[1] Therefore, the positively charged metal atoms and surrounding delocalized electrons attract each other to form metallic bonds. Covalent, ionic, and metallic bonds are usually considered short-range interactions with typical interatomic distances below 1.5 Å. Unlike these bonds, which give rise to a new molecule, non-covalent interactions tend to draw the molecules together with a closest intersystem distance of about 2 Å.[2] Non-covalent interactions are considerably weaker (by 1 or 2 orders of magnitude) than the covalent interaction.[3]

There are many classifications of intermolecular force in the literature (such as long- and short-range interactions, electrostatic interaction, polarization, van der Waals, etc.). Here I will classify the intermolecular forces in the most common way: dipole force, induced dipole force, hydrogen bonding force, and London (dispersion) force.

Chemical bonds tend to be polarized towards the more electronegative atoms. A molecule with this asymmetrical distribution of electron density has a dipole moment with a partial negative charge on the more electronegative atom and a partial positive charge on the less electronegative atom. The attractive force between the partial positive charge in one molecule and the partial negative charge in another molecule is the dipolar force. When an ion or a permanent dipole approaches a non-polar molecule, it can induce the rearrangement of the electron distribution of the non-polar molecule and form a temporary dipole. The attractive interaction between an ion or a permanent dipole and an induced dipole is induced dipole force. The International Union of Pure and Applied Chemistry (IUPAC) has established the hydrogen bond as "an attractive interaction between a hydrogen atom from a molecule or a molecular fragment X-H in which X is more electronegative than H, and an atom or a group of atoms in the same or a different molecule."[4] The typical hydrogen bond strength ranges from 16 kJ/mol to 120 kJ/mol and can reach a mostly covalent level such as in the HF_2 ion (170 kJ/mol).[3] Due to the constant movement of the electrons, a temporary dipole can be formed within the molecule. The attractive interaction between the temporary dipoles is the dispersion interaction, which is the weakest intermolecular force (0.1 kJ/mol ~ 5 kJ/mol).

1.2 **Halogen Bonding Interaction**

1.2.1 History of Halogen Bonding Interactions

The recognition of a halogen bonding interaction can be traced back to two centuries ago. As early as 1814, adduct formation between iodine and ammonia was observed by Colin first,[5] and this complex was further identified as $NH_3\cdots I_2$ by Guthrie 50 years later.[6] Shortly after Colin's report, in 1819 Pelletier and Caventou reported the first experimental evidence revealing the ability of dihalogens to interact with anions. In this study, they synthesized triiodide I_3^-, which was formed via the interaction of $I_2\cdots I^-$.[7] The formation of halogen bonds involving bromine and chlorine was firstly reported by I. Remsen and J. F. Norris, who described the formation of 1:1 dimers between Br_2 and Cl_2 with various amines.[8] Later studies in analogous complexes with dihalogens followed. Benesi and Hildebrand, in 1948, published the first donor-acceptor molecule featuring interactions between I_2 and aromatic hydrocarbons.[9] In 1950, R. S. Mulliken (Nobel Prize in Chemistry, 1966) reported similar complexes with ether, thioether, and carbonyl derivatives and ascribed the interaction to intermolecular charge transfer process.[10,11]

The X-ray crystallographic studies by O. Hassel (Nobel Prize in Chemistry, 1969) were crucial in identifying the intermolecular interaction occurring between dihalogens and several electron donors. In 1954, Hassel and Hvoslef revealed the structure of the bromine-dioxanate adduct, observed the elongation of Br-Br bond, and measured the Br···O bond distance.[12] Later he also reported the crystal structures of $Br_2\cdots C_6H_6$[13] and $Cl_2\cdots C_6H_6$[14], and described the interaction of the methanol-bromine adduct as featuring a "halogen molecular bridge"[15]. In his Nobel lecture, he summarized his results and showed the importance of halogen atoms in molecular assembly phenomena.[16]A review published by H. A. Bent in

1968 highlighted the most distinctive geometric features of this interaction: (1) the distance between the halogen atom and electron donor atom were shorter than the sum of their van der Waals radii; (2) the angle between this short intermolecular interaction and the adjacent intramolecular interaction is approximately 180°.[17] Halogen bonding involving F_2 was not established until 1977 when the most reactive member among trihalides, F_3^-, was isolated under extreme conditions (in argon matrices at 15 K).[18] In early 1970s, infrared measurements showed that halogen bonds can compete with hydrogen bonds, and the order of hydrogen bond-breaking potency in the order of F < Cl < Br < I implied the halogen bonding strength scales in the order of F < Cl < Br < I.[19] In 1983, Dumas et al. were the first to use name *halogen bonding* to describe the interactions involving CCl_4, CBr_4, $SiCl_4$, and $SiBr_4$ with pyridine, tetrahydrofuran, tetrahydropyran, and anisole and analyzed them with a variety of techniques (*e.g.*, UV-Vis, IR, Raman, NMR, etc.)[20] Legon and coworkers were the first to provide a systematic analysis of a variety of halogen-bonded systems in the gas phase to show the similarities between halogen bonding and hydrogen bonding using high-resolution microwave spectroscopy.[21] Recently, astatine has also been found to exhibit halogen bonding and its halogen bond donor ability is observed to be greater than iodine.[22]

Gradually, the nature and applications of halogen bonding started to be extensively studied. Currently there have been a wide range of applications of halogen bonds across various fields.[23,24]

1.2.2 Definition of The Halogen Bond

An IUPAC definition states halogen bonding is “a net attractive interaction between an electrophilic region associated with a halogen atom in a molecular entity and a

nucleophilic region in another, or the same, molecular entity". [25] A schematic representation displaying halogen bonding is provided in Figure 1.2.1. Two geometric features of the halogen bond are: (1) the distance between the halogen bond (X) donor and the nucleophilic atom (Y) tends to be less than the sum of the van der Waals radii ($d_{X\cdots Y} \leq \sum d_{vdW}$); (2) halogen bond angle ($\theta_{R\text{-}X\ldots Y}$) tends to approach 180˚. One of the parameters used to characterize halogen bonds is the normalized distance parameter (R_{XB}), which is the ratio of the short contact distance between the halogen bond donor (X) and halogen bond acceptor (Y) to the sum of their van der Waals radii (Eq 1.2.1). Since halogen bonds can involve atoms with different size, it would be meaningless to just compare bond distances. However, the R_{XB} value can be used to compare bond lengths across different bond donor/acceptor atoms. A smaller value represents a shorter bond and a bigger value represents a longer bond. It is a qualitative measurement, but it does not necessarily represent the strength of the halogen bond since bond strength can be affected by secondary effects, such as stabilization by additional interactions such as hydrogen bonding.[26]

$$R_{XB} = \frac{d_{X\cdots Y}}{\sum d_{vdW}} \qquad \text{Eq 1.2.1}$$

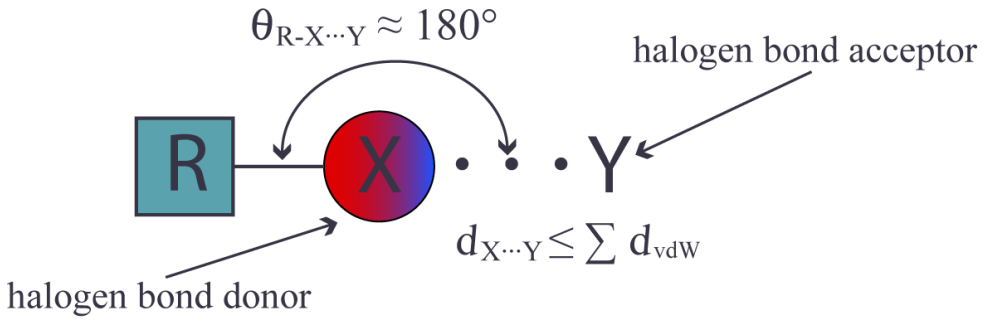

Figure 1.2.1. Schematic representation of a halogen bonding interaction. X = F, Cl, Br, I At. R represents the electron-withdrawing group. Y represents the electron-rich moiety. Colour gradient represents the anisotropic distribution of electron density on the halogen atom, where the blue area is the electrophilic region, σ-hole.

The σ-hole concept, which was first introduced by Politzer,[27] rationalized the role of the halogen atom acting as an electrophile in this interaction. Based on their position in the periodic table, the halogen group contains the more electronegative elements of the periodic table, and covalently bonded halogen atoms are usually considered to be electron-withdrawing groups. The electrostatic potential $V(r)$ at any point in the molecule is given by:

$$V(r) = \sum_A \frac{Z_A}{|R_A - r|} - \int \frac{\rho(r')dr'}{|r' - r|} \qquad \text{Eq 1.2.2}$$

where Z_A is the charge on the nucleus A, located at R_A, $\rho(r)$ is the electronic density of the molecule at r. r' designates the infinite number of points in space.

A free ground-state atom has a spherically symmetric positive electrostatic potential due to the nuclear attraction being dominant over the surrounding electrons.[28,29] When atoms are bonded, the surrounding electronic density will be rearranged, becoming polarized towards the bonding region and resulting in less electron density at the bond

terminus. For halogen atoms covalently bonded to an electron-withdrawing group R, three unshared pairs of electrons form a negative electrostatic potential around the central region of the halogen atom, generating a positive electrostatic potential on the outermost surface at elongation of the R-X bond, known as the σ-hole. [27] In order to visualize this anisotropic charge distribution, the electrostatic potential $V(r)$ is plotted on the molecular surface, which is often taken to be the 0.001 a.u. (electrons $Bohr^{-3}$) contour of the electron density $\rho(r)$. This surface potential is usually designated as $V_S(r)$.

Figure 1.2.2 displays the calculated molecular electrostatic potential on the 0.001 a.u. isodensity surface of hexafluorobenzene, chloropentafluorobenzene bromopentafluorobenzene, and iodopentafluorobenzene. Fluorine has a negative hemisphere, with a maximum electrostatic potential value ($V_{S,max}$) of -13 kJ/mol. However, when chlorine is substituted, a positive potential (shown in blue) develops at the outmost region of its surface, along the elongation of the Cl-C bond. The size of this positive potential region increases with the size of the halogen atom: F < Cl < Br < I; so is the positivity of this region: F ($V_{S,max}$ = -13 kJ/mol) < Cl ($V_{S,max}$ = +82 kJ/mol) < Br ($V_{S,max}$ = +105 kJ/mol) < I ($V_{S,max}$ = +138 kJ/mol).

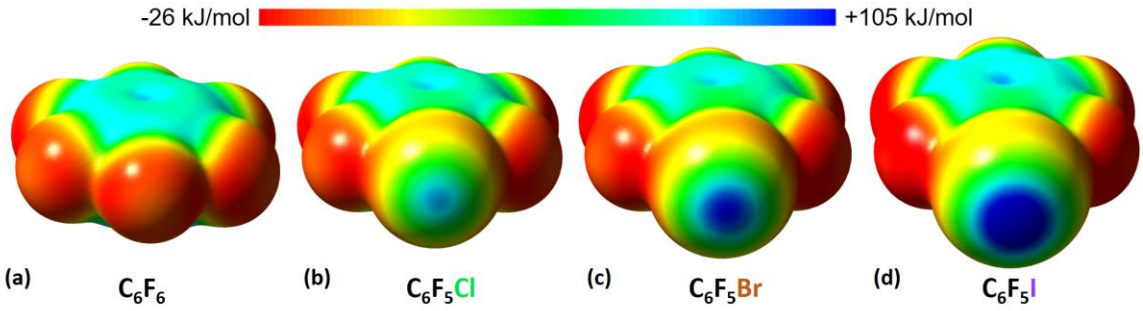

Figure 1.2.2. The DFT calculated molecular electrostatic potential at the 0.001 a.u. isodensity surface of hexafluorobenzene (a), chloropentafluorobenzene (b), bromopentafluorobenzene(c), and iodopentafluorobenzene (d). Color ranges in kJ/mol: red is more negative and blue is more positive. The calculations were performed using B3LYP with def2-TZVP basis set for iodopentafluorobenzene and 6-311++G basis set for all the other compounds.

It is this σ-hole that is responsible for the key features of halogen bonding, since this non-covalent interaction is a result of the polarization of the halogen atom's electron density towards the covalent bond. Things that can improve this polarization can strengthen the halogen bonding interaction: introducing electron-withdrawing groups and / or improving the polarizability of the halogen atom itself. Therefore, the strength of the halogen bonding interaction can be fine-tuned by attaching different electron-withdrawing groups or by changing the halogen bond donor atom. This was demonstrated by the $V_{S,max}$ on iodine in CH_3-I vs. CF_3-I vs NC-I, which increases in the order CH_3-I < CF_3-I < NC-I.[30,31] Tunability makes halogen bond interaction cover a wide energy ranges, varying from 5 kJ/mol (*e.g.*, N···Cl contact in azaaromatic chloride compounds[32,33]) to 150 kJ/mol (*e.g.*, the very strong interaction observed in I_2···I^- adduct[34]), which is comparable to or sometimes even stronger than hydrogen bonds. Also, the formation of a σ-hole on the elongation of an R-X covalent bond makes halogen bonding highly directional, where the

R-X···Y angle between the covalent bond and non-covalent interaction around the halogen is approximately 180°.

As discussed above, the σ-hole concept, introduced by Politzer,[27] has been commonly used to rationalize the behaviour of the halogen as an electrophile in the interaction. However, there are examples of halogen bonding interactions that cannot be simply explained by the σ-hole or electrostatic concepts. In the case of $CX_3I\cdots X'$ complexes (where X, X' = F, Cl, Br, I), the highest polarization and greatest σ-hole correlates with a weaker interaction instead.[35]

As stated in the IUPAC definition of halogen bonding, "the forces involved in the formation of the halogen bond are primarily electrostatic, but polarization, charge transfer, and dispersion contributions all play an important role."[25] Some of the charge transfer character present in halogen bonding have been summarized: 1) UV-Vis spectral features of complexes containing CBr_4 with different XB acceptors demonstrate the linear dependence of their absorption energy with the oxidation potential of the acceptors, which is the most characteristic feature of charge transfer; 2) a charge transfer to the σ* orbital of the C-Br bond was also confirmed by X-ray diffraction analysis, which showed the lengthening of the C-Br bond.[36] Moreover, Vinakos and his coworkers visualized the highest occupied molecular orbitals (HOMO) of bromometallates and compared the C-$Br\cdots Br^-$ halogen bond direction with the electrostatic potential surface and molecular orbital shapes.[37] The results pointed out that the halogen bonds directed toward HOMO/LUMO overlap and demonstrated the importance of the covalent component in halogen bonding. To investigate the origin of the attractive interaction occurring in halogen-bonded complexes, the intermolecular interaction energy was partitioned into four

additive energy terms by symmetry-adapted perturbation theory (SAPT) and its density functional theory version (DFT-SAPT): electrostatic, induction or polarization, dispersion and exchange repulsion.[38] This method was applied to a series of $H_nF_{3-n}CBr\cdots NH_3$ complexes to generate binding energy decomposition curves, which highlighted the important contribution from the dispersion and electrostatics term to the stabilization of halogen bonds, with a small contribution from induction.[39] This was confirmed by a more recent variational energy decomposition analysis based on absolutely localized molecular orbitals (ALMO-EDA) conducted on the interaction energy composition of the CX_3-I·· halides by Head-Gordon group.[40]

1.2.3 Applications of Halogen Bonding Interactions

As a result of the strength of halogen bonding and its tunability and linearity, this interaction has been a very powerful tool in diverse research fields, such as crystal engineering, functional material, organocatalysis, and biological systems.

Crystal Engineering

Supramolecular chemistry might be defined as “chemistry beyond molecules”, which studies the ensemble of two or more chemical species held by intermolecular forces to form supermolecules with higher complexity.[41] Crystal engineering is a branch of supramolecular chemistry. The definition of crystal engineering presented by Desiraju stated that, “crystal engineering is the understanding of intermolecular interactions in the context of crystal packing and the utilization of such understanding in design of new solids with desired physical and chemical properties.”[42] The halogen bond has become a very popular supramolecular synthon in the field of crystal engineering.[43,44] The directionality

and tunability of halogen bonding can be successfully employed as a general protocol to drive the self-assembly of molecular modules in supramolecular chemistry.[44,45,46,47]

As mentioned above, halogen bond angles tend to be close to 180°. This angle can determine the halogen-bonded adduct geometry. 1D halogen-bonded structures can be obtained from either homomeric systems, in which molecules containing both bonding donor and acceptor sites can self-assemble, or heteromeric systems, in which a ditopic halogen bond donor and a ditopic halogen bond acceptor self-assemble to form halogen bonding interaction.[24] Figure 1.2.3 shows some examples of homomeric and heteromeric halogen-bonded one dimensional chains. The heteromeric 1D chain system is the most commonly designed complex among the halogen-bonded cocrystals. The geometry can be fine-tuned by changing the substitution positions. If the axes of bond donor and acceptor sites are parallel and coaxial, an infinite chain with linear geometry will be formed. If binding sites are parallel but not colinear, a stepped infinite chain will be formed instead. If the axes of halogen bond donors or the axes of the halogen bond acceptor sites are not parallel, zigzag arrangements will be formed.

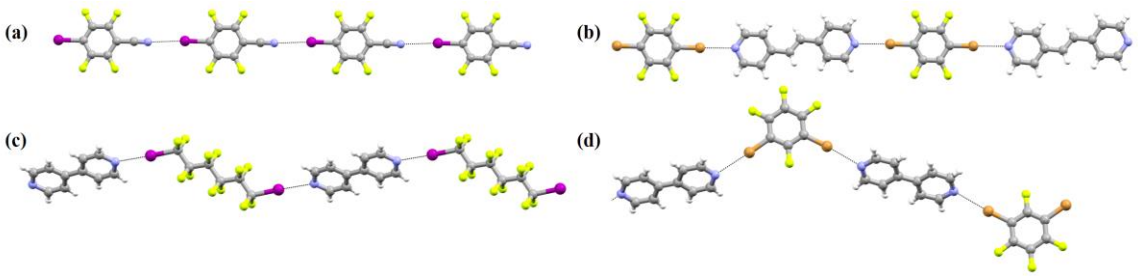

Figure 1.2.3. Single-crystal structures of one-dimensional chain: linear chain formed in (a) homomeric system of 4-[2-[1-hexyl-5-[2-(tetrafluoro-4-iodophenyl)-vinyl]-1*H*-pyrrol-2-yl]vinyl]pyridine (CSD Refcode: ACOKIM), and (b) heteromeric system of 4,4'-vinylenedipyridine and 1,4-dibromotetrafluorobenzene (CSD Refcode: IKUHUR), (c) a stepped chain formed in heteromeric system of 4,4'-dipyridyl and 1,6-

diiodoperfluorohexane (CSD Refcode: LOQBAU), and (d) a zigzag chain formed in heteromeric system of 4,4'-dipyridyl and 1,3-dibromotetrafluorobenzene (CSD Refcode: IKUJIH).

Increasing the number of halogen bond donor/acceptor sites and building the binding site to be oriented in such a way to display desired interacting pattern has been applied to extend the one-dimensional system to two-dimensional and/or three-dimensional networks. Pigge and coworkers reported an infinite honeycomb-like layer formed by the self-assembly of a self-complementary molecule 1,3,5-tris(4-iodophenoxycarbonyl)benzene.[48] The bifurcated I···O and I···π halogen bonds give rise to a 2D hexagonal patterns arranged in a parallel fashion. Porphyrin-based supramolecular architectures, which can act as both halogen bond donor and acceptor, are also able to construct 2D networks via halogen bonds.[49,50,51] F. Silly demonstrated concentration-dependent assembly of 1,3,5-tris(4-iodophenyl)benzene at the 1-phenyloctane/graphite surface.[52] The molecules orient along the same direction and self-assemble into a hexagonal porous network at low concentration (< 10^{-9} M), whereas at high concentration (10^{-6} M) the adjacent molecules are antiparallel to each other and form a porous parallelogram halogen-bonded structure. Hu et al. demonstrated the effect of variation in the position and number of the halogen substituents on the aromatic framework on the outcome of their self-assembly.[53] There are also few examples of 2D open porous networks constructed by halogen-heteroatom interactions. Zheng et al. reported for the first time the formation of a halogen bond based open porous networks formed from the halogen bond between 1,3,5-tris(pyridine-4-ylethynyl)benzene and perfluoro-iodobenzenes.[54] Further study has been performed by Mali and coworkers to observe the 2D networks formed by the halogen bond between 1,3,5-tris[(4-pyridyl)ethynyl]mesitylene and

perfluoroiodobenzenes by modifying the position and number of the XB donor and acceptor in iodobenzonitrile derivatives.[55]

Three-dimensional halogen-bonded networks can be formed when one or both of the modules are tetradentate.[24] For example, tetrabromomethane can form 3D "diamondoid" networks with electron-rich halide anions.[56] Ayhan and coworkers varied the number and position of iodine (XB donor) and nitrile groups (XB acceptors) in iodophthalonitrile derivatives, which self-assembled to different supramolecular architectures: varying from two-dimensional layer to three-dimensional triple helix spiral staircase.[57]

Functional Materials

The great potential of halogen bonding in the design of new and high-value functional materials is now emerging.[58,59,60,61,62] For example, halogen bonding has been a promising tool to design and induce the formation of liquid crystals (an intermediate state between the isotropic liquid and crystalline solid phase).[63] Nguyen et al. reported the first halogen-bonded liquid crystal, in which alkoxystilbazole acted as the halogen bond acceptor and pentafluoroiodobenzene acted as the halogen bond donor.[64] Xu et al. reported a trimeric liquid crystal which was stabilized by halogen bonds between the bis(diiodotetrafluorophenol)alkane halogen-bond donor and alkoxystilbazole halogen-bond acceptor.[65] Halogen bonding has also been applied to prepare polymeric liquid crystals.[66] Recently, Saccone et al. changed the degree of fluorination at photoresponsive halogen-bond donors to fine-tune the halogen bond strength and thereby provided control over the temperature range of the mesophase.[67] Halogen bond-driven cocrystal formation has also been used as a design element in the optical or photoresponsive materials.[68] C-

I···π halogen bonding was exploited in the phosphorescent cocrystals assembled by 1,4-diiodotetrafluorobenzene with fluorene and its heterocyclic analogues,[69] carbazole,[70] naphthalene, and phenanthrene.[71] In addition to incorporation in phosphorescent compounds to form cocrystals, purely organic crystals were also designed to demonstrate phosphorescence that can be tuned by the presence of halogen bonding in the crystal.[72]

Halogen bonding has been proven very efficient in engineering conducting or magnetic molecular materials.[73,74] Halogenated radical species acting as halogen bond donors, such as iodinated tetrathiafulvalene derivatives, can interact with different counterions to yield a family of highly conducting, halogen-bonded salts.[75,76,77] The introduction of halogen bonding interactions involving radical molecules, which act as halogen bond acceptors, has been found in isoindoline-based nitroxide,[78,79] and nitronyl nitroxide radicals[80] with perfluoro-iodobenzenes. Jin and coworkers reported halogen bond-induced modulation of crystal packing of cocrystals between [4-(benzoyloxy)-2,2,6,6-tetramethylpiperidin-1-yl]oxy free radicals with different substituted perfluoro-iodobenzenes, and the introduction of halogen bonding also strengthened the magnetic coupling.[81] Recently, Mercuri et al. have highlighted the roles of halogen bonding in tailoring the magnetic properties of molecular materials.[82]

Organocatalysis

Examples of hydrogen-bonding-donating organocatalysts are prevalent in the literature.[83,84,85,86] The similarities between hydrogen bonding and halogen bonding led researchers to start investigating the possible use of halogen bond donors as catalysts in organosynthesis.[87,88,89] From a structural point of view, halogen bonding is more directional and tunable compared to hydrogen bonding. From a catalytic point of view,

since halogen bond donors are usually polyfluorinated and thereby relatively non-polar, they can be used for applications in systems that rely on low polarity whereas hydrogen bonding systems are not efficient in such conditions.[90]

The first halogen-bonding based halide abstraction reactions were reported in the Ritter-type solvolysis of benzhydryl bromide in acetonitrile, in which acetonitrile acts as both solvent and nucleophile.[87] In 2011, the Huber group reported a dicationic haloimidazolium halogen bond donor which promotes halide abstraction in the Ritter reaction with acetonitrile. The high yield of up to 80% was achieved in the presence of a stoichiometric amount of this bidentate XB donor.[91] Later they also demonstrated the catalytic ability of multidentate 4,4'-azobis(halopyridinium) derivatives[92] and 5-iodo-1,2,3-triazolium-based halogen bond donors[93] in this type of secondary halides activation. Very recently, Aakeröy and coworkers synthesized a neutral iodoethynyl-based multidentate halogen-bond donor and used it as an organocatalyst also in a benchmark Ritter-type solvolysis reaction.[94] The addition of a stoichiometric amount of this catalyst yielded 90% conversion from starting material to the product after 96 hours. The use of non-halogenated analogue and a weaker halogen-bond donor in the reaction confirmed that the source of this catalytic activity is halogen bonding interaction. In addition to solvolysis of the intermediate in Ritter-type reaction, 1,2,3-triazolium-based halogen bond donors can also activate the C-Br bond of benzhydryl bromide to generate the benzhydryl cation in a halide-abstraction-induced Friedel-Crafts alkylation reaction, where the benzhydryl cation will be further attached to one equivalent of nucleophile 1,3,5-trimethoxybenzene.[95]

The utilization of a halogen bond donor as an organocatalyst has been also applied to other types of reactions: such as Diels-Alder reaction,[96] Michael addition reaction[97,98]

and so on. Furthermore, it has been theoretically and experimentally showed an increase in anion binding from halogen to chalcogen and ultimately to pnictogen bonding and this trend was also applied to an increased catalytic activity for C-Cl bond activation.[99]

Biological systems

Halogen bonds are not limited only to applications in functional materials and synthetic chemistry; as a stabilizing inter- and intramolecular interaction, they can also affect ligand binding and molecular folding, which has been applied to biochemical processes, drug design, and medicinal chemistry.[23,24,100,101]

One of the first clear examples of Br···O contacts in biological systems was in the structure of a four-stranded Holliday junction.[102] A Holliday junction is a four-stranded cross-shaped intermediate structure formed during genetic recombination.[103] Ho and coworkers introduced the DNA sequence CCAFTACBr^{5}UGG by substituting a thymine with a 5-bromouracil in order to phase crystallographic data.[102] The Br···O halogen bond facilitated formation of the four-stranded Holliday junction. Furthermore, they manipulated a conformational switch between the halogen bond and hydrogen bond in a four-stranded Holliday junction by replacing a cytosine with a 5-bromouracil.[104] A Br···O halogen bond was observed between brominated uracil and the oxygen atom of a phosphate group on the DNA backbone, which competed against the conventional hydrogen bonding formed from cytosine. The halogen-bonded structure was estimated to be about 5 kcal/mol more stable than the hydrogen-bonded structure.

Halogen bonding was also observed in the structure of epidermal growth factor receptor mutant in a complex with its halogenated inhibitor,[105] which demonstrated the significance of halogen bonding in antitumor targets. Halogen bonds are also applicable in

protein engineering. Danelius et al. have designed a 10-amino acid model system in which a chlorine-centered halogen bond was incorporated and provided a conformational stabilization compared to that of a hydrogen bond analogue.[106] The iodinated thyroid hormones contain naturally occurring I···O halogen bond, which plays an important role in molecular recognition of thyroid hormones to their transporter proteins.[107] The potential of halogen bonds in molecular recognition of small molecules in protein complexes makes halogen bonding an important interaction to be taken into account in drug design.[108,109,110] For example, Wei and coworkers designed different nitrilase enzymes, which can catalyze the hydrolysis of nitriles to the corresponding acids during biosynthesis.[111] The selective substrate recognition, resulting from different halogen bonding interactions present in the substrate-enzyme binding pocket, can selectively synthesize *para*-, *ortho*-, *meta*-chlorophenylacetic acid, which provides an efficient tool in enzymatic drug synthesis.

1.3 References for Chapter 1

[1] Silberberg, M. *Chemistry: The Molecular Nature of Matter and Change*; McGraw-Hill: New York, 2012.

[2] Novoa, J. J.; D'Oria, E.; Carvajal, M. A. Understanding the Nature of the Intermolecular Interactions in Molecular Crystals. A Theoretical Perspective. In *Making Crystals by Design, Methods, Techniques and Applications*; Braga, D., Grepioni, F., Eds.; Wiley-VCH Verlag GmbH: Weinheim, Germany, 2007; pp 25–57.

[3] Varshey, D. B.; Sander, J. R. G.; Friščić, T.; MacGillivray, L. R. Supramolecular Interactions. In *Supramolecular Chemistry: From Molecules to Nanomaterials*; Gale, P. A., Steed, J. W., Eds; Wiley & Sons: New York, 2012.

[4] Desiraju, G. R. A Bond by Any Other Name. *Angew. Chem., Int. Ed.* **2011**, *50*, 52–59.

[5] Colin, M. Note Sur Quelques Combinaisons de L'iode. *Ann. Chim.* **1814**, *91*, 252–272.

[6] Guthrie, F. On the Iodide of Iodammonium. *J. Chem. Soc.* **1863**, 239–244.

[7] Pelletier, P.; Caventou, J. Sur Un Nouvel Alcali Vegé Tal (La´ Strychine) Trouvé Dans La Feve de Saint-Ignace, La Noix Vomique` Etc. *Ann. Chim. Phys.* **1819**, *10*, 142–177.

[8] Remsen, L.; Norris, J. F. Action of the Halogens on the Methylamines. *Am. Chem. J.* **1896**, *18*, 90–95.

[9] Benesi, H. A.; Hildebrand, J. H. Ultraviolet Absorption Bands of Iodine in Aromatic Hydrocarbons. *J. Am. Chem. Soc.* **1948**, *70*, 2832–2833.

[10] Mulliken, R. S. Structures of Complexes Formed by Halogen Molecules with Aromatic and with Oxygenated Solvents. *J. Am. Chem. Soc.* **1950**, *72*, 600–608.

[11] Mulliken, R. S. Molecular Compounds and Their Spectra. III. The Interaction of

Electron Donors and Acceptors. *J. Phys. Chem.* **1952**, *56*, 801–822.

[12] Hassel, O.; Hvoslef, J. The Structure of Bromine 1,4-Dioxanate. *Acta Chem. Scand.* **1954**, *8*, 873–873.

[13] Hassel, O.; Strømme, K. O. Structure of the Crystalline Compound Benzene-Bromine (1:1). *Acta Chem. Scand.* **1958**, *12*, 1146–1146.

[14] Hassel, O.; Strømme, K. O. Crystal Structure of the Addition Compound Benzene-Chlorine (1:1). *Acta Chem. Scand.* **1959**, *13*, 1781–1786.

[15] Groth, P.; Hassel, O. The 2:1 Addition Compound Methanol-Bromine, a Crystalline Substance Exhibiting Both Hydrogen and Halogen Molecule Bridges between Oxygen Atoms. *Acta Chem. Scand.* **1964**, *18*, 402–408.

[16] Hassel, O. Structural Aspects of Interatomic Charge-Transfer Bonding. *Science* **1970**, *170*, 497–502.

[17] Bent, H. A. Structural Chemistry of Donor-Acceptor Interactions. *Chem. Rev.* **1968**, *68*, 587–648.

[18] Ault, B. S.; Andrews, L. Infrared and Raman Spectra of the $M^+F_3^-$ Ion Paris and Their Mixed Chlorine-Fluorine Counterparts in Solid Argon. *Inorg. Chem.* **1977**, *16*, 2024–2028.

[19] Di Paolo, T.; Sandorfy, C. On the Hydrogen Bond Breaking Ability of Flurocarbons Containing Higher Halogens. *Can. J. Chem.* **1974**, *52*, 3612–3622.

[20] Dumas, J. M.; Gomel, M.; Guerin, M. Molecular Interactions Involving Orgainic Halides. In *Halides, Pseudo-Halides and Azides*; Patai, S., Rappoport, Z., Eds.; John Wiley & Sons Ltd: Chichester, U. K., 1983; pp 985–1020.

[21] Legon, A. C. Prereactive Complexes of Dihalogens XY with Lewis Bases B in the Gas

Phase: A Systematic Case for the Halogen Analogue B···XY of the Hydrogen Bond B···HX. *Angew. Chem., Int. Ed.* **1999**,*38* , 2686–2714.

[22] Guo, N.; Maurice, R.; Teze, D.; Graton, J.; Champion, J.; Montavon, G.; Galland, N. Experimental and Computational Evidence of Halogen Bonds Involving Astatine. *Nat. Chem.* **2018**, *10*, 1–7.

[23] Gilday, L. C.; Robinson, S. W.; Barendt, T. A.; Langton, M. J.; Mullaney, B. R.; Beer, P. D. Halogen Bonding in Supramolecular Chemistry. *Chem. Rev.* **2015**, *115*, 7118–7195.

[24] Cavallo, G.; Metrangolo, P.; Milani, R.; Pilati, T.; Priimagi, A.; Resnati, G.; Terraneo, G. The Halogen Bond. *Chem. Rev.* **2016**, *116*, 2478–2601.

[25] Desiraju, G. R.; Ho, P. S.; Kloo, L.; Legon, A. C.; Marquardt, R.; Metrangolo, P.; Politzer, P.; Resnati, G.; Rissanen, K. Definition of the Halogen Bond (IUPAC Recommendations 2013). *Pure Appl. Chem.* **2013**, *85*, 1711–1713.

[26] Puttreddy, R.; Rautiainen, J. M.; Mäkelä, T.; Rissanen, K. Strong N−X···O−N Halogen Bonds: A Comprehensive Study on N-Halosaccharin Pyridine N-Oxide Complexes. *Angew. Chem., Int. Ed.* **2019**, *58*, 18610–18618.

[27] Clark, T.; Hennemann, M.; Murray, J. S.; Politzer, P. Halogen Bonding: The σ-Hole. *J. Mol. Model* **2007**, *13*, 291–296.

[28] Weinstein, H.; Politzer, P.; Srebrenik, S. A Misconception Concerning the Electronic Density Distribution of an Atom. *Theor. Chim. Acta* **1975**, *38*, 159–163.

[29] Politzer, P.; Murray, J. S. The Fundamental Nature and Role of the Electrostatic Potential in Atoms and Molecules. *Theor. Chem. Acc.* **2002**, *108*, 134–142

[30] Bundhun, A.; Ramasami, P.; Murray, J. S.; Politzer, P. Trends in σ-Hole Strengths and Interactions of F_3MX Molecules (M = C, Si, Ge and X = F, Cl, Br, I). *J. Mol. Model*

2013, *19*, 2739–2746.

[31] Politzer, P.; Murray, J. S.; Clark, T. σ-Hole Bonding: A Physical Interpretation. *Top Curr Chem* **2015**, *358*, 19–42.

[32] Xu, K.; Ho, D. M.; Pascal, R. A. Azaaromatic Chlorides: A Prescription for Crystal Structures with Extensive Nitrogen-Chlorine Donor-Acceptor Interactions. *J. Am. Chem. Soc.* **1994**, *116*, 105–110.

[33] Lommerse, J. P. M.; Stone, A. J.; Taylor, R.; Allen, F. H. The Nature and Geometry of Intermolecular Interactions between Halogens and Oxygen or Nitrogen. *J. Am. Chem. Soc.* **1996**, *118*, 3108–3116.

[34] Landrum, G. A.; Goldberg, N.; Hoffmann, R. Bonding in the Trihalides (X_3^-), Mixed Trihalides (X_2Y^-) and Hydrogen Bihalides (X_2H^-). The Connection between Hypervalent, Electron-Rich Three-Center, Donor-Acceptor and Strong Hydrogen Bonding. *J. Chem. Soc. - Dalt. Trans.* **1997**, No. 19, 3605–3613.

[35] Huber, S. M.; Jimenez-Izal, E.; Ugalde, J. M.; Infante, I. Unexpected Trends in Halogen-Bond Based Noncovalent Adducts. *Chem. Commun.* **2012**, *48*, 7708–7710.

[36] Rosokha, S. V.; Neretin, I. S.; Rosokha, T. Y.; Hecht, J.; Kochi, J. K. Charge-Transfer Character of Halogen Bonding: Molecular Structures and Electronic Spectroscopy of Carbon Tetrabromide and Bromoform Complexes with Organic σ- and Pi-Donors. *Heteroat. Chem.* **2006**, *17*, 449–459.

[37] Rosokha, S. V.; Vinakos, M. K. Hybrid Network Formation via Halogen Bonding of the Neutral Bromo-Substituted Organic Molecules with Anionic Metal-Bromide Complexes. *Cryst. Growth Des.* **2012**, *12*, 4149–4156.

[38] Heßelmann, A. DFT-SAPT Intermolecular Interaction Energies Employing Exact-

Exchange Kohn-Sham Response Methods. *J. Chem. Theory Comput.* **2018**, *14*, 1943–1959.

[39] Riley, K. E.; Hobza, P. The Relative Roles of Electrostatics and Dispersion in the Stabilization of Halogen Bonds. *Phys. Chem. Chem. Phys.* **2013**, *15*, 17742–17751.

[40] Thirman, J.; Engelage, E.; Huber, S. M.; Head-Gordon, M. Characterizing the Interplay of Pauli Repulsion, Electrostatics, Dispersion and Charge Transfer in Halogen Bonding with Energy Decomposition Analysis. *Phys. Chem. Chem. Phys.* **2018**, *20*, 905–915.

[41] Lehn, J.-M. Supramolecular Chemistry-Scope and Perspectives Molecules, Supermolecules, and Molecular Devices. *Angew. Chem., Int. Ed. Engl.* **1988**, *27*, 89–112.

[42] Desiraju, G. R. Crystal Engineering: From Molecule to Crystal. *J. Am. Chem. Soc.* **2013**, *135*, 9952–9967.

[43] Teyssandier, J.; Mali, K. S.; De Feyter, S. Halogen Bonding in Two-Dimensional Crystal Engineering. *ChemistryOpen* **2020**, *9*, 225–241.

[44] Mukherjee, A.; Tothadi, S.; Desiraju, G. R. Halogen Bonds in Crystal Engineering: Like Hydrogen Bonds yet Different. *Acc. Chem. Res.* **2014**, *47*, 2514–2524.

[45] Bolton, O.; Lee, K.; Kim, H.-J.; Lin, K. Y.; Kim, J. Activating Efficient Phosphorescence from Purely Organic Materials by Crystal Design. *Nat. Chem.* **2011**, *3*, 205–210.

[46] Metrangolo, P.; Meyer, F.; Pilati, T.; Resnati, G.; Terraneo, G. Halogen Bonding in Supramolecular Chemistry. *Angew. Chem., Int. Ed.* **2008**, *47*, 6114–6127.

[47] Metrangolo, P.; Resnati, G.; Pilati, T.; Biella, S. Halogen Bonding in Crystal Engineering. In *Halogen Bonding: Fundamentals and Applications*; Metrangolo, P., Resnati, G., Eds.; Springer-Verlag: Berlin, Heidelberg, 2008; pp 105–136.

[48] Pigge, F. C.; Vangala, V. R.; Kapadia, P. P.; Swenson, D. C.; Rath, N. P. Hexagonal Crystalline Inclusion Complexes of 4-Iodophenoxy Trimesoate. *Chem. Commun.* **2008**, 4726–4728.

[49] Titi, H. M.; Patra, R.; Goldberg, I. Exploring Supramolecular Self-Assembly of Tetraarylporphyrins by Halogen Bonding: Crystal Engineering with Diversely Functionalized Six-Coordinate Tin(L)2-Porphyrin Tectons. *Chem. -Eur. J.* **2013**, *19*, 14941–14949.

[50] Syssa-Magalé, J. L.; Boubekeur, K.; Leroy, J.; Chamoreau, L.-M.; Fave, C.; Schöllhorn, B. Directed Synthesis of a Halogen-Bonded Open Porphyrin Network. *CrystEngComm* **2014**, *16*, 10380–10384.

[51] Titi, H. M.; Nandi, G.; Tripuramallu, B. K.; Goldberg, I. Exploring Supramolecular Self-Assembly of Tetraarylporphyrins by Halogen Interactions. 3. Tin(L)$_2$(A_2B_2-Porphyrin) Arrays Supported by Concerted Halogen and Hydrogen Bonding. *Cryst. Growth Des.* **2015**, *15*, 3063–3075.

[52] Silly, F. Concentration-Dependent Two-Dimensional Halogen-Bonded Self-Assembly of 1,3,5-Tris(4-Iodophenyl)Benzene Molecules at the Solid-Liquid Interface. *J. Phys. Chem. C* **2017**, *121*, 10413–10418.

[53] Hu, X.; Zha, B.; Wu, Y.; Miao, X.; Deng, W. Effects of the Position and Number of Bromine Substituents on the Concentration-Mediated 2D Self-Assembly of Phenanthrene Derivatives. *Phys. Chem. Chem. Phys.* **2016**, *18*, 7208–7215.

[54] Zheng, Q. N.; Liu, X. H.; Chen, T.; Yan, H. J.; Cook, T.; Wang, D.; Stang, P. J.; Wan, L. J. Formation of Halogen Bond-Based 2D Supramolecular Assemblies by Electric Manipulation. *J. Am. Chem. Soc.* **2015**, *137*, 6128–6131.

[55] Mukherjee, A.; Teyssandier, J.; Hennrich, G.; De Feyter, S.; Mali, K. S. Two-Dimensional Crystal Engineering Using Halogen and Hydrogen Bonds: Towards Structural Landscapes. *Chem. Sci.* **2017**, *8*, 3759–3769.

[56] Lindeman, S. V.; Hecht, J.; Kochi, J. K. The Charge-Transfer Motif in Crystal Engineering. Self-Assembly of Acentric (Diamondoid) Networks from Halide Salts and Carbon Tetrabromide as Electron-Donor/Acceptor Synthons. *J. Am. Chem. Soc.* **2003**, *125*, 11597–11606.

[57] Ateş, Ö. D.; Zorlu, Y.; Kanmazalp, S. D.; Chumakov, Y.; Gürek, A. G.; Ayhan, M. M. Halogen Bonding Driven Crystal Engineering of Iodophthalonitrile Derivatives. *CrystEngComm* **2018**, *20*, 3858–3867.

[58] Metrangolo, P.; Resnati, G.; Pilati, T.; Liantonio, R.; Meyer, F. Engineering Functional Materials by Halogen Bonding. *J. Polym. Sci., Part A: Polym. Chem.* **2007**, *45*, 1–15.

[59] Meyer, F.; Dubois, P. Halogen Bonding at Work: Recent Applications in Synthetic Chemistry and Materials Science. *CrystEngComm* **2013**, *15*, 3058–3071.

[60] Priimagi, A.; Cavallo, G.; Metrangolo, P.; Resnati, G. The Halogen Bond in the Design of Functional Supramolecular Materials: Recent Advances. *Acc. Chem. Res.* **2013**, *46*, 2686–2695.

[61] Saccone, M.; Catalano, L. Halogen Bonding beyond Crystals in Materials Science. *J. Phys. Chem. B* **2019**, *123*, 9281–9290.

[62] Berger, G.; Frangville, P.; Meyer, F. Halogen Bonding for Molecular Recognition: New Developments in Materials and Biological Sciences. *Chem. Commun.* **2020**, *56*, 4970–4981.

[63] Wang, H.; Bisoyi, H. K.; Urbas, A. M.; Bunning, T. J.; Li, Q. The Halogen Bond: An

Emerging Supramolecular Tool in the Design of Functional Mesomorphic Materials. *Chem. -Eur. J.* **2019**, *25*, 1369–1378.

[64] Nguyen, H. L.; Horton, P. N.; Hursthouse, M. B.; Legon, A. C.; Bruce, D. W. Halogen Bonding: A New Interaction for Liquid Crystal Formation. *J. Am. Chem. Soc.* **2004**, *126*, 16–17.

[65] Xu, J.; Liu, X.; Lin, T.; Huang, J.; He, C. Synthesis and Self-Assembly of Difunctional Halogen-Bonding Molecules: A New Family of Supramolecular Liquid-Crystalline Polymers. *Macromolecules* **2005**, *38*, 3554–3557.

[66] Cho, C. M.; Wang, X.; Li, J. J.; He, C.; Xu, J. Synthesis and Self-Assembly of Halogen-Bond Donor-Spacer-Hydrogen-Bond Donor Molecules: Polymeric Liquid Crystals Induced by Combination of Intermolecular Halogen- and Hydrogen-Bonding Interactions. *Liq. Cryst.* **2013**, *40*, 185–196.

[67] Saccone, M.; Spengler, M.; Pfletscher, M.; Kuntze, K.; Virkki, M.; Wölper, C.; Gehrke, R.; Jansen, G.; Metrangolo, P.; Priimagi, A.; Giese, M. Photoresponsive Halogen-Bonded Liquid Crystals: The Role of Aromatic Fluorine Substitution. *Chem. Mater.* **2019**, *31*, 462–470.

[68] Christopherson, J. C.; Topić, F.; Barrett, C. J.; Friščić, T. Halogen-Bonded Cocrystals as Optical Materials: Next-Generation Control over Light-Matter Interactions. *Cryst. Growth Des.* **2018**, *18*, 1245–1259.

[69] Gao, H. Y.; Zhao, X. R.; Wang, H.; Pang, X.; Jin, W. J. Phosphorescent Cocrystals Assembled by 1,4-Diiodotetrafluorobenzene and Fluorene and Its Heterocyclic Analogues Based on C-I···π Halogen Bonding. *Cryst. Growth Des.* **2012**, *12*, 4377–4387.

[70] Gao, H. Y.; Shen, Q. J.; Zhao, X. R.; Yan, X. Q.; Pang, X.; Jin, W. J. Phosphorescent

Co-Crystal Assembled by 1,4-Diiodotetrafluorobenzene with Carbazole Based on C-I···π Halogen Bonding. *J. Mater. Chem.* **2012**, *22*, 5336–5343.

[71] Shen, Q. J.; Pang, X.; Zhao, X. R.; Gao, H. Y.; Sun, H. L.; Jin, W. J. Phosphorescent Cocrystals Constructed by 1,4-Diiodotetrafluorobenzene and Polyaromatic Hydrocarbons Based on C-I···π Halogen Bonding and Other Assisting Weak Interactions. *CrystEngComm* **2012**, *14*, 5027–5034.

[72] Bolton, O.; Lee, K.; Kim, H. J.; Lin, K. Y.; Kim, J. Activating Efficient Phosphorescence from Purely Organic Materials by Crystal Design. *Nat. Chem.* **2011**, *3*, 205–210.

[73] Fourmigué, M. Halogen Bonding in Conducting or Magnetic Molecular Materials. *Struct. Bond.* **2008**, *126*, 181–207.

[74] Fourmigué, M.; Lieffrig. Organizing Radical Species in the Solid State with Halogen Bonding. *Top Curr Chem* **2015**, *359*, 91–114.

[75] Domercq, B.; Devic, T.; Fourmigué, M.; Auban-Senzier, P.; Canadell, E. Hal···Hal Interactions in a Series of Three Isostructural Salts of Halogenated Tetrathiafulvalenes. Contribution of the Halogen Atoms to the HOMO-HOMO Overlap Interactions. *J. Mater. Chem.* **2001**, *11*, 1570–1575.

[76] Hervé, K.; Cador, O.; Golhen, S.; Costuas, K.; Halet, J.-F.; Shirahata, T.; Muto, T.; Imakubo, T.; Miyazaki, A.; Ouahab, L. Iodine Substituted Tetrathiafulvalene Radical Cation Salts with $[M(Isoq)_2(NCS)_4]^-$ Anions Where M = Cr^{III}, Ga^{III}: Role of I···S and S···S Contacts on Structural and Magnetic Properties. *Chem. Mater.* **2006**, *18*, 790–797.

[77] Imakubo, T.; Shirahata, T.; Hervé, K.; Ouahab, L. Supramolecular Organic Conductors Based on Diiodo-TTFs and Spherical Halide Ion X^- (X = Cl, Br). *J. Mater. Chem.* **2006**,

16, 162–173.

[78] Davy, K. J. P.; McMurtrie, J.; Rintoul, L.; Bernhardt, P. V.; Micallef, A. S. Vapour Phase Assembly of a Halogen Bonded Complex of an Isoindoline Nitroxide and 1,2-Diiodotetrafluorobenzene. *CrystEngComm* **2011**, *13*, 5062–5070.

[79] Hanson, G. R.; Jensen, P.; McMurtrie, J.; Rintoul, L.; Micallef, A. S. Halogen Bonding between an Isoindoline Nitroxide and 1,4- Diiodotetrafluorobenzene: New Tools and Tectons for Self-Assembling Organic Spin Systems. *Chem. -Eur. J.* **2009**, *15*, 4156–4164.

[80] Espallargas, G. M.; Recuenco, A.; Romero, F. M.; Brammer, L.; Libri, S. One-Dimensional Organization of Free Radicals via Halogen Bonding. *CrystEngComm* **2012**, *14*, 6381–6383.

[81] Pang, X.; Zhao, X. R.; Wang, H.; Sun, H. L.; Jin, W. J. Modulating Crystal Packing and Magnetic Properties of Nitroxide Free Radicals by Halogen Bonding. *Cryst. Growth Des.* **2013**, *13*, 3739–3745.

[82] Atzori, M.; Serpe, A.; Deplano, P.; Schlueter, J. A.; Mercuri, M. L. Tailoring Magnetic Properties of Molecular Materials through Non-Covalent Interactions. *Inorg. Chem. Front.* **2015**, *2*, 108–115.

[83] Hine, J.; Linden, S.-M.; Kanagasabapathy, V. M. 1,8-Biphenylenediol Is a Double-Hydrogen-Bonding Catalyst for Reaction of an Epoxide with a Nucleophile. *J. Am. Chem. Soc.* **1985**, *107*, 1082–1083.

[84] Schreiner, P. R. Metal-Free Organocatalysis through Explicit Hydrogen Bonding Interactions. *Chem. Soc. Rev.* **2003**, *32*, 289–296.

[85] Zhang, Z.; Schreiner, P. R. (Thio)Urea Organocatalysis—What Can Be Learnt from

Anion Recognition? *Chem. Soc. Rev.* **2009**, *38*, 1187–1198.

[86] Doyle, A. G.; Jacobsen, E. N. Small-Molecule H-Bond Donors in Asymmetric Catalysis. *Chem. Rev.* **2007**, *107*, 5713–5743.

[87] Bulfield, D.; Huber, S. M. Halogen Bonding in Organic Synthesis and Organocatalysis. *Chem. -Eur. J.* **2016**, *22*, 14434–14450.

[88] Sutar, R. L.; Huber, S. M. Catalysis of Organic Reactions through Halogen Bonding. *ACS Catal.* **2019**, *9*, 9622–9639.

[89] Yang, H.; Wong, M. W. Application of Halogen Bonding to Organocatalysis: A Theoretical Perspective. *Molecules* **2020**, *25*, 1–25.

[90] Beckendorf, S.; Asmus, S.; Mück-Lichtenfeld, C.; García Mancheño, O. "Click" Bis-Triazoles as Neutral C-H···anion-Acceptor Organocatalysts. *Chem. -Eur. J.* **2013**, *19*, 1581–1585.

[91] Walter, S. M.; Kniep, F.; Herdtweck, E.; Huber, S. M. Halogen-Bond-Induced Activation of a Carbon-Heteroatom Bond. *Angew. Chem., Int. Ed.* **2011**, *50* (31), 7187–7191.

[92] Kniep, F.; Walter, S. M.; Herdtweck, E.; Huber, S. M. 4,4'-Azobis(Halopyridinium) Derivatives: Strong Multidentate Halogen-Bond Donors with a Redox-Active Core. *Chem. -Eur. J.* **2012**, *18*, 1306–1310.

[93] Kniep, F.; Rout, L.; Walter, S. M.; Bensch, H. K. V.; Jungbauer, S. H.; Herdtweck, E.; Huber, S. M. 5-Iodo-1,2,3-Triazolium-Based Multidentate Halogen-Bond Donors as Activating Reagents. *Chem. Commun.* **2012**, *48*, 9299–9301.

[94] Perera, M. D.; Aakeröy, C. B. Organocatalysis by a Multidentate Halogen-Bond Donor: An Alternative to Hydrogen-Bond Based Catalysis. *New J. Chem.* **2019**, *43*,

8311–8314.

[95] Dreger, A.; Engelage, E.; Mallick, B.; Beer, P. D.; Huber, S. M. The role of charge in 1,2,3-triazol(ium)-based halogen bonding activators. *Chem. Commun.* **2018**, *54*, 4013-4016.

[96] Jungbauer, S. H.; Walter, S. M.; Schindler, S.; Rout, L.; Kniep, F.; Huber, S. M. Activation of a Carbonyl Compound by Halogen Bonding. *Chem. Commun.* **2014**, *50*, 6281–6284.

[97] von der Heiden, D.; Bozkus, S.; Klussmann, M.; Breugst, M. Reaction Mechanism of Iodine-Catalyzed Michael Additions. *J. Org. Chem.* **2017**, *82*, 4037–4043.

[98] Gliese, J.-P.; Jungbauer, S. H.; Huber, S. M. A Halogen-Bonding-Catalyzed Michael Addition Reaction. *Chem. Commun.* **2017**, *53*, 12052–12055.

[99] Benz, S.; Poblador-Bahamonde, A. I.; Low-Ders, N.; Matile, S. Catalysis with Pnictogen, Chalcogen, and Halogen Bonds. *Angew. Chem., Int. Ed.* **2018**, *57*, 5408–5412.

[100] Auffinger, P.; Hays, F. A.; Westhof, E.; Ho, P. S. Halogen Bonds in Biological Molecules. *Proc. Natl. Acad. Sci. U. S. A.* **2004**, *101*, 16789–16794.

[101] Wilcken, R.; Zimmermann, M. O.; Lange, A.; Joerger, A. C.; Boeckler, F. M. Principles and Applications of Halogen Bonding in Medicinal Chemistry and Chemical Biology. *J. Med. Chem.* **2013**, *56*, 1363–1388.

[102] Hays, F. A.; Vargason, J. M.; Ho, P. S. Effect of Sequence on the Conformation of DNA Holliday Junctions. *Biochemistry* **2003**, *42*, 9586–9597.

[103] Holliday, R. A Mechanism for Gene Conversion in Fungi. *Genet. Res.* **1964**, *5*, 282–304.

[104] Voth, A. R.; Hays, F. A.; Ho, P. S. Directing Macromolecular Conformation through Halogen Bonds. *Proc. Natl. Acad. Sci. U. S. A.* **2007**, *104*, 6188–6193.

[105] Yun, C. H.; Boggon, T. J.; Li, Y.; Woo, M. S.; Greulich, H.; Meyerson, M.; Eck, M. J. Structures of Lung Cancer-Derived EGFR Mutants and Inhibitor Complexes: Mechanism of Activation and Insights into Differential Inhibitor Sensitivity. *Cancer Cell* **2007**, *11*, 217–227.

[106] Danelius, E.; Andersson, H.; Jarvoll, P.; Lood, K.; Gräfenstein, J.; Erdélyi, M. Halogen Bonding: A Powerful Tool for Modulation of Peptide Conformation. *Biochemistry* **2017**, *56*, 3265–3272.

[107] Johnson, S. M.; Connelly, S.; Wilson, I. A.; Kelly, J. W. Biochemical and Structural Evaluation of Highly Selective 2-Arylbenzoxazole-Based Transthyretin Amyloidogenesis Inhibitors. *J. Med. Chem.* **2008**, *51*, 260–270.

[108] Ho, P. S. Halogen Bonding in Medicinal Chemistry: From Observation to Prediction. *Futur. Med. Chem* **2017**, 637–640.

[109] Xu, Z.; Yang, Z.; Liu, Y.; Lu, Y.; Chen, K.; Zhu, W. Halogen Bond: Its Role beyond Drug-Target Binding Affinity for Drug Discovery and Development. *J. Chem. Inf. Model.* **2014**, *54*, 69–78.

[110] Costa, P. J.; Nunes, R.; Vila-Viçosa, D. Halogen Bonding in Halocarbon-Protein Complexes and Computational Tools for Rational Drug Design. *Expert Opin. Drug Discov.* **2019**, *14*, 805–820.

[111] Jiang, S.; Zhang, L.; Cui, D.; Yao, Z.; Gao, B.; Lin, J.; Wei, D. The Important Role of Halogen Bond in Substrate Selectivity of Enzymatic Catalysis. *Sci. Rep.* **2016**, *6*, 1–7.

Chapter 2. Introduction to Nuclear Magnetic Resonance

Atomic nuclei have an intrinsic property called spin. Spin is a particular kind of angular momentum. The number of spin states is determined by the principal nuclear spin quantum number I; there are $2I+1$ allowed spin states with spin magnetic quantum number (m) ranging from $-I$ to $+I$, which are degenerate in the absence of an external field. The nucleus of an atom is composed of protons with positive charge and neutrons with no charge. Both proton and neutron particles possess a spin quantum number of 1/2. Nuclides with both even numbers of protons and neutrons, the ground state nuclear spin is given by $I = 0$, which is known as NMR-inactive nuclei (such as ^{12}C, ^{16}O, ^{32}S etc.). Nuclides with both odd numbers of protons and neutrons have an integer spin quantum number; nuclides with an odd number of protons or neutrons have a half-integer spin quantum number.[1]

2.1 Zeeman Interaction

The nucleus also exhibits a magnetic moment (**μ**), which is proportional to the spin angular momentum (**I**), shown in Eq 2.1.1.

$$\hat{\boldsymbol{\mu}} = \gamma \hat{\mathbf{I}} \qquad \text{Eq 2.1.1}$$

where ^ indicates that they are quantum mechanical operators. γ is the gyromagnetic ratio. A positive γ indicates that the magnetic moment is parallel to the spin angular momentum whereas a negative value indicates that the directions of the magnetic moment and spin angular momentum are opposite.

The angular momentum of a particle with a spin can be treated as a vector. The direction of the vector, or the direction of the spin angular momentum, is also called spin polarization. As shown in Figure 2.1.1, nuclei with spin I are $(2I+1)$-fold degenerate in the

absence of an external magnetic field. The application of a magnetic field B_0 breaks the degeneracy and leads to ($2I$+1) sublevels with different energy states (E_m). This is known as the Zeeman effect.[2] The energy separation between the sublevels in a magnetic field is called the Zeeman splitting and depends on the magnetic moment and the magnetic field strength (Eq 2.1.3).

$$E_m = -\frac{m\gamma h B_0}{2\pi} \qquad \text{Eq 2.1.2}$$

$$\Delta E = \frac{\gamma h B_0}{2\pi} \qquad \text{Eq 2.1.3}$$

where h is Planck's constant (6.62607×10^{-34} J·s).

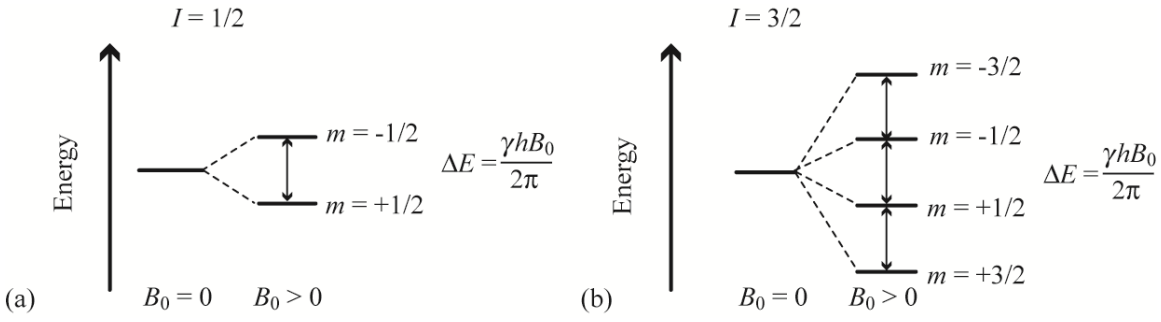

Figure 2.1.1. Nuclear Zeeman splittings for spin-1/2 (a) and spin-3/2 (b) with γ>0 in the absence of an external magnetic field (B_0 = 0), and in the presence of an external magnetic field (B_0 = 0).

At thermal equilibrium, the population of nuclei with I = 1/2 in the lower energy state (N_α) is slightly more than the population in the higher energy state (N_β), following the Boltzmann distribution. The population ratio between two spin states is given by Boltzmann equation:

$$\frac{N_\beta}{N_\alpha} = e^{-\frac{\Delta E}{kT}} \qquad \text{Eq 2.1.4}$$

where k is the Boltzmann constant (1.3806×10^{-23} J·K^{-1}), and T is the absolute temperature (K).

This small difference in population between α and β states, for example, a ratio of 0.999855 for ^{1}H in a magnetic field strength of 21.1 T at 298 K, generates a net magnetization aligned with the magnetic field direction, and the slight excess population in the lower energy level contributes to the insensitivity of NMR.

2.2 NMR Pulse and Signal Detection

In the absence of the magnetic field, the magnetic moments (**μ**) of a sample point in all possible directions and the distribution is completely isotropic. As mentioned, in the presence of magnetic field, there is a net distribution of **μ** gradually building up along the direction of the applied magnetic field (z axis), generating a bulk magnetization of the sample expressed by vector **M**. This is known as longitudinal or spin-lattice relaxation and the time taken to reach the thermal equilibrium (M_0) is the longitudinal or spin-lattice relaxation time constant (T_1).[3] The build-up of magnetization along z axis (M_z) follows an exponential trend:

$$M_z(t) = M_0(1 - e^{-\frac{t}{T_1}}) \qquad \text{Eq 2.2.1}$$

When a magnetic field is applied, the magnetization vector will move on a cone with a constant angle between the **M** and field direction, which is called precession (shown in Figure 2.2.1). The angle of the cone depends on the initial condition of the magnetization

M: if the magnetization vector is exactly along the field, the angle of the cone will be zero; if the **M** is perpendicular to field direction, it will move within a plane perpendicular to the *z* axis. The frequency of precession is called the Larmor frequency and the value can be expressed in Hz (ν_0) or in rad·s^{-1} (ω_0), given by Eq 2.2.2

$$\nu_0 = -\frac{\gamma B_0}{2\pi} \text{ or } \omega_0 = -\gamma B_0 \qquad \text{Eq 2.2.2}$$

In the NMR experiment, instead of longitudinal magnetization, the transverse magnetization is measured. If the magnetization is rotated into the plane perpendicular to the magnetic field (*xy* plane) by a pulse, the net magnetic moment will precess within the *xy* plane at Larmor frequency and slowly decay, which is called the transverse relaxation (T_2).[4] The magnetization components at time *t* after the pulse are:

$$M_y(t) = -M_0 \cos(\omega_0 t)\, e^{-t/T_2}$$

$$M_x(t) = M_0 \sin(\omega_0 t)\, e^{-t/T_2} \qquad \text{Eq 2.2.3}$$

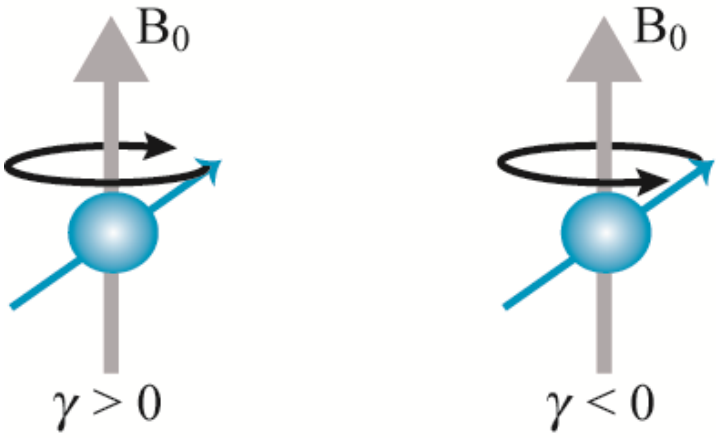

Figure 2.2.1. Direction of precession of nuclear spin with $\gamma > 0$ and $\gamma < 0$ in the presence of external magnetic field $\mathbf{B_0}$

Firstly, it is useful to introduce the concept of a reference rotating frame that processes about B_0 at $\omega_{rot,frame}$.[5,6] In such a frame, the relative precession frequency of **M** is called offset and is given by Ω_{off} ($\Omega_{off} = \omega_0 - \omega_{rot,frame}$). If the $\omega_{rot,frame}$ is equal to the Larmor frequency, the offset will be zero and the relative precession of **M** appears to be static in the rotating frame (see Figure 2.2.2(a)). Therefore, in the rotating frame, the apparent magnetic field is different from the actual applied magnetic field B_0 and is called the reduced field ($\Delta B = -\Omega_{off}/\gamma$). When a radiofrequency power is applied to the coil along the *x*-direction the resulting oscillating current produces an oscillating magnetic field (B_1) that can be decomposed into components that rotate about B_0 at a radiofrequency of ω_{RF}. If the reference rotating frame is chosen to be $\omega_{rot,frame} = -\omega_{RF}$ and $\Omega_{off} = \omega_0 + \omega_{RF}$, the resulting effective field is the vector sum of reduced field ΔB and B_1, given in Eq 2.2.4 and shown in Figure 2.2.2(c). In order to rotate the magnetization **M** into the *xy* plane, offset Ω_{off}

needs to be close to zero so that B_{eff} lies close to the plane. Therefore, the applied radiofrequency pulse matches the Larmor frequency of the chosen nuclei-that is resonant

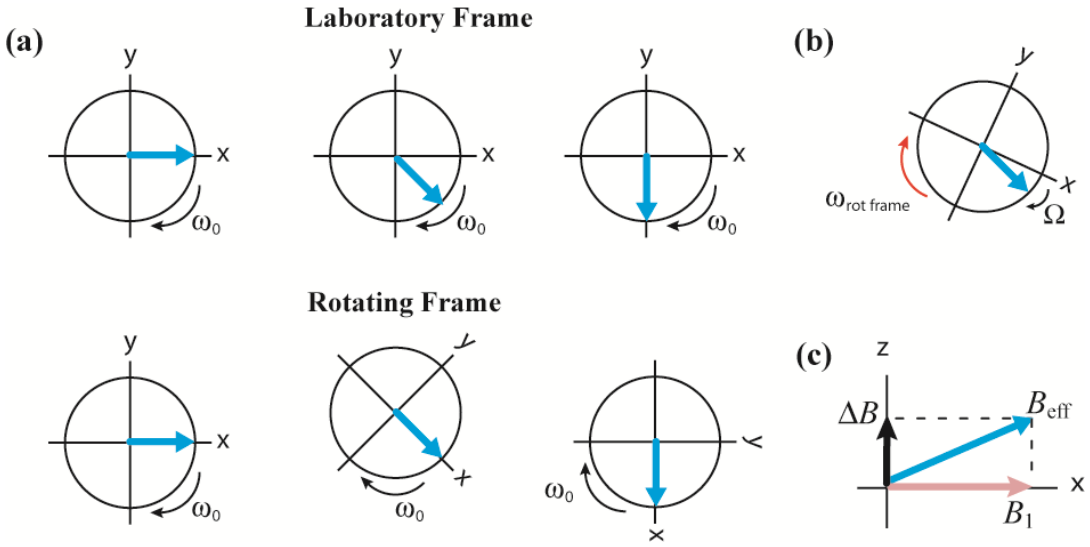

Figure 2.2.2. (a) Top view of the precession of **M** in a fixed axis system, or laboratory frame (top) and top view of the precession of **M** in an axis system which is rotating about the *z*-axis at ω_0, or laboratory frame (bottom). In this rotating frame, M appears to be static relative to the axis system. **(b)** Top view of the precession of **M** in a rotating frame which is rotating at different frequency ($\omega_{rot,frame}$) instead of ω_0, shown as red arrow. The relative precession frequency of **M** is Ω_{off}, shown as black arrow. (c) The effective field B_{eff} in the rotating frame.

with Larmor frequency.[7] An introduction of this rotating frame eliminates the large Zeeman interaction due to the effect of the reduced field $\Delta B \approx 0$ instead of the actual value of B_0 in this reference frame.

$$B_{eff} = \sqrt{\Delta B^2 + {B_1}^2} = \sqrt{\left(-\frac{\Omega_{off}}{\gamma}\right)^2 + {B_1}^2} \qquad \text{Eq 2.2.4}$$

The schematic representation of a single pulse experiment is shown in Figure 2.2.3. A 90° pulse is applied long enough to rotate the magnetization into the *xy* plane. After the pulse is off, the oscillation in the tuned circuit arising from the precession of the transverse magnetization is recorded, yielding the free induction decay (FID).[6] A Fourier transform converts the FID, which is a function of time, to an NMR signal, which is a function of frequency.[8] Some more complex pulses sequences will be provided in Section 2.5.

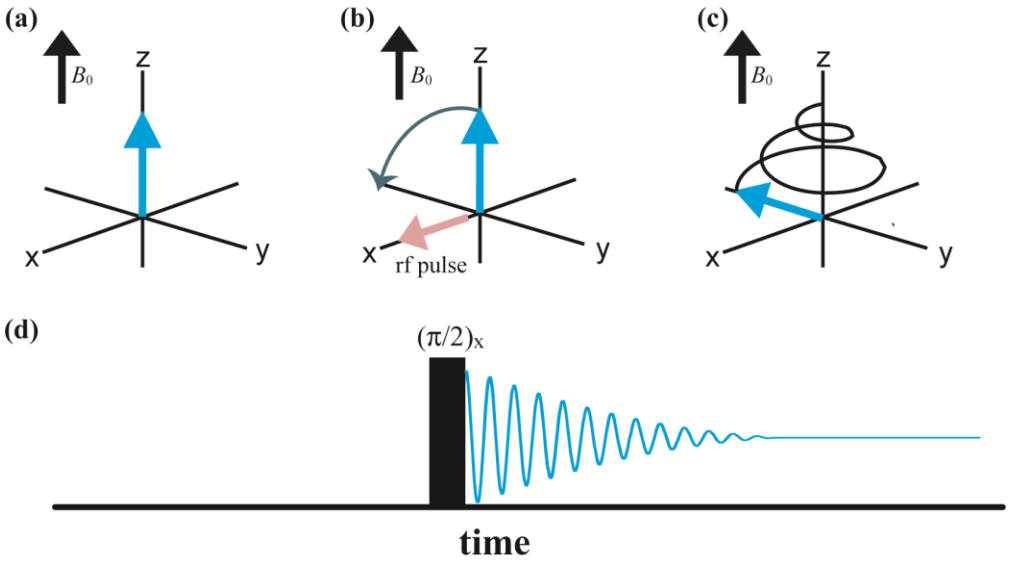

Figure 2.2.3. A vector diagram shows the bulk magnetization **M** at equilibrium (a), pulse excitation (b) and pulse detection (c). (d) Pulse sequence of a simple one-pulse experiment. Before the excitation of an rf pulse, the magnetization **M** is aligned with the magnetic field, an rf pulse, aligned with the *x* axis, rotates **M** to the *–y* axis on the transverse plane, The pulse is then turned off to allow the free precession of the magnetization.

2.3 NMR Interactions

When a nucleus is placed in a homogeneous magnetic field, the relevant Hamiltonian operator governing the NMR spectrum is composed of the Zeeman interaction, nuclear magnetic shielding interaction (σ), the nuclear quadrupolar coupling

interaction (*Q*), the direct dipolar coupling interaction (*D*), and the indirect nuclear spin-spin coupling interaction (*J*).

$$\widehat{H} = \widehat{H}_Z + \widehat{H}_\sigma + \widehat{H}_Q + \widehat{H}_D + \widehat{H}_J \qquad \text{Eq 2.3.1}$$

The last four interactions are treated as perturbations to the Zeeman interaction. All the interactions can be represented in Cartesian form:

$$\widehat{H}_A = \hat{I} \cdot \boldsymbol{A} \cdot \hat{S} \qquad \text{Eq 2.3.2}$$

where $\hat{I}$ is a nuclear spin operator ($\hat{I} = (\hat{I}_x, \hat{I}_y, \hat{I}_z)$) and $\boldsymbol{A}$ is a second-rank Cartesian tensor ($\boldsymbol{A} = \begin{pmatrix} A_{xx} & A_{xy} & A_{xz} \\ A_{yx} & A_{yy} & A_{yz} \\ A_{zx} & A_{zy} & A_{zz} \end{pmatrix}$) and dependent on the interaction $\hat{S}$ can be either another vector or second spin operator. In the following sections, each interaction will be explained in detail.

2.3.1 Magnetic Shielding Interaction

The electrons surrounding the molecule can partially shield a nucleus from the magnetic field, resulting in frequency shifts in the NMR spectrum. This is known as magnetic shielding interaction. According to Ramsey's theory, there are two mechanisms (diamagnetic and paramagnetic contributions) that contribute to the magnetic shielding of the nucleus.[9] Diamagnetic shielding is from circulation of the electrons induced by the application of the external magnetic field, which induces a small magnetic field opposite to the applied magnetic field. The paramagnetic shielding is from the mixing of the electron ground state with the excited states electrons induced by the application of the external magnetic field. The Zeeman Hamiltonian including the magnetic shielding contribution is shown as following:

$$\hat{H}_{Z+\sigma} = \frac{\gamma}{2\pi}\hat{I}\cdot(1-\boldsymbol{\sigma})\cdot\hat{B}_0 = \frac{\gamma}{2\pi}(\hat{I}_x,\hat{I}_y,\hat{I}_z)\begin{pmatrix}1-\sigma_{xx} & \sigma_{xy} & \sigma_{xz}\\ \sigma_{yx} & 1-\sigma_{yy} & \sigma_{yz}\\ \sigma_{zx} & \sigma_{zy} & 1-\sigma_{zz}\end{pmatrix}\begin{pmatrix}0\\0\\B_0\end{pmatrix} \quad \text{Eq 2.3.3}$$

where the axes labeled *x*, *y*, *z* refer to a laboratory-fixed axis system in which *z* axis is along the applied magnetic field (B_0) direction.

Under the secular approximation,[10] the Hamiltonian can be re-written as:

$$\hat{H}_{Z+\sigma} = \frac{\gamma B_0}{2\pi}(1-\sigma_{zz})\hat{I}_z \quad \text{Eq 2.3.4}$$

σ_{zz} is the magnetic shielding along the applied magnetic field direction or in a laboratory-fixed axis system where the magnetic field direction is *z* axis. Polycrystalline samples have a random distribution of crystallite orientations with respect to magnetic field, so each molecule will have a different orientation relative to the laboratory-fixed axis system, giving different shielding values. Therefore, the shielding tensors can also be fixed with respect to the molecule and diagonalized into its own principal axis system. The shielding tensor in the laboratory frame can be re-expressed as:

$$\sigma_{zz} = \sigma_{11}\sin^2\vartheta\cos^2\phi + \sigma_{22}\sin^2\vartheta\sin^2\phi + \sigma_{33}\cos^2\vartheta \quad \text{Eq 2.3.5}$$

where σ_{ii} are the principal components ($\sigma_{33} \geq \sigma_{22} \geq \sigma_{11}$) of the magnetic shielding tensor (in the molecular frame of reference) and ϑ, ϕ are the polar angles that define the orientation of the magnetic shielding tensor in the Cartesian coordinate system.

σ describes the degree of magnetic shielding in a molecule with respect to the bare nucleus. In practical application, it is more convenient to convert the magnetic shielding to the chemical shift (δ) by Eq 2.3.6:

$$\delta_{ij} = \frac{\sigma_{iso,ref} - \sigma_{ij}}{1-\sigma_{iso,ref}} \quad \text{Eq 2.3.6}$$

where $\sigma_{iso,ref}$ is the isotropic shielding constant of an arbitrary reference sample, σ_{ij} is a

magnetic shielding tensor component and δ_{ii} is the corresponding chemical shift tensor component. Because the chemical shift is a small number, it is common to specify them in terms of parts per million (ppm).

In solution, the presence of rapid molecular tumbling (Brownian motion) [11] averages the anisotropic component of the shielding interaction over all the possible orientations to yield the isotropic chemical shift (δ_{iso}):

$$\delta_{iso} = \frac{\delta_{11} + \delta_{22} + \delta_{33}}{3} \qquad \text{Eq 2.3.7}$$

In the solid state, the anisotropic part cannot be averaged. The presence of anisotropic interactions results in the broadening of the spectrum. The line shapes are described by three parameters in the Herzfeld-Berger convention: [12] δ_{iso}, span (Ω), and skew (κ). Ω is used to quantify the breadth of the chemical shift tensor. κ ($-1 \leq \kappa \leq 1$) is used to describe the asymmetry of the powder pattern, where a value of -1 or 1 represents the chemical shift tensors that are axially symmetric.

$$\Omega = \delta_{11} - \delta_{33} \qquad \text{Eq 2.3.8}$$

$$\kappa = \frac{3(\delta_{22} - \delta_{iso})}{\Omega} \qquad \text{Eq 2.3.9}$$

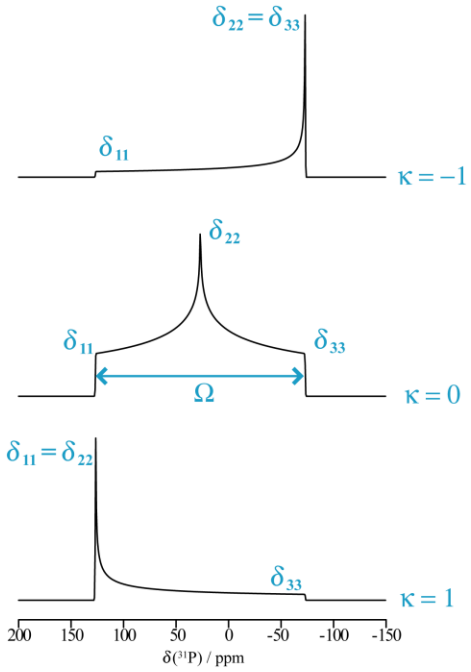

Figure 2.3.1. Simulated static spectra for ^{31}P at a magnetic field strength of 9.4 T.

2.3.2 Quadrupolar Interaction

Quadrupolar nuclei are those with spin $I > 1/2$ (*i.e.*, ^{2}H, ^{17}O, ^{127}I). They have an asymmetric nuclear charge distribution as opposed to spin-1/2 nuclei with a spherical charge distribution, and generate a nuclear electric quadrupole moment, Q. A positive Q indicates that the nucleus is prolate whereas a negative Q indicates that the nucleus is oblate. The interaction between the quadrupole moment and the electric field gradient (EFG), generated by the electrons at the site of nucleus, is called the quadrupolar interaction.[13] The EFG tensor is described by a second-rank tensor:

$$\mathbf{V} = \begin{pmatrix} V_{xx} & V_{xy} & V_{xz} \\ V_{yx} & V_{yy} & V_{yz} \\ V_{zx} & V_{zy} & V_{zz} \end{pmatrix} = \begin{pmatrix} V_{11} & 0 & 0 \\ 0 & V_{22} & 0 \\ 0 & 0 & V_{33} \end{pmatrix}_{PAS} \qquad \text{Eq 2.3.10}$$

The tensor is traceless ($V_{xx} + V_{yy} + V_{zz} = 0$) and is symmetric ($V_{ij} = V_{ji}$), and can be diagonalized into its principal axis system to generate three principal components: V_{11}, V_{22} and V_{33} ($|V_{11}| \leq |V_{22}| \leq |V_{33}|$).

There are two parameters used to characterize the EFG tensors. One of them is the quadrupolar coupling constant C_Q (MHz), which represents the magnitude of the quadrupolar interaction, and is defined by the following equation:[7]

$$C_Q = \frac{eQV_{33}}{h} \qquad \text{Eq 2.3.11}$$

where e is the unit charge, Q is the nuclear quadrupole moment.

Another one is the asymmetry parameter, indicated by η_Q, which describes the symmetry of the EFG tensor and ranges from 0 to 1:

$$\eta_Q = \frac{(V_{11} - V_{22})}{V_{33}} \qquad \text{Eq 2.3.12}$$

If $\eta_Q = 0$ ($V_{11} = V_{22} = 1/2V_{33}$), the EFG tensor is axially symmetric, and the axial symmetry is about the axis of the largest EFG component.[14]

The Hamiltonian operator describes the electric interaction between the non-symmetric charge distribution within the nucleus and the electric field gradient at the nucleus as follows:[15]

$$\hat{H}_Q = \frac{eQ}{2I(2I-1)\hbar}\hat{I}\mathbf{V}\hat{I} = \frac{eQ}{2I(2I-1)\hbar}(\hat{I}_x, \hat{I}_y, \hat{I}_z)\begin{pmatrix} V_{xx} & V_{xy} & V_{xz} \\ V_{yx} & V_{yy} & V_{yz} \\ V_{zx} & V_{zy} & V_{zz} \end{pmatrix}\begin{pmatrix} \hat{I}_x \\ \hat{I}_y \\ \hat{I}_z \end{pmatrix} \qquad \text{Eq 2.3.13}$$

where $\mathbf{V}$ is the EFG tensor, $\hbar$ is the reduced Planck constant.

In the principal axis system of EFG tensor, the spin Hamiltonian can be written as:

$$\hat{H}_Q^{PAS} = \frac{eQ}{6I(2I-1)\hbar}\left[V_{11}\left(3\hat{I}_x^{\,2} - \hat{I}\right) + V_{22}\left(3\hat{I}_y^{\,2} - \hat{I}\right) + V_{33}\left(3\hat{I}_z^{\,2} - \hat{I}\right)\right] \qquad \text{Eq 2.3.14}$$

or

$$\hat{H}_Q^{PAS} = \frac{eQ}{4I(2I-1)\hbar} V_{33} \left[\left(3\hat{I}_z{}^2 - \hat{I} \right) + \eta_Q \left(\hat{I}_x{}^2 - \hat{I}_y{}^2 \right) \right]$$

Under the high field approximation, where the quadrupolar interaction is much smaller than the Zeeman interaction, the quadrupolar interaction is treated as a perturbation to the Zeeman.

$$\hat{H}_Q = \hat{H}_Q{}^{(1)} + \hat{H}_Q{}^{(2)} + \hat{H}_Q{}^{(3)} + \cdots \qquad \text{Eq 2.3.15}$$

The first order term of quadrupolar interaction is given by:[15]

$$\hat{H}_Q{}^{(1)} = \frac{C_Q}{8I(2I-1)} \left(3\cos^2\vartheta' - 1 + \eta_Q \sin^2\vartheta' \cos 2\phi' \right) (3m^2 - I(I+1)) \qquad \text{Eq 2.3.16}$$

where ϑ' and ϕ' are polar angles describing the magnetic field direction in the principal axis system of the EFG tensors.

Therefore, the first-order quadrupolar interaction can give rise to a large energy shift from the pure Zeeman levels, and the frequency shifts are given by:

$$\upsilon_{m,m-1}{}^{(1)} = \frac{3C_Q}{8I(2I-1)} (1-2m) \left(3\cos^2\vartheta' - 1 + \eta_Q \sin^2\vartheta' \cos 2\phi' \right) \qquad \text{Eq 2.3.17}$$

The $(1-2m)$ term indicates that the m = ½ to -½ transition is unaffected by the first order quadrupolar interaction and remains at the Larmor frequency ν_0 (shown in Figure 2.3.2). This transition is known as the central transition (CT). However, the other single quantum transitions, known as satellite transitions (ST), deviate from ν_0.

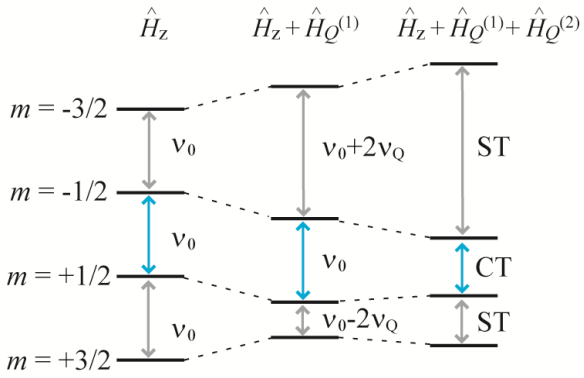

Figure 2.3.2. Schematic energy level diagram for a spin-3/2 nucleus in the magnetic field, showing the effect of the Zeeman, first-order and second-order quadrupolar interaction. The central transition (CT, shown as blue arrows) is unaffected by the first-order quadrupolar interaction whereas the satellite transitions (ST, shown as grey arrows) show a significant perturbation.

The first-order approximation is not sufficient to describe the Hamiltonian; a second-order perturbation is also evaluated:

$$\begin{aligned}\hat{H}_Q{}^{(2)} = -\left(\frac{C_Q}{4I(2I-1)}\right)^2\left(\frac{m}{\upsilon_0}\right)\Big\{&-\frac{1}{5}(I(I+1)-3m^2)\left(3+\eta_Q^2\right)\\&+\frac{1}{28}(8I(I+1)-12m^2-3)\Big[\left(\eta_Q^2-3\right)\left(3\cos^2\vartheta'-1\right)\\&+6\eta_Q\sin^2\vartheta'\cos 2\phi'\Big]\\&+\frac{1}{8}(18I(I+1)-34m^2\\&-5)\left[\frac{1}{140}\left(18+\eta_Q^2\right)\left(35\cos^4\vartheta'-30\cos^2\vartheta'+3\right)\right.\\&+\frac{3}{7}\eta_Q\sin^2\vartheta'\left(7\cos^2\vartheta'-1\right)\cos 2\phi'\\&\left.+\frac{1}{4}\eta_Q^2\sin^4\vartheta'\cos 4\phi'\right]\Big\}\end{aligned} \qquad \text{Eq 2.3.18}$$

The second-order quadrupolar Hamiltonian does affect both CT and STs and shifts the frequencies away from ν_0. Due to the orientation dependence of the quadrupolar

interaction, each orientation can potentially create a different shift, leaving a very broad powder pattern NMR spectrum. As a result, it is more practical to measure the CT. The breadth of the CT powder pattern is, given by Eq 2.3.19, related to the square of C_Q and inversely related to ν_0, which implies the advantage in applying an ultrahigh magnetic field when studying the quadrupolar nuclei since the strong field can narrow the breadth of the CT powder pattern.[16]

$$\Delta\upsilon_{-\frac{1}{2},\frac{1}{2}} = \left(\frac{25 + 22\eta_Q + \eta_Q^2}{144}\right)\frac{\left(3C_Q\right)^2}{\left(2I(2I-1)\right)^2}\left(\frac{I(I+1) - 3/4}{\nu_0}\right) \qquad \text{Eq 2.3.19}$$

2.3.3 Spin-Spin Coupling Interactions

Individual spins can also couple with each other, leading to a spin-spin coupling interaction that can provide information about the connectivity and spatial distance among atoms. There are two different spin-spin coupling interactions: the direct dipolar coupling interaction (*D*) and the indirect nuclear spin-spin coupling interaction (*J*). One of the nuclear spins can generate magnetic field; other spins that are close in space can experience this field. This direct dipolar coupling interaction involves the coupling through space, which depends on the internuclear space between spins (*r*). The dependence of dipolar coupling on the internuclear distance between the spins allows for the measurement of the internuclear distances.[17,18,19]The dipolar coupling Hamiltonian for a single spin pair can be written as following:

$$\hat{H}_D = (\gamma_1\gamma_2\hbar^2)\frac{\mu_0}{4\pi}\left\{\frac{\hat{I}_1 \cdot \hat{I}_2}{r^3} - 3\left[\frac{\left(\hat{I}_1 \cdot \vec{r}\right)\left(\hat{I}_2 \cdot \vec{r}\right)}{r^5}\right]\right\} \qquad \text{Eq 2.3.20}$$

where I_1 and I_2 and γ_1 and γ_2 are the spin quantum numbers and corresponding gyromagnetic ratios of two nuclei. $\vec{r}$ is the internuclear vector. μ_0 is the permeability constant, $4\pi \times 10^{-7}$ kg·m·s^{-2}·A^{-2}.

The dipolar coupling Hamiltonian can also be diagonalized into its principal axis system:[20]

$$\hat{H}_D{}^{PAS} = hR_{DD}(\hat{I}_{1x}, \hat{I}_{1y}, \hat{I}_{1z}) \begin{pmatrix} 1 & 0 & 0 \\ 0 & 1 & 0 \\ 0 & 0 & -2 \end{pmatrix} \begin{pmatrix} \hat{I}_{2x} \\ \hat{I}_{2y} \\ \hat{I}_{2z} \end{pmatrix} \quad \text{Eq 2.3.21}$$

R_{DD} is the dipolar coupling constant and is defined as:

$$R_{DD} = \left(\frac{\mu_0}{4\pi}\right)\left(\frac{\hbar}{2\pi}\right)(\gamma_1\gamma_2)\langle r_{1,2}{}^{-3}\rangle \quad \text{Eq 2.3.22}$$

After secular approximations, the secular part of $\hat{H}_D$ for both homonuclear and heteronuclear spins is given by:

$$\hat{H}_D = hR_{DD}\left(\frac{3\cos^2\vartheta'' - 1}{2}\right)(3\hat{I}_{1z}\hat{I}_{2z} - \hat{I}_1 \cdot \hat{I}_2) \quad \text{Eq 2.3.23}$$

where ϑ'' is defined as the angle between the dipolar vector connecting two spins, $\vec{r}$, and the applied magnetic field, B_0.

For heteronuclear spins, $\hat{H}_D$ is obtained as: $\hat{H}_D = hR_{DD}(3\cos^2\vartheta'' - 1)\hat{I}_{1z}\hat{I}_{2z}$. For both homonuclear and heteronuclear spins, there is $(3\cos^2\vartheta'' - 1)$ dependence present in the dipolar Hamiltonian, which can be averaged to zero under rapid MAS condition in solids or isotropic motion in liquid.

The second spin-spin coupling is indirect nuclear spin-spin coupling (*J*-coupling), which is mediated by intervening electrons and is referred to as “through-bond coupling”. According to Ramsey,[21] there are five different mechanisms which contribute to *J* coupling: diamagnetic spin-orbital coupling (DSO), paramagnetic spin-orbital coupling

(PSO), Fermi-contact coupling (FC), spin-dipolar coupling (SD) and Fermi-contact spin-dipolar cross-coupling (FC × SD). The (usually) dominant FC term is the interaction between the magnetic moment of the nuclei and the electronic charge inducing an orbital current, which creates a magnetic field at the other nuclei, and this interaction can only occur with the *s*-orbitals. This mechanism is similar to the magnetic shielding. The DSO and PSO mechanisms involve the interaction between the nuclear spin angular momentum and the orbital angular momentum of the electrons. SD involves the direct dipolar coupling interaction between the magnetic moment and electronic spin. The first four mechanisms contribute to the isotropic part of *J* coupling and FC × SD contribute to the anisotropy of **J**. The Hamiltonian can be written as:

$$\hat{H}_J = h\hat{I}_1\mathbf{J}\hat{I}_2 = h\left(\hat{I}_{1x}, \hat{I}_{1y}, \hat{I}_{1z}\right)\begin{pmatrix} J_{\mathrm{xx}} & J_{\mathrm{xy}} & J_{\mathrm{xz}} \\ J_{\mathrm{yx}} & J_{\mathrm{yy}} & J_{\mathrm{yz}} \\ J_{\mathrm{zx}} & J_{\mathrm{zy}} & J_{zz} \end{pmatrix}\begin{pmatrix} \hat{I}_{2x} \\ \hat{I}_{2y} \\ \hat{I}_{2z} \end{pmatrix} \qquad \text{Eq 2.3.24}$$

Diagonalization of **J** gives rise to three principal components: J_{11}, J_{22}, and J_{33} and its orientation with respect to the molecular frame. Similar to the magnetic shielding, **J** is a general rank-2 tensor, and there are three parameters used to characterize the *J*-coupling tensors: the isotropic *J* coupling constant, the anisotropy of **J** and the asymmetry of **J.**

$$J_{iso} = (J_{11} + J_{22} + J_{33})/3 \qquad \text{Eq 2.3.25}$$

$$\Delta J = J_{33} - (J_{11} + J_{22})/2 \qquad \text{Eq 2.3.26}$$

$$\eta_J = (J_{22} - J_{11})/(J_{33} - J_{iso}) \qquad \text{Eq 2.3.27}$$

The three components are defined and ordered as ($|J_{33} - J_{\mathrm{iso}}| \geq |J_{11} - J_{\mathrm{iso}}| \geq |J_{22} - J_{\mathrm{iso}}|$). Unlike the traceless dipolar coupling tensor, the isotropic *J* coupling constant is observed in the solution and in the solid state, leaving multiplets in the NMR signals. Much literature ignores the anisotropic part of **J** and refers to the *J* coupling as "scalar coupling". This

anisotropic part of **J** is usually inseparable from the previously mentioned direct dipolar coupling constant (R_{DD}) in NMR experiments. In practice, only an effective dipolar coupling constant (R_{eff}) may be measurable in NMR experiments.

$$R_{\mathrm{eff}} = R_{\mathrm{DD}} - \Delta J/3 \qquad \text{Eq 2.3.28}$$

2.4 Single-Crystal NMR

The background given above refers generally to powdered samples. However, these conventional powder methods are generally only able to determine the magnitude of NMR parameters and only the relative orientations between NMR interaction tensors, but provide no information about the absolute orientation of each tensor in the molecular frame. Furthermore, polycrystalline experiments can be very challenging when quadrupolar nuclei are involved. Broad quadrupolar spectral patterns and/or spectral overlap from multiple crystallographically distinct sites in the sample can render the weak chemical shift anisotropy difficult to measure precisely.[22] An alternative to polycrystalline solid-state NMR experiments is single-crystal NMR, which typically requires an NMR probe with a goniometer which allows for a series of stepwise rotations of a single crystal, with dimensions of a few mm, about three arbitrary orthogonal axes in the applied magnetic field, shown in Figure 2.4.1(a). Fitting the rotation plots of frequency as a function of rotation angle allows for the measurement of both the magnitude and the orientation of the anisotropic NMR interactions in the molecular frame, resulting in a complete analysis of chemical shifts (CS) [23,24,25,26,27,28], spin-spin couplings[27], and quadrupole couplings.[22-26] The details of our approach are given below.

In a case of spin-1/2 nuclei, the expression of σ_{zz} in the PAS was given previously by Eq 2.3.5. Consider the shielding tensor from a crystal in a goniometer inside the probe as $\boldsymbol{\sigma}_G$. Then the shielding tensor in the orthogonal G system (X, Y, Z) can be related to the laboratory frame where the *z* axis aligns with the applied magnetic field direction,

$$\boldsymbol{\sigma_{Lab}} = R(\alpha,\beta,\gamma)\boldsymbol{\sigma_G}R^{-1}(\alpha,\beta,\gamma) \qquad \text{Eq 2.4.1}$$

where α, β, γ are the Euler angles that relate the goniometer G frame to the laboratory system. The definition of the Euler angles was explained previously.[29] The transformation from one system to another can be achieved by a first rotation by an angle of α about the *z*-axis of the original system, then a second rotation by an angle of β about the new *y*-axis, and a final rotation by an angle of γ about the new *z*-axis. These angles (α', β' and γ') can also be used to relate the chemical shift tensor and the intermediate quadrupolar coupling tensor (see Figure 2.4.1(b)). A rotation matrix can be constructed using the Euler angles as follows:

$$R(\alpha,\beta,\gamma) \qquad \text{Eq 2.4.2}$$
$$= \begin{bmatrix} \cos\alpha\cos\beta\cos\gamma - \sin\alpha\sin\gamma & \sin\alpha\cos\beta\cos\gamma + \cos\alpha\sin\gamma & -\sin\beta\cos\gamma \\ -\cos\alpha\cos\beta\sin\gamma - \sin\alpha\cos\gamma & -\sin\alpha\cos\beta\sin\gamma + \cos\alpha\cos\gamma & \sin\beta\sin\gamma \\ \cos\alpha\sin\beta & \sin\alpha\sin\beta & \cos\beta \end{bmatrix}$$

Therefore, σ_{zz} can be written as:[30]

$$(\sigma_{\boldsymbol{Lab},zz}) = \sum_{k,l}^{3,3} r_{3k} r_{3l} (\sigma_{\boldsymbol{G}})_{k,l} \qquad \text{Eq 2.4.3}$$

$$= \cos^2\alpha \sin^2\beta\,(\sigma_{G,\mathrm{XX}}) + \sin^2\alpha \sin^2\beta\,(\sigma_{G,\mathrm{YY}})$$
$$+ \cos^2\beta\,(\sigma_{G,\mathrm{ZZ}}) + 2(\cos\alpha \sin\alpha \sin^2\beta\,(\sigma_{G,\mathrm{XY}})$$
$$+ \sin\alpha \sin\beta \cos\beta\,(\sigma_{G,\mathrm{YZ}}) + \cos\alpha \sin\beta \cos\beta\,(\sigma_{G,\mathrm{XZ}}))$$

The crystal is rotated sequentially about each one of the three axes (X, Y, Z) aligned perpendicular to the magnetic field. As shown in Figure 2.4.1(a), when the crystal is rotated about the Z axis, the rotation angle θ is from the position where the X axis is aligned with the applied magnetic field direction. The other two directions (*x* and *y*) are chosen to ensure that the *x*, *y*, *z* laboratory system coincides with the initial directions of Y, Z, X in the cube frame. The corresponding rotation $R(\alpha, \beta, \gamma)$ that brings the G system back to the laboratory frame is $R(-\theta, 90, 90)$. Therefore, Eq 2.4.3 can be re-written as:[30]

$$(\sigma_{Lab,zz}) = \cos^2\theta\,(\sigma_{G,\mathrm{XX}}) + \sin^2\theta\,(\sigma_{G,\mathrm{YY}}) - 2\cos\theta \sin\theta\,(\sigma_{G,\mathrm{XY}}) \qquad \text{Eq 2.4.4}$$

$$= \frac{1}{2}\big((\sigma_{G,\mathrm{XX}}) + (\sigma_{G,\mathrm{YY}})\big) + \frac{1}{2}\big((\sigma_{G,\mathrm{XX}}) - (\sigma_{G,\mathrm{YY}})\big)\cos 2\theta$$
$$- (\sigma_{G,\mathrm{XY}}) \sin 2\theta$$

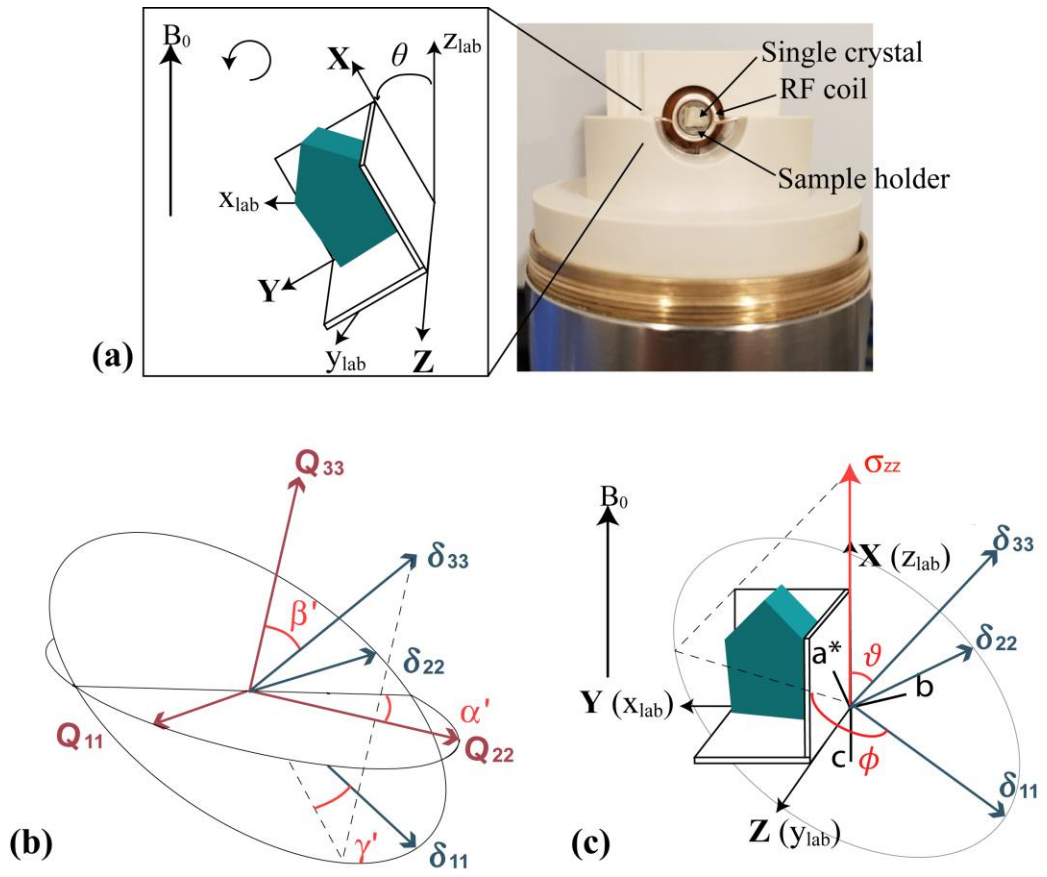

Figure 2.4.1. A photograph of (a) the NMR goniometer probe head with the crystal mounted inside. Shown in inset is an illustration of relative orientations between the laboratory frame (*x*, *y*, and *z*) and crystal holder, referred to as the orthogonal NMR cube system (X, Y, Z), when the crystal is rotated about the Z axis. The rotation angle θ is from the position where the X axis aligns with the applied magnetic field direction, which is chosen to be the *z* axis in the laboratory system. The other two directions (*x* and *y*) are chosen to make *x*, *y*, *z* in the laboratory system coincide with the initial position of Y, Z, X in the cube frame. (b) Relationship between the orientations of the PASs for the intermediate quadrupolar coupling tensors Q_{ii} and chemical shift δ_{ii} tensors in terms of the general Euler angles α', β', γ'.(c) An illustration of relative orientations between the laboratory frame (*x*, *y*, and *z*) and crystal holder, referred to as the orthogonal NMR cube system (X, Y, Z) and polar angle that define the orientation of magnetic shielding relative to the principal axis system (PAS) for chemical shift tensors.

When rotation is about the X axis, the transformation from the cube system to the G system is $\sigma_G = R(0, 90, 90)\sigma_{cube}R^{-1}(0, 90, 90)$, and the right-hand side of equation Eq 2.4.4 becomes $(\sigma_{Lab'_{ZZ}}) = \frac{1}{2}\left((\sigma_{G,YY}) + (\sigma_{G,ZZ})\right) + \frac{1}{2}\left((\sigma_{G,YY}) - (\sigma_{G,ZZ})\right)\cos 2\theta - (\sigma_{G,YZ})\sin 2\theta$.

Similarly, when rotation is about the Y axis, the transformation from the cube system to G system will be $\sigma_G = R(-90, -90, 0)\sigma_{cube}\ R(-90, -90, 0)$.

In a case of quadrupolar nuclei, the nuclear quadrupole interaction needs to be taken in account in addition to the magnetic shielding. In order to simplify the expression shown below, $\mathbf{Q} = \frac{eQ}{2I(2I-1)h}\mathbf{V}$, an intermediate variable related to the quadrupolar coupling tensor, is introduced to replace the EFG tensor (**V**). Therefore, it is a scalar multiple of **V**, which is also symmetric and traceless:

$$\mathbf{Q} = \begin{pmatrix} Q_{xx} & Q_{xy} & Q_{xz} \\ Q_{yx} & Q_{yy} & Q_{yz} \\ Q_{zx} & Q_{zy} & -Q_{xx} - Q_{yy} \end{pmatrix} = \begin{pmatrix} Q_{11} & 0 & 0 \\ 0 & Q_{22} & 0 \\ 0 & 0 & Q_{33} \end{pmatrix}_{PAS} \qquad \text{Eq 2.4.5}$$

Q_{ii} are the principal components of the intermediate quadrupolar coupling tensor ($|Q_{33}| \geq |Q_{22}| \geq |Q_{11}|$). They can be used to determine the quadrupolar coupling constant C_Q ($C_Q = \frac{eQV_{33}}{h} = 2I(2I-1)Q_{33}$) and asymmetry parameter η_Q ($\eta_Q = (Q_{11} - Q_{22})/Q_{33}$).

For half-integer quadrupolar nuclei, the frequency of the CT depends only on the chemical shift and the second-order quadrupolar interaction, while the splittings between the symmetric satellite peaks are determined by the first-order quadrupolar interaction. In this dissertation, only the frequency of the CT will be analyzed in order to derive the chemical shift and quadrupolar interaction parameters. Under static conditions, the second-order quadrupolar shift the CT is given by:[15]

$$v^{(2)}_{-\frac{1}{2},\frac{1}{2}} - v_0 = -\frac{1}{6v_0}\left(\frac{3e^2qQ}{2I(2I-1)h}\right)^2\left[I(I+1)-\frac{3}{4}\right] \times \left[A(\phi',\eta_Q)\cos^4\vartheta' + B(\phi',\eta_Q)\cos^2\vartheta' + C(\phi',\eta_Q)\right] \quad \text{Eq 2.4.6}$$

$$A(\phi',\eta) = \frac{-27}{8} + \frac{9}{4}\eta_Q\cos 2\phi' - \frac{3}{8}\left(\eta_Q\cos 2\phi'\right)^2$$

$$B(\phi',\eta) = \frac{30}{8} - \frac{1}{2}{\eta_Q}^2 - 2\eta_Q\cos 2\phi' + \frac{3}{4}\left(\eta_Q\cos 2\phi'\right)^2$$

$$C(\phi',\eta) = -\frac{3}{8} + \frac{1}{3}{\eta_Q}^2 - \frac{1}{4}\eta_Q\cos 2\phi' - \frac{3}{8}(\eta_Q\cos 2\phi')^2$$

ϑ' and ϕ' are the polar angles that define the orientation of the quadrupolar coupling tensor in the Cartesian coordinate system with respect to the magnetic field direction. As described by Volkoff,[31] there is a dependence of the displacement with respect to the unperturbed Larmor frequency ν_0 on the orientation of the crystal in the applied magnetic field. The dependence for X rotation has been adapted and described as[25]

$$(\nu_m - \nu_0)_X = A^{(X)} + B^{(X)}\cos 2\theta + C^{(X)}\sin 2\theta + D^{(X)}\cos 4\theta + E^{(X)}\sin 4\theta \quad \text{Eq 2.4.7}$$

with the coefficients:

$$A^{(X)} = \left(\frac{q}{8}\right)[-11(Q_{YY}^2 + Q_{ZZ}^2) - 50Q_{YY}Q_{ZZ} + 28Q_{YZ}^2 + 16(Q_{XZ}^2 + Q_{XY}^2)]$$

$$B^{(X)} = \left(\frac{3q}{2}\right)[Q_{YY}^2 - Q_{ZZ}^2 + 4Q_{XY}^2 - 4Q_{XZ}^2]$$

$$C^{(X)} = (-3q)[(Q_{YY} + Q_{ZZ})Q_{YZ} + 4Q_{XZ}Q_{XY}]$$

$$D^{(X)} = (-9q/8)[(Q_{YY} - Q_{ZZ})^2 - 4Q_{YZ}^2]$$

$$E^{(X)} = (9q/2)(Q_{YY} - Q_{ZZ})Q_{YZ}$$

$$q = [3 - 4I(I+1)]/16\nu_0$$

Therefore, the resonance frequency for the central transition ($m = \frac{1}{2} \leftrightarrow -\frac{1}{2}$) depends on both the quadrupolar interaction and the chemical shift and is given as:[25]

$$\nu^{(i)}_{\frac{1}{2}\leftrightarrow-\frac{1}{2}}(\theta) = A^{(i)} + B^{(i)}\cos 2\theta + C^{(i)}\sin 2\theta + D^{(i)}\cos 4\theta + E^{(i)}\sin 4\theta \qquad \text{Eq 2.4.8}$$

with the coefficients[25]

$$A^{(i)} = \left(\frac{q}{8}\right)[-11(Q^2_{jj} + Q^2_{kk}) - 50Q_{jj}Q_{kk} + 28Q^2_{jk} + 16(Q^2_{ki} + Q^2_{ij})] + (\delta_{jj} + \delta_{kk})\nu_0/2$$

$$B^{(i)} = \left(\frac{3q}{2}\right)[Q^2_{jj} - Q^2_{kk} + 4Q^2_{ij} - 4Q^2_{ki}] + (\delta_{jj} - \delta_{kk})\nu_0/2$$

$$C^{(i)} = (-3q)\left[(Q_{jj} + Q_{kk})Q_{jk} + 4Q_{ki}Q_{ij}\right] - \delta_{jk}\nu_0$$

$$D^{(i)} = (-9q/8)[(Q_{jj} - Q_{kk})^2 - 4Q^2_{jk}]$$

$$E^{(i)} = (9q/2)(Q_{jj} - Q_{kk})Q_{jk}$$

Here, (*i*, *j*, *k*) = (X, Y, Z) and this follows cyclic permutations. Q_{ii} describe the intermediate quadrupolar coupling tensor and δ_{ii} describe the CS tensor with respect to the cube axes or more generally to axes about which the crystal is rotated. These 11 variables (5 for the traceless intermediate quadrupolar coupling tensors and 6 for CS tensors) can be obtained from the best fit to experimental rotation data. These parameters can be used to build a 3 x 3 matrix which can then be diagonalized to produce the eigenvalues, which are

the three principal components of the intermediate quadrupolar coupling tensors (Q_{11}, Q_{22} and Q_{33}) and CS tensors (δ_{11}, δ_{22} and δ_{33}), and the eigenvectors, which are the direction cosines with respect to the cube axes.

For two nuclei possessing direct dipolar (D) and indirect spin-spin coupling (J) interactions. For two coupled spins (I_1 and I_2), ^{17}O and ^{31}P in this dissertation, the interaction energy is: [27]

$$E_{I_1 I_2} = hJ_{\text{iso}} I_1 I_2 + hI_1 R_{\text{eff}} I_2 \qquad \text{Eq 2.4.9}$$

Since the scalar part of the ^{31}P-^{17}O spin-spin coupling is independent of the anisotropic component, these data were analyzed analogously to the CS tensor part provided in Eq 2.4.8 as described by Lumsden et al.[27] The adapted fitting function for the splitting in (Hz) is shown as follows:

$$\Delta\nu^{(i)} = J_{\text{iso}} + A^{(i)} + B^{(i)} \cos 2\theta + C^{(i)} \sin 2\theta \qquad \text{Eq 2.4.10}$$

where $A^{(i)} = \left(R_{eff,jj} + R_{eff,kk}\right)\upsilon_0/2$, $B^{(i)} = \left(R_{eff,jj} - R_{eff,kk}\right)\upsilon_0/2$, $C^{(i)} = -R_{eff,jk}\upsilon_0$

2.5 NMR Experiments

2.5.1 Magic Angle Spinning

In conventional solid-state NMR experiments, the sample used for analysis is typically a polycrystalline powder, which has a random distribution of crystallite orientations. The orientation dependence (anisotropy) of the NMR interactions and the general lack of rapid molecular tumbling in solids result in broad lineshapes. In order to

improve the resolution of the NMR spectra, magic angle spinning (MAS) is usually applied. In this technique, the sample is tightly packed into a rotor which spins at the "magic angle" of 54.74° with respect to the applied magnetic field to average the first-order interaction such as dipolar coupling and chemical shift anisotropy to obtain "solution-like" spectra (Figure 2.5.1).[32,33]

Simulated NMR spectra at static condition and at MAS condition with different spinning speed are shown in Figure 2.5.1. When the spinning frequency is fast enough to be greater than the internal anisotropic interaction, only the isotropic peak will be observed. Even though currently available spinning speeds up to 150 kHz can be achieved, usually the spinning speed cannot completely average out the anisotropy, resulting in the presence of spinning sidebands generated by rotational echoes in the FID.[34] The spinning sidebands appear as a series of peaks spaced at multiples of the MAS rate from the isotropic peak. Spectra are acquired at different MAS frequencies or at different magnetic fields to differentiate the isotropic peaks (indicated by asterisks) from the spinning sidebands since the position of the isotropic peak is independent of the spinning frequency.

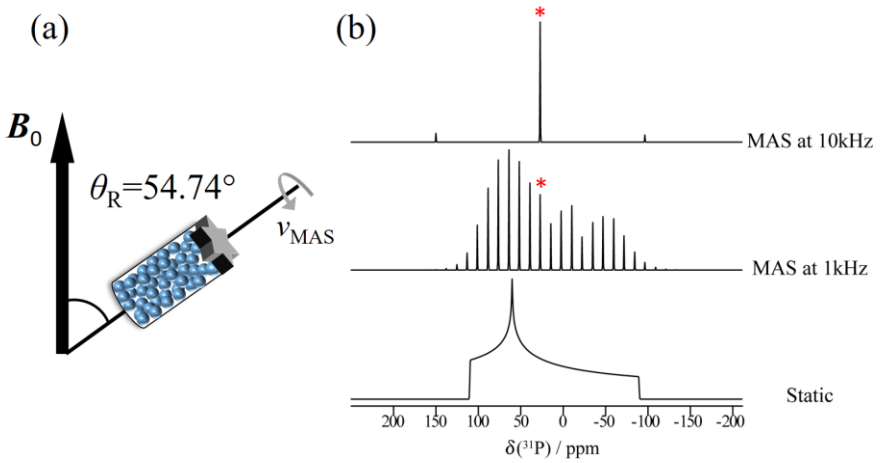

Figure 2.5.1. (a) Schematic representation displaying the orientation of the rotor with respect to the applied magnetic field (θ_R) during MAS experiment. (b) Simulated NMR spectra at static condition and at MAS condition with different spinning speeds (1 kHz and 10 kHz). The isotropic peaks are indicated by red asterisks.

The mathematical explanation of the "magic angle" of 54.74° with respect to the applied magnetic field relates to the $(3\cos^2\vartheta - 1)$ orientation dependency of the main NMR interactions. In order to average out the anisotropy, this term $(3\cos^2\vartheta - 1)$ needs to be zero. However, ϑ is the angle between the magnetic field and the *z* axis of the relevant NMR interaction tensor in its PAS and cannot be manipulated. The angle controlled experimentally is θ_R, which is the angle between the magnetic field and sample spinning axis. For a sample spinning around the axis with respect to the magnetic field θ_R with a rate of ν_{MAS}, the time averaged$(3\cos^2\vartheta - 1)$, $\langle 3\cos^2\vartheta - 1\rangle$, can be expressed as:

$$\langle 3\cos^2\vartheta - 1\rangle = \frac{1}{2}(3\cos^2\theta_R - 1)(3\cos^2\rho - 1) \qquad \text{Eq 2.5.1}$$

where ρ is the difference between θ_R and ϑ ($\rho = \theta_R - \vartheta$).

Therefore, when a sample is spinning at 54.74° with respect to the applied magnetic field ($(3\cos^2\theta_R - 1) = 0$), NMR interaction, such as magnetic shielding, first-order

quadrupolar interaction, heteronuclear dipolar interaction, *J*-coupling, can be averaged and second-order quadrupolar interaction can be reduced.

2.5.2 Cross-Polarization

Cross-polarization (CP)[35] is a signal enhancement technique used to transfer the magnetization from abundant spins (such as ^{1}H) to rare spins X (such as ^{13}C, ^{77}Se). The essence of CP is to bring the two coupled spins into "contact". This can be achieved by applying RF pulse to irradiate both resonance frequencies so that the nutation frequencies of these two spins are equal, known as "Hartmann Hahn condition".

$$|\gamma_H|B_{1,H} = |\gamma_{\mathrm{X}}|B_{1,\mathrm{X}} \qquad \text{Eq 2.5.2}$$

where γ_{H} and γ_{X} are the gyromagnetic ratio of abundance ^{1}H and rare spin X, respectively.

A general schematic representation of CP pulse scheme is displayed in Figure 2.5.2. After an initial 90 degree excitation pulse on ^{1}H, RF spin-lock pulses are applied to both spins. The magnitude of the pulses $B_{1,\mathrm{H}}$ and $B_{1,\mathrm{X}}$ can be chosen to match the Hartmann Hann condition. This period is called contact time. During the contact time, the magnetization can be transferred from abundant ^{1}H to rare nuclei X. Then the NMR signal of X can be acquired. The CP experiments can improve the signal to noise (S/N) ratio by a factor of up to $\gamma_{\mathrm{abundant}}/\gamma_{\mathrm{rare}}$. Moreover, the initial excitation is applied on ^{1}H nuclei, which has faster T_1 relaxation and hence shorter recycle delay (shorter waiting time between

repetition of the experiments). Therefore, another advantage of CP experiment (for example $^{1}H \rightarrow ^{31}P$ CP experiment in this dissertation) is to decrease the experimental time.[36]

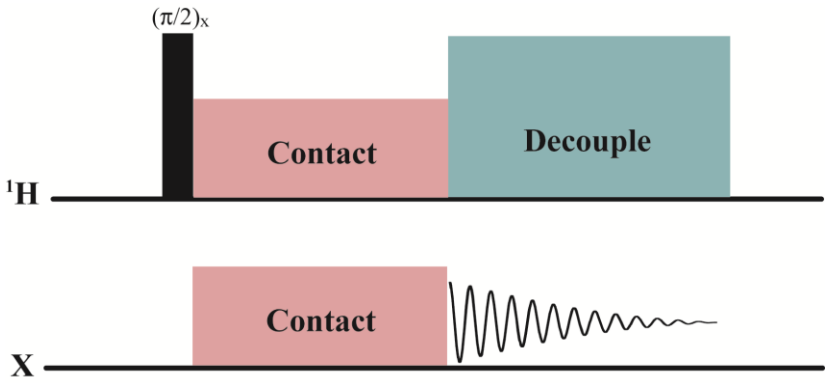

Figure 2.5.2. The pulse sequence for $^{1}H \rightarrow X$ cross polarization experiment.

2.5.3 Spin-Echo

In solid samples, especially under static conditions, the duration of the FID can be extremely short, resulting from the broadness of the anisotropic lineshape. This can be a problem when the first few data points are lost during the dead time (time between the end of pulse and time when the receiver is on to collect data). The Hahn echo technique is to refocus the dephasing effect caused by chemical shift anisotropy, dipolar coupling, quadrupolar coupling interaction, and magnetic field inhomogeneity. The Hahn echo pulse sequence can be described as a $\pi/2$-τ-π (or 90°-τ-180°) pulse. The pulse sequence is shown in Figure 2.5.3. An initial 90° excitation pulse brings the magnetization to transverse plane. After the first delay τ, spins precess at different rate causing the signal to diphase. After a 180° pulse, which is to flip the spins to another site, the spins maintain their initial precession frequency and precession direction, refocusing to form a spin echo after another

period of τ so that the dephase effect is removed and the beginning of FID is able to be recorded.

Hahn echo sequence gives the maximum signal but also induces distortions. Another echo experiment is quadrupolar echo (or solid echo), which consists of two π/2 or 90° pulses., This sequence gives half of the signal obtained from Hahn echo, but with the resulting better lineshape, it is a reasonable compromise.

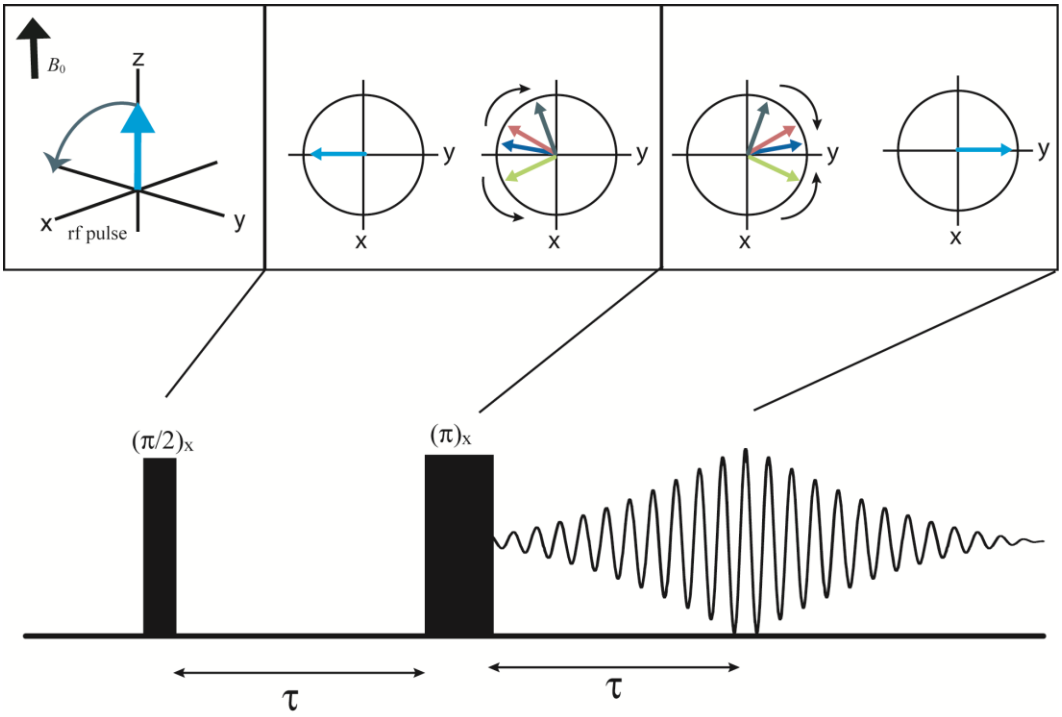

Figure 2.5.3. Schematic representation of vector diagram (top) and pulse sequence of the Hahn echo experiment (bottom). Light blue arrow represents the net magnetization. Light green, dark blue, pink and dark green arrows represent the dephasing. Black arrow represents the movement of the spins within *xy* plane, causing the dephasing and refocusing.

2.6 Quantum Chemical Calculations on NMR

A quantum computational study can be conducted to provide a comparison between experimental results and the theoretical values, and also to provide insights into the correlation of electronic structure and the observed NMR parameters. Calculation models are generated using atomic coordinates either obtained experimentally from the X-ray crystal structures or created using software such as GaussView[37]. In this thesis, the atomic coordinates were obtained from the X-ray crystal structures. The proton geometry is generally optimized due to the limitations of X-ray diffraction for determining proton positions.[38,39] As a result, this technique becomes less reliable in systems with proton disorder, proton exchange, etc.[40,41] The magnitude and the orientation of the NMR parameters, such as magnetic shielding, quadrupolar coupling interaction, and *J* coupling interaction can be calculated using density functional theory (DFT) method.[42,43,44] The magnetic shielding and EFG tensors can be extracted through software such as EFGShield.[29]

Unlike ab initio methods, which are based on the Schrödinger equation ($\hat{H}\Psi = \mathrm{E}\Psi$) and attempts to find an approximate wave function (Ψ), DFT expresses the energy of a molecular system as a functional of the total electron density. A functional is a function of a function; the total electron density is a function of nuclear coordinates. The total energy can be expressed as a sum of kinetic and Coulombic energies, which can be calculated as Hartree-Fock method, and exchange-correlation energy. The challenge for DFT calculation is that the exact exchange-correlation functional is unknown; therefore, various approximate functionals have been developed to provide improved results. The simplest exchange-correlation functional is the local density approximation (LDA),[45] which

assumes the exchange-correlation energy of each point in space is equal to the exchange-correlation energy of a uniform electron gas with same charge density at that point. A better approximation is given by the generalized gradient approximation (GGA) which adds electron density gradients.[46]

Relativistic effects can strongly influence the chemical properties of the heavier elements.[47] As atomic nuclear charge increases, *s* electrons increase their average velocity, which is closer to the speed of light, and travel in smaller orbitals. Therefore, *s* electrons are more strongly bound and the *d* and *f* electrons are less bound and occupy larger orbitals. The zeroth-order regular approximation (ZORA)[48,49] formalism accounts for scalar and spin-orbit relativistic effects.

Molecular orbital (MO) is a linear combination of atomic orbitals, given in Eq 2.6.1.:[14]

$$\psi(\vec{r})^{MO} = \sum_{i=1}^{K} \chi_i(\vec{r}) C_i \qquad \text{Eq 2.6.1}$$

where C_i is the mixing coefficient (variational parameter), χ_i is the atomic orbital. The number and nature of the functions that molecular orbital can be expanded form a basis set. The more basis sets, the more variational parameters, the more accurately the wave function can be represented.

Natural bond orbitals (NBOs) are used to calculate localized distribution of electron density in the bonds between atoms, and provide a quantum-mechanical description that is highly close to the natural Lewis structure. One of the most popular methods to obtain localized MOs is via the concept of natural localized molecular orbitals (NLMOs), which

arise from the delocalization of the natural bond orbitals (NBOs). The NLMOs can be written as: [14,50,51]

$$\phi_j^{NLMO} = \Omega_j W_{jj} + \sum_{n \neq j}^{NBO} \Omega_n W_{nj} \qquad \text{Eq 2.6.2}$$

where the Ω_n are a set of strongly localized NBOs that are closely associated to the Lewis structure of the molecule. The $n = j$ term is referred to as "Lewis" part. If the Lewis formula provides a good description of the electronic structure, the W_{jj} tend to be close to unity. The remaining part is referred to as the "non-Lewis" delocalization tail of the NLMO, which is significant for systems with electron delocalization.

Some of the DFT calculations presented in the first study were carried out using the Amsterdam Density Functional (ADF) package.[52] The NLMO analysis included can decompose the orbital contributions to the NMR observables (magnetic shielding,[53] EFG tensors,[14] and *J* coupling[51]) into orbitals representing core, bonding, lone pairs etc. This can provide a great understanding of the origins of the NMR interactions and the electronic structures of the molecules.

In order to include long-range effects in accurate calculations of NMR parameters, infinite crystals instead of simple cluster models will be simulated. Due to the presence of translational symmetry, the unit cell (smallest repetitive unit in the crystal lattice) subject to periodic boundary conditions is sufficient to generate the input file. For calculations of periodic systems, plane-wave basis functions are used instead of atom-centered basis functions, providing the gauge-including projector-augmented wave (GIPAW) approach[54] to calculate the NMR parameters. Chemical bonding is mainly characterized by valence

electrons, and thus the core electrons are less important. The oscillation of the core electrons with high kinetic energy requires a huge number of plane waves to represent their behaviour, which is computationally costly. In the GIPAW method, core electrons can be assumed not to participate in any chemical bonding and stay unchanged; this is the frozen core approximation. A smooth potential replaces the wave functions of core electrons and valence electrons closed to nucleus. This is known as a pseudopotential.[55] Prior to the actual calculations, there are two parameters which need to be optimized to achieve energy convergence: *k*-points and cut-off energy. *k*-points are the spaced points used in the primitive unit cell in the reciprocal unit. The *k*-points chosen need to be sufficiently large to converge the energy. Cut-off energy determines the truncation of the planewaves used in the basis set. Both parameters are to increase until the desired convergence is reached. All the GIPAW calculations in this thesis were carried out using CASTEP with Materials Studio.[56]

2.7 References for Chapter 2

[1] Levitt, M. H. *Spin Dynamics, second edition*, John Wiley & Sons: Chichester, 2009.

[2] Zeeman, P. Doublets and triplets in the spectrum produced by external magnetic forces. *Phil. Mag.* **1897**, *44*, 55-60.

[3] Torchia, D. A.; Szabo, A. Spin-lattice relaxation in solids *J. Magn. Reson.* **1982**, *49*, 107-121.

[4] Bloch, F. Nuclear induction. *Phys. Rev.* **1946**, *70*, 460-474.

[5] Duer, M. J. *Introduction to Solid-State NMR Spectroscopy*, Wiley-Blackwell: Oxford, 2004

[6] Keeler, J. *Understanding NMR Spectroscopy*, John Wiley & Sons: Chichester, 2005.

[7] Purcell, E. M.; Torrey, H. C.; Pound, R. V. Resonance Absorption by Nuclear Magnetic Moments in a Solid. *Phys. Rev.* **1946**, *69*, 37-38.

[8] Ernst, R. R.; Anderson, W. A. Application of Fourier Transform Spectroscopy to Magnetic Resonance. *Rev. Sci. Instrum.* **1966**, *37*, 93-102.

[9] Ramsey, N. F. Magnetic shielding of nuclei in molecules. *Phys. Rev.* **1950**, *78*, 699-703.

[10] Apperley, D. C.; Harris, R. K.; Hodgkinson, P. *Solid-state NMR Basic Principles & Practice*; Momentum Press: New York, 2012.

[11] Woessner, D. E. Brownian motion and its effects in NMR chemical exchange and relaxation in liquids. *Concepts Magn. Reson.* **1996**, *8*, 397-421.

[12] Herzfeld, J.; Berger, A. E. Sideband intensities in NMR spectra of samples spinning at the magic angle. *J. Chem. Phys.* **1980**, *73*, 6021-6030.

[13] Wasylishen, R. E.; Ashbrook, S. E.; Wimperis, S. *NMR of Quadrupolar Nuclei in Solid Materials*; John Wiley & Sons: Chichester, 2012.

[14] Autschbach, J.; Zheng, S.; Schurko, R. W. Analysis of Electric Field Gradient Tensors at Quadrupolar Nuclei in Common Structural Motifs. *Concepts Magn. Reson. Part A* **2010**, *36*, 84–126.

[15] Man, P. P., Quadrupolar Interactions. In *Encyclopedia of Nuclear Magnetic Resonance*; Harris, R. K., Wasylishen, R. E., Eds; John Wiley & Sons: Chichester, 2011.

[16] Gan, Z.; Gor'kov, P.; Cross, T. A.; Samoson, A.; Massiot, D. Seeking Higher Resolution and Sensitivity for NMR of Quadrupolar Nuclei at Ultrahigh Magnetic Fields. *J. Am. Chem. Soc.* **2002**, *124*, 5634-5635.

[17] Jaroniec, C. P.; Filip, C.; Griffin, R. G. 3D TEDOR NMR Experiments for the Simultaneous Measurement of Multiple Carbon−Nitrogen Distances in Uniformly ^{13}C,^{15}N-Labeled Solids *J. Am. Chem. Soc.* **2002**, *124*, 10728-10742

[18] Reichert, D.; Pascui, O.; Judeinstein, P.; Gullion, T. Determination of intermolecular distances in solid polymer electrolytes by ^{13}C–^{7}Li REDOR NMR. *Chem. Phys. Lett.* **2005**, *402*, 43-47.

[19] Potnuru, L. R.; Duong, N. T.; Ahlawat, S.; Raran-Kurussi, S.; Ernst, M.; Nishiyama, Y.; Agarwal, V. Accuracy of ^{1}H–^{1}H distances measured using frequency selective recoupling and fast magic-angle spinning. *J. Chem. Phys.* **2020**, *153*, 084202.

[20] Wasylishen, R. E. Dipolar and Indirect Coupling: Basics. In *NMR Crystallography*; Harris, R. K., Wasylishen, R. E., Duer, M. J., Eds.; John Wiley & Sons: Chichester, 2009; pp 127−136.

[21] Ramsey, N. F. Electron Coupled Interactions between Nuclear Spins in Molecules. *Phys. Rev.* **1953**, *91*, 303-307

[22] Vosegaard, T.; Hald, E.; Langer, V.; Skov, H. J.; Daugaard, P.; Bildsøe, H.; Jakobsen, H. J. Improved Hardware and Software for Single-Crystal NMR Spectroscopy. *J. Magn. Reson.* **1998**, *135*, 126–132.

[23] Vosegaard, T.; Skibsted, J.; Bildsøe, H.; Jakobsen, H. J. Quadrupole Coupling and Anisotropic Shielding from Single-Crystal NMR of the Central Transition for Quadrupolar Nuclei. ^{87}Rb NMR of $RbClO_4$ and Rb_2SO_4. *J. Magn. Reson. - Ser. A* **1996**, *122*, 111–119.

[24] Vosegaard, T.; Byriel, I. P.; Jakobsen, H. J. Characterization of the Two Rubidium Sites in Rb_2CrO_4 by ^{87}Rb Single-Crystal NMR. *J. Phys. Chem. B* **1997**, *101*, 8955–8958.

[25] Power, W. P.; Kirby, C. W.; Taylor, N. J. A Single-Crystal ^{59}Co NMR Study of Vitamin B_{12}. *J. Am. Chem. Soc.* **1998**, *120*, 9428–9434.

[26] Eichele, K.; Chan, J. C. C.; Wasylishen, R. E.; Britten, J. F. Single-Crystal Cobalt-59 NMR Study of Tris(2,4-Pentanedionato-*O,O'*)cobalt(III). *J. Phys. Chem. A* **1997**, *101*, 5423–5430.

[27] Lumsden, M. D.; Eichele, K.; Wasylishen, R. E.; Cameron, T. S.; Britten, J. F. Determination of a ^{199}Hg-^{31}P Indirect Spin-Spin Coupling Tensor via Single-Crystal Phosphorus NMR Spectroscopy. *J. Am. Chem. Soc.* **1994**, *116*, 11129–11136.

[28] Eichele, K.; Ossenkamp, G. C.; Wasylishen, R. E.; Cameron, T. S.; Phosphorus-31 Solid-State NMR Studies of Homonuclear Spin Pairs in Molybdenum Phosphine Complexes: Single-Crystal, Dipolar-Chemical Shift, Rotational-Resonance, and 2D Spin−Echo NMR Experiments. *Inorg. Chem.* **1999**, *38*, 639–651.

[29] Adiga, S.; Aebi, D.; Bryce, D. L. EFGShield — A Program for Parsing and Summarizing the Results of Electric Field Gradient and Nuclear Magnetic Shielding Tensor Calculations. *Can. J. Chem.* **2007**, *85*, 496–505.

[30] Kennedy, M. A.; Ellis, P. D. The Single-Crystal NMR Experiment: An Experimentalist's Guide *Concepts Magn. Reson.* **1989**, *1*, 109–129.

[31] Volkoff, G. M. Second Order Nuclear Quadrupole Effects in Single Crystals. *Can. J. Phys.* **1953**, *31*, 820-836.

[32] Andrew, E. R.; Bradburry, A.; Eades, R. G. Fine Structure of the Nuclear Magnetic Resonance Spectra of Solids: Chemical Shift Structure of the Spectrum of Phosphorus Pentachloride. *Nature*, **1958**, *182*, 1659.

[33] Lowe, I. J. Free Induction Decays of Rotating Solids. *Phys. Rev.* **1959**, *2*, 285-287.

[34] Herzfeld, J.; Roufosse, R. A.; Haberkorn, R. A.; Griffin, R. G.; Glimcher, M. J. Magic angle sample spinning in inhomogeneously broadened biological systems. *Phil. Trans. R. Soc. Lond. B* **1980**, *289*, 459–469.

[35] Pines, A.; Gibby, M. G.; Waugh, J. S. Proton-Enhanced Nuclear Induction Spectroscopy. A Method for High Resolution NMR of Dilute Spins in Solids. *J. Chem. Phys.* **1972**, *56*, 1776–1777.

[36] Hartmann, S. R.; Hahn, E. L. Nuclear double resonance in the rotating frame. *Phys. Rev.* **1962**, *128*, 2042–2053

[37] Frisch, M. J. et al. Gaussian. Gaussian, Inc., Wallingford CT, 2016.

[38] Woińska, M; Grabowsky, S.; Dominiak, P. M.; Woźniak, K.; Jayatilaka, D. Hydrogen atoms can be located accurately and precisely by X-ray crystallography *Sci. Adv.* **2016**, *2*, 1–8.

[39] Schmidtmann, M.; Coster, P. Henry, P. F.; Ting, V. P.; Weller, M. T.; Wilson, C. C. Determining hydrogen positions in crystal engineered organic molecular complexes by joint neutron powder and single crystal X-ray diffraction. *CrystEngComm*, **2014**, *16*, 1232–1236.

[40] Wilson, C. C. The evolution of hydrogen atom parameters under changing external conditions by time-of-flight single crystal neutron diffraction. *Crystallogr. Rev.* **2007**, *13*, 143–198.

[41] Dittrich, B.; Warren, J. E.; Fabbiani, F. P. A.; Morgenroth, W. Temperature dependence of rotational disorder in a non-standard amino acid from X-ray crystallography and molecular dynamics simulation. *Phys. Chem. Chem. Phys.*, **2009**, *11*, 2601–2609.

[42] Schreckenbach, G.; Ziegler, T. Density functional calculations of NMR chemical shifts and ESR *g*-tensors. *Theor Chem Acc*, **1998**, *99*, 71–82.

[43] Bonhomme, C.; Gervais, C.; Babonneau, F.; Coelho, C.; Pourpoint, F.; Azaïs, T.; Ashbrook, S. E.; Griffin, J. M.; Yates, J. R.; Mauri, F.; Pickard, C. J. First-Principles Calculation of NMR Parameters Using the Gauge Including Projector Augmented Wave Method: A Chemist's Point of View. *Chem. Rev.* **2012**, *112*, 5733– 5779.

[44] Casabianca, L. B. Calculating nuclear magnetic resonance chemical shifts in solvated systems. *Magn Reson Chem.* **2020**, *58*, 611–624.

[45] Vosko, S. H.; Wilk, L.; Nusair, M. *Can. J. Phys.* **1980**, *58*, 1200–1211.

[46] Perdew, J. P.; Burke, K.; Ernzerhof, M. *Phys. Rev. Lett.* **1996**, *77*, 3865–3868.

[47] Yatsimirskii, K. B. Relativistic Effects in Chemistry. *Theor. Exp. Chem.*, **1995**, *31*, 153–168.

[48] van Lenthe, E.; Baerends, E. J.; Snijders, J. G. *J. Chem. Phys.* **1994**, *101*, 9783–9792.

[49] van Lenthe, E.; Ehlers, A.; Baerends, E.-J. *J. Chem. Phys.* **1999**, *110*, 8943–8953.

[50] Reed, A. E.; Weinhold, F. Natural localized molecular orbitals. *J. Chem. Phys.* **1985**, *83*, 1736–1740.

[51] Autschbach, J. Analyzing NMR shielding tensors calculated with two-component relativistic methods using spin-free localized molecular orbitals. *J. Chem. Phys*., **2008**, *128*, 164112.

[52] ADF2017, SCM, Theoretical Chemistry, Vrije Universiteit, Amsterdam, The Netherlands.

[53]. Sutrisno, A.; Lo, A. Y. H.; Tang, J. A.; Dutton, J. L.; Farrar, G. J.; Ragogna, P. J.; Zheng, S.; Autschbach, J.; Schurko, R. W. Experimental and theoretical investigations of selenium nuclear magnetic shielding tensors in Se-N heterocycles. *Can. J. Chem.* **2009**, *87*, 1546–1564.

[54] Pickard, C. J.; Mauri, F. All-electron magnetic response with pseudopotentials: NMR chemical shifts. *Phys. Rev. B* **2001**, *63*, 245101.

[55] Yates, J. R.; Pickard, C. J.; Mauri, F. Calculation of NMR chemical shifts for extended systems using ultrasoft pseudopotential. *Phys. Rev. B* **2001**, *76*, 024401.

[56] Clark, S. J.; Segall, M. D.; Pickard, C. J.; Hasnip, P. J.; Probert, M. I. J.; Refson, K.; Payne, M. C. First Principles Methods Using CASTEP *Z. Kristallogr. - Cryst. Mater.* **2005**, *220*, 567–570.

PART 2 POLYCRYSTALLINE EXPERIMENTS

Chapter 3. Solid-State NMR Study on Halogen-Bonded P=O···I–C Motifs

3.1 Introduction

As mentioned in Chapter 1, the halogen bonding (XB) interaction has been receiving an increasing amount of attention in various research fields. Solution NMR has played an important role in studying the halogen bonding interaction. Recently, Bowling and coworkers studied the effect of solvents on intramolecular XB by ^{13}C, ^{15}N, and ^{19}F solution-state NMR.[1] Ciancaleoni et al. used a combination of nuclear Overhauser effect (NOE) NMR and density functional theory (DFT) calculations to roughly quantify the XB/non-XB adducts in solution.[2] However, there is a relative dearth of studies on XB using solid-state NMR. Weingarth et al. reported a measurement of the N···I halogen bond distance by ^{15}N solid-state NMR.[3] Our group is interested in the characterization of non-covalent interactions (*i.e.*, halogen bonds, tetrel bonds, etc.) via SSNMR.[4] This approach provides various advantages which are not available to solution-state NMR, such as eliminating potential interactions with solvent as well as the measurement of complete electric field gradient (EFG) and chemical shift (CS) tensors. From previous investigations in our group, we have demonstrated various relationships between NMR observables and the XB environments. For example, a series of halogen solid-state NMR experiments and gauge-including projector-augmented wave (GIPAW) DFT calculations showed that the ^{81}Br isotropic chemical shift and span both decrease as the bromide-halogen XB is weakened.[5] An indirect study on cocrystallization of halide salts and *para*-diiodotetrafluorobenzene using ^{13}C NMR showed that the ^{13}C chemical shift increases as the C-I distance increases.[6] Also, multinuclear solid-state magnetic resonance and molecular orbital analysis revealed that halogen quadrupolar coupling constants and asymmetry parameters correlate with the local halogen bonding geometry of type I···X^-···I

(X = Br or Cl).[7] Most recently, a direct study on halogen-bonded P=Se···I motifs showed an increase in the magnitude of $J(^{31}P, ^{77}Se)$ and ^{77}Se chemical shift values as the XB weakens.[8]

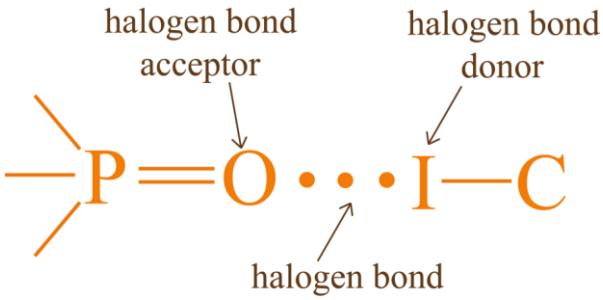

Figure 3.1.1. General halogen bonded P=O···I–C moiety.

Here, we exploit recent progress in mechanochemistry[9] to prepare and study a series of cocrystals featuring P=O···I–C halogen bonds (Figure 3.1.1) using a combination of X-ray diffraction (XRD) and solid-state multinuclear magnetic resonance methods. We apply a mechanochemical approach, liquid-assisted grinding (LAG),[10] as an alternative method to synthesize halogen-bonded cocrystals. Since cocrystallization via LAG generates less potentially toxic solvent waste (only a few drops of liquid are needed), it may be more environmentally acceptable than solution crystallization.[11] Also, this method offers an attractive alternative when difficulties are encountered in preparing cocrystals via solution methods. The potential of phosphine oxides as XB acceptors has recently attracted attention. Friščić and coworkers prepared, via LAG, various cocrystals of methyldiphenylphosphine oxide and *para*-diiodotetrafluorobenzene and characterized them with X-ray diffraction.[12] Bowmaker et al. have reported on the mechanochemical preparation of various cocrystals of phosphines and studied them via ^{31}P SSNMR, among other methods.[13] In our study, new halogen-bonded compounds have been prepared

through mechanochemical LAG and subsequent slow recrystallization. The geometry of the halogen-bonded compounds has been characterized by single-crystal XRD. ^{31}P cross polarization magic-angle spinning (CP/MAS) SSNMR spectra are reported and the ^{31}P chemical shift tensors, which are indirectly characteristic of halogen bonding, are extracted for all halogen-bonded compounds and starting materials.

The ^{17}O isotope is more difficult to observe by NMR spectroscopy due to its electric quadrupole moment (Q = -2.558 fm^2), low natural abundance (0.038%) and its extremely low NMR sensitivity relative to ^{1}H (0.0291).[14] Even though the quadrupolar interaction contributes to broad ^{17}O SSNMR line shapes, this method is a proven sensitive tool for probing structure,[15,16] dynamics,[17] and bonding. [16,18,19] Here, we also provide a direct investigation of the relationships between the halogen bonding interaction and the measured NMR parameters for the half-integer spin quadrupolar nucleus ^{17}O (I = 5/2), such as the quadrupolar coupling constant, C_Q, asymmetry parameter, η_Q, and indirect spin-spin (J) coupling between ^{31}P and ^{17}O, using ^{17}O SSNMR experiments. All of the NMR parameters have also been calculated and interpreted via DFT methods. The computed values are related to the halogen bond strength to help interpret the correlation between the NMR parameters and halogen bonding environment. A further natural localized molecular orbital (NLMO) DFT analysis was conducted to investigate the relationship between the local electronic environment in the presence of halogen bonding interaction and the observed NMR parameters, J(^{31}P, ^{17}O) and C_Q (^{17}O).

3.2 **Experimental Section**

3.2.1 Synthesis

(i) Halogen-bonded compounds

Two halogen bond acceptors (CH_3Ph_2PO, Ph_3PO) and three halogen bond donors (*p*-$C_6F_4I_2$, *o*-$C_6F_4I_2$, *sym*-$C_6F_3I_3$) were purchased from Sigma Aldrich and used without further purification except for Ph_3PO. The purchased Ph_3PO, which was a mixture of two polymorphs (monoclinic and orthorhombic), was recrystallized from acetone to give a monoclinic polymorph before use in further reactions. The preparations of two halogen-bonded compounds containing *p*-$C_6F_4I_2$ were performed using a procedure adapted from the literature.[12, 20] Halogen-bonded compounds were produced by LAG, whereby equimolar amounts of starting material were ground in a mortar and pestle with a trace amount of acetonitrile for about 20 minutes.[21] The amounts of starting materials used for synthesis are listed in Table A1 in the Appendix A. The mixture was subsequently dissolved in a small vial containing a minimum amount of acetonitrile and slowly evaporated at room temperature until the products crystallized, yielding the halogen-bonded compounds: (Ph_3PO)(*p*-$C_6F_4I_2$)$_2$ (**A1**), (Ph_3PO)(*o*-$C_6F_4I_2$)$_2$ (**A2**), (Ph_3PO)(*sym*-$C_6F_3I_3$) (**A3**), (CH_3Ph_2PO)(*p*-$C_6F_4I_2$)(CH_3CN) (**B1**) and (CH_3Ph_2PO)(*sym*-$C_6F_3I_3$)$_2$ (**B3**). Comparison between PXRD and solid-state NMR data acquired before and after recrystallization from slow evaporation (Figure A3) confirmed that the halogen-bonded cocrystals were produced by LAG.

(ii) ^{17}O-labeled halogen-bonded compounds

The synthesis of ^{17}O-labeled Ph_3PO was carried out as described in the literature.[22] An amount of 1.5 g Ph_3P was dissolved in 20 mL dry dichloromethane in an ice bath under

argon. An amount of 0.3 mL of bromine dissolved in another 20 mL of dry dichloromethane was added dropwise to the previous solution under continuous cooling. After the solution was allowed to warm to room temperature, 0.1 mL of 40% ^{17}O-enriched H_2O was added and stirred overnight, which formed a separate water phase at first but disappeared later to give a clear dark orange solution. The solution was washed three times with 10% Na_2CO_3 solution, which yielded a light yellow product but turned colorless eventually. Finally, the solution was dried with $MgSO_4$. An amount of 1.1080 g (70% yield) of monoclinic $Ph_3P^{17}O$ was obtained after crystallization from acetone. ^{17}O-labeled halogen-bonded compounds were synthesized as described above, using $Ph_3P^{17}O$ as starting material.

3.2.2 Single-Crystal X-Ray Crystallography

Data collection results for compounds **A1**, **A2**, **A3**, **B1**, and **B3** represent the best data sets obtained in several trials for each sample. The crystals were mounted on thin glass fibers using paraffin oil. Prior to data collection, crystals were cooled to 200 K. Data were collected on a Bruker AXS SMART single crystal diffractometer equipped with a sealed Mo tube source (wavelength 0.71073 Å) APEX II CCD detector. Raw data collection and processing were performed with the APEX II software package from BRUKER AXS.[23] Diffraction data for **B1, A1**, and **B3** samples were collected with a sequence of 0.3° ω scans at 0, 120, and 240° in φ. Due to lower unit cell symmetry, in order to ensure adequate data redundancy, diffraction data for **A2** and **A3** were collected with a sequence of 0.3° ω scans at 0, 90, 180, and 270° in φ. Initial unit cell parameters were determined from 60 data frames with 0.3° ω scan each, collected at the different sections of the Ewald sphere. Semiempirical absorption corrections based on equivalent

reflections were applied.[24] Systematic absences in the diffraction dataset and unit cell parameters were consistent with triclinic $P\bar{1}$ (No. 2) for compounds **A2** and **A3,** monoclinic $P2_1/c$ (No. 14) for compound **A1,** monoclinic $P2_1/n$ (No. 14, alternative settings) for compound **B3** and orthorhombic P*nma* (No. 62) for **B1**. Solutions in the centrosymmetric space groups for all reported compounds yielded chemically reasonable and computationally stable results of refinement. The structures were solved by direct methods, completed with difference Fourier synthesis, and refined with full-matrix least-squares procedures based on F^2.

For all compounds, all hydrogen atomic positions were calculated based on the geometry of related non-hydrogen atoms and constrained to the riding model. All hydrogen atoms were treated as idealized contributions during the refinement. All scattering factors are contained in several versions of the SHELXTL program library, with the latest version used being v.6.12.[25]

3.2.3 Powder X-Ray Diffraction

Sample purity was verified by X-ray powder diffraction analysis (shown in Figure A1 and Figure A2 in the Appendix A) using a Rigaku Ultima IV Diffractometer at room temperature (298±1 K) with a copper source and one diffracted beam monochromator, and with 2θ ranging from 5º to 50º in increments of 0.02º at a rate of 1º per minute. Simulations were generated using Mercury 3.6 software from the Crystallographic Data Center.

3.2.4 Solid-State NMR

Bruker consoles were used to acquire data at the University of Ottawa using 4.7 T, 9.4 T, and 11.7 T magnets and at the National Ultrahigh-field NMR Facility for Solids in

Ottawa using a 21.1 T magnet. A 7 mm Bruker HXY MAS probe was employed for experiments at 4.7 T. Experiments at 9.4 T and 11.7 T used a 4 mm Bruker HXY probe or 7 mm Bruker HXY MAS probe, while experiments at 21.1 T used a 4 mm Bruker HX MAS probe and a home-built solenoid 5 mm HX static probe (PM#7).

(i) ^{31}P SSNMR

The ^{31}P SSNMR spectra of all halogen-bonded compounds were acquired at 4.7 T ($\nu_L(^{31}P)$ =80.997 MHz) and at 9.4 T ($\nu_L(^{31}P)$ = 161.976 MHz). The chemical shifts were referenced to ammonium dihydrogen phosphate (δ_{iso} = 0.81 ppm with respect to H_3PO_4 in 85% D_2O). The MAS frequency was varied from 6 kHz to 2.5 kHz to obtain spectra with a sufficient number of sidebands for spectral fitting purposes. A standard cross-polarization pulse sequence was employed. The $\pi/2$ pulse length and contact time were 3.6 μs and 1.5 ms, respectively. The relaxation delay varied from 50 s to 120 s for Ph_3PO compounds and from 2 to 15 s for CH_3Ph_2PO compounds. Compound **B2** is a noncrystalline solid and has a low decomposition point (39 ℃). Only one phase cycle (^{31}P CP/MAS) was acquired for this compound at 4.7 T before the sample decomposed, as assessed in a second experiment with a larger number of scans.

(ii) ^{17}O SSNMR

The ^{17}O chemical shifts were referenced to liquid water (δ_{iso} = 0.00 ppm). Synthesized ^{17}O-Ph_3PO was packed into a 7 mm o.d. zirconia rotor, and halogen-bonded compounds were packed into a 4 mm o.d. zirconia rotor. The ^{17}O SSNMR spectra of all halogen-bonded compounds were acquired at 9.4 T ($\nu_L(^{17}O)$ = 54.250 MHz), 11.7 T ($\nu_L(^{17}O)$ = 67.800 MHz), and also at 21.1 T ($\nu_L(^{17}O)$ = 121.984 MHz).

9.4 T

^{17}O MAS and stationary solid-state NMR spectra of ^{17}O-labeled Ph_3PO were obtained at 9.4 T using a 7 mm triple resonance MAS probe. A Hahn-echo experiment (*i.e.*, $\pi/2-\tau_1-\pi-\tau_2$–acq) with TPPM proton decoupling was employed. The π/2 pulse length was 7.5 μs. The CT selective pulse length was 2.5 μs, and interpulse delay was 6 μs. A relaxation delay of 4 s was used to acquire 30720 scans for static spectra and 15456 scans for MAS spectra. The MAS rate was 6.5 kHz.

11.7 T

A solid echo (*i.e.*, $\pi/2-\tau_1-\pi/2-\tau_2$–acq) pulse sequence with CW proton decoupling was applied for the solid-state ^{17}O MAS experiments at a spinning rate of 10 kHz using 4 mm low γ double resonance MAS probe with a relaxation delay of 10 s for **A1** and **A3** compounds and 5 s for **A2**. The π/2 pulse length was 3.9 μs, while the echo delay was 98.7 μs. The CT selective pulse length was 1.3 μs, and 20 k to 30 k scans were required.

21.1 T

A one-pulse sequence without proton decoupling was applied for the solid-state MAS NMR experiments at a spinning rate of 10 kHz along with a relaxation delay of 5 s for all of the ^{17}O-labeled halogen-bonded samples. The π/2 pulse length was 9 μs. The CT selective pulse length was 3 μs. 6144 scans were acquired. Static ^{17}O NMR spectra were acquired using a solid echo (*i.e.*, $\pi/2-\tau_1-\pi/2-\tau_2$–acq) pulse sequence with CW proton decoupling. The echo delay was 50 μs. A relaxation delay of 5 s was used to acquire 10k scans.

Spectra were simulated using Herzfeld-Berger Analysis (HBA)[26] and WSolids[27] programs.

3.2.5 Quantum Chemical Calculations

The ^{31}P and ^{17}O magnetic shielding tensors and ^{17}O EFG tensors were calculated with Materials Studio and CASTEP[28] software version 4.4 using periodic boundary conditions and the GIPAW DFT method, and in a second instance with Amsterdam Density Functional (ADF) software[29] using cluster models.

The input file generated from Materials Studio used "on-the-fly" pseudopotentials to perform the geometry optimization of the hydrogen positions. The energy cut-offs in eV and *k*-point grids used are shown in Table A3 in the Appendix A. The GIPAW DFT calculations were applied to calculate all the NMR parameters.[30]

Cluster models were generated using the X-ray crystal structures' atomic coordinates. The ADF calculation was carried out using the High Performance Computing Virtual Laboratory (HPCVL). First, optimization of the hydrogen positions was done at the TPSS/6-311++G** level using Gaussian 09[31] before the NMR calculation. Calculations of $J(^{31}P, ^{17}O)$ were performed using ADF with scalar relativistic effects via the zeroth-order regular approximation (ZORA). The meta-GGA TPSS functional was used with the ZORA/DZP basis set. Magnetic shielding and EFG tensors were also determined using the ADF but with the revPBE functional and the ZORA/TZP basis set including scalar relativistic effects. NLMO analyses were further carried out to calculate all contributions to the *J* coupling tensors and EFG tensors, and the orbitals were visualized with the program adfview.

The magnetic shielding tensors (σ in ppm) were converted to CS tensors (δ in ppm) using the following equation: $\delta_{ij} = \frac{\sigma_{ref} - \sigma_{ij}}{1 - \sigma_{ref}}$ (where $\sigma_{\text{ref}} = 331.51$ for phosphorus, δ_{ij} is the chemical shift tensor component, and σ_{ij} is the magnetic shielding tensor component).[32] The absolute chemical shift scale for oxygen[33] $\sigma_{\text{ref}} = 287.5$, was employed to convert the ^{17}O magnetic shielding tensors to chemical shifts.

3.3 **Results and Discussion**

3.3.1 X-Ray Crystal Structures

Although the LAG method inherently does not generally allow one to characterize the products by single-crystal XRD, and one may be left with unreacted starting materials, this mechanochemical method is still attractive due to its ability to increase the yield of reaction and efficiency when the solubility of the compounds is limited.[21] With high efficiency and yield in mind, we have used LAG as a synthetic and screening method to discover a series of halogen-bonded compounds, (Ph_3PO)(*o*-$C_6F_4I_2$)$_2$ (**A2**), (Ph_3PO)(*sym*-$C_6F_3I_3$) (**A3**), (Ch_3Ph_2PO)(*sym*-$C_6F_3I_3$)$_2$ (**B3**), (Ph_3PO)(*p*-$C_6F_4I_2$)$_2$ (**A1**), and (CH_3Ph_2PO)(*p*-$C_6F_4I_2$)(CH_3CN) (**B1**). For characterization by single-crystal XRD, samples were recrystallized. The consistency between the cocrystals obtained first by LAG and then by subsequent slow evaporation was verified by powder X-ray diffraction (see Appendix A).

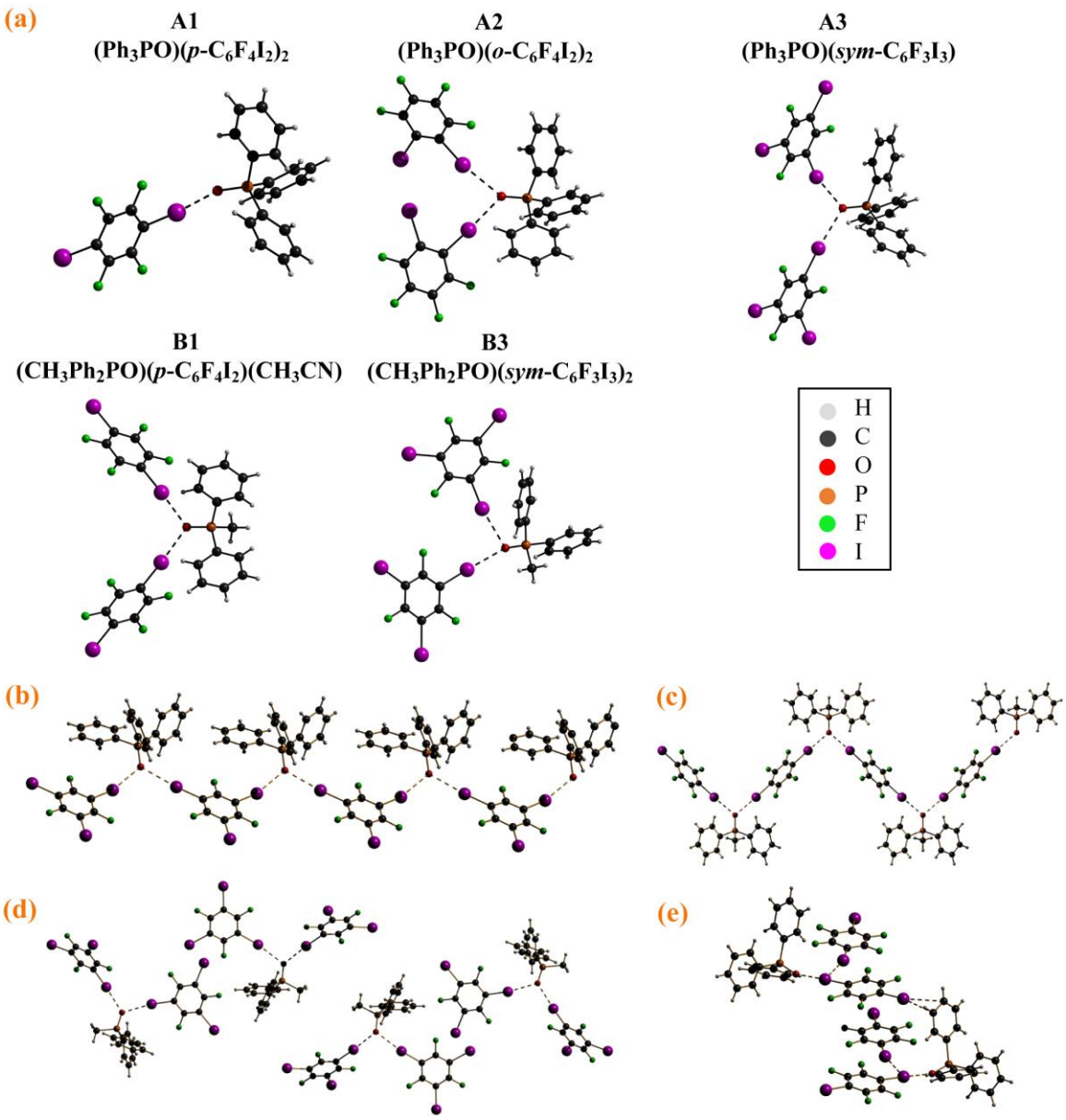

Figure 3.3.1. (a) Intermolecular geometries for halogen-bonded compounds **A1**, **A2**, **A3**, **B1**, and **B3** from single crystal X-ray diffraction. The crystal structure of **A2** shows 2-fold disorder of one of the aromatic rings. Atom colors: iodine is violet; fluorine is green; oxygen is red; phosphorus is orange; carbon is black; and hydrogen is white. (b) Zigzag fragment of the halogen-bonded framework in compound **A3**. (c) Zigzag fragment of the halogen-bonded framework in compound **B1**. (d) Discrete halogen-bonded entities in compound **B3**. (e) Fragment of the cocrystal structure of **A1**, displaying short I···I and I···C contacts.

The local halogen bonding environments as determined by single-crystal XRD are shown in Figure 3.3.1(a) for **A1**, **A2**, **A3**, **B1**, and **B3**. The structures of **A1** and **B1** represent previously unidentified crystalline compounds which do not correspond to similar previously reported systems.[12,20] (CH_3Ph_2PO)(*o*-$C_6F_4I_2$) (**B2**) is a non-crystalline solid (no crystal structure is accessible). We report several selected intermolecular contact distances and angles in Table 3.3.1 that are used to characterize the halogen bonding interaction and geometry, which include the halogen bond length, $d_{I\cdots O}$, the carbon-iodine bond length, $d_{I\cdots C}$, the phosphorus-oxygen bond length, $d_{P=O}$, O⋯I-C angle, $\theta_{O\cdots I\text{-}C}$, P=O⋯I angle, $\theta_{P=O\cdots I}$, I⋯O⋯I angle, $\theta_{I\cdots O\cdots I}$, and R_{XB}. The van der Waals radii for oxygen and iodine that are used to calculate R_{XB} are taken from previous literature.[34] The crystallographic data for all compounds are given in Table A2.

Table 3.3.1. Local Halogen Bonding Geometrical Information from Single-Crystal X-ray Diffraction

	compound	#I	$d_{I\cdots O}$ / Å	$d_{I\cdots C}$ / Å	$d_{P=O}$ / Å	R_{XB}[a]	$\theta_{O\cdots I\text{-}C}$ / °	$\theta_{P=O\cdots I}$ / °	$\theta_{I\cdots O\cdots I}$ / °	R_{DD}[b] / Hz
A1[c]	$(Ph_3PO)(p\text{-}C_6F_4I_2)_2$	1	2.725	2.092	1.495	0.779	175.7	152.1	n.a.	-1975
A2	$(Ph_3PO)(o\text{-}C_6F_4I_2)_2$	1	2.896	2.095	1.498	0.827	176.8	132.9	92.4	-1964
		2	2.888	2.106		0.825	169.4	132.0		
A3	$(Ph_3PO)(sym\text{-}C_6F_3I_3)$	1	2.920	2.091	1.491	0.834	174.5	127.0	107.0	-1991
		2	2.979	2.081		0.851	163.8	116.4		
B1[d]	$(CH_3Ph_2PO)(p\text{-}C_6F_4I_2)(CH_3CN)$	1	2.847	2.089	1.500	0.813	175.7	130.4	90.4	-1956
B3	$(CH_3Ph_2PO)(sym\text{-}C_6F_3I_3)_2$	1	2.915	2.083	1.497	0.833	171.0	118.2	95.3	-1968
		2	2.826	2.097		0.808	176.1	123.9		

[a] R_{XB} is the normalized distance parameter, $R_{XB} = d_{I\cdots O} / \sum d_{VDW}$, where $d_{I\cdots O}$ is the shortest distance between the oxygen and iodine and $\sum d_{VDW}$ is the sum of their van der Waals radii (1.52 Å for O and 1.98 Å for I).

[b] $^{31}P,^{17}O$ indirect dipolar coupling constant, $R_{DD} = \frac{\mu_0}{4\pi}\frac{\hbar}{2\pi}\gamma_P\gamma_O < r_{PO}{}^{-3} >$, where γ_P and γ_O are the magnetogyric ratios for ^{31}P and ^{17}O, respectively and $< r_{PO}{}^{-3} >$ is the motionally averaged inverse cube of the phosphorus-oxygen internuclear distance.

[c] Contains one extra $p\text{-}C_6F_4I_2$, which is not involved in halogen bonding.

[d] This compound is a solvate (acetonitrile).

A polymorph of **A1** has been described previously as a zigzag halogen-bonded chain since oxygen acts as a bifurcated halogen bond acceptor.[20] Here, we report another $P2_1/c$ monoclinic crystal system in which oxygen acts as a single halogen bond acceptor with a near linear angle of 175.7º and which forms a discrete 1:1 entity through interaction

with the iodine atom in *p*-$C_6F_4I_2$. It has a low R_{XB} value, 0.779, (the smallest in the present study), which implies a strong halogen bond. As shown in Figure 3.3.1(e), the other iodine atom in the same *p*-$C_6F_4I_2$ molecule interacts with a phenyl ring in Ph_3PO with I···C distances of 3.426 Å and 3.378 Å. Another crystallographically distinct *p*-$C_6F_4I_2$ molecule has a weak I···I interaction with the first *p*-$C_6F_4I_2$ with a distance of 3.854 Å.

Compound **A2** packs in the triclinic crystal system and $P\bar{1}$ space group and features 2-fold disorder of one of the *o*-$C_6F_4I_2$ molecules. One of the two orientations is depicted in Figure 3.3.1 (a); both orientations and full crystallographic information are given in the Appendix A. Two halogen bond donors with iodine atoms facing each other, interact with one oxygen atom with an I···O···I angle of 92.4º. One of the iodines interacts with oxygen with a near linear O···I-C angle of 176.8º and R_{XB} value of 0.827. The O···I-C angle for the second *o*-$C_6F_4I_2$ moiety is 169.4º, and the R_{XB} value is 0.825.

Compound **A3** packs in the triclinic crystal system and $P\bar{1}$ space group. The oxygen acts as a bifurcated halogen bond acceptor, interacting with two iodines with O···I-C angles of 174.5º and 163.8º, providing a zigzag chain (Figure 3.3.1 (b)). The I···O···I angle is 107.0º. The halogen bonds are moderately strong, as characterized by R_{XB} values of 0.834 and 0.851.

The crystal structure of **B1**, which is orthorhombic, shows a crystallographic symmetry between two *p*-$C_6F_4I_2$ molecules, with a bifurcated I···O···I angle of 90.4º, which is different from that observed for a different polymorph.[12] The O···I-C angle is 175.7º and the R_{XB} value is 0.813. Acetonitrile molecules crystallize in the unit cell. Instead of acting as a single halogen bond acceptor, the oxygen interacts with two iodine atoms with the same angle and the same distance yielding a bidentate acceptor, thus forming a polymeric

zigzag chain and providing a one-dimensional network (Figure 3.3.1 (c)). We were unfortunately unable to obtain an X-ray powder pattern which matched this crystal structure (shown in Figure A1), which suggests that grinding or recrystallization has an influence on the structure.

B3 crystallizes in the $P2_1/n$ monoclinic space group. The oxygen atom again halogen bonds with two iodine atoms, forming a I···O···I angle of 95.3º. The R_{XB} values are 0.833 and 0.808. The two O···I-C angles are 171.0º and 176.1º. However, unlike the crystal structure of **A3**, in which other iodines can form additional halogen bonding interactions to create a zigzag chain, the structure of **B3** shows only one halogen bonding interaction for each *sym*-$C_6F_3I_3$. As a result, discrete halogen-bonded entities, as opposed to the zigzag chains found in **A3**, are observed for **B3** (shown in Figure 3.3.1 (d)).

3.3.2 Solid-State NMR Spectroscopy

(i) ^{31}P CP/MAS NMR

Since ^{16}O is NMR-silent and ^{127}I has a large quadrupole moment (Q) leading to broad resonances, we first focus on a solid-state NMR study of ^{31}P (I = ½; natural abundance of 100%), which is indirectly involved in the halogen bonding interaction, to probe the halogen bond acceptor moieties (see a general P=O···I-C moiety in Figure 3.1.1).

The ^{31}P CP/MAS SSNMR spectra of the starting materials, Ph_3PO and CH_3Ph_2PO, and their respective halogen-bonded compounds, are shown in Figure 3.3.2. The CS tensor parameters (isotropic chemical shift (δ_{iso}), span (Ω), and skew (κ)) are reported in Table 3.3.2. Spinning the sample at different MAS frequencies helps to differentiate the isotropic peaks from the spinning sidebands and provides improved precision in the fitted parameters (^{31}P CP/MAS SSNMR spectra acquired at 4.7 T with different spinning speeds are

provided in Figure A6 in the Appendix A). The purchased Ph_3PO is a mixture of two polymorphs, monoclinic (δ_{iso} = 26.6 ppm) and orthorhombic (δ_{iso} = 28.1 ppm) (see relevant ^{31}P NMR spectra in Figure A5 in the Appendix A), consistent with previous work by Arumugam and coworkers.[35] Further recrystallization from acetone generated pure monoclinic Ph_3PO.

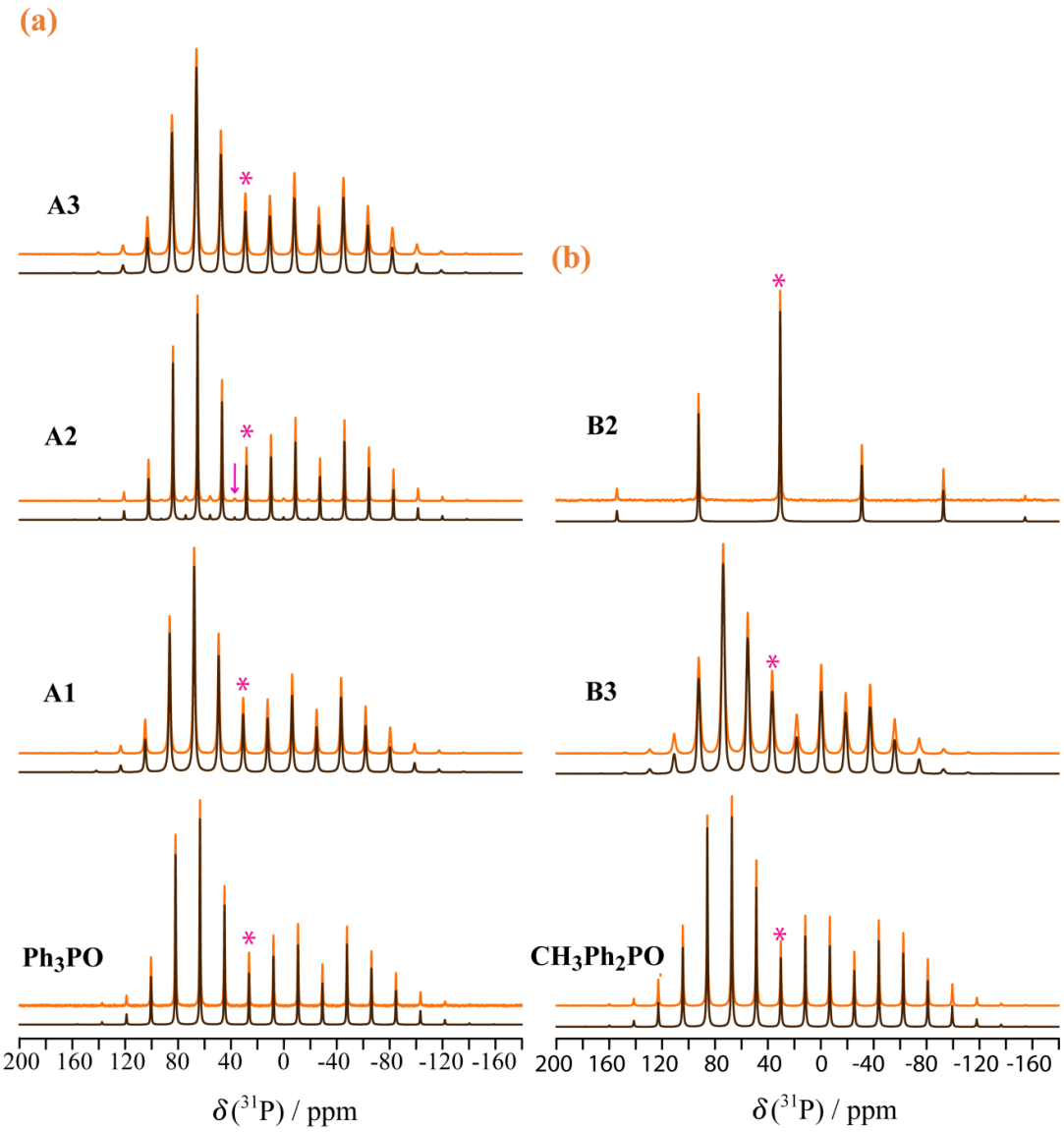

Figure 3.3.2. Experimental ^{31}P CP/MAS SSNMR spectra (orange) obtained at 9.4 T for (a) monoclinic Ph_3PO and its halogen-bonded compounds (**A1**, **A2**, **A3**) and (b) CH_3Ph_2PO

and its halogen bonded compound (**B3**). The corresponding simulated spectra are shown at the bottom (brown). The isotropic peaks are indicated by pink asterisks. The spectra were acquired at a spinning speed of 3 kHz to obtain a good number of spinning sidebands. The ^{31}P centerband of a small impurity in compound **A2** is shown with a pink arrow. The spectrum for **B2** was obtained at 4.7 T and the spinning speed was 5 kHz.

Table 3.3.2. Experimental ^{31}P Chemical Shift Tensors and $J(^{31}P, ^{17}O)$ Values[c]

	compound	δ_{iso} **/ ppm**	Ω **/ ppm**	κ	$J_{iso}(^{31}P, ^{17}O)$ **/ Hz**	R_{eff} **/ Hz**	ΔJ **/ Hz**[d]
	monoclinic Ph_3PO[a]	26.3 (0.3)	198 (7)	0.87 (0.01)	160 (4)	-1800 (50)	-650 (150)
A1	$(Ph_3PO)(p\text{-}C_6F_4I_2)_2$	30.7 (0.2)	183 (4)	0.98 (0.06)	157 (5)	-1800 (100)	-790 (300)
A2[b]	$(Ph_3PO)(o\text{-}C_6F_4I_2)_2$	28.3 (0.2)	193 (2)	0.88 (0.01)	154 (4)	-1800 (100)	-570 (300)
A3	$(Ph_3PO)(sym\text{-}C_6F_3I_3)$	29.1 (0.1)	190 (4)	0.84 (0.08)	155 (4)	-1700 (200)	-800 (600)
	CH_3Ph_2PO	30.2 (0.1)	216 (4)	0.69 (0.02)	---	---	---
B2	$(CH_3Ph_2PO)(o\text{-}C_6F_4I_2)$	30.7 (0.1)	215 (4)	0.70 (0.03)	---	---	---
B3	$(CH_3Ph_2PO)(sym\text{-}C_6F_3I_3)_2$	36.7 (0.1)	171 (2)	0.84 (0.03)	---	---	---

[a] CS tensors have also been previously reported by Arumugam et al.,[35] and $J(^{31}P, ^{17}O)$ has been previously reported by Bryce et al. [22]

[b] **A2** contains a trace impurity (δ_{iso} = 37.2(0.2) ppm, Ω = 143(15) ppm, κ = 0.84(0.17)).

[c] Error bounds are in brackets.

[d] Errors in ΔJ are calculated from errors in R_{eff}.

The halogen-bonded compounds **A1**, **A2**, and **A3** have larger ^{31}P isotropic chemical shifts and marginally smaller ^{31}P CS tensor spans compared to starting material monoclinic Ph_3PO (δ_{iso} =26.3 ppm, Ω = 198 ppm). The same holds when comparing halogen-bonded compounds **B2** and **B3** to CH_3Ph_2PO (δ_{iso} = 30.2 ppm, Ω = 216 ppm). Although the spectral differences are small, this is perhaps unsurprising given that ^{31}P is an indirect probe of the O···I interaction, one bond removed. The trend observed here for δ_{iso}(^{31}P) mirrors that for δ_{iso}(^{13}C) of the *ipso* carbon atoms in a series of halogen-bonded diiodotetrafluorobenzene complexes.[6] Taken together, the values of δ_{iso}, Ω, and κ reported for ^{31}P in Table 3.3.2 are sensitive enough to distinguish between all of the halogen-bonded and non-halogen bonded compounds in this study.

(ii) ^{31}P and ^{17}O SSNMR spectroscopy of halogen-bonded cocrystals of ^{17}O-labeled Ph_3PO

The monoclinic ^{17}O-enriched Ph_3PO from the corresponding phosphine was prepared according to literature.[22] $Ph_3P^{17}O$ was used as the starting material to further synthesize ^{17}O-labeled halogen-bonded compounds. ^{17}O EFG and CS tensors are expected to provide new insights into the nature of the halogen-bonded P=O···I–C motif.

The ^{31}P CP/MAS NMR spectrum of monoclinic ^{17}O-labeled Ph_3PO, acquired at 4.7 T, is shown in Figure 3.3.3(a). The ^{31}P CS tensors magnitude and J_{iso} (^{31}P, ^{17}O) can be extracted by fitting the ^{31}P CP/MAS spectra. All of the values obtained are consistent with the values reported by Bryce[22] and presented in Table 3.3.2. The ^{17}O MAS and static NMR spectra of ^{17}O-labeled Ph_3PO were acquired at 9.4 T and are shown in Figure 3.3.4. Simulation of the ^{17}O NMR spectra provide the following ^{17}O NMR parameters which are consistent with those of Bryce[22] and which are shown in Table 3.3.3: δ_{iso}, the magnitude of

$|C_Q|$ and η_Q from MAS spectra, as well as the CS tensor span (Ω), skew (κ), and three Euler angles (α', β', γ') from static spectra.[36] Also, the magnitude of $J_{iso}(^{31}P,^{17}O)$ obtained from ^{31}P MAS NMR spectra can also be confirmed in the ^{17}O MAS spectrum through the measurement of the splittings of each spectral discontinuity. All these NMR parameters for $Ph_3P^{17}O$ were determined to be in agreement with previous reported values[22] before use in LAG synthesis.

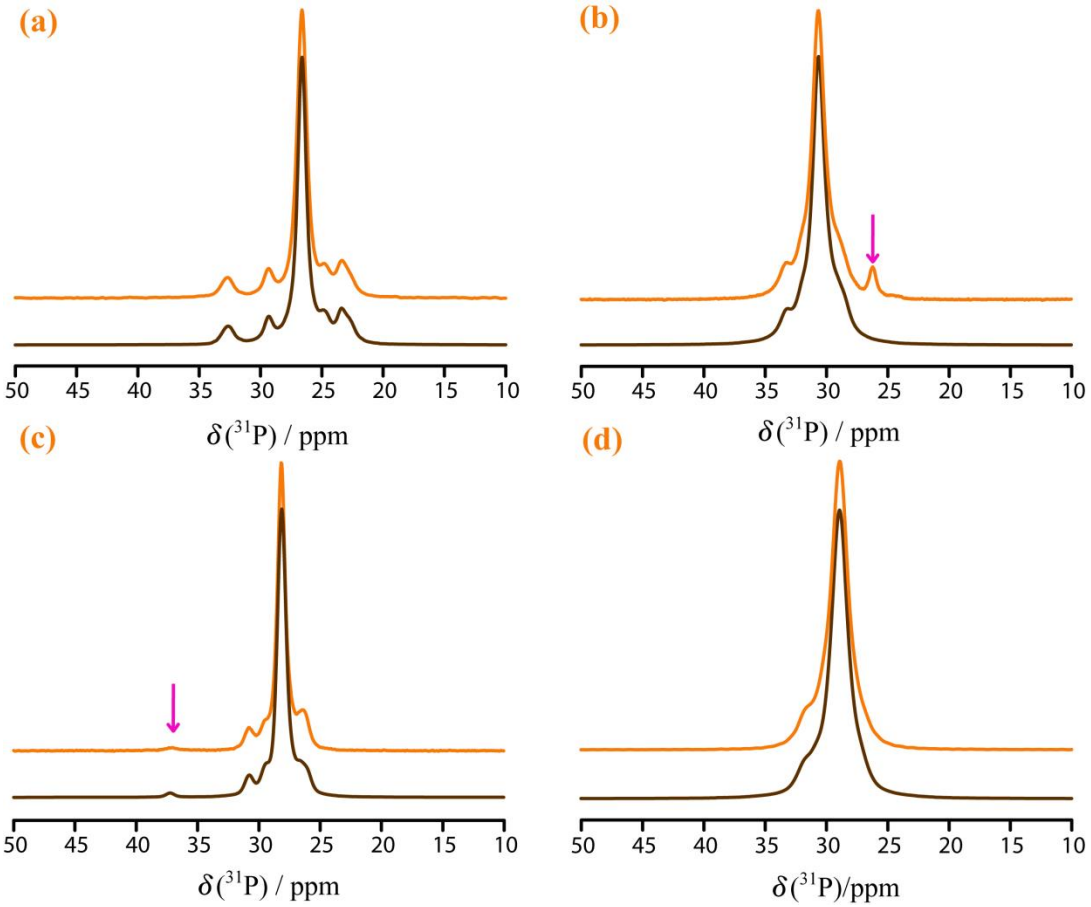

Figure 3.3.3. Experimental ^{31}P CP/MAS SSNMR spectra (orange) obtained at 4.7 T for (a) Ph_3PO and 9.4 T for its halogen-bonded compounds (b) **A1**, (c) **A2**, and (d) **A3**. The corresponding simulated spectra are shown at the bottom (brown). The MAS speed varies from 4 kHz to 5 kHz. Impurities in **A1** and **A2** are shown with pink arrows.

Table 3.3.3. Experimental ^{17}O EFG and CS Tensor Parameters for Ph_3PO and Its Halogen-Bonded Compounds[b]

	δ_{iso} / ppm	Ω / ppm	κ	$\lvert C_Q(^{17}O)\rvert$ / MHz	η_Q	α' / °	β' / °	γ' / °
monoclinic Ph_3PO[a]	53.0 (0.2)	155 (5)	-0.75 (0.02)	4.57 (0.01)	0.030 (0.002)	66.5 (3.5)	86.3 (0.5)	8.1 (0.5)
A1	45.6 (0.2)	120 (1)	-0.81 (0.02)	5.03 (0.03)	0.13 (0.01)	78 (1)	81.6 (0.2)	1.9 (0.1)
A2[c]	39.8 (0.2)	121 (1)	-0.89 (0.01)	4.92 (0.01)	0.12 (0.005)	63 (2)	93.4 (0.1)	0.3 (0.2)
A3	59.1 (0.4)	159 (2)	-0.74 (0.01)	4.81 (0.02)	0.13 (0.005)	81 (2)	96.7 (0.2)	11.9 (0.2)

[a] From ref.22.

[b] Error bounds are in brackets.

[c] The ^{17}O NMR parameters for the impurity in compound **A2** are: δ_{iso} = 53.0(0.4) ppm, $\lvert C_Q(^{17}O)\rvert$ = 4.64(0.06) MHz, η_Q = 0.10(0.01).

^{31}P SSNMR.

^{31}P CP/MAS SSNMR spectra were recorded 9.4 T for the ^{17}O-labeled halogen-bonded samples. Spectra were acquired at two different spinning frequencies (ν_{rot} = 3 and 5 kHz) and at two applied magnetic field strengths (4.7 and 9.4 T) to identify the centerband as well as to distinguish the effects of $J_{iso}(^{31}P, ^{17}O)$ from possible impurities. Only the isotropic ^{31}P peaks are shown in Figure 3.3.3. The most intense peak in the middle corresponds to those ^{31}P nuclei which are adjacent to zero-spin ^{16}O. The sensitivity of the simulated ^{31}P CP/MAS NMR spectra to the value of $J_{iso}(^{31}P, ^{17}O)$ is demonstrated in Figure A7 for compound **A2**.

Simulations were adjusted by including the effective dipolar coupling constant (R_{eff}) between ^{31}P and ^{17}O, which incorporates the anisotropic part of the J tensor ($R_{eff} = R_{DD}-\Delta J/3$). R_{DD} values were calculated based on the halogen bond geometry from X-ray crystal structures (see Table 3.3.1). The R_{eff} values were obtained through iterative spectral fitting. However, the large error in R_{eff} indicates that the R_{eff} values cannot discriminate among the different samples. Therefore, the anisotropy in the J coupling tensor also has low precision. All the ^{31}P CS tensors and J coupling values are summarized in Table 3.3.2.

^{17}O-enriched **A2** has a small amount of unknown impurity shown in Figure 3.3.3(c) with a pink arrow, which can be observed also in unlabeled **A2**. However, the poor resolution and low intensity made it impossible measure the value of J_{iso} (^{31}P, ^{17}O).

The J_{iso}(^{31}P, ^{17}O) coupling constants, ranging from 154(4) Hz in compound **A2** to 157(5) Hz in compound **A1**, decrease in the halogen-bonded compounds compared to the starting material (J_{iso}(^{31}P, ^{17}O) = 160(4) Hz). Comparing the two ^{31}P CP/MAS spectra obtained at two different applied magnetic fields can isolate the impurity peak in compound **A1** (shown with pink arrow in Figure 3.3.3 (b)) from peaks associated with J_{iso} (^{31}P, ^{17}O).

^{17}O SSNMR.

Compared to ^{31}P NMR spectroscopy, ^{17}O NMR is expected to provide more straightforward insight into the relationship between NMR properties and halogen bonding since oxygen is a direct participant in the halogen bond; however, it can be more difficult to acquire and interpret the ^{17}O NMR data because the second-order quadrupolar coupling interaction cannot be averaged under MAS,[37,38] resulting in additional spectral broadening. The ^{17}O MAS NMR spectra for halogen-bonded compounds were acquired at 21.1 T

(shown in Figure 3.3.4(a)) and at 11.7 T (shown in the insets) with a spinning rate of 10 kHz. The parameters are summarized in Table 3.3.3.

The ^{17}O isotropic chemical shift ranges from 39.8(0.2) ppm for compound **A2** to 59.1(0.4) ppm for compound **A3**. The ^{17}O isotropic chemical shifts for all compounds fall in the known range for phosphine oxides (20 - 100 ppm).[39] We note that the experimental ^{17}O isotropic chemical shifts in the halogen-bonded compounds do not show a clear trend relative to pure Ph_3PO. Compared to the sometimes substantial effect of hydrogen bonding on oxygen chemical shifts, *e.g.*, a change of 29 ppm for COH groups of α-oxalic acid dihydrate[19] and a change of 125 ppm for carboxyl group in nucleic acids[16], the difference caused by halogen bonding in the present study is far less striking.

The magnitude of the quadrupolar coupling constant, $|C_Q(^{17}O)|$, ranges from 4.92(0.01) MHz for compound **A2** to 5.03(0.03) MHz for compound **A1**. The asymmetry parameter, η_Q, is essentially constant at 0.13 for the halogen-bonded compounds. Importantly, however, the value of the ^{17}O quadrupolar coupling constant increases in the presence of the halogen bonding interaction compared with monoclinic ^{17}O-labeled Ph_3PO (see Table 3.3.3).

Fitting the ^{17}O MAS NMR spectra obtained at both 11.7 T and 21.1 T for compound **A1** allows for the identification of the impurity as the starting material, ^{17}O–labeled Ph_3PO (Figure 3.3.4; simulations are shown with light brown dashed lines). This is consistent with the small impurity peak found in the ^{31}P CP/MAS NMR spectrum at 4.7 T, whose corresponding chemical shift is 26.3 ppm. It is clear under ^{17}O MAS that compound **A2** contains an unknown < 10% impurity (δ_{iso} = 53.0(0.4) ppm, $|C_Q(^{17}O)|$ = 4.64(0.06) ppm, η_Q = 0.10(0.01)). This can be observed at both 11.7 T and 21.1 T.

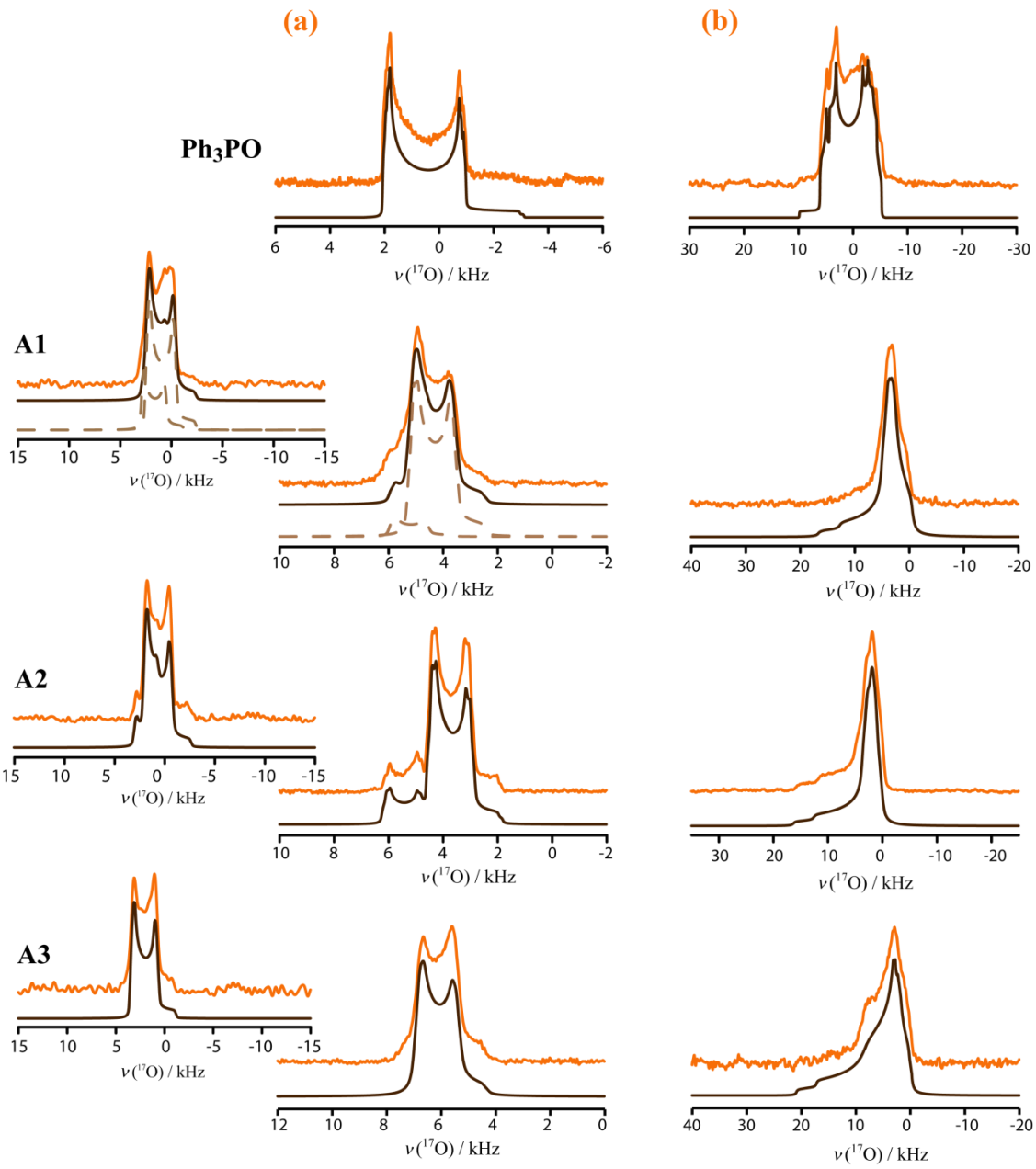

Figure 3.3.4. Experimental ^{17}O NMR spectra (orange) of MAS (a) and static (b) $Ph_3P^{17}O$ (40%) acquired at 9.4 T and its halogen-bonded compounds (**A1**, **A2**, **A3**) acquired at 21.1 T. The corresponding simulated spectra are shown at the bottom (brown). Shown in the insets (left) are the experimental and simulated ^{17}O MAS NMR spectra acquired at 11.7 T. MAS spectra were obtained with spinning speeds of 5.2 kHz at 9.4 T, and 10 kHz at 11.7 T and 21.1 T.

The ^{17}O static NMR spectra (21.1 T) are shown in Figure 3.3.4(b). These simulations can provide ^{17}O CS tensors and three Euler angles (α', β', γ'), which are summarized in Table 3.3.3. However, there is no clear correlation observed between CS tensors or Euler angles and halogen bonding geometry.

3.3.3 Computational Analysis

(i) Calculated Chemical Shifts and the Halogen Bond Geometry

Calculations of ^{31}P and ^{17}O magnetic shielding tensors were carried out using either GIPAW DFT with the PBE functional in CASTEP or ZORA DFT with the revPBE functional implemented in ADF. In Figure 3.3.5(a), the calculated ^{17}O isotropic chemical shifts are plotted versus the experimental values. The calculated isotropic chemical shifts from GIPAW DFT more strongly overestimate the experimental data than do the values obtained from ZORA DFT. This overestimation might result from a lack of inclusion of relativistic effects associated with the iodine involved in halogen bonding.[40] However, the trend in $\delta_{iso}(^{17}O)$ is well-reproduced by both sets of calculations, with correlation coefficients, R^2, of 0.9075 and 0.9287, respectively. Figure 3.3.5(b) shows an inverse linear correlation between the R_{XB} values and calculated $\delta_{iso}(^{17}O)$ values for both sets of calculations (R^2 = 0.9685 for GIPAW; R^2 = 0.9201 for ZORA). For those cocrystals with more than one iodine halogen bond donor to each oxygen site, a cumulative R_{XB} value was used (*i.e.*, R_{XB} = 1 - (1 - R_{XB} (donor1)) - (1 - R_{XB} (donor2)) - …).[8] Two outlier points for **A2** are excluded from the linear fit in Figure 3.3.5(b). Since the calculated $\delta_{iso}(^{17}O)$ for **A2** are in good agreement with the experimental values, it is not immediately clear why they are outliers in the second plot. Compared to the other compounds, an additional iodine atom in *o*-$C_6F_4I_2$ is close to the oxygen atom. Perhaps extra relativistic effects and/or XB

effects from the nearby heavy iodine atom may lead to further chemical shift changes in compound **A2**.

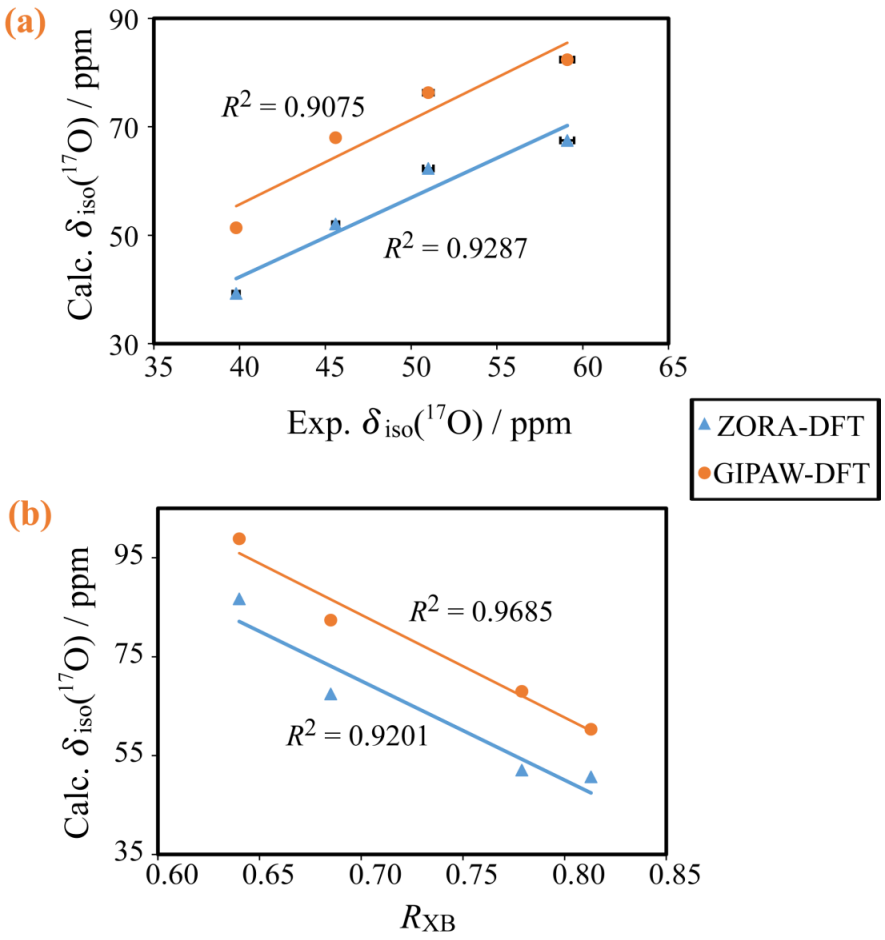

Figure 3.3.5. (a) Calculated versus experimental δ_{iso} (^{17}O) for the ^{17}O-labeled compounds monoclinic Ph_3PO, **A1**, **A2**, and **A3**. (b) A plot of calculated δ_{iso} (^{17}O) versus R_{XB} values for the halogen-bonded compounds listed in Table 3.3.1. Two outliers from **A2** are not plotted in (b). Two different types of DFT calculation were performed: GIPAW DFT calculation using CASTEP (orange circles), and ZORA DFT using ADF (blue triangles). Lines represent the best linear fits: (a) GIPAW: calc. $\delta_{iso}(^{17}O)$ = 1.5609 exp $\delta_{iso}(^{17}O)$ - 6.767, ZORA: calc. $\delta_{iso}(^{17}O)$ = 1.4624 exp $\delta_{iso}(^{17}O)$ -16.19; (b) GIPAW: calc.$\delta_{iso}(^{17}O)$ = -207.79 R_{XB} + 228.93, ZORA: calc.δ_{iso} (^{17}O) = -200.33 R_{XB} + 210.32.

There is no clear correlation between calculated $\delta_{iso}(^{31}P)$ and R_{XB} values or P=O bond distance that could be distinguished for the halogen-bonded compounds (see Figure A8 (b) and (c)). There are two factors which explain the poor correlation. First, the phosphorus is indirectly involved in halogen bonding interaction. The effect of the iodine-oxygen halogen bond on the ^{31}P NMR parameters might not be the major contribution. Second, Alvarado and coworkers found that phosphine-chalcogen bond angles and geometry heavily impact ^{31}P chemical shifts, leading to a poor correlation between ^{31}P chemical shifts and phosphine-chalcogen bond energy.[41] In our case, the presence of halogen bonding results in widely variable P=O···I angles, ranging from 116.4° to 152.1º (see in Table 3.3.1). This variability likely also contributes to the ^{31}P chemical shifts.

(ii) Analysis of Calculated Oxygen Quadrupolar Coupling Tensors. Halogen Bond Geometry and NLMO Contributions

A plot of experimental vs calculated ^{17}O quadrupolar coupling constants for Ph_3PO**, A1, A2,** and **A3** is presented in Figure 3.3.6(a). PAW DFT provides a better correlation (R^2 = 0.9188) relative to a calculation done using a cluster model in ADF (R^2 = 0.7797). The weaker correlation could be due to the neglect of the full crystal lattice. Shown in Figure 3.3.6 (b) is a plot of the calculated $|C_Q(^{17}O)|$ values versus the cumulative R_{XB} value determined from X-ray crystallography for all of the halogen-bonded compounds. While the calculated $|C_Q\ (^{17}O)|$ tends to increase as the halogen bonding weakens, there is a significant degree of scatter in these data.

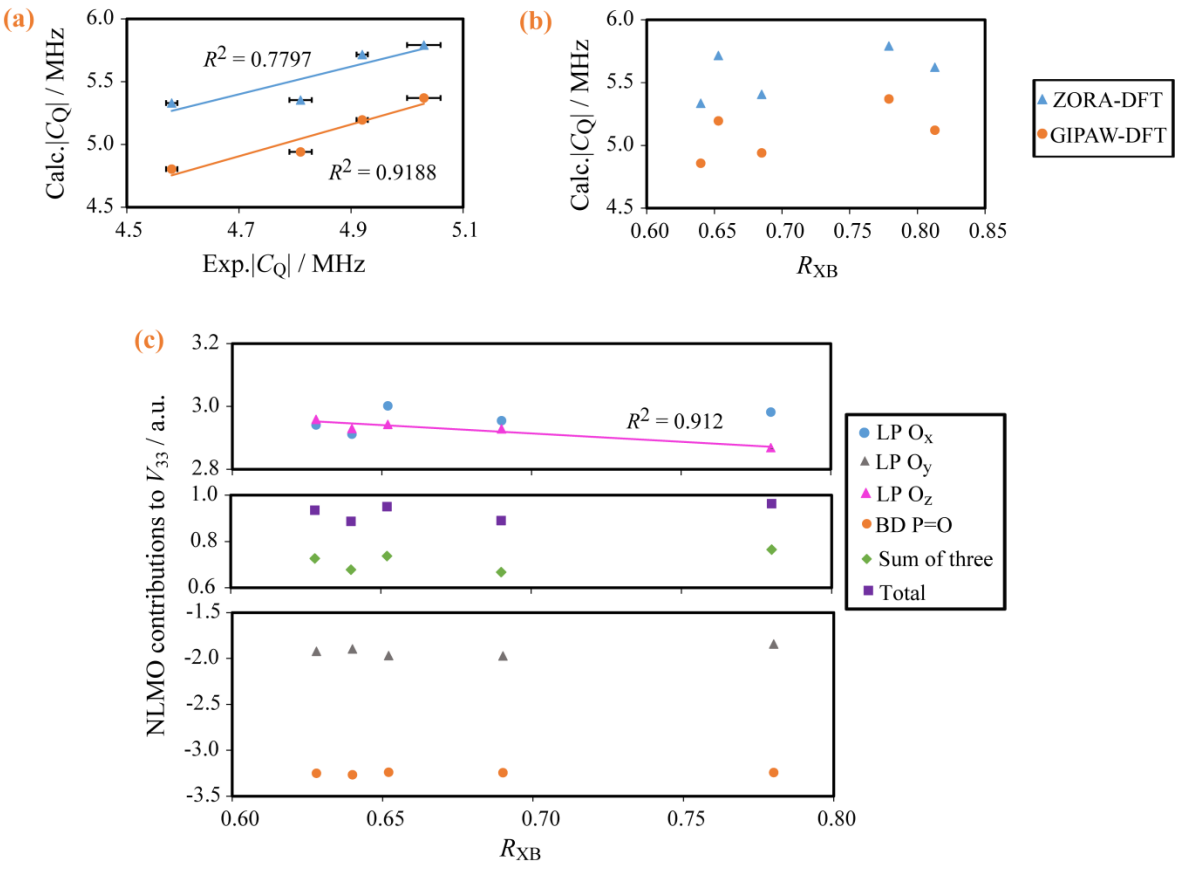

Figure 3.3.6. (a) Calculated versus experimental $|C_Q(^{17}O)|$ values for monoclinic Ph_3PO, **A1**, **A2**, and **A3**. (b) A plot of calculated $|C_Q(^{17}O)|$ values versus R_{XB} values for all of the halogen-bonded compounds listed in Table 3.3.1. Two different types of DFT calculation were performed: GIPAW DFT calculation using CASTEP (orange circles), and ZORA DFT using ADF (blue triangles). (c) A plot of the sum of Lewis and non-Lewis largest NLMO contributions to the largest EFG tensor principal component V_{33} as a function of R_{XB} values for the compounds listed in Table 3.3.1. Orange circles represent the contribution from the P=O bonding orbital. Blue circles, grey triangles, and pink triangles represent contributions from the oxygen lone pairs along *x*, *y* and *z* axes, respectively. Green diamonds represent the sum of the four orbitals. Purple squares represent the total contribution. Lines represent the best linear fits: (a) GIPAW: calc. $|C_Q(^{17}O)|$ = 1.2652 exp.$|C_Q(^{17}O)|$ - 1.0401; ZORA: calc.$|C_Q(^{17}O)|$ = 1.101 exp.$|C_Q(^{17}O)|$ + 0.2242; (c) LP O_z: V_{33} = -0.5289R_{XB} + 3.2846.

A further NLMO analysis elucidates the connection between the ^{17}O EFG tensor and the electronic structure of the halogen bond (Table A5). Since the largest principal component, V_{33}, determines the value of $C_Q(^{17}O)$, the NLMO analysis is conducted on V_{33} for all halogen-bonded compounds. As shown in Figure 3.3.6 and Figure 3.3.7, four key molecular orbitals contribute to the value of V_{33}: the bonding orbital between phosphorus and oxygen and three different oxygen lone pair orbitals. If we treat the P=O bond as *y* axis, the first oxygen lone pair orbital (LP O_x) is always along the *x* axis, which is perpendicular to the phenyl ring in Ph_3PO or methyl group in CH_3Ph_2PO, whereas the second oxygen lone pair orbital (LP O_z) is always aligned with the *z* axis. The oxygen lone pair orbital (LP O_y) which is aligned with the P=O bond makes a negative contribution to oxygen EFG tensors.

Each major NLMO contribution related to halogen bonding is plotted as a function of the R_{XB} value (Figure 3.3.6(c)). It is noted that most of the major NLMO contributions, *i.e.*, the bonding orbitals between P and O and the oxygen lone pair orbital along the *x* and *y* axes, are not well-correlated with the R_{XB} values. This corroborates the lack of a clear correlation between oxygen quadrupolar coupling and R_{XB} values (Figure 3.3.6 (b)). However, it is clear that the contribution from the oxygen lone pair orbital along the *z* axis, the p_z-type orbital,[42] correlates in a linear fashion ($R^2 = 0.91$) with R_{XB}. Since the lobes of this oxygen lone pair are oriented towards the iodine atom, especially when oxygen acts as a bifurcated halogen bond acceptor (see LP O_z in Figure 3.3.7), the contribution from this orbital correlates strongly to the halogen bond. Finally, the contribution from the P=O bonding orbital reduces the overall value of V_{33}. As the halogen bonding interaction weakens, the contribution from the P=O bonding orbital decreases.

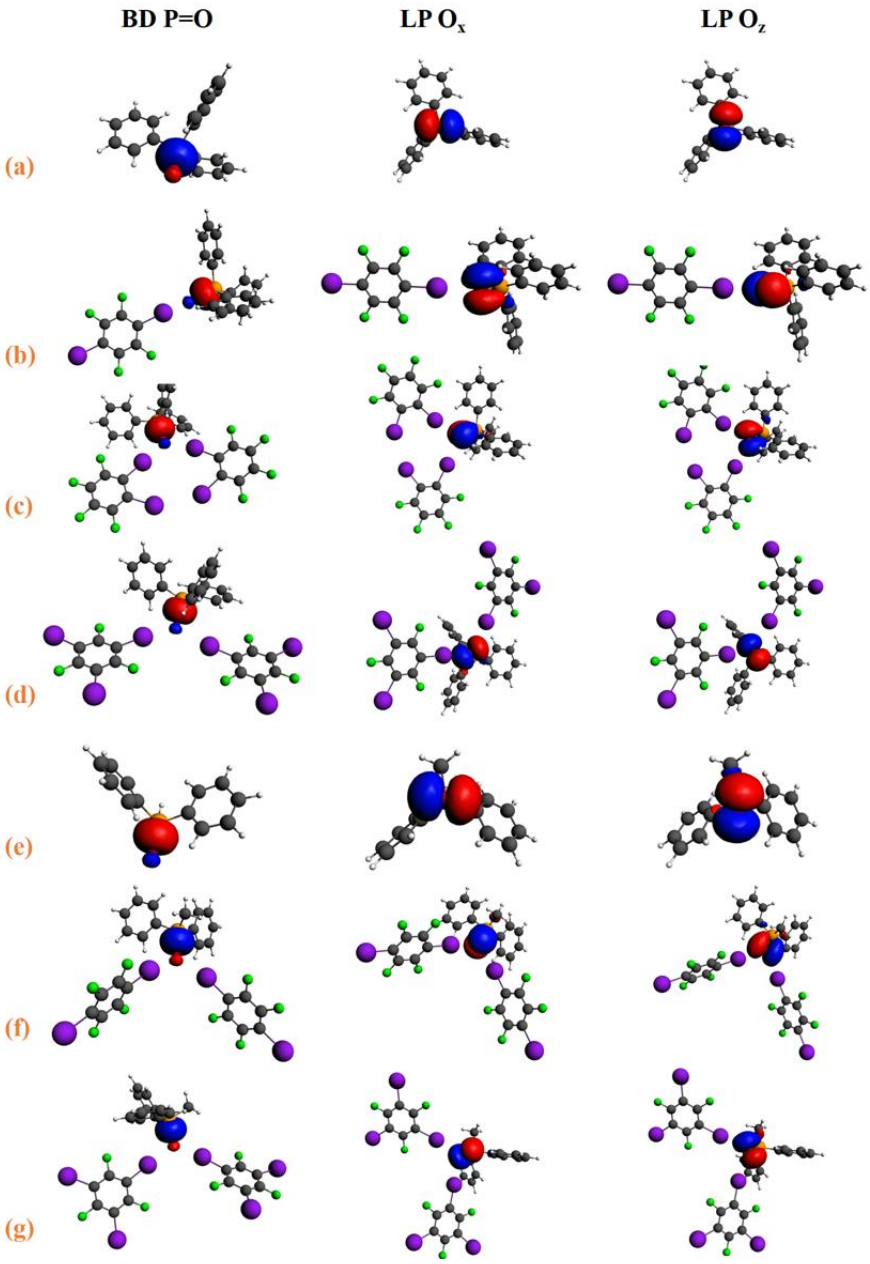

Figure 3.3.7. Three major NLMO contributions to ^{17}O EFG tensors for Ph_3PO (a), CH_3Ph_2PO (b) and halogen-bonded compounds (**A1** (c), **A2** (e), **A3** (g), **B1** (d), and **B3** (f)). The main NLMO contributions are from the bonding orbitals between P and O (BD P=O), the O lone pair along *x* axis (LP O_x), and the O lone pair along *z* axis (LP O_z).

(iii) Analysis of Computed $J(^{31}P, ^{17}O)$ Values

A plot of the calculated $J(^{31}P, ^{17}O)$ coupling constant versus the experimental values for ^{17}O-labeled Ph_3PO and its related halogen-bonded cocrystals (**A1, A2, A3**) is provided in Figure 3.3.8(a). Even though the calculated $J(^{31}P, ^{17}O)$ values are overestimated, they are still well-reproduced ($R^2 = 0.9977$).

A plot of calculated $J(^{31}P, ^{17}O)$ coupling constants versus R_{XB} values shows a strong positive correlation (shown in Figure 3.3.8 (b)). The $J(^{31}P, ^{17}O)$ coupling constant increases as the halogen bonding interaction weakens, which is consistent with what we have previously reported for $J(^{31}P, ^{77}Se)$ coupling constants in halogen-bonded phosphine selenides.[8] In order to probe the origins of the $J(^{31}P, ^{17}O)$ coupling constant, we performed an NLMO analysis to determine the major molecular orbital contributions (see Table A4). The three main NLMO contributions are: the bonding P=O orbital, one O lone pair orbital along the P=O bond axis, and one O core orbital. The results are shown in Figure 3.3.9. The key contribution to the $J(^{31}P, ^{17}O)$ coupling constant is from the oxygen lone pair orbital, and the second contribution is from the bonding P=O orbitals and oxygen core orbital. Unlike the NLMO contributions to the ^{17}O EFG tensors, the oxygen lone pair orbital aligned with the P=O bond, which is the p_y orbital, makes a large positive contribution to $J(^{31}P, ^{17}O)$. The percentages shown in Figure 3.3.9 represent how much each molecular orbital contributes to the calculated $J(^{31}P, ^{17}O)$ coupling constant. A negative contribution to calculated $J(^{31}P, ^{17}O)$ values arises from the P=O bonding orbitals, opposite in sign to the total NLMO contribution value. The presence of halogen bonding will lengthen the P=O bond and thus reduce the $J(^{31}P, ^{17}O)$ coupling constant. A plot of each major contribution, the sum of three major contributions and the total contributions

including all minor contributions as a function of R_{XB} values are presented in Figure 3.3.8(c). It can be seen how the sum of the three main contributions and the total contributions follow the same trend relative to the R_{XB} values. Only the oxygen lone pair and core orbitals closely follow the overall linear trend. However, there is no real correlation between the contribution from the P=O bonding orbital and the R_{XB} values (R^2 = 0.1874).

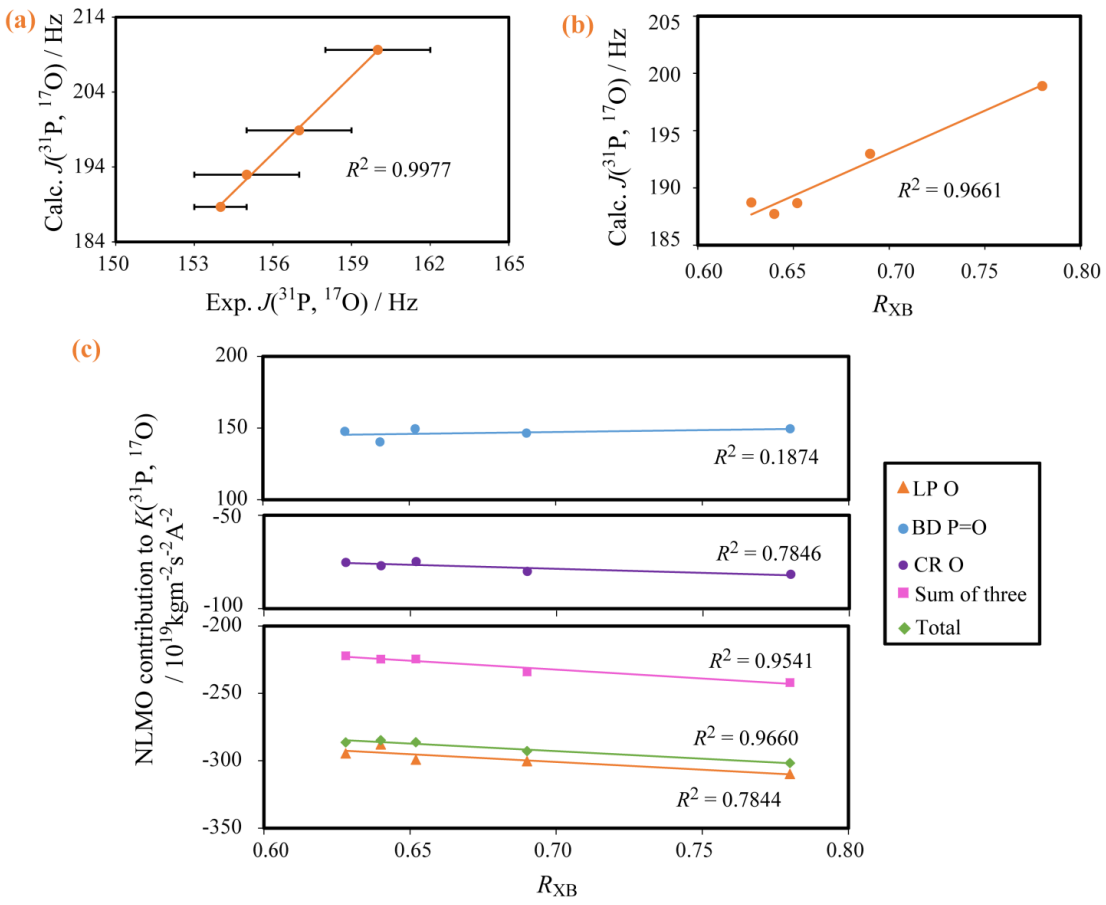

Figure 3.3.8. (a) Calculated versus experimental $J(^{31}P, ^{17}O)$ values for monoclinic Ph_3PO, **A1**, **A2**, and **A3**. (b) Plot of calculated $J(^{31}P, ^{17}O)$ values versus R_{XB} values for the compounds listed in Table 3.3.1. (c) A plot of the sum of Lewis and non-Lewis largest NLMO contributions to $J(^{31}P, ^{17}O)$ as a function of R_{XB} values for **A1**, **A2**, **A3**, **B1**, and **B3**. Blue circles represent the contribution from the P=O bonding orbital (BD P=O). Orange triangles represent the contribution from the oxygen lone pair (LP O_y). Purple circles represent the contribution from the oxygen core orbital (CR O), and pink squares represent the sum of the three major contributions (the oxygen lone pair orbital, the oxygen core orbitals, and the P=O bonding orbitals). Green diamonds represent the total contribution. Lines represent the best linear fits: (a) calc. $J(^{31}P, ^{17}O)$ = 3.4296 exp. $J(^{31}P, ^{17}O)$ – 339.2; (b) calc. $J(^{31}P, ^{17}O)$ = 74.375R_{XB} + 140.97; (c) BD P=O: K = 26.487R_{XB} + 128.68; LP O_y: K = -115.54R_{XB} – 219.95; CR O: K = -43.081R_{XB} - 48.541; sum of three orbitals: K = -132.14R_{XB} – 139.8; total: K = -112.23R_{XB} – 214.25.

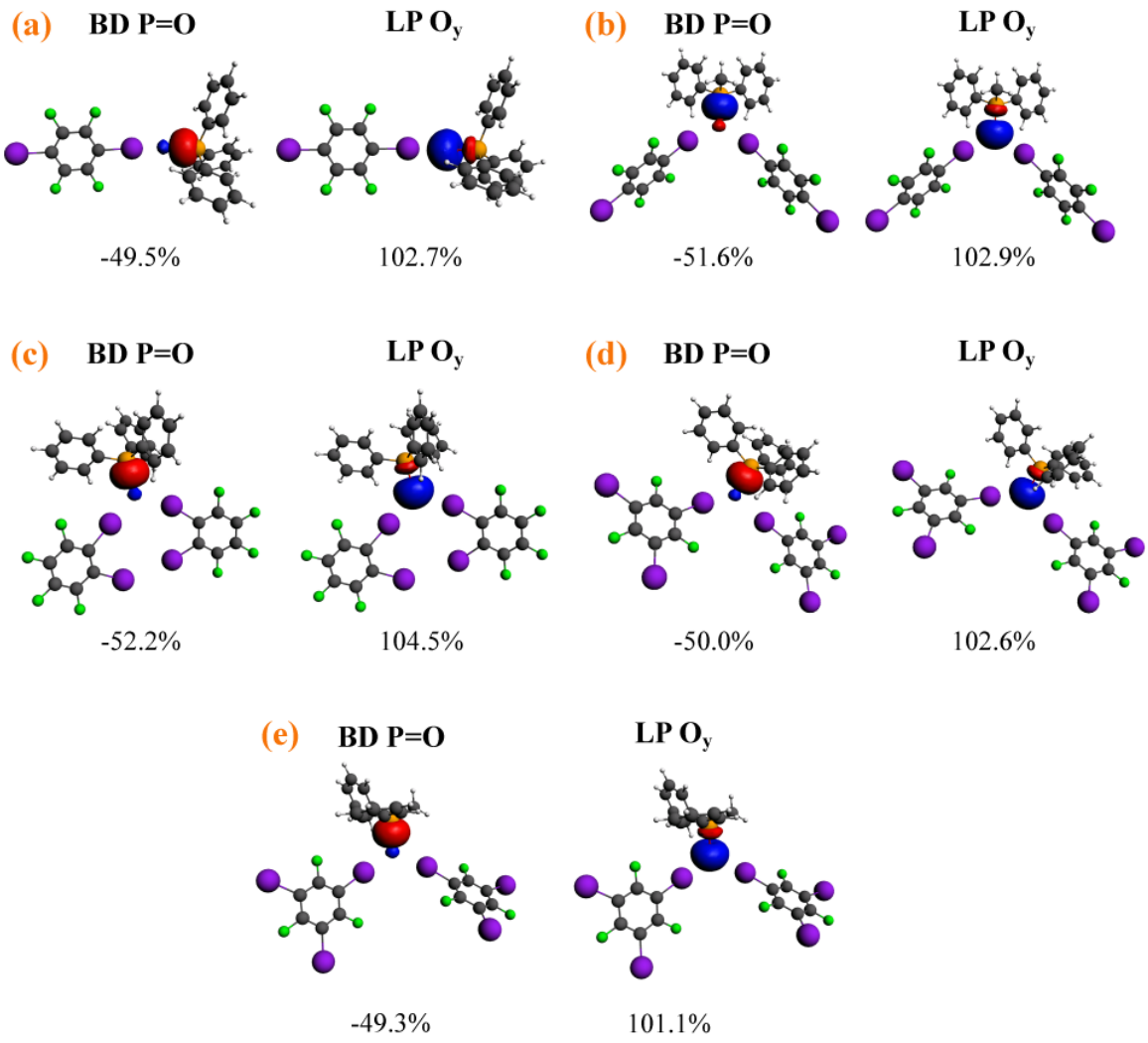

Figure 3.3.9. Two major NLMO contributions to the isotropic $J(^{31}P, ^{17}O)$ coupling values for all the halogen-bonded compounds (**A1** (a), **B1** (b), **A2** (c), **A3** (d), and **B3** (e)). The main NLMO contributions are from the bonding orbitals between P and O (BD P=O) and the O lone pair along the *y* axis (LP O_y).

3.4 Conclusions

A series of halogen-bonded compounds containing P=O···I–C motifs have been prepared by simple mechanochemical liquid-assisted grinding. Nonlabeled and ^{17}O-labeled compounds have been characterized by single crystal X-ray diffraction and ^{31}P and ^{17}O solid-state NMR. Using atomic coordinates extracted from the crystal structures, two types of density functional theory computations have been applied to interpret the correlation between the halogen bonding distance, quantified by R_{XB}, and the NMR parameters (^{31}P and ^{17}O chemical shifts, ^{17}O quadrupolar coupling constants, and J(^{31}P, ^{17}O) coupling constants).

The following main conclusions may be drawn from these studies:

(1) From the ^{31}P CP/MAS NMR spectra, the complete ^{31}P chemical shift tensors have been measured. We observe a small increase in the ^{31}P chemical shift and a small decrease in the span in the halogen-bonded compounds relative to the pure starting materials. Therefore, the ^{31}P CS tensors can be an indirect indication of the presence of halogen bonding interaction.

(2) ^{31}P solid-state NMR spectra of ^{17}O-labeled halogen-bonded compounds reveal an increase in the value of the J(^{31}P, ^{17}O) coupling constant when the P=O···I–C halogen bond weakens.

(3) A direct ^{17}O solid-state NMR study of the halogen bonding acceptor provides several correlations between the NMR parameters and halogen bonding strength. The measurement of ^{17}O EFG tensors shows that both the ^{17}O quadrupolar coupling constant and asymmetry parameter increase in the presence of a halogen

bonding interaction. However, there is no clear relationship noted between the experimental ^{17}O isotropic chemical shift and halogen bonding.

(4) DFT calculations of the NMR parameters reveal several remarkable trends. The GIPAW DFT calculations, which take the full crystal packing into account, are in good agreement with experiment. The calculations also indicate correlations between the ^{17}O isotropic chemical shift as well as $J(^{31}\text{P}, ^{17}\text{O})$ coupling, and halogen bonding distance.

(5) A natural localized molecular orbital analysis provided insight into the orbital contributions to the $J(^{31}\text{P}, ^{17}\text{O})$ and ^{17}O EFG tensors in the P=O···I–C motif. The values of $J(^{31}\text{P}, ^{17}\text{O})$ arise mainly due to contributions from the bonding orbital between phosphorus and oxygen, the oxygen lone pair aligned with the P=O bond, and the oxygen core orbital. The key contributions to the ^{17}O quadrupolar coupling constant are due to the bonding orbital between phosphorus and oxygen, and the oxygen lone pair orbitals. The contribution from the oxygen p_z orbital has a linear correlation with the distance of the halogen bonding interaction.

Overall, this first study of ^{17}O NMR parameters in halogen bonded solids has provided key experimental and computational insights into the relationship between NMR observables and the nature of the halogen bond.

3.5 References for Chapter 3

[1] Thorson, R. A.; Woller, G. R.; Driscoll, Z. L.; Geiger, B. E.; Moss, C. A.; Schlapper, A. L.; Speetzen, E. D.; Bosch, E.; Erdélyi, M.; Bowling, N. P. *Eur. J. Org. Chem.* **2015**, 1685–1695.

[2] Ciancaleoni, G.; Bertani, R.; Rocchigiani, L.; Sgarbossa, P.; Zuccaccia, C.; Macchioni, A. *Chem. -Eur. J.* **2015**, *21*, 440–447.

[3] Weingarth, M.; Raouafi, N.; Jouvelet, B.; Duma, L.; Bodenhausen, G.; Boujlel, K.; Schöllhorn, B.; Tekely, P. *Chem. Commun.* **2008**, 5981–5983.

[4] Bryce, D. L.; Viger-Gravel, J. in *Halogen Bonding I*; Metrangolo, P., Resnati, G., Eds.; Springer: Heidelberg, 2015; pp.183–203.

[5] Attrell, R. J.; Widdifield, C. M.; Korobkov, I.; Bryce, D. L. *Cryst. Growth Des.* **2012**, *12*, 1641–1653.

[6] Viger-Gravel, J.; Leclerc, S.; Korobkov, I.; Bryce, D. L. *CrystEngComm* **2013**, *15*, 3168–3177.

[7] Viger-Gravel, J.; Leclerc, S.; Korobkov, I.; Bryce, D. L. *J. Am. Chem. Soc.* **2014**, *136*, 6929–6942.

[8] Viger-Gravel, J.; Meyer, J. E.; Korobkov, I.; Bryce, D. L. *CrystEngComm* **2014**, *16*, 7285–7297.

[9] "*Mechanochemistry: From Functional Solids to Single Molecules*", *Faraday Discuss.* **2014**, *170*, 1–432.

[10] Shan, N.; Toda, F.; Jones, W. *Chem. Commun.* **2002**, 2372–2373.

[11] Fernandes, J. A.; Sardo, M.; Mafra, L.; Choquesillo-Lazarte, D.; Masciocchi, N. *Cryst. Growth Des.* **2015**, *15*, 3674–3683.

[12] Oh, S. Y.; Nickels, C. W.; Garcia, F.; Jones, W.; Friščić, T. *CrystEngComm* **2012**, *14*, 6110–6114.

[13] Bowmaker, G. A.; Hanna, J. V.; Hart, R. D.; Healy, P. C.; King, S. P.; Marchetti, F.; Pettinari, C.; Skelton, B. W.; Tabacaru, A.; White, A. H. *Dalton Trans.* **2012**, *41*, 7513–7525.

[14] Gerothanassis, I. P. Oxygen-17 NMR. In *Encyclopedia of Nuclear Magnetic Resonance*; Grant, D. M., Harris, R. K., Eds.; John Wiley & Sons: Chichester, U. K., 1996; pp 3430–3438.

[15]Wu, G.; Mason, P.; Mo, X.; Terskikh, V. *J. Phys. Chem. A* **2008**, *112*, 1024–1032.

[16] Wu, G.; Dong, S.; Ida, R.; Reen, N. *J. Am. Chem. Soc.* **2002**, *124*, 1768–1777.

[17] Wang, W. D.; Lucier, B. E. G.; Terskikh, V. V.; Wang, W.; Huang, Y. *J. Phys. Chem. Lett.* **2014**, *5*, 3360–3365.

[18] Vogt, F. G.; Yin, H.; Forcino, R. G.; Wu, L. *Mol. Pharmaceutics.* **2013**, *10*, 3433–3446.

[19] Zhang, Q.-W.; Chekmenev, E. Y.; Wittebort, R. J. *J. Am. Chem. Soc.* **2003**, *125*, 9140–9146.

[20] Cinčić, D.; Friščić, T.; Jones, W. *CrystEngComm* **2011**, *13*, 3224–3231.

[21] Friščić, T.; Trask, A. V.; Jones, W.; Motherwell, W. D. S. *Angew. Chem., Int. Ed. Engl.* **2006**, *45*, 7546–7550.

[22] Bryce, D. L.; Eichele, K.; Wasylishen, R. E. *Inorg. Chem.* **2003**, *42*, 5085–5096.

[23] APEX Software Suite; Bruker AXS Inc.: Madison, WI, 2012.

[24] SADABS; Bruker AXS Inc.: Madison, WI, 2001.

[25] Sheldrick, G. M. *Acta Cryst.* **2015**, *71*, 3–8.

[26] Eichele, K. Herzfeld-Berger analysis program,version 1.7.5.; Universität Tübingen: Tübingen , Germany, 2015.

[27] Eichele, K. WSolids1, version 1.20.21.; Universität Tübingen: Tübingen , Germany, 2013.

[28] Clark, S. J.; Segall, M. D.; Pickard, C. J.; Hasnip, P. J.; Probert, M. I. J.; Refson, K.; Payne, M. C. *Z. Kristallogr.* **2005**, *220*, 567–570.

[29] Baerends, E. J.; et al. Amsterdam Density Functional Software, ADF2012.01 SCM; Theoretical Chemistry, Vrije Universiteit: Amsterdam, The Netherlands, 2012.

[30] Pickard, C. J.; Mauri, F. *Phys. Rev. B* **2001**, *63*, 2451011–2451013.

[31] Frisch, M. J.; et al. Gaussian 09, Revision A.02; Gaussian Inc.: Wallingford, CT, 2009.

[32] Jameson, C. J.; De Dios, A.; Jameson, A. K. *Chem. Phys. Lett.* **1990**, *167*, 575–582.

[33] Wasylishen, R. E.; Bryce, D. L. *J. Chem. Phys.* **2002**, *117*, 10061–10066.

[34] Bondi, A. *J. Phys. Chem.* **1964**, *68*, 441–451.

[35] Arumugam, S.; Glidewell, C.; Harris, K. D. M. *J. Chem. Soc., Chem. Commun.* **1992**, 724–726.

[36] Bryce, D. L. Tensor Interplay. In *NMR Crystallography*; Harris, R. K.; Wasylishen, R. E.; Duer, M. J., Eds.; John Wiley and Sons Ltd.: Chichester, U. K., 2009; pp 289–301.

[37]Bryce, D. L.; Bernard, G. M.; Gee, M.; Lumsden, M. D.; Eichele, K.; Wasylishen, R. E. *Can. J. Anal. Sci. Spectrosc.* **2001**, *46*, 46–82.

[38] Kentgens, A. P. M. *Geoderma* **1997**, *80*, 271–306.

[39] Berger, S.; Braun, S.; Kalinowski, H. -O. NMR Spectroscopy of the Non-Metallic Elements; Becconsali, J., English language translation; John Wiley & Sons: Chichester, U. K., 1997; Chapter 5.

[40] Kutzelnigg, W. Fundamentals of Nonrelativistic and Relativistic Theory of NMR and EPR Parameters. In *Calculation of NMR and EPR Parameters: Theory and Applications*; Kaupp, M., Bühl, M., Malkin, V. G., Eds.; Wiley-VCH: Weinheim, 2004; pp 43–82.

[41] Alvarado, S. R.; Shortt, I. A.; Fan, H.-J.; Vela, J. *Organometallics* **2015**, *34*, 4023–4031.

[42] Autschbach, J.; Zheng, S.-H.; Schurko, R. W. *Concepts Magn. Reson. A* **2010**, *36A*, 84–126

Chapter 4. A Rare Example of a Phosphine as a Halogen Bond Acceptor.

Permission: Chapter 4 was from: Y. Xu, J. Huang, B. Gabidullin and D. L. Bryce, *Chem. Commun.*, 2018, **54**, 11041 (**DOI:**10.1039/C8CC06019C). –Reproduced by permission of The Royal Society of Chemistry.

4.1 Introduction

Numerous halogen-bonded cocrystals have been engineered, prepared, and studied in several publications as mentioned in Section 1.2.3; these typically feature nitrogen, oxygen, sulfur, selenium, or halide ions as the electron donor (XB acceptor). [1] Although the phosphorus atoms of phosphines would seem to represent an obvious choice as an electron donor, it is very rare for phosphorus to act in this capacity, especially as part of a phosphine. The interaction between phosphine complexes and halogens on other molecules is more likely to result in a covalent P-X bond due to the strongly polarizing nature of the phosphorus atom.[2] A search for structures involving P···X contacts (X = Cl, Br, I) in the Cambridge Structural Database (CSD) reveals fifteen examples containing P and X at distances closer than the sum of their van der Waals' radii (but significantly longer than the sum of their covalent radii). Most of these are single component systems with weak contacts likely resulting from crystal packing or are solvates (see Table B1 in the Appendix B). The only example of a halogen-bonded cocrystal featuring a phosphine as a halogen bond acceptor seems to be 1-diphenylphosphino-2-methyl-1,2-dicarbadodecaborane(10) hemikis(iodine), where I_2 acts as the halogen bond donor.[3] However, to our knowledge there are no reports to date of an engineered cocrystal featuring phosphorus as an electron donor, and certainly none with the iconic iodoperfluorobenzene halogen bond donors (*e.g.*, 1,3,5-trifluoro-2,4,6-triiodobenzene (*sym*-$C_6F_3I_3$)). Given the explosion of activity in the design, preparation, and study of halogen-bonded cocrystals, this dearth of structures is somewhat surprising.

Here we report on a cocrystal of triphenylphosphine with 1,3,5-trifluoro-2,4,6-triiodobenzene ($(Ph_3P)\cdot(sym\text{-}C_6F_3I_3)$) (**1**), featuring a moderately strong and linear phosphorus-iodine halogen bond.

4.2 **Experimental Section**

4.2.1 Sample Preparation

Triphenylphosphine (Ph_3P) was purchased from Sigma Aldrich, and 1,3,5-trifluoro-2,4,6-triiodobenzene (*sym*-$C_6F_3I_3$) was purchased from Alfa Aesar. Both starting materials were used without any further purification. Equimolar amounts of these two starting materials were dissolved into a minimum volume of diethyl ether, chloroform, or acetonitrile. Slow evaporation from diethyl ether or chloroform at room temperature produced crystals of **1**, along with a trace amount of **2**. Slow evaporation from acetonitrile at room temperature produced a crystal of **2**. Single cocrystals of **1** and **2** were individually wrapped in aluminum foil and stored in the freezer. Storage at room temperature or under light for more than two days caused the cocrystals to start decomposing and change from colourless to yellow.

The mechanochemical preparation of **1** was carried out using a Retsch MM 400 ball mill. 0.0872 g Ph_3P and 0.1663 g *sym*-$C_6F_3I_3$ were added with 50 μL acetonitrile to 10 mL stainless steel milling jars. The mixture was milled for 30 min at room temperature with a milling frequency of 30 Hz using two 5 mm stainless steel grinding balls.

Equimolar amounts of Ph_3P (0.1020 g) and *sym*-$C_6F_3I_3$ (0.2005 g) were first dissolved in a minimum of nearly boiling diethyl ether. The mixture was left in the freezer overnight. The precipitation of cocrystal **1** was effected by filtering under vacuum. The

phase purity of compounds obtained from each method was verified by powder X-ray diffraction (see Figure B1-Figure B3 in the Appendix B).

4.2.2 ^{31}P Solution NMR Spectroscopy

^{31}P NMR spectra were recorded in $CDCl_3$ using a 300 MHz Bruker Avance II spectrometer. A sealed capillary tube containing 85% H_3PO_4 was inserted into the 5 mm o.d. NMR tube in each experiment to serve as an internal reference. ^{31}P NMR chemical shifts were referenced to 85% H_3PO_4 in H_2O ($\delta = 0$ ppm).

4.2.3 ^{31}P Solid-State NMR Spectroscopy

Data were acquired with a 9.4 T magnet, Bruker AVANCE III console, and a 4 mm Bruker HXY probe (University of Ottawa, Ottawa, Canada). Samples were packed into 4 mm o.d. zirconia rotors. ^{31}P chemical shifts were referenced to ammonium dihydrogen phosphate (δ_{iso} = 0.81 ppm with respect to 85% H_3PO_4). A standard cross-polarization pulse sequence was employed. The $\pi/2$ pulse length and contact time were 3.5 μs and 3 ms, respectively. The recycle delay was set to be 4 minutes and the number of scans was 16 for Ph_3P. The recycle delay was set to be 2 min for the cocrystals and the number of scans was 312 for **1** and 576 for **2**. Data were acquired for Ph_3P under static and MAS conditions. Data for cocrystal **1** were acquired at different magnetic fields (4.7 T and 9.4 T) to identify the isotropic peak and to obtain spectra with a larger number of sidebands for spectral fitting purposes.

4.2.4 Powder X-Ray Diffraction

All PXRD patterns were obtained using a Rigaku Ultima IV powder diffractometer at room temperature (298 ± 1 K) with a copper source and one diffracted beam

monochromator from 5° to 50° (2θ range) in increments of 0.02° with a scan rate of 1° per minute. Simulations were generated using Mercury 3.8 software from the Crystallographic Data Center. Comparisons between experimental PXRD patterns and simulated patterns were used to verify sample phase purity.

4.2.5 Computational Details

For DFT calculations on cluster models, electrostatic potential calculations were performed using B3LYP.[4] The calculation for Ph_3P was carried out using the 6-311++G(d,p) basis set. The def2-TZVP basis set was used for *sym*-$C_6F_3I_3$ and cocrystal **1** which contain the heavy atom iodine. Models were constructed and visualized using GaussView 4.1 software.[5]

4.2.6 Single-Crystal X-Ray Diffraction

The crystal of **1** and **2** were mounted on a thin glass fiber using paraffin oil. Prior to data collection the crystal was cooled to 200 ± 2 K. Data was collected on Bruker AXS single crystal diffractometer equipped with a sealed Mo tube source (wavelength 0.71073 Å) and APEX II CCD detector. Raw data collection and processing were performed with Bruker APEX II software package.[6] Semi-empirical absorption corrections based on equivalent reflections were applied.[7] The structure was solved by direct methods and refined with a full-matrix least-squares procedure based on F^2, using SHELXL[8] and WinGX[9]. All non-hydrogen atoms were refined anisotropically. The positions of hydrogen atoms were calculated based on the geometry of related non-hydrogen atoms. No additional restraints or constraints were applied during the refinement.

4.3 Results and Discussion

A single crystal obtained through slow evaporation from diethyl ether was characterized by X-ray diffraction (see Table B2 in the Appendix B). The local halogen bonding environment is shown in Figure 4.3.1. Several selected intermolecular contact distances and angles that are used to characterize the halogen bonding interaction and geometry are shown in Table 4.3.1.

Table 4.3.1. Compound Numbering and Local Halogen Bonding Geometrical Information from Single-Crystal X-ray Diffraction

cocrystal	$d_{I\cdots P}$ /Å	$d_{I\cdots O}$ /Å	d_{I-C} /Å	$d_{P=O}$ /Å	R_{XB}[a]	$\theta_{C-I\cdots P}$ /deg	$\theta_{C-I\cdots O}$ /deg	$\theta_{P=O\cdots I}$ /deg
1	3.376(1)	-	2.104(3)	-	0.857	165.26(9)	-	-
2	-	2.776(2)	2.097(3)	1.499(2)	0.784	-	174.19(9)	148.0(1)

[a] The van der Waals radii (1.90 Å for P, 1.50 Å for O and 2.04 Å for I) used to calculate R_{XB} values were taken from ref [10]

Compound **1** packs in the triclinic crystal system and $P\bar{1}$ space group. As shown in Figure 4.3.1(a), there is only one crystallographically distinct phosphorus site, and it is halogen-bonded to iodine with a nearly linear P···I-C angle of 165.3° and moderate R_{XB} value of 0.857. The crystal packing is shown in Figure 4.3.1(b). Another iodine atom in the same *sym*-$C_6F_3I_3$ molecule forms two interactions with carbon atoms of the phenyl ring (I···C distances of 3.609 Å and 3.398 Å) in a second Ph_3P molecule, with a separation between the iodine atom and the midpoint of the C-C bond (dark green ball in Figure 4.3.1 (b)) of 3.435 Å. These two Ph_3P molecules are related by inversion symmetry and interact *via* a weak sextuple phenyl embrace[11] with a P···P distance of 7.053 Å. The third iodine

forms a short I···F contact of 3.128 Å (orange dashed line in Figure 4.3.1 (b)), building a chain along the *a* axis. The presence of the P···I halogen bonding interaction and phenyl···I contacts allows the Ph_3P molecules to bridge two layers of *sym*-$C_6F_3I_3$ sheets.

To demonstrate the preparation of powdered **1** on a bulk scale, we have used (i) mechanochemical liquid-assisted grinding (LAG) with 50 μL acetonitrile, (ii) cocrystallization from cold diethyl ether, (iii) slow evaporation from chloroform or diethyl ether. The consistency between the cocrystals obtained by slow evaporation from different solvents (diethyl ether and chloroform) and different methods (slow evaporation, crystallization from cold solvent and mechanochemistry) was verified by powder X-ray diffraction (see Figure B2 and Figure B3 in the Appendix B). All methods generate the same polymorph reproducibly.

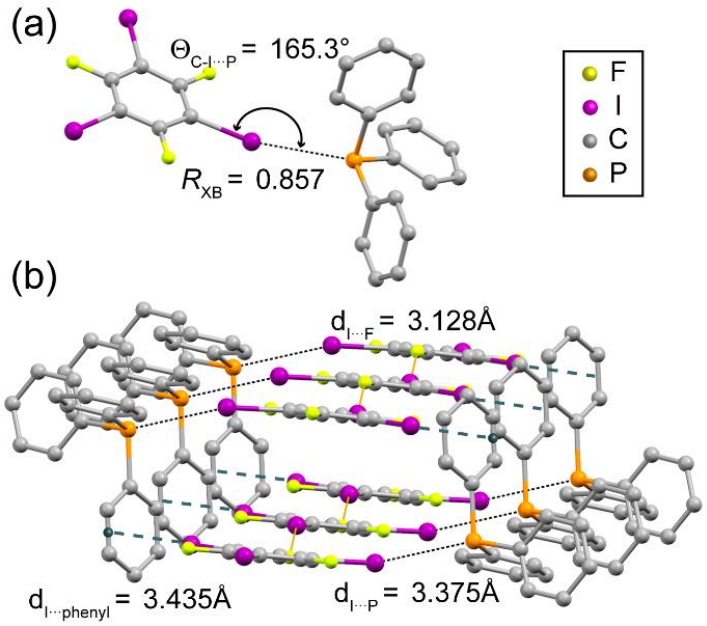

Figure 4.3.1. (a) Halogen bond geometry in cocrystal **1** from single-crystal X-ray diffraction. (b) Fragment of the cocrystal **1** structure showing short contacts.

^{31}P is a spin-1/2 nucleus with a natural abundance of 100%. Its broad chemical shift range of several hundred ppm suggest that it should be a sensitive probe of halogen bonding to phosphorus in **1**. Our group has indirectly probed and characterized the halogen bonding interaction in cocrystals of phosphine oxides and selenides by ^{31}P solid-state NMR;[12,13,14] however, in these cases the influence of halogen bonding interaction on ^{31}P chemical shifts is not clear since the phosphorus is only indirectly involved in the halogen bond. The ^{31}P cross-polarization magic-angle spinning (CP/MAS) NMR spectra for powdered Ph_3P and its halogen bonded cocrystal **1** are shown in Figure 4.3.2. The corresponding ^{31}P chemical shift tensors (Table 4.3.2) were obtained by fitting the spectra obtained at different spinning speeds or in different applied magnetic fields (see Figure B5 in Appendix B). The ^{31}P chemical shift (δ_{iso} = -9.5 ppm) of PPh_3 is consistent with literature reports;[15,16] however, these seem to vary by a couple of ppm. (This could be due to different polymorphs of triphenylphosphine. In this report, Ph_3P packs in the monoclinic unit cell $P2_1/a$.) The ^{31}P chemical shift (δ_{iso} = -16.0 ppm) of cocrystal **1** is more shielded, consistent with the single previous relevant report in solution, where shielding of the ^{31}P NMR signal was also observed.[3] The change in ^{31}P chemical shift ($\Delta\delta_{iso}$ = -6.5 ppm) upon cocrystal formation is in the opposite direction to what is observed when Ph_3PO and *sym*-$C_6F_3I_3$ are cocrystallized (~ + 2.9 ppm) and when CH_3Ph_2PO and *sym*-$C_6F_3I_3$ are cocrystallized (~ + 6.5 ppm).[13] The line width of the ^{31}P CP/MAS NMR signal for **1** is significantly broader (1149 Hz) than that of Ph_3P (43 Hz), perhaps in part due to weak dipolar couplings to ^{127}I in the cocrystal (*i.e.*, further evidence of cocrystal formation). The reduction of ¬20 ppm in the span of the phosphorus chemical shift tensor in the cocrystal relative to Ph_3P is

consistent with the creation of a pseudo-tetrahedral phosphorus coordination environment as a result of the close contact with iodine in the cocrystal.

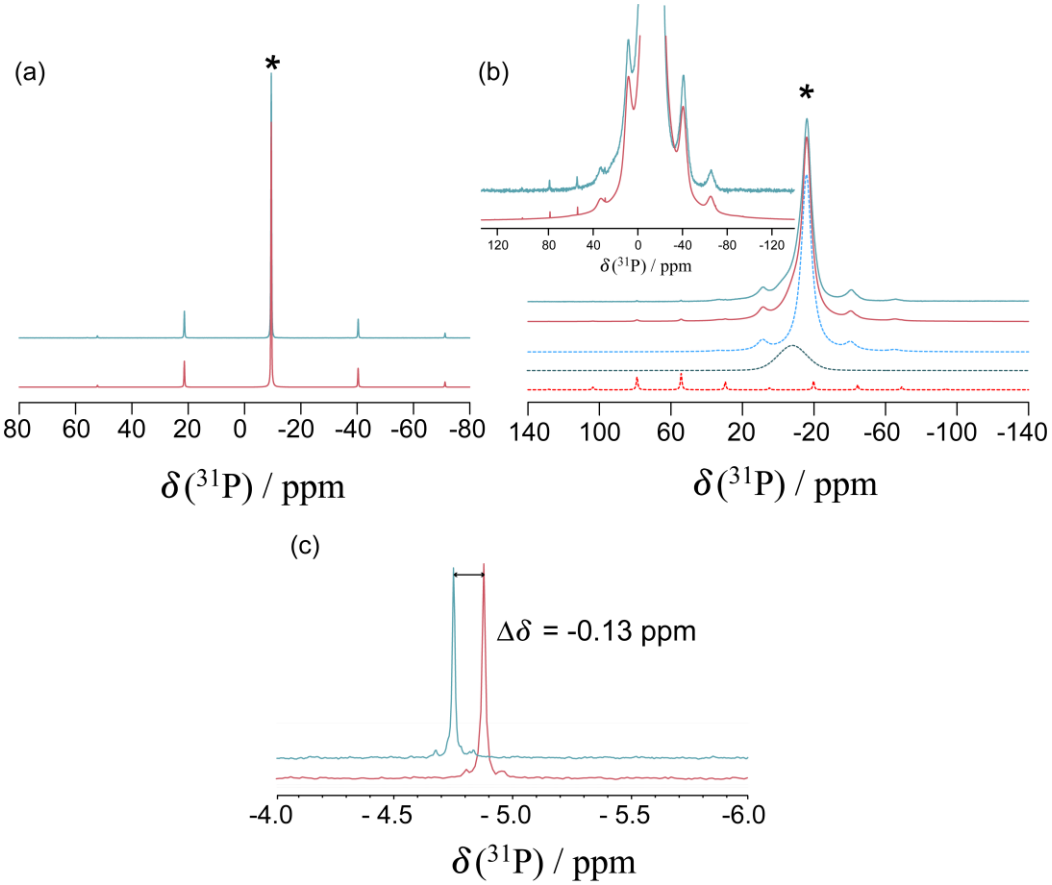

Figure 4.3.2. Experimental ^{31}P CP/MAS SSNMR spectra (green) obtained at 9.4 T for (a) Ph_3P and (b) its halogen-bonded cocrystal **1**. The corresponding simulated spectra are shown in red. The isotropic peaks are indicated by asterisks. The spectra were acquired at a spinning speed of 5 kHz for Ph_3P and 4 kHz for cocrystal **1**. The spectrum of **1** shows a trace amount of cocrystal **2** (red dashed line), and a broad amorphous phase and/or contribution from ^{31}P-^{127}I residual dipolar coupling (dark green dashed line). Shown in the inset is a magnification of the spectra. (c) Experimental solution ^{31}P NMR spectra of Ph_3P (green) and **1** (red) obtained at 7.05 T. The samples were dissolved in $CDCl_3$ and referenced to 85% H_3PO_4 (δ = 0 ppm).

There is trace amount of a new halogen-bonded cocrystal formed between Ph_3PO and *sym*-$C_6F_3I_3$ (**2**) present in the polycrystalline sample used in the solid-state NMR studies. This cocrystal can be reproducibly prepared in bulk powdered form by dissolving Ph_3P and *sym*-$C_6F_3I_3$ in acetonitrile and allowing slow evaporation at room temperature. The structure **2** is a new polymorph, different from what was reported in a previous study.[13] The relevant local halogen bonding geometrical information for **2** is provided in Table 4.3.1.. PXRD and ^{31}P SSNMR spectra of **2** are provided in Figure B4 of the Appendix B.

Table 4.3.2. Experimental ^{31}P Chemical Shift Tensors of Ph_3P and Halogen Bonded Cocrystals

	δ_{iso} / ppm	Ω / ppm	κ
Ph_3P	-9.5 ± 0.2	51± 3	0.70 ± 0.05
1	-16.0 ± 0.8	31± 11	0.3 ± 0.1
2	29.2 ± 0.2	174± 2	0.96 ± 0.01

We next aimed to establish whether the phosphorus-iodine halogen bond in **1** persists in solution. Using ^{31}P solution NMR, the same chemical shift trend was also observed, where there is a shielding of $\Delta\delta$ = - 0.13 ppm between Ph_3P (δ = -4.75 ppm) and a solution containing equimolar quantities of Ph_3P and *sym*-$C_6F_3I_3$ (δ = -4.88 ppm) (see Figure 4.3.2(c)). Satellites arising from the *J* coupling between ^{31}P and ^{13}C at the *ipso* position in the phenyl ring are visible in the spectra; the value of $^1J(^{31}P, ^{13}C)$ is 18.2 Hz in Ph_3P and 17.3 Hz in the equimolar solution. The clear decrease in chemical shift indicates that the P···I interaction persists in solution.

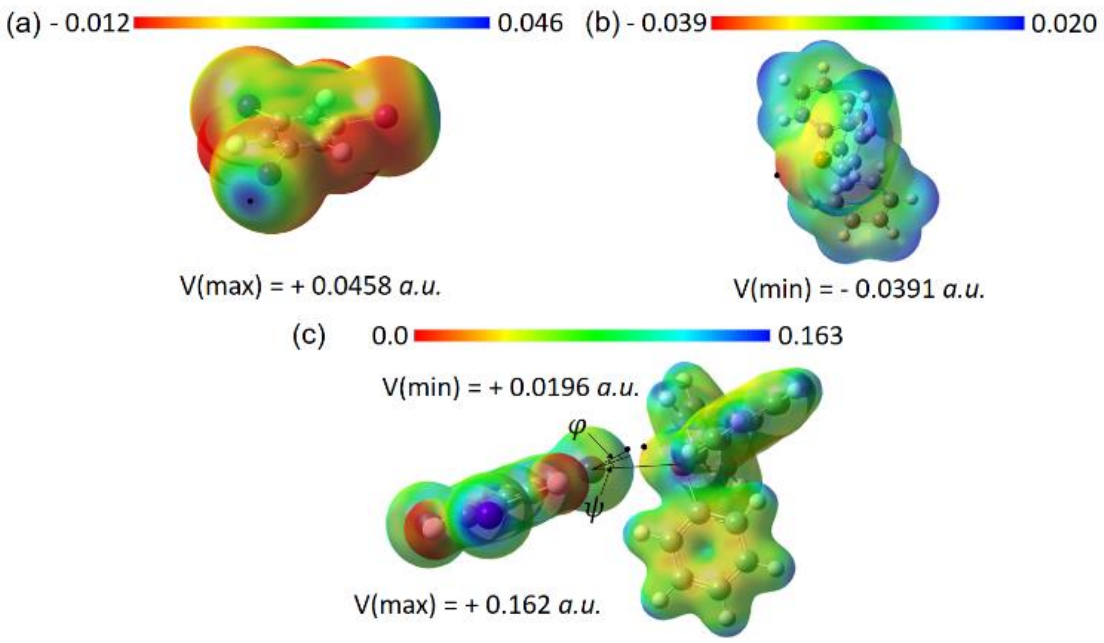

Figure 4.3.3. Electrostatic potential (ESP) map of the halogen bond donor *sym*-$C_6F_3I_3$ (a), acceptor Ph_3P (b), and cocrystal **1** (c). Blue and red depict the largest (positive) and negative potentials, respectively. The corresponding scales are shown on the top. Electrostatic potentials are calculated on the 0.001 electrons bohr^{-3} molecular surface in (a) and (b) and 0.02 electrons bohr^{-3} for (c). The black dots represent the maximum or minimum potential area and the corresponding ESP values are in *a.u.*

Figure 4.3.3 shows the computed electrostatic potential maps of Ph_3P, *sym*-$C_6F_3I_3$, and **1**. The value of $\theta_{P\cdots I\text{-}C}$ = 165.3° falls in the typical halogen bonding angle range, which can be also explained using the σ-hole-based electrostatic potential model. As seen in Figure 4.3.3 (a) and (b), the most positive potential on the surface of the I atom is observed along the extension of the C-I covalent bond with the maximum of electrostatic potential (V(max) = + 0.0458 *a. u.*) and the most negative potential (V(min) = - 0.0391 *a. u.*) on the P surface is observed to be at the intersection of the extensions of the three P-C covalent bonds. Thus, to maximize electrostatic attraction, P is expected to approach the iodine

along the extension of the C-I bond. The formation of the cocrystal shifts the position of *V*(max) away from the extension of the C-I bond by $\varphi = 7°$, and the deviation of the P···I vector from the I-V(max) axis is $\psi = 26°$.

4.4 Conclusion

In summary, we have reported a rare example of a phosphine as a halogen bond acceptor. To our knowledge, the (Ph_3P)·(*sym*-$C_6F_3I_3$) cocrystal is the first to be purposely engineered with the goal of forging a phosphorus-iodine halogen bond. That phosphines can act as halogen bond acceptors may open up new directions in crystal engineering and the design of materials, where it is well-known that non-covalent interactions play key roles in determining the final structures and their associated properties

4.5 References for Chapter 4

[1] Cavallo, G.; Metrangolo, P.; Milani, R.; Polati, T.; Priimagi, A.; Resnati, G.; Terraneo,G. *Chem. Rev.* **2016**, *116*, 2478–2601.

[2] Oliveira, V.; Kraka, E.; Cremer, D. *Phys. Chem. Chem. Phys.* **2016**, *18*, 33031–33046.

[3] Núñez, R.; Farràs, P.; Teixidor, F.; Viñas, C.; Sillanpää, R.; Kivekäs, R. *Angew. Chem., Int. Ed.* **2006**, *45*, 1270–1272.

[4] Frisch, M. J.; et al. Gaussian 09, Revision A.02; Gaussian Inc.: Wallingford, CT, 2009.

[5] Dennington, R.; Keith, T.; Milliam, J. GaussView, Version 4.1; Semichem Inc.: Shawnee Mission, KS, 2007

[6] APEX 2, Bruker AXS Inc.: Madison, Wisconsin, USA, 2012.

[7] Sheldrick, G. M. SADABS, Program for empirical X-ray absorption correction, Bruker AXS Inc.: Madison, Wisconsin, USA, 2004.

[8] Sheldrick, G. M. *Acta Crystallogr. C* **2015**, *71*, 3–8.

[9] Farrugia, L. J. *J. Appl. Crystallogr.* **1999,** *32*, 837–838.

[10] Alvarez, S. *Dalton Trans.* **2013**, *42*, 8617–8636.

[11] Dance, I.; Scudder, M. *Chem. -Eur. J.* **1996**, *2*, 481–486.

[12] Viger-Gravel, J.; Meyer, J. E.; Korobkov, I.; Bryce, D. L. *CrystEngComm* **2014**, *16*, 7285–7297.

[13] Xu, Y.; Viger-Gravel, J.; Korobkov I.; Bryce, D. L. *J. Phys. Chem. C* **2015**, *119*, 27104–27117.

[14] Xu, Y.; Champion, L.; Gabidullin, B.; Bryce, D. L. *Chem Commun.* **2017**, *53*, 9930–9933.

[15] Power, W. P. *J. Am. Chem. Soc.* **1995**, *117*, 1800–1806.

[16] Bemi, L.; Clark, H. C.; Davies, J. A.; Fyfe, C. A.; Wasylishen, R. E. *J. Am. Chem. Soc.* **1982**, *104*, 438–445.

PART 3 SINGLE-CRYSTAL NMR

Chapter 5. Single-Crystal NMR Characterization of Halogen Bonds

5.1 Introduction

In Part 2, the investigation of polycrystalline halogen-bonded cocrystals has been characterized using conventional polycrystalline solid-state NMR experiments. This type of investigation of polycrystalline halogen-bonded cocrystals has been a subject of interest in our laboratory, where we have been applying multinuclear magnetic resonance experiments under both magic angle spinning (MAS) and static conditions. These studies have provided insights into the correlation between several NMR observables (chemical shift tensors,[1,2] quadrupolar coupling constants, [2,3,4] and *J* coupling[5,6]) and the molecular and electronic structures of the halogen-bonded compounds. However, the conventional powder methods used to date are generally only able to determine, at best, relative orientations between NMR interaction tensors, but provide no information about the absolute orientation of each tensor in the molecular frame. As mentioned in Section 2.4., single-crystal NMR can yield both the magnitude of the NMR interaction tensors and their orientation in the molecular frame, which can provide insights into the correlations between the magnitude and orientation of various NMR interaction tensors and the local geometry of the halogen bond. Over several decades, single-crystal NMR studies of *hydrogen* bonds have provided important insights into the relationship between proton CS tensors and the hydrogen bond geometry.[7,8] However, to date there have been no comparable single-crystal NMR studies of halogen bonds. Legon and co-workers have, however, reported extensively on the magnitude and orientation of nuclear quadrupolar coupling tensors in halogen-bonded systems (and related weakly interacting systems) in the gas phase using high-resolution microwave spectroscopy.[9,10,11]

Here, we report the first single-crystal NMR investigations of halogen bonds. As the spectral breadths associated with the halogen atoms themselves (*i.e.*, iodine in the present work) are prohibitively broad to be studied via this approach, we examine the ^{17}O and ^{31}P isotopes in a series of P=O···I halogen bonds, wherein oxygen is the electron donor and phosphorus is a remote probe nucleus. Single-crystal ^{17}O and ^{31}P NMR studies of triphenylphosphine oxide ($Ph_3P^{17}O$) provide the ^{17}O intermediate quadrupolar coupling tensor, the ^{17}O and ^{31}P CSA tensors, and ^{17}O-^{31}P spin-spin coupling tensor relative to the molecular frame. Subsequently, these same tensors are investigated in a series of three halogen-bonded cocrystals with two different iodoperfluorobenzene derivatives as the XB donors: 1,4-diiodotetrafluorobenzene (*p*-$C_6F_4I_2$) and 1,3,5-trifluoro-2,4,6-triiodobenzene (*sym*-$C_6F_3I_3$). The cocrystals, shown in Figure 5.1.1, consist of (Ph_3PO)(*p*-$C_6F_4I_2$) (**1**), (Ph_3PO)(*sym*-$C_6F_3I_3$) (**2**) and the solvate (Ph_3PO)(*sym*-$C_6F_3I_3$)(CH_3CN) (**2·ACN**). Some of these compounds have been characterized using MAS and stationary ^{31}P and ^{17}O SSNMR methods, reported in Chapter 3. The present work aims to investigate in particular the changes in NMR tensor *orientations* as a result of halogen bonding, thereby providing a novel connection between the electronic structure and the XB interaction. Gauge-including project-augmented wave density functional theory (GIPAW DFT) computations of the relevant NMR interaction tensors are also employed to further investigate the relationships between the tensor orientations and the local XB geometry.

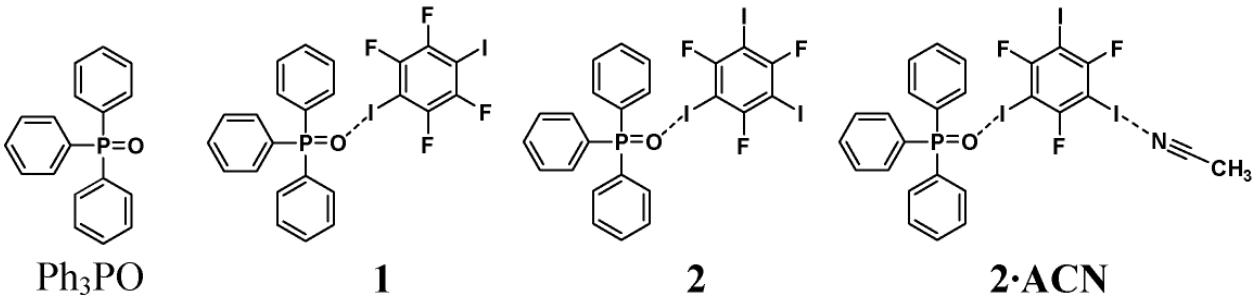

Figure 5.1.1. Chemical structures of compounds under investigation: triphenylphosphine oxide (Ph_3PO) and its halogen-bonded cocrystals, (Ph_3PO)(*p*-$C_6F_4I_2$) (**1**), (Ph_3PO)(*sym*-$C_6F_3I_3$) (**2**), and solvate (Ph_3PO)(*sym*-$C_6F_3I_3$)(ACN) (**2·ACN**).

5.2 Experimental Section

5.2.1 Crystal Preparation

The synthesis of ^{17}O-labeled triphenylphosphine oxide ($Ph_3P^{17}O$) was carried out using 41.4% ^{17}O-enriched H_2O (Cortecnet) and triphenylphosphine (Sigma Aldrich) as described in the literature.[12] *p*-$C_6F_4I_2$ was purchased from Sigma Aldrich and *sym*-$C_6F_3I_3$ was purchased from Alfa Aesar. The single crystal of $Ph_3P^{17}O$ used in this experiment was obtained by recrystallization from acetone to form a monoclinic polymorph. ^{17}O-labeled halogen-bonded cocrystals were prepared by slow evaporation of a mixture of the halogen bond acceptor ($Ph_3P^{17}O$) and two different halogen bond donors (*p*-$C_6F_4I_2$ and *sym*-$C_6F_3I_3$) at equal molar ratios, which were dissolved in a minimum amount of acetonitrile. The solution was allowed to slowly evaporate over 2-3 weeks at room temperature in order to form a single crystal with dimensions of about 3 mm × 4 mm × 4 mm. These crystals were washed with cold solvent (acetone for $Ph_3P^{17}O$ and acetonitrile for halogen-bonded

cocrystals) to remove any impurities present on the surface. All crystals were individually coated with epoxy glue and mounted on three-sided alumina half-cubes with axes 4 mm in length. The axes normal to the solid faces of this crystal holder were labeled X, Y, Z in a right-handed fashion. This axis system is referred to as the "cube frame" (see Figure 2.4.1). The crystals were stored in a -4°C freezer to prevent degradation or desolvation. However, it was observed that the single crystal of $Ph_3P^{17}O$ was stable at room temperature for months.

5.2.2 Single-Crystal X-Ray Diffraction

The orientation of the cube axes with respect to the crystallographic axes was determined using a Bruker AXS single crystal diffractometer equipped with a four-circle goniometer with Kappa geometry. The data were collected on a Bruker AXS diffractometer equipped with Mo Kα radiation (wavelength of λ = 0.71073 Å) with an APEX II CCD detector. The crystal-cube was inserted in a crystallographic goniometer and the cube axes were aligned with the φ system where all the instrument angles were set to zero.[13] The crystals were indexed ($Ph_3P^{17}O$: a = 11.0784 Å, b = 8.8359 Å, c =16.2718 Å, $\alpha = \gamma$ = 90°, β = 107.9829°; **1**: a= 9.0569 Å, b = 25.1012 Å, c =13.7353 Å, $\alpha = \gamma$ = 90°, β = 105.2685°; **2**: a= 9.7968 Å, b = 10.9310 Å, c =13.8269 Å, α = 113.6507°, β = 97.1651°, γ = 106.6354°) to confirm agreement with the space group and unit cell constants in the originally reported crystal structures.[5] The orientation matrix which relates the φ-axis system to the crystal Cartesian system can be used to determine the orientation of the cube axes relative to the crystal Cartesian system.

5.2.3 Single-Crystal NMR Spectroscopy

A Bruker Avance III console was used to acquire NMR data at the University of Ottawa with an applied external magnetic field of 9.4 T. A static high-power broadband goniometer probe system (HPBBON) with goniometer display assembly H121227 from Bruker was employed for all single-crystal NMR experiments. A photograph of the probe head is shown in Figure 2.4.1(a). A brass bevel gear in the bottom casing is used for mechanical transmission to the driving axis through the probe. A digital optical sensor angle indicator display unit was used to show the rotation angle. The cube with the crystal was mounted on a goniometer in the probe and rotated manually around an axis perpendicular to the magnetic field. Rotations about the three orthogonal cube axes X, Y, and Z were performed from 0° to 180° in 9° intervals. A positive rotation about the X axis will take the Y axis to the Z axis; a positive rotation about the Y axis will take the Z axis to the X axis; and a positive axis about the Z axis will take the X axis into the Y axis. This is the so-called right-handed coordinate system.[14] Spectra were acquired at room temperature except for those of cocrystals **2** and **2·ACN**, which were obtained at 5 ℃ due to their degradation at room temperature. To fit the spectral frequencies obtained from each rotation of the crystal, we have developed single-crystal NMR analysis software, which provides a non-linear least square fit of Eq 2.4.8 to obtain 11 parameters using Python's LMFIT[15]module. This software will be described in the next Chapter.

The single-crystal ^{31}P NMR spectra of all compounds were acquired at 9.4 T ($\nu_L(^{31}P)$ = 161.976 MHz) using a standard $^{1}H \rightarrow {}^{31}P$ cross-polarization (CP) pulse sequence. The chemical shifts were referenced to H_3PO_4 85% in H_2O (δ_{iso} = 0 ppm). The $\pi/2$ pulse length was optimized to be 4.1 to 6.3 μs using ammonium dihydrogen phosphate (δ_{iso} =

0.81 ppm with respect to 85% H_3PO_4). The CP contact time varied from 1000 to 3500 μs and the recycle delay varied from 2 min to 10 min. The total number of transients was 4 for each spectrum.

The ^{17}O single-crystal NMR spectra of all the ^{17}O-labeled compounds were acquired at 9.4 T ($\nu_L(^{17}O)$ = 54.243 MHz). The chemical shifts were referenced to distilled water (δ_{iso} = 0 ppm). The CT selective pulse length was 2.9 μs. Double frequency sweeps (DFSs)[16,17] from ±15 kHz to ±1500 kHz were applied prior to a selective π/2 pulse, and the two-pulse phase modulation (tppm)[18] decoupling scheme was applied during acquisition. Any potential for nonuniform excitation is not of major concern in the present work as we are interested in resonance frequencies rather than quantitative intensities. The number of transients acquired ranged from 8 to 128 for each spectrum, and the recycle delays ranged from 15 s to 20 s.

5.2.4 Density Functional Theory Calculations

The ^{31}P and ^{17}O magnetic shielding tensors and ^{17}O EFG tensors were calculated with Materials Studio and CASTEP[19] software (version 4.4) using periodic boundary conditions and the gauge-including projector-augmented wave density functional theory (GIPAW DFT) method.[20,21] The input file generated from Materials Studio used "ultra-soft" pseudopotentials to perform geometry optimization of the hydrogen positions. Unit cells were fixed according to the experimental SCXRD data. The cutoff energy and *k*-point grids were determined after performing a set of convergence tests. The energy cutoff was 380 eV for all compounds except for **2·ACN** (260 eV), and *k*-point grids used were 3×4×2 for Ph_3PO, 3×1×2 for **1**, 3×3×2 for **2** and 3×3×2 for **2·ACN**. Coordinate output files

including tensor orientations were generated from EFGShield[22] and displayed using Diamond 4.5.2 software.

5.3 Results and Discussion

5.3.1 X-Ray Diffraction

The local halogen bond environments of **1** and **2** have been previously described,[5] while compound **2·ACN** is a new structure featuring an acetonitrile solvent molecule. Several selected intermolecular contact distances and angles that are used to characterize the XB interaction and its geometry are summarized in Table 5.3.1, *i.e.*, the halogen bond length ($d_{I\cdots O}$ and $d_{I\cdots N}$ (the distance between I and N in the acetonitrile molecule)), the carbon-iodine bond length ($d_{I\text{-}C}$), the phosphorus-oxygen bond length ($d_{P=O}$), the O···I-C angle ($\theta_{O\cdots I\text{-}C}$), the N···I-C angle ($\theta_{N\cdots I\text{-}C}$), the P=O···I angle ($\theta_{P=O\cdots I}$), and R_{XB} parameter.

Table 5.3.1. Local XB Geometrical Information from Single-Crystal X-Ray Diffraction for **2·ACN**

#O[a]	$d_{I\cdots O}$ / Å	$d_{I\text{-}C}$ / Å	$d_{P=O}$ / Å	R_{XB}[b]	$\theta_{O\cdots I\text{-}C}$ / °	$\theta_{P=O\cdots I}$ / °	$d_{I\cdots N}$ / Å	$\theta_{N\cdots I\text{-}C}$ / °
O1	2.809(4)	2.087(7)	1.476(5)	0.794	175.7(2)	147.9(2)	3.059(9)	173.1(2)
O2	2.878(4)	2.094(7)	1.488(5)	0.813	176.4(2)	144.6(2)	3.08(1)	173.1(2)
O3	2.743(4)	2.080(6)	1.484(6)	0.775	176.0(2)	145.2(2)	3.066(8)	175.6(2)

[a] There are three crystallographically distinct triphenylphosphine oxide molecules in the unit cell. The oxygen atoms are labeled and shown in Figure 5.3.1.

[b] R_{XB} is the normalized distance parameter, $R_{XB} = d_{I\cdots O} / \sum d_{VDW}$, where $d_{I\cdots O}$ is the distance between the oxygen and iodine and $\sum d_{VDW}$ is the sum of their van der Waals radii (1.50 Å for O and 2.04 Å for I).[23]

Compound **2·ACN** crystallizes in the triclinic crystal system and $P\bar{1}$ space group. As shown in the inset in Figure 5.3.1, there are three crystallographically distinct Ph_3PO molecules involved in XB interactions with *sym*-$C_6F_3I_3$, labeled as **2·ACN_1**, **2·ACN_2** and **2·ACN_3**. The corresponding oxygen atoms involved are labeled as labeled as O1, O2, and O3. The unit cell is shown in Figure C1 in the Appendix C. **2·ACN_1** and **2·ACN_3** share similar environments while **2·ACN_2** is oriented in the opposite direction in the cell. They interact with three *sym*-$C_6F_3I_3$ molecules with different I···O distances of 2.809 (4) Å, 2.878 (4) Å, 2.743 (4) Å and O···I–C angles of 175.7 (2)°, 176.4 (2)°, and 176.0 (2)°, respectively. Another iodine atom in each *sym*-$C_6F_3I_3$ molecule acts as both the halogen bond donor and halogen bond acceptor. The σ–hole region forms a halogen bond with the nitrogen atom of the acetonitrile molecule (see orange dashed line). The side region of the iodine, where a belt of negative electrostatic potential around the iodine central region is found,[24] acts as a halogen bond acceptor and interacts with an adjacent *sym*-$C_6F_3I_3$ molecule (see cyan dashed line), which generates a chain of *sym*-$C_6F_3I_3$ moieties with I···I contact distances ranging from 3.8270 (8) to 3.8923 (8) Å and nearly linear I···I–C angles (161.0 (2)° – 163.7 (2)°). Oxygen acts as a bifurcated acceptor of both hydrogen bonds and halogen bonds. The formation of a weak hydrogen bond between two Ph_3PO molecules allows different sheets to stack together. These hydrogen bonds show geometric features of weak hydrogen bonding interaction based on the information provided in previous report.[25]

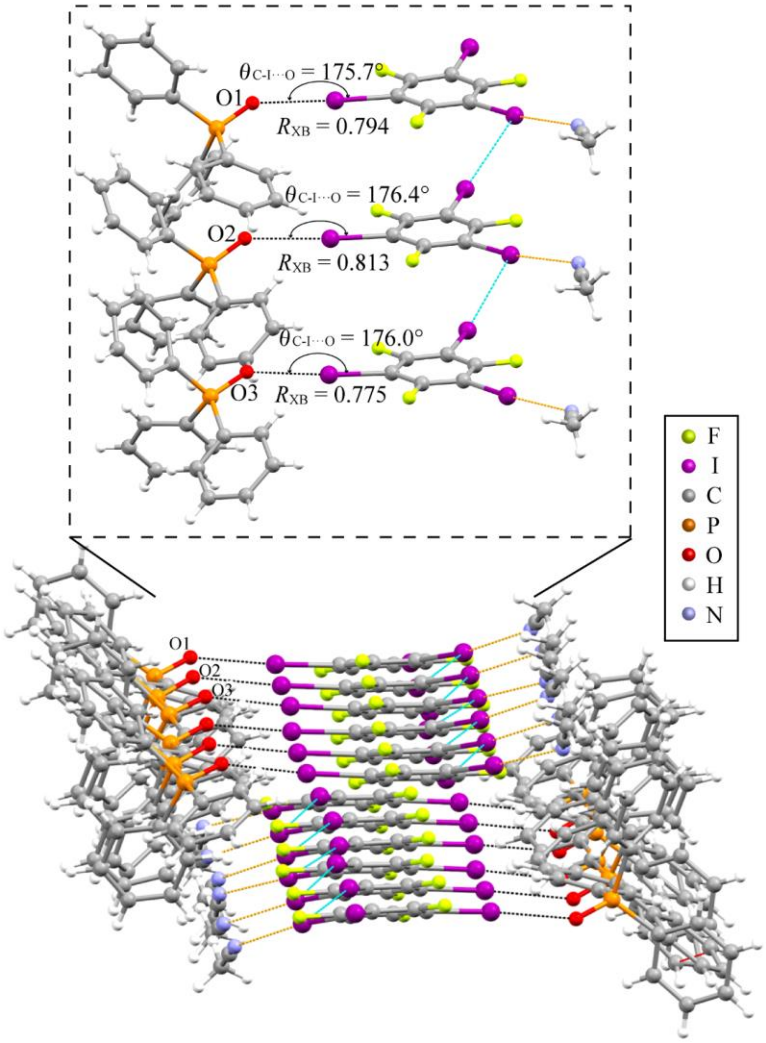

Figure 5.3.1. Halogen bond geometry in cocrystal **2·ACN** from single-crystal X-ray diffraction. Shown in the inset is a magnification of the three crystallographic distinct sites with site labels and corresponding XB geometrical information.

5.3.2 Analysis of ^{31}P Single-Crystal NMR Spectra

a) Magnitudes

The single-crystal ^{31}P NMR spectra of $Ph_3P^{17}O$ resulting from the rotation about the X, Y, and Z axes are shown in Figure C2. The corresponding single-crystal ^{31}P NMR spectra of the halogen-bonded cocrystals are provided in Figure 5.3.2. Because NMR interactions are insensitive to rotation about the magnetic field direction,[26] the spectrum for a crystal orientation of θ = 90° about the X axis is identical to the spectrum for θ = 0° about the Y axis; the spectrum for crystal orientation at θ = 90° about the Y axis is identical to the spectrum for θ = 0° about the Z axis; the spectrum for crystal orientation at θ = 90° about the Z axis is identical to the spectrum for θ = 0° about the X axis. This was used to determine the zero point for each rotation, and provides a check of internal consistency of the data. As shown in Figure C4, the unit cells of $Ph_3P^{17}O$ and of **1** each contain four crystallographically equivalent phosphorus nuclei. Each pair related by a *c* glide plane is magnetically non-equivalent. However, the remaining two pairs of ^{31}P nuclei are magnetically equivalent because of the presence of an inversion center. Therefore, in general, peaks from two magnetically distinct sites are observed. However, for the triclinic unit cell of **2**, because of an inversion center, there are two magnetically equivalent ^{31}P nuclei. Consequently, for a general orientation of a single crystal of **2** in an external magnetic field, only one ^{31}P NMR peak is observed. There are three crystallographically distinct phosphorus sites present in **2·ACN**, resulting in principle in three distinct ^{31}P NMR peaks observed during the rotation. However, due to the similarity of the XB environments in which these three ^{31}P nuclei are found, the three ^{31}P NMR peaks were found to often overlap. Weak ^{31}P satellite peaks are due to ^{31}P-^{17}O spin-spin coupling (Figure C2). The

magnitudes of the coupling constants estimated here are consistent with the values measured using ^{17}O single-crystal NMR (*vide infra*) and from MAS NMR studies of related systems.[5]

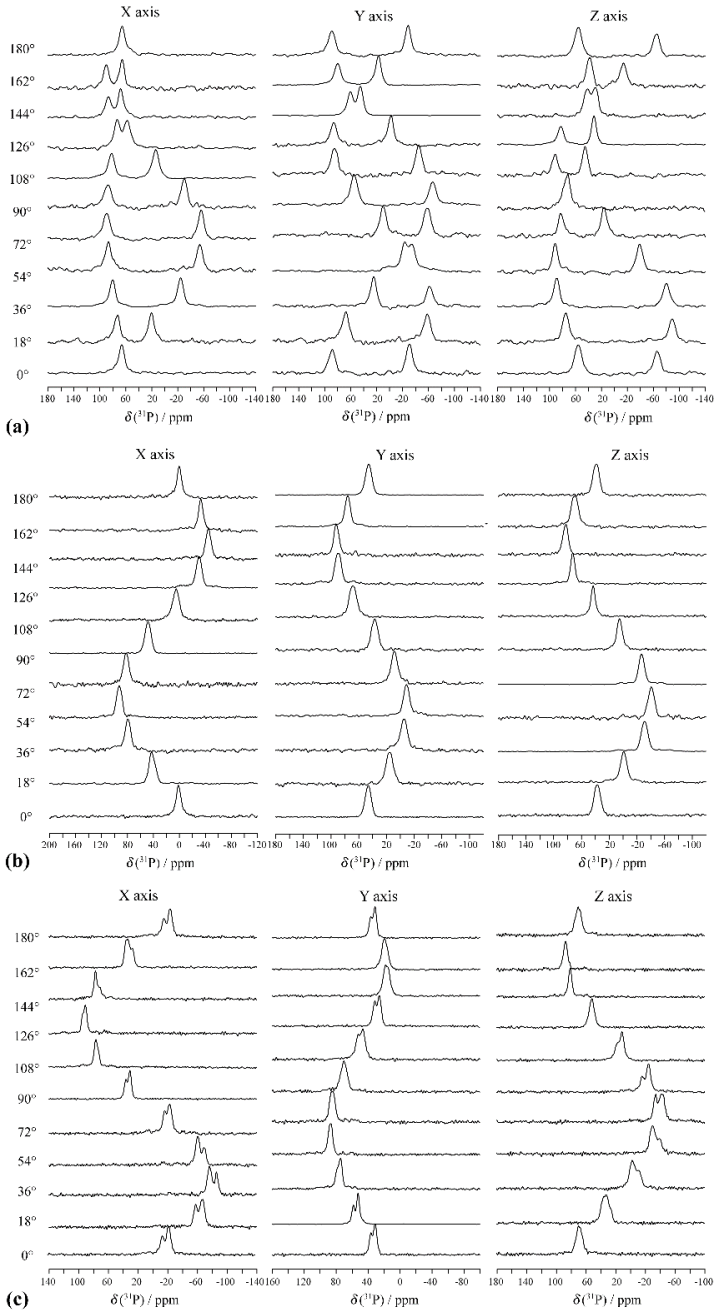

Figure 5.3.2. Single-crystal ^{31}P NMR spectra (B_0 = 9.4 T) for **1** (a), **2** (b) and **2·ACN** (c). Spectra were obtained following rotations in 9°increments about the X, Y, and Z axes. Here, only every second spectrum is shown.

The variation in resonance frequency of the uncoupled ^{31}P NMR peak with orientation of the single crystal in the external magnetic field is solely a function of the anisotropic phosphorus magnetic shielding interaction. Therefore, monitoring the resonance frequency during rotations about the three orthogonal cube axes perpendicular to the external magnetic field can be used to determine the phosphorus CS tensors. Figure 5.3.3 displays the rotation plots about the each of the three orthogonal cube axes (X, Y, Z) of the ^{31}P resonance frequency for $Ph_3P^{17}O$ and three halogen-bonded cocrystals. They are fit using only the CS part of Eq 2.4.8. The solid lines in Figure 5.3.3 correspond to the best-fit values generated from optimized parameters. As explained in the section 2.4, these parameters can be used to build a matrix which is then diagonalized to produce the eigenvalues, which are the three principal components of the ^{31}P CS tensors, and the eigenvectors, which are the direction cosines with respect to the cube axes.

The magnitudes of the ^{31}P CS tensors agree with what was obtained from powdered samples[5] (see Table 5.3.2). As explained previously, the most shielded component δ_{33} increases (the magnitude decreases) and the most deshielded component δ_{11} decreases upon halogen bonding, leading to slightly smaller span values (from 186(1) to 197(8) ppm) in the cocrystals compared to the starting material (Ω = 198(1) ppm). The isotropic CSs (from 26.7(4) to 30.2(2) ppm) are larger in the halogen-bonded cocrystals compared to $Ph_3P^{17}O$ (δ_{iso} = 26.2(3) ppm). As phosphorus is only indirectly involved in the XB interaction, the effect of the I···O halogen bond is expected to be small and may not even be the main contribution to the changes of the ^{31}P NMR tensors. For instance, it has been found[27] that bond angles and geometry have a significant impact on ^{31}P CSs and phosphine-chalcogen bond energy. The principal components were plotted as a function of the main angles

associated with the XB: $\theta_{P=O\cdots I}$ and $\theta_{O\cdots I-C}$. No correlation was observed with $\theta_{O\cdots I-C}$; the plot as a function of the halogen bond angle $\theta_{P=O\cdots I}$ is presented in Figure 5.3.4(a). The plot indicates that there is a slight increase in the value of the intermediate δ_{22} component (82.5(7) ppm to 89.1(7) ppm) when $\theta_{P=O\cdots I}$ becomes more linear (R^2 = 0.8796). This indicates that the magnitude of the ^{31}P chemical shift tensor correlates more strongly to the halogen bond angle than to its distance.

Table 5.3.2. Experimental ^{31}P Chemical Shift Tensors Obtained from ^{31}P Single-Crystal SSNMR Experiments

compound	#P	δ_{iso} / ppm	Ω / ppm	κ / ppm
Ph_3PO		26.2(3)	198(1)	0.86(1)
1		30.2(2)	186(1)	0.95(1)
2[a]		28.9(3)	188(1)	0.85(1)
2·ACN[a]	1/3[b]	28.2(1)	186(3)	0.93(1)
	2	26.7(4)	197(8)	0.93(1)
	3/1[b]	27.1(1)	189(3)	0.95(1)

[a] Compounds **2** and **2·ACN** cannot provide error values generated from comparison between two crystallographic equivalent but magnetically distinct sites like Ph_3PO and **1**. Uncertainties from single-crystal NMR data fitting are only on the order of 0.1 ppm. Therefore, we estimate the error to be similar to the largest error present in analysis of Ph_3PO and **1**.

[b] The two sites are unable to be distinguished due to peak overlap.

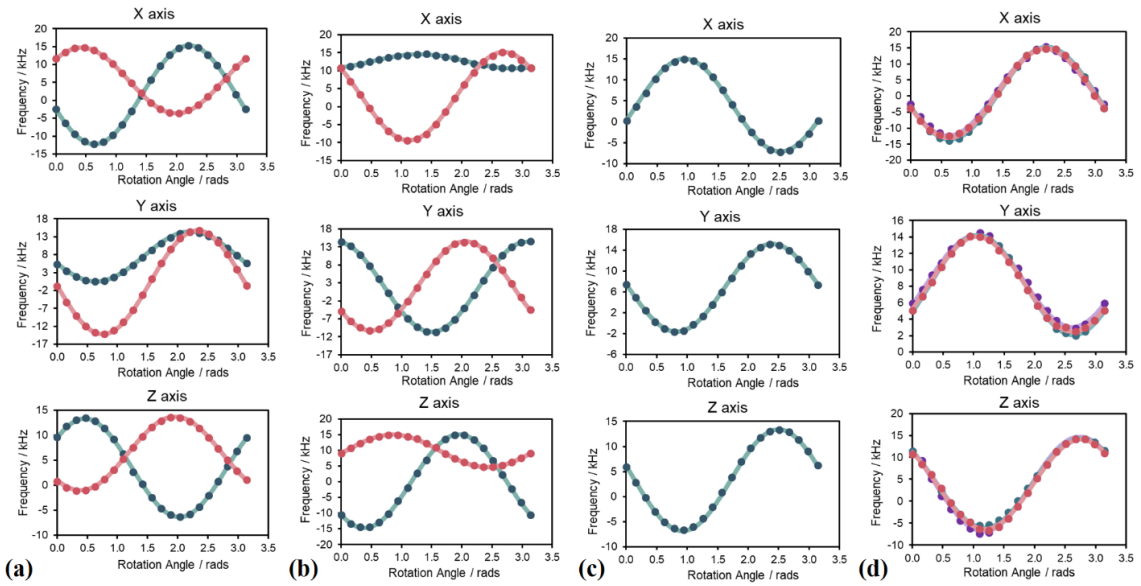

Figure 5.3.3. Rotation plots displaying the variation in the ^{31}P NMR frequency for rotations about the cube X, Y, Z axes for the starting material $Ph_3P^{17}O$ (a), and its halogen-bonded cocrystals: **1** (b), **2** (c), and **2·ACN** (d). $Ph_3P^{17}O$ and 1 have two magnetically non-equivalent sites shown in dark green and pink. **2·ACN** has three crystallographically distinct site shown in dark green, pink and purple. The solid lines correspond to the best-fit values generated from optimized parameters.

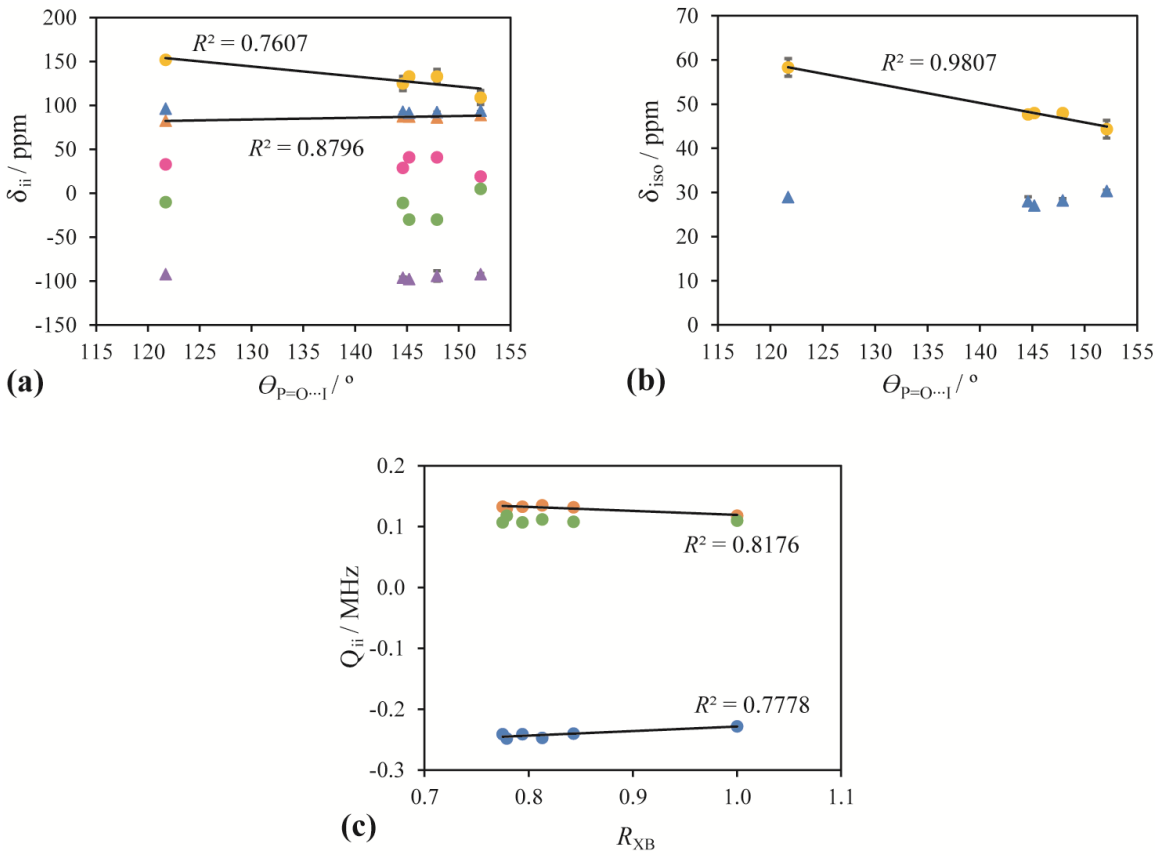

Figure 5.3.4. (a) Plot of three principal components of ^{31}P (triangles) and ^{17}O (circles) CS tensors vs $\theta_{P=O\cdots I}$. δ_{11}, δ_{22}, and δ_{33} of ^{31}P CS tensors are shown in blue, orange, and purple respectively. δ_{11}, δ_{22}, and δ_{33} of ^{17}O CS tensors are shown in yellow, magenta and green, respectively. (b) Plot of δ_{iso} values for ^{31}P (blue triangles) and ^{17}O (yellow circles) vs $\theta_{P=O\cdots I}$. (c) Plot of the three principal components of ^{17}O intermediate quadrupolar coupling tensors: Q_{11} (green), Q_{22} (orange), Q_{33} (blue) vs R_{XB} values. Lines represent the best linear fits: (a) $\delta_{11}(^{17}O) = -1.1407\theta_{P=O\cdots I} + 292.72$ and $\delta_{22}(^{31}P) = 0.1941\theta_{P=O\cdots I} + 58.844$; (b) $\delta_{iso}(^{17}O) = -0.4414\theta_{P=O\cdots I} + 112.07$; (c) $Q_{33}(^{17}O) = 0.0740R_{XB} - 0.3026$ and $Q_{22}(^{17}O) = -0.0657R_{XB} + 0.1849$.

b) Orientations

The measurement of the orientation of the unit cell with respect to the three orthogonal cube axes by SCXRD enables the measurement of the orientation of the principal components of the NMR tensors in the molecular frame. However, the assignment of each NMR-detected site to each crystallographic site remains ambiguous. Fortunately, under the assumption that the pseudo-unique component of ^{31}P CS tensors (δ_{33}) should be roughly along the P=O bond due to approximate local C_{3v} symmetry,[12] this ambiguity can be resolved. GIPAW DFT calculations further confirm the assignments. Moreover, both $Ph_3P^{17}O$ and halogen-bonded cocrystal **1** have two crystallographically equivalent but magnetically distinct sites related by 2-fold rotation about the crystallographic *b* axis in the unit cell plus an *a* translation, which are indistinguishable by the NMR experiment. Therefore, the general NMR tensor matrices representing these two sites which are related by this symmetry are:[28]

$$(\delta \; or \; Q)_{\,site\;1} = \begin{bmatrix} a & b & c \\ d & e & f \\ g & h & i \end{bmatrix}, \quad (\delta \; or \; Q)_{site\;2} = \begin{bmatrix} a & -b & c \\ -d & e & -f \\ g & -h & i \end{bmatrix} \qquad \text{Eq 5.3.1}$$

This important symmetry information offers some redundancy which provides a built-in mechanism to estimate the error in the determination of the NMR tensor orientations. For **2·ACN**, there are three crystallographically distinct Ph_3PO molecules in the unit cell; however, two of the molecules (**2·ACN_1** and **2·ACN_3**) are oriented roughly parallel to each other, whereas the second molecule (**2·ACN_2**) is oriented antiparallel with respect to the crystallographic cell axis (see Figure C1). Therefore, similar NMR tensor orientations are expected for molecules **2·ACN_1** and **2·ACN_3** but a slightly different

orientation is plausible for molecule **2·ACN_2**, which provides a way to tentatively assign one of the NMR-detected sites to molecule **2·ACN_2**. Unfortunately, the error due to peak overlap hinders the ability to distinguish between molecules **2·ACN_1** and **2·ACN_3**. Therefore, the eigenvectors were applied to both sites and the difference between each set of results was used to estimate the error in the tensor orientations.

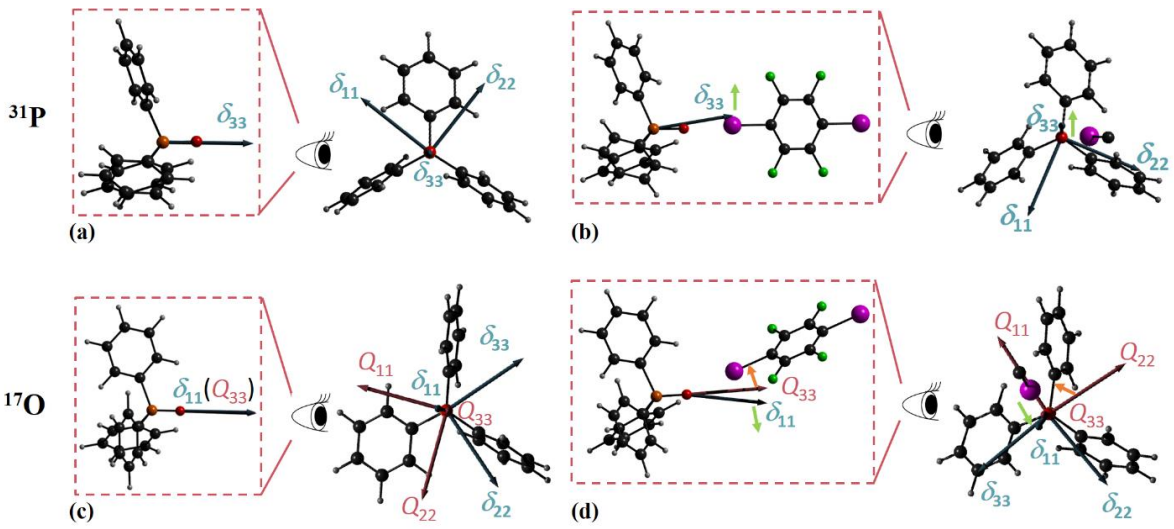

Figure 5.3.5. Projection of the crystal structure of the starting material $Ph_3P^{17}O$ (a, c) and its halogen-bonded cocrystals **1** (b, d) when P=O bond is perpendicular to the plane for illustration of the orientation of ^{31}P CS principal components (indicated as dark green vectors at the top) and ^{17}O CS (dark green vectors at the bottom) and intermediate quadrupolar coupling tensors (pink vectors at the bottom) in the molecular frame. The green and orange arrows indicate the direction of δ_{33} (^{31}P), δ_{11}(^{17}O), and Q_{33} movement, respectively, when XB interaction is involved. In (b, d), only iodine-carbon fragments are shown and the remaining part of the molecules are omitted to more clearly show the vectors. Shown in the insets is the projection of the structures when the P=O bond is within the plane to illustrate the change of the direction of all the vectors. The complete orientation of ^{31}P CS tensor and ^{17}O CS and intermediate quadrupolar coupling tensors for all the compounds are provided in Figure C5 and Figure C7.

Perspective drawings of the orientation of the ^{31}P CS tensors for $Ph_3P^{17}O$ and cocrystal **1** in the molecular frame are shown in Figure 5.3.5(a) and (b). The complete ^{31}P CS tensor orientations for all the compounds are provided in Figure C5 and the corresponding direction cosines are given in Table C2. Orientations obtained from GIPAW DFT calculations are shown in Figure C6. The most shielded component of the ^{31}P CS tensor for $Ph_3P^{17}O$ and the halogen-bonded cocrystals roughly aligns with the P=O bond. GIPAW DFT calculations suggest that δ_{33} deviates slightly from the direction of the P=O bond towards the iodine atom in the halogen-bonded systems. This small effect is not seen experimentally, possibly due to the size of the angular changes involved relative to the size of the experimental errors on the tensor orientations.

Table 5.3.3. Experimental Orientation and Calculated Orientation of the δ_{33}(^{31}P) Eigenvector with Respect to the P=O Bond and to the I···O Halogen Bond

compound	#P	#I[a]	experimental		DFT	
			$\theta_{\delta\cdots O\cdots I}$ / °	$\theta_{\delta\cdots P=O}$/ °	$\theta_{\delta\cdots I\cdots O}$ / °	$\theta_{\delta\cdots P=O}$/ °
Ph_3PO			---	2(3)	---	2.40
1			28.7(3)	3(2)	28.62	0.64
2		I1	58.2(3)	6(2)	55.63	2.97
		I2	57.5(3)	6(2)	61.26	2.97
2·ACN	P1		28.3(1)	3.9(4)	29.91	2.31
	P2		30.2(2)	5.4(5)	33.59	2.24
	P3		32.5(2)	3.4(5)	32.84	2.48

[a] In cocrystal **2,** the Ph_3PO acts as a bifurcated acceptor with two iodine donors which are labeled in Figure C5.

The experimentally measured angles between δ_{33} and the P=O bond ($\theta_{\delta\cdots P=O}$), and the angles between δ_{33} and the I···O halogen bond vector ($\theta_{\delta\cdots O\cdots I}$), are provided in Table 5.3.3. These angles are correlated as long as the δ_{33} eigenvector lies in the plane defined

by the three atoms, which is a good approximation in all cases. Correlations between these angles and (i) the reduced XB distance parameter, (ii) the O···I-C angle, and (iii) the halogen bond angle were explored. Shown in Figure 5.3.6(a) is the experimental correlation of $\theta_{\delta\cdots O\cdots I}$ with the halogen bond angle, $\theta_{P=O\cdots I}$ (blue triangles; linear fit: R^2 = 0.9627; exponential fit: R^2 = 0.9638); the trend is corroborated by GIPAW DFT calculations (orange triangles; linear fit: R^2 0.9957; exponential fit: R^2 = 0.9967). Both experimentally and theoretically, $\theta_{\delta\cdots O\cdots I}$ is observed to decrease as $\theta_{P=O\cdots I}$ approaches 180°. This provides a direct link between the phosphorus CS tensor orientation and the linearity of the halogen bond.

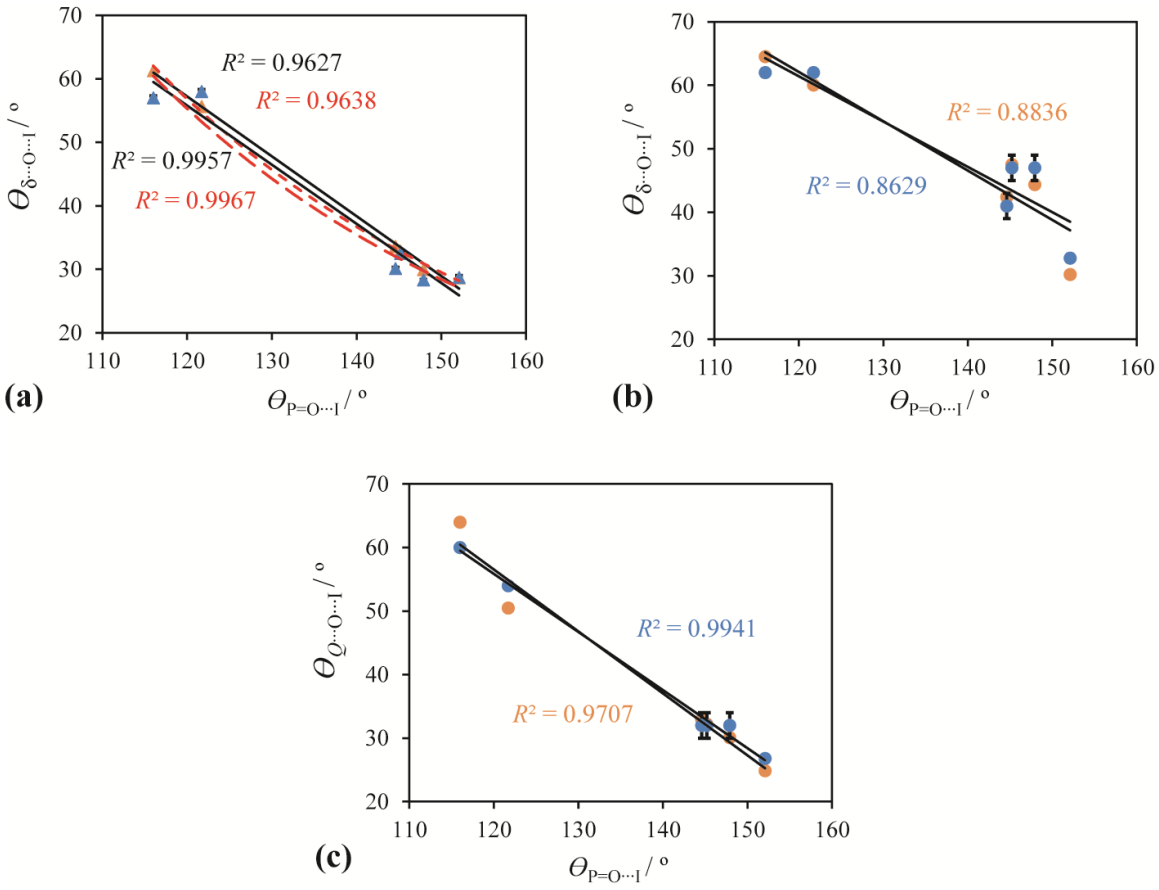

Figure 5.3.6. (a) Plot of the angle between the $\delta_{33}(^{31}P)$ eigenvector and the O···I halogen bond vector vs $\theta_{P=O\cdots I}$. The solid black line corresponds to a linear fit and a dashed red line corresponds to an exponential fit. (b) Plot of the $\delta_{11}(^{17}O)$-O···I angle vs $\theta_{P=O\cdots I}$. (c) Plot of the $Q_{33}(^{17}O)$-O···I angle vs $\theta_{P=O\cdots I}$. The experimental data are shown in blue and DFT data are shown in orange. Lines represent the best fits: (a) experimental: $\theta_{\delta(^{31}P)\cdots O\cdots I}$ = -0.9304 $\theta_{P=O\cdots I}$ + 167.41 or $\theta_{\delta(^{31}P)\cdots O\cdots I}$ = 794.96 $e^{-0.022\theta_{P=O\cdots I}}$ and calculated: $\theta_{\delta(^{31}P)\cdots O\cdots I}$ = -0.9428 $\theta_{P=O\cdots I}$ + 170.33 or $\theta_{\delta(^{31}P)\cdots O\cdots I}$ = 781.64 $e^{-0.022\theta_{P=O\cdots I}}$; (b) experimental: $\theta_{\delta(^{17}O)\cdots O\cdots I}$ = -0.7124$\theta_{P=O\cdots I}$ + 146.89 and calculated: $\theta_{\delta(^{17}O)\cdots O\cdots I}$ = -0.7759$\theta_{P=O\cdots I}$ + 155.19; (c) experimental: $\theta_{Q(^{17}O)\cdots O\cdots I}$ = -0.9145$\theta_{P=O\cdots I}$ + 165.59 and calculated: $\theta_{Q(^{17}O)\cdots O\cdots I}$ = -0.9752$\theta_{P=O\cdots I}$ + 173.59.

5.3.3 Analysis of ^{17}O Single-Crystal NMR Spectra

Compared to ^{31}P NMR spectroscopy, ^{17}O NMR may provide more conclusive insights into the relationship between NMR properties and halogen bonding because oxygen is directly participating in the halogen bond. Because of the low natural abundance of 0.038% and the nuclear quadrupolar interaction (spin-5/2), it is significantly more challenging to acquire and interpret the ^{17}O NMR data. Despite ^{17}O isotopic enrichment, the loss of magnetization in the unused satellite transitions (ST) can lead to prohibitively long experiment times, requiring signal enhancement.[29] Consequently, we applied double frequency sweeps (DFS)[16,17], whereby a smooth amplitude-modulated pulse is employed to sweep both the high- and low-frequency STs toward the CT in a symmetric manner. The enhancement of the CT reduced the experimental time for each spectrum from 16 min to 2 min for $Ph_3P^{17}O$ and 2 h to 20 min for the ^{17}O-enriched halogen-bonded cocrystals.

The single-crystal ^{17}O NMR spectra of $Ph_3P^{17}O$ resulting from rotation about the X, Y, and Z axes are shown in Figure C3 in Appendix C. The single-crystal ^{17}O NMR spectra of **1**, **2**, and **2·ACN** are provided in Figure 5.3.7. In general, resonances arising from two magnetically distinct oxygen sites are observed as explained above for ^{31}P. However, for each site, a total of two peaks are obtained due to the presence of spin-spin coupling between ^{17}O and 100% naturally abundant ^{31}P. Consequently, for a general orientation of a single crystal of $Ph_3P^{17}O$ or of **1** in an external magnetic field, four peaks are observed. For cocrystals **2** and **2·ACN**, a maximum of two and six peaks are observed for each orientation because of the presence of one and three crystallographically inequivalent $Ph_3P^{17}O$ molecules, respectively, in the unit cell and the presence of spin-spin coupling.

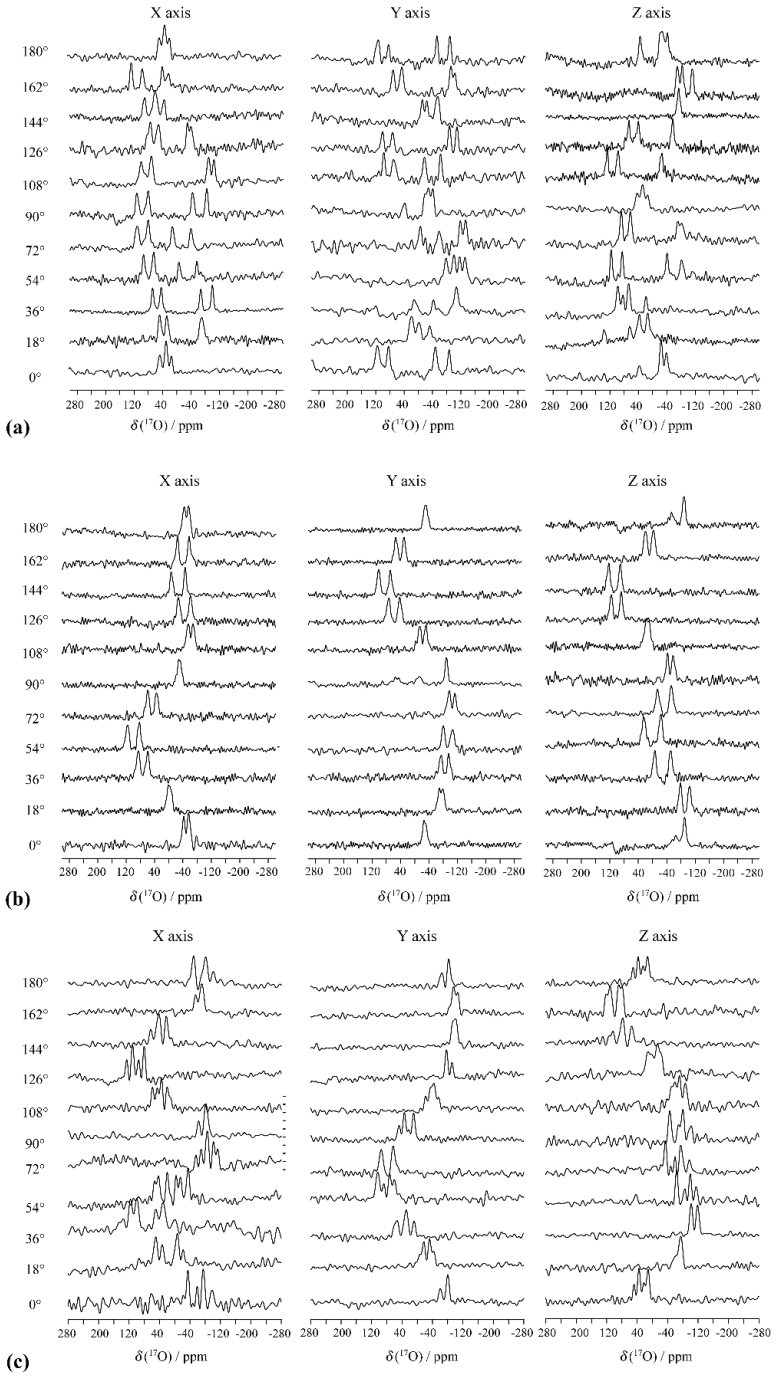

Figure 5.3.7. Single-crystal ^{17}O NMR spectra (B_0 = 9.4 T) for **1** (a), **2** (b), and **2·ACN** (c). Spectra were obtained following rotations in 9° increments about the X, Y, and Z axes. Here, only every second spectrum is shown.

The variation in the uncoupled resonance frequency is a function of the combined effect of the anisotropic ^{17}O CS and quadrupolar interactions. The analysis of coupling data is independent of the CS and quadrupolar interactions, where the anisotropy in the splittings can be analyzed to obtain the sum of the ^{17}O-^{31}P direct and indirect spin-spin coupling tensors as a function of the rotation angle. The details will be discussed in the following subsections.

a) Analysis of intermediate quadrupolar coupling and CS tensors

The frequency of the CT depends only on the CS and second-order quadrupolar interactions. The spin-spin coupling between ^{31}P and ^{17}O generates two peaks in the ^{17}O NMR spectrum with similar intensities. The dependence of the CT on the orientation of the crystal in the magnetic field can be used to determine the orientation of intermediate quadrupolar coupling tensors and CS tensor, which was first described by Volkoff.[30] In order to provide 11 parameters that fully describe the orientation dependence of the CS and intermediate quadrupolar coupling tensors, here we fit the average resonance frequency of two peaks with similar intensities as a function of rotation angle θ about each of the three axes (X, Y, Z). The fitting function is given in Eq 2.4.8. The data obtained from these three rotations for all the compounds as well as their best-fits are presented in Figure 5.3.8. From the 11 parameters, tensors corresponding to the ^{17}O intermediate quadrupolar coupling and CS were constructed with respect to the X, Y and Z axes of the cube. Diagonalization of these two tensor matrices again can provide the eigenvalues, which represent the magnitude of the principal components of the CS tensor and intermediate quadrupolar coupling tensor, and the eigenvectors, which provide the cosine values of the three components with respect to the cube axes. These data are tabulated in Table C3 and Table C4. In this way, the

complete CS tensor and intermediate quadrupolar coupling tensors are obtained. Tensor magnitudes are given in Table 5.3.4. The C_Q and η_Q values are consistent with the values obtained from NMR powder patterns.[5] Small deviations outside the experimental error bounds are noted for some elements of the CS tensors obtained from single-crystal NMR experiments versus those obtained from powder NMR experiments.

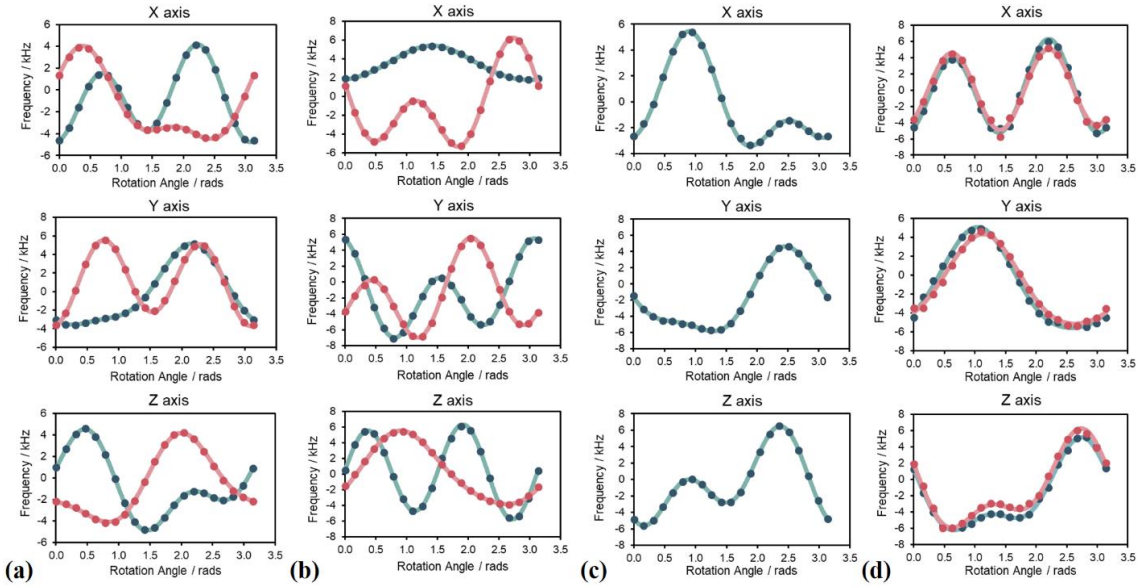

Figure 5.3.8. Rotation plots displaying the variation in the ^{17}O NMR frequency for rotations about the cube X, Y, Z axes for the starting material $Ph_3P^{17}O$ (a), and its halogen-bonded cocrystals: **1** (b), **2** (c), and **2·ACN** (d). $Ph_3P^{17}O$ and **1** have two magnetically non-equivalent sites shown in dark green and pink. **2·ACN** has three crystallographically distinct sites; however, only two of them were resolved due to the peak overlap and are shown in dark green and pink here. The solid lines correspond to the best-fit values generated from optimized parameters.

The three principal components of these two NMR tensors were plotted as a function of three characteristic XB geometrical features: R_{XB}, $\theta_{P=O\cdots I}$, and $\theta_{O\cdots I-C}$. No correlations to $\theta_{O\cdots I-C}$ were observed; the data related to R_{XB} and $\theta_{P=O\cdots I}$ are shown in Figure 5.3.4. The magnitude of the ^{17}O CS tensor has a stronger correlation with $\theta_{P=O\cdots I}$ whereas the intermediate quadrupolar coupling tensor magnitudes have a stronger correlation with the R_{XB} values. The largest component of the ^{17}O CS tensors, and δ_{iso}, decreases as the $\theta_{P=O\cdots I}$ increases. The magnitude of Q_{33} increases in the halogen-bonded cocrystals, ranging from 0.240(2) to 0.248(1) MHz, compared to pure triphenylphosphine oxide (0.228(2) MHz). This increase follows a linear trend (R^2 = 0.7778) with decreasing R_{XB} value, consistent with the increases in ^{17}O intermediate quadrupolar coupling constant observed in the presence of the XB interaction in related systems.[5] The Q_{11} values (0.110(3) MHz in $Ph_3P^{17}O$ and 0.107(3) MHz to 0.118(1) MHz in the cocrystals) do not appear to correlate with any geometrical feature of the halogen bond. However, Q_{22} increases slightly in magnitude, from 0.130(2) MHz to 0.133(2) MHz, resulting in less axially symmetric intermediate quadrupolar coupling tensors in the halogen-bonded systems (η_Q ranges from 0.05(1) to 0.10(1)).

Table 5.3.4. Experimental ^{17}O Chemical Shift Tensors and Electric Field Gradient Tensors Obtained from ^{17}O Single-Crystal NMR Experiments

compound	**#O**	**$\lvert C_Q \rvert$ / MHz**	**η_Q**	**δ_{iso} / ppm**	**Ω / ppm**	**κ**
Ph_3PO		4.57(5)	0.03(1)	52(2)	159(10)	-0.74(1)
1		4.96(2)	0.05(1)	44(1)	103(5)	-0.72(4)
2[a]		4.80(5)	0.10(1)	58(2)	162(10)	-0.48(1)
2·ACN[a]	O2	4.92(5)	0.09(1)	47(2)	136(10)	-0.45(1)
	O1/ O3[b]	4.83(5)	0.10(1)	48(2)	163(10)	-0.13(1)

[a] Compounds **2** and **2·ACN** cannot provide error values generated from comparison between two crystallographic equivalent but magnetically distinct sites like Ph_3PO and **1**. Uncertainties from single-crystal NMR data fitting are only on the order of 0.01 MHz for EFG tensors and 0.1 ppm for CS tensors. Therefore, we estimate the error to be similar to the largest error present in analysis of Ph_3PO and **1**.

[b] The two sites are unable to be distinguished due to peak overlap.

The orientations of ^{17}O intermediate quadrupolar coupling tensors and CS tensors in the molecular frame of reference are also obtained from the analysis of the single-crystal NMR data. The method used for the assignment of the ^{31}P CS tensors to different crystallographic sites holds here as well. The largest component of the EFG tensor at oxygen generally lies along the P=O bond. Figure 5.3.5(c) and (d) show the perspective drawings of the orientation of the ^{17}O intermediate quadrupolar coupling tensors (pink) and

CS tensors (dark green) for $Ph_3P^{17}O$ and cocrystal **1** in the molecular frame. The complete tensor orientations for all the compounds are provided in Figure C7 (direction cosines are given in Table C3 and Table C4). The orientations obtained from GIPAW DFT calculations are provided in Figure C8. For triphenylphosphine oxide, the experimental and the calculated results indicate that the most deshielded component of the ^{17}O CS tensor (δ_{11}) and the largest component of the ^{17}O intermediate quadrupolar coupling tensor (Q_{33}) lie along the P=O bond. The changes of the direction of δ_{11} and Q_{33} in the cocrystals compared to $Ph_3P^{17}O$ are indicated by green and orange arrows, respectively, in Figure 5.3.5. Changes in the δ_{11} direction (2° – 8°) are more significant than changes in the Q_{33} direction (0.6° – 3°) upon halogen bonding.

Furthermore, the angles between δ_{11} and Q_{33} and the P=O bond ($\theta_{\delta\cdots P=O}$ and $\theta_{Q\cdots P=O}$, respectively) and the angle between δ_{11} and Q_{33} and the I···O halogen bond ($\theta_{\delta\cdots O\cdots I}$ and $\theta_{Q\cdots O\cdots I}$, respectively) are measured and provided in Table 5.3.5. These two angles were plotted as a function of the three XB geometrical features: R_{XB}, $\theta_{P=O\cdots I}$ and $\theta_{O\cdots I-C}$. There is a lack of correlation between these two angles and R_{XB} and $\theta_{O\cdots I-C}$. Therefore, only the correlation with the halogen bond angle $\theta_{P=O\cdots I}$ is shown (see blue circles in Figure 5.3.6(b) and (c)). The calculated angles from GIPAW DFT are shown in orange circles. As shown in the figure, both experimentally and theoretically there are strong correlations. The $\theta_{\delta\cdots O\cdots I}$ angle decreases linearly as the halogen bond angle $\theta_{P=O\cdots I}$ approached linearity (R^2 = 0.8629 for the experimental data and R^2 = 0.8836 for GIPAW DFT data). The $\theta_{Q\cdots O\cdots I}$ angles are also correlated inversely with the halogen bond angles $\theta_{P=O\cdots I}$ (R^2 = 0.9941 for the experimental data and R^2 = 0.9707 for GIPAW DFT data).

These data establish a link between the ^{17}O NMR tensor orientations and the linearity of the halogen bond.

Table 5.3.5. Experimental Orientation and Calculated Orientation of $\delta_{11}(^{17}O)$ and $Q_{33}(^{17}O)$ with Respect to the P=O Bond and to the I···O Halogen Bond

compound	#O	#I[a]	Experimental				DFT			
			$\theta_{\delta\cdots I\cdots O}$ / °	$\theta_{\delta\cdots P=O}$/ °	$\theta_{Q\cdots I\cdots O}$ / °	$\theta_{Q\cdots P=O}$/ °	$\theta_{\delta\cdots I\cdots O}$ / °	$\theta_{\delta\cdots P=O}$/ °	$\theta_{V\cdots I\cdots O}$ / °	$\theta_{V\cdots P=O}$/ °
Ph_3PO			---	6.6(5)	---	1(1)		9.768		0.335
1			32.8(6)	8(2)	26.8(3)	1(2)	30.209	7.975	24.868	3.172
2		I1	62(6)	12(2)	54(3)	4(2)	60.032	11.861	50.487	3.020
		I2	62(6)	---	60(3)	---	64.508	---	63.993	---
2·ACN	O1		---	---	---	---	44.385	13.380	30.084	2.115
	O2		41(6)	6(2)	32(3)	4(2)	42.418	6.970	32.927	2.528
	O3		47(2)	14.7(4)	32 (2)	1.6(1)	47.542	13.529	32.205	2.602

[a] In cocrystal **2,** the Ph_3PO acts as a bifurcated acceptor with two iodine donors which are labeled in Figure C5 and Figure C7.

b) Analysis of spin-spin coupling tensors

As mentioned in the Section 2.4, the magnitude of the observed ^{31}P-^{17}O doublet splittings for each orientation of the single crystal in the external magnetic field is a function of both the direct and indirect spin-spin coupling interaction. The variations in the splittings as a function of the rotation angle about the three orthogonal cube axes are illustrated in Figure 5.3.9. Five parameters describe the orientation dependence of the traceless effective dipolar coupling tensor ($R_{\text{eff,xx}} + R_{\text{eff,yy}} + R_{\text{eff,zz}} = 0$), ignoring antisymmetry in **J**. From the 5 variables obtained from the fit, tensors corresponding to the effective dipolar coupling interaction were obtained, which were diagonalized to provide the principal components, $R_{\text{eff,11}}$, $R_{\text{eff,22}}$ and $R_{\text{eff,33}}$, and their corresponding orientations (see Figure C9 in the Appendix C). Expectedly, the largest component $R_{\text{eff,33}}$ is always aligned with the P=O bond in all samples and there is no significant change in the direction as a result of halogen bonding. This is consistent with a dominant contribution from direct dipolar coupling to R_{eff}.

By subtracting out the direct dipolar coupling from the effective dipolar coupling tensors (Eq 2.3.28: $R_{\text{eff}} = R_{\text{DD}} - \Delta J/3$), the three principal components of the traceless part of the ^{31}P-^{17}O tensors for $Ph_3P^{17}O$ and its halogen-bonded cocrystals were determined and provided in Table 5.3.6. This analysis assumes negligible librational averaging of the direct dipolar coupling. Upon halogen bonding to oxygen, there is a clear decrease in anisotropy of **J**, ranging from -325(30) to -281(65) Hz, and an increase in asymmetry of **J**, ranging from 0.43(13) to 0.47(13), compared to pure $Ph_3P^{17}O$ (ΔJ = -512(65) Hz and η_J = 0.15(4)).

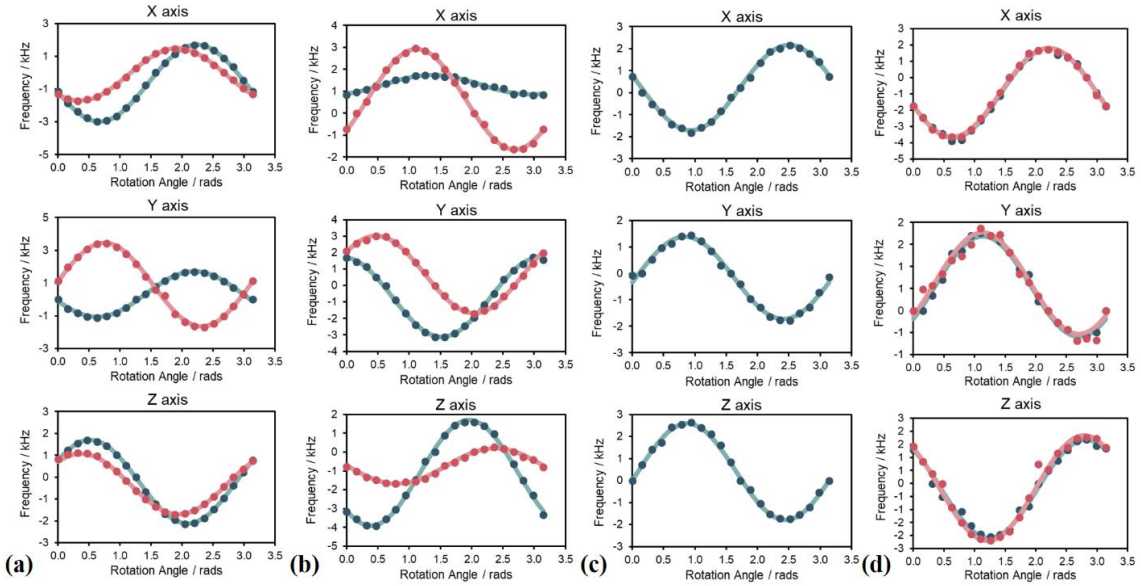

Figure 5.3.9. Rotation plots displaying the variation in the ^{17}O-^{31}P spin-spin coupling for rotations about the cube X, Y, Z axes for the starting material $Ph_3P^{17}O$ (a), and its halogen-bonded cocrystals: **1** (b), **2** (c), and **2·ACN** (d). $Ph_3P^{17}O$ and **1** have two magnetically non-equivalent sites shown in dark green and pink. **2·ACN** has three crystallographically distinct sites, however, only two of them were resolved because the peak overlap and the data are shown in dark green and pink. The solid lines correspond to the best-fit values generated from optimized parameters.

Table 5.3.6. Indirect ^{17}O-^{31}P Spin-Spin Coupling Tensors[a]

compound		components / Hz
	J_{iso}[b]	167(5)
	J_{33} - $\underline{J}_{iso}$	-341(42)
Ph_3PO	J_{22} - $\underline{J}_{iso}$	145(10)
	J_{11} - $\underline{J}_{iso}$	196(32)
	ΔJ	-512(65)
	η_J	0.15(4)
	J_{iso}[b]	179(8)
	J_{33} - $\underline{J}_{iso}$	-216(20)
1	J_{22} - $\underline{J}_{iso}$	62(33)
	J_{11} - $\underline{J}_{iso}$	155(11)
	ΔJ	-325(30)
	η_J	0.43(13)
	J_{iso}[b]	153(11)
	J_{33} - $\underline{J}_{iso}$	-187(42)
2[c]	J_{22} - $\underline{J}_{iso}$	49(33)
	J_{11} - $\underline{J}_{iso}$	138(32)
	ΔJ	-281(65)
	η_J	0.47(13)

[a] Obtained from the effective dipolar coupling tensor (provided in Table C5 in the Appendix C) by subtracting the direct dipolar coupling contribution, R_{DD}.

[b] Values obtained from fitting using equation Eq 2.4.10.

[c] Compound 2 cannot provide error values generated from comparison between two crystallographic equivalent but magnetically distinct sites like Ph_3PO and **1**. Uncertainties from single-crystal NMR data fitting are only on the order of 10 Hz. Therefore, we estimate the error to be similar to the largest error present in analysis of Ph_3PO and **1**.

5.4 Conclusions

This work has established single-crystal NMR spectroscopy as a novel probe of halogen bonds. Detailed ^{31}P and ^{17}O single-crystal NMR analyses of triphenylphosphine oxide and three of its halogen-bonded cocrystals have revealed several new correlations and insights. The main findings may be summarized as follows:

(i) single-crystal NMR on halogen-bonded systems is feasible and the resulting data are sufficiently sensitive to discriminate between different halogen bond environments;

(ii) the angular deviation of the unique component of the ^{31}P CS tensor from the direction of the oxygen-iodine halogen bond correlates with the deviation from linearity of the halogen bond;

(iii) the angular deviation of the unique component of the ^{17}O CS tensor from the direction of the oxygen-iodine halogen bond correlates with the deviation from linearity of the halogen bond;

(iv) the angular deviation of the unique component of the ^{17}O intermediate quadrupolar coupling tensor from the direction of the oxygen-iodine halogen bond correlates with the deviation from linearity of the halogen bond;

(v) the magnitudes of the various NMR interaction tensors are sensitive to halogen bond formation, as described in part in our earlier study;[5]

(vi) there is a decrease in anisotropy and an increase in asymmetry of the $\mathbf{J}(^{31}P,^{17}O)$ coupling tensors attributable to the formation of iodine-oxygen halogen bonds.

These findings are corroborated by GIPAW DFT calculations. Overall, this work has thus established the orientations of NMR interaction tensors as unique probes of halogen bonds.

5.5 References for Chapter 5

[1] Viger-Gravel, J.; Leclerc, S.; Korobkov, I.; Bryce, D. L. *CrystEngComm* **2013**, *15*, 3168–3177.

[2] Szell, P. M. J.; Bryce, D. L. *J. Phys. Chem. C* **2016**, *120*, 11121–11130.

[3] Viger-Gravel, J.; Leclerc, S.; Korobkov, I.; Bryce, D. L. *J. Am. Chem. Soc.* **2014**, *136*, 6929–6942.

[4] Cerreia Vioglio, P.; Szell, P. M. J.; Chierotti, M. R.; Gobetto, R.; Bryce, D. L. *Chem. Sci.* **2018**, *9*, 4555–4561.

[5] Xu, Y.; Viger-Gravel, J.; Korobkov, I.; Bryce, D. L. *J. Phys. Chem. C* **2015**, *119*, 27104–27117.

[6] Viger-Gravel, J.; Meyer, J. E.; Korobkov, I.; Bryce, D. L. *CrystEngComm* **2014**, 7285–7297.

[7] McKnett, C. L.; Dybowski, C. R.; Vaughan, R. W. *J. Chem. Phys.* **1975**, *63*, 4578–4581.

[8] Berglund, B.; Vaughan, R. W. *J. Chem. Phys.* **1980**, *72*, 3424–3426.

[9] Legon, A. C. *Struct. Bond.* **2008**, *126*, 17–64.

[10] Davey, J. B.; Legon, A. C.; Waclawik, E. R. *Chem. Phys. Lett.* **1999**, *306*, 133–144.

[11] Herrebout, W. A.; Legon, A. C.; Waclawik, E. R. *Phys. Chem. Chem. Phys.* **1999**, *1*, 4961–4966.

[12] Bryce, D. L.; Eichele, K.; Wasylishen, R. E. *Inorg. Chem.* **2003**, *42*, 5085–5096.

[13] Busing, W. R.; Levy, H. A. *Acta Crystallogr.* **1967**, *22*, 457–464.

[14] Kennedy, M. A.; Ellis, P. D. *Concepts Magn. Reson.* **1989**, *1*, 109–129.

[15] Newville, M.; Stensitzki, T.; Allen, D. B.; Ingargiola, A. LMFIT: Non-Linear Least-Square Minimization and Curve-Fitting for Python. September 2014. https://doi.org/10.5281/zenodo.11813.

[16] Kentgens, A. P. M.; Verhagen, R. *Chem. Phys. Lett.* **1999**, *300*, 435–443.

[17] Iuga, D.; Schäfer, H.; Verhagen, R.; Kentgens, A. P. M. *J. Magn. Reson.* **2000**, *147*, 192–209.

[18] Bennett, A. E.; Rienstra, C. M.; Auger, M.; Lakshmi, K. V.; Griffin, R. G. *J. Chem. Phys.* **1995**, *103*, 6951–6958.

[19] Clark, S. J.; Segall, M. D.; Pickard, C. J.; Hasnip, P. J.; Probert, M. I. J.; Refson, K.; Payne, M. C. *Z. Kristallogr.* **2005**, *220*, 567–570.

[20] Bonhomme, C.; Gervais, C.; Babonneau, F.; Coelho, C.; Pourpoint, F.; Azaïs, T.; Ashbrook, S. E.; Griffin, J. M.; Yates, J. R.; Mauri, F.; Pickard, C, J. *Chem. Rev.* **2012**, *112*, 5733–5779.

[21] Pickard, C. J.; Mauri, F. *Phys. Rev. B* **2001**, *63*, 245101.

[22] Adiga, S.; Aebi, D.; Bryce, D. L. *Can. J. Chem.* **2007**, *85*, 496–505.

[23] Alvarez, S. *Dalton Trans.* **2013**, *42*, 8617–8636

[24] Clark, T.; Hennemann, M.; Murray, J. S.; Politzer, P. *J. Mol. Model* **2007**, *13*, 291–296.

[25] Steiner, T. *Angew Chem., Int. Ed.* **2002**, *41*, 48–76.

[26] Vosegaard, T.; Hald, E.; Langer, V.; Skov, H. J.; Daugaard, P.; Bildsøe, H.; Jakobsen, H. J. *J. Magn. Reson.* **1998**, *135*, 126− 132

[27] Alvarado, S. R.; Shortt, I. a.; Fan, H.-J.; Vela, J. *Organometallics* **2015**, *34*, 4023–4031.

[28] Kennedy, M. A.; Ellis, P. D. *Concepts Magn. Reson.* **1989**, *1*, 35–47.

[29] Perras, F. A.; Viger-Gravel, J.; Burgess, K. M. N.; Bryce, D. L. *Solid State Nucl. Magn. Reson.* **2013**, *51–52*, 1–15.

[30] Volkoff, G. M. *Can. J. Phys.* **1953**, *31*, 820−836.

Chapter 6. SCFit: Software for Single-Crystal NMR Analysis

6.1 Introduction

Single-crystal NMR spectroscopy (SCNMR), while often considered to be tedious, is the premier method for determining absolute tensor orientations with respect to the molecular frame of reference.[1,2,3,4,5,6] This information is particularly valuable when one wishes to interpret NMR tensors in the context of the local molecular and electronic structure of the compound under investigation. Traditional SCNMR studies require the growth of a large (on the order of mm) single crystal which is rotated stepwise about three orthogonal axes perpendicular to the magnetic field. Vosegaard and others have introduced improvements to the standard method, including techniques where rotations about only two axes can be used, thereby speeding up the analysis.[7,8,9]

SCNMR offers some potential further advantages over the study of powdered samples. For example, multiple crystallographically distinct sites can give rise to complex powder patterns which may be difficult to unambiguously deconvolute. For quadrupolar nuclei, subtle effects from chemical shift anisotropy may be obscured by dominant quadrupolar broadenings. Of course, these challenges can be addressed in some cases through the use of data acquired at very high applied magnetic field and/or at multiple field strengths. Nuclear quadrupole resonance (NQR),[10] multiple quantum magic angle spinning (MQMAS),[11] double rotation (DOR),[12,13,14,15,16,17] or dynamic-angle spinning (DAS)[13,18,19] may also improve the situation. However, as noted above, none of these powder methods provide the absolute orientation of each tensor in the molecular frame.

There are at least two freely available software packages available to analyze single-crystal NMR spectra: Analysis of SIngle-Crystal Spectra (ASICS)[20] and a web-based software interface[21], both developed by Vosegaard et al. ASICS is designed for

Varian's VNMR file format, the popularity of which is in decline. Both packages are designed to fit spectra affected by chemical shift anisotropy and/or the quadrupolar coupling interaction.

Taking inspiration from these two software packages, we present here our own custom single-crystal NMR analysis software (SCFit). In addition to being able to customize this software for our own purposes, it was designed with two particular goals in mind. Firstly, the need arose in our work on halogen-bonded cocrystals to analyze spectra which are influenced simultaneously by anisotropic chemical shift, quadrupolar, direct dipolar, and indirect nuclear spin-spin coupling tensors. Secondly, we wanted to test the hypothesis that by constraining certain tensor elements which may be known independently of the SCNMR experiment, the fitting process could be improved by increasing the precision of the final results. Below, we therefore refer to a 'free fit', where the SCNMR data are freely fit without constraints, or to a 'constrained fit', where certain tensor elements are fixed during the fitting process. The software is written in the Python programming language (Python Software Foundation, https://www.python.org/). The processing algorithms are written using the Numpy scientific computing libraries and the plotting in the software is performed using the Matplotlib library.

Below, we provide a brief introduction to data processing using the software and some examples of its versatile fitting routines. A comparison between the single-crystal NMR results analyzed with and without fixed eigenvalues is made in an effort to provide a comparison of the accuracy and reliability of the orientation of each NMR tensor determined by these methods.

6.2 Theory

The relevant theory relating to the analysis of SCNMR data featuring anisotropic chemical shifts, quadrupolar coupling, and spin-spin coupling has been summarized Section 2.4.

Briefly, the resonance frequency for the central transition ($m = \frac{1}{2} \leftrightarrow m = -\frac{1}{2}$) of an isolated quadrupolar nucleus depends on both the quadrupolar interaction and the chemical shift and is given as:[3]

$$\nu^{(i)}_{\frac{1}{2}\leftrightarrow-\frac{1}{2}}(\theta) = A^{(i)} + B^{(i)}\cos 2\theta + C^{(i)}\sin 2\theta + D^{(i)}\cos 4\theta + E^{(i)}\sin 4\theta \qquad \text{Eq 6.2.1}$$

with the coefficients:

$$A^{(i)} = \left(\frac{q}{8}\right)\left[-11\left(Q_{jj}^2 + Q_{kk}^2\right) - 50Q_{jj}Q_{kk} + 28Q_{jk}^2 + 16\left(Q_{ki}^2 + Q_{ij}^2\right)\right] + (\delta_{jj} + \delta_{kk})\nu_0/2$$

$$B^{(i)} = \left(\frac{3q}{2}\right)\left[Q_{jj}^2 - Q_{kk}^2 + 4Q_{ij}^2 - 4Q_{ki}^2\right] + (\delta_{jj} - \delta_{kk})\nu_0/2$$

$$C^{(i)} = (-3q)\left[\left(Q_{jj} + Q_{kk}\right)Q_{jk} + 4Q_{ki}Q_{ij}\right] - \delta_{jk}\nu_0$$

$$D^{(i)} = (-9q/8)\left[\left(Q_{jj} - Q_{kk}\right)^2 - 4Q_{jk}^2\right]$$

$$E^{(i)} = (9q/2)\left(Q_{jj} - Q_{kk}\right)Q_{jk}$$

$$q = [3 - 4I(I+1)]/16\nu_0$$

Here, (*i*, *j*, *k*) = (X, Y, Z) and this follows cyclic permutations. Q_{ii} are the intermediate variables related to the quadrupolar coupling tensor (Q_{ii} is defined as:$Q_{ii} = \frac{eQ}{2I(2I-1)h}V_{ii}$,

where V_{ii} are the electric field gradient (EFG) tensor components) and δ_{i} describe the CS tensor principal components with respect to the cube axes or axes about which the crystal is rotated. The 11 variables (five for the traceless quadrupolar coupling tensors and six for the CS tensors) can be obtained from the best fit to the experimental SCNMR data. The antisymmetric part of the CS tensor is ignored. The resulting parameters can be used to build a 3 x 3 matrix for each tensorial interaction which can further be diagonalized according to:

$$\mathbf{Q} = \begin{pmatrix} Q_{\mathrm{XX}} & Q_{\mathrm{XY}} & Q_{\mathrm{XZ}} \\ Q_{\mathrm{YX}} & Q_{\mathrm{YY}} & Q_{\mathrm{YZ}} \\ Q_{\mathrm{ZX}} & Q_{\mathrm{ZY}} & -Q_{\mathrm{XX}} - Q_{\mathrm{YY}} \end{pmatrix} = R(\alpha_1, \beta_1, \gamma_1) \begin{pmatrix} Q_{11} & 0 & 0 \\ 0 & Q_{22} & 0 \\ 0 & 0 & Q_{33} \end{pmatrix}_{PAS} R^{-1}(\alpha_1, \beta_1, \gamma_1) \quad \text{Eq 6.2.2}$$

$$\boldsymbol{\delta} = \begin{pmatrix} \delta_{\mathrm{XX}} & \delta_{\mathrm{XY}} & \delta_{\mathrm{XZ}} \\ \delta_{\mathrm{YX}} & \delta_{\mathrm{YY}} & \delta_{\mathrm{YZ}} \\ \delta_{\mathrm{ZX}} & \delta_{\mathrm{ZY}} & \delta_{\mathrm{ZZ}} \end{pmatrix} = R(\alpha_2, \beta_2, \gamma_2) \begin{pmatrix} \delta_{11} & 0 & 0 \\ 0 & \delta_{22} & 0 \\ 0 & 0 & \delta_{33} \end{pmatrix}_{PAS} R^{-1}(\alpha_2, \beta_2, \gamma_2) \quad \text{Eq 6.2.3}$$

which produces the eigenvalues, *i.e.*, the three principal components of the intermediate quadrupolar coupling tensors (Q_{11}, Q_{22}, $Q_{33;}$ $|Q_{33}| \geq |Q_{22}| \geq |Q_{11}|$) and CS tensors ($\delta_{11}$, δ_{22}, δ_{33}; $\delta_{11} \geq \delta_{22} \geq \delta_{33}$), and the eigenvectors or matrix describing the direction cosines with respect to the cube axes using the Euler angles (α_1, β_1, γ_1) for intermediate quadrupolar coupling tensors and the Euler angles (α_2, β_2, γ_2) for CS tensors, where these Euler angles can be used to construct a rotation matrix as Eq 2.4.2.

Instead of optimizing all 11 elements in the matrix to obtain the best fit, the three principal components of each tensor, which can be obtained by simulating the powder pattern spectra of polycrystalline samples, can instead be fixed and only the eigenvectors,

more specifically the 2 sets of Euler angles, will be varied during the fit. Consequently, the two 3 x 3 matrices may be re-constructed using the final eigenvalues and eigenvectors according to equations Eq 6.2.2, Eq 6.2.3, and Eq 2.4.2 to replace 11 parameters in equation Eq 6.2.1.

The above equations are easily modified to exclude the quadrupolar interaction in the case of an isolated spin-1/2 nucleus. The magnitude and symmetry of the CS tensor are typically expressed using δ_{iso}, Ω, and κ, (Eq 2.3.7–Eq 2.3.9), while those of the intermediate quadrupolar coupling tensor are typically expressed using the quadrupolar coupling constant and asymmetry parameter:

$$C_Q = 2I(2I-1)Q_{33} \qquad \text{Eq 6.2.4}$$

$$\eta_Q = \frac{Q_{11} - Q_{22}}{Q_{33}} \qquad \text{Eq 6.2.5}$$

Two nuclei may be spin-spin coupled to one another through direct dipolar (*D*) and indirect spin-spin coupling (*J*) interactions. The fitting function used in the SCFit software is provided in Eq 2.4.10 in Section 2.4. Similarly, the fitting can generate the three principal components of the effective dipolar coupling tensor: $R_{eff,11}$, $R_{eff,22}$, $R_{eff,33}$ with $|R_{eff,33}| \geq |R_{eff,11}| \geq |R_{eff,22}|$.

6.3 Software

The main interface of the SCFit software is shown in Figure 6.3.1. The spin quantum number, *I*, and the Larmor frequency are entered manually. The software can be used for (i) the central transition of an isolated quadrupolar nucleus, (ii) an isolated spin-1/2 nucleus, or (iii) the central transition of a quadrupolar nucleus subject to the combined

effects of quadrupolar coupling (treated to second order) and chemical shift anisotropy. (Note: for spin-1/2 nuclei, the computed *q* value is zero (Eq 2.4.7) and consequently the final quadrupolar frequency coupling tensor will be zero.) Analysis of satellite transitions has not been implemented. There are two options in the software which control the fitting of single-crystal NMR data: (i) Free fitting and (ii) fitting with known eigenvalues (a constrained fit), as described in the Theory Section. The software also includes a second module wherein the analysis of spin-spin coupling interaction between a pair of spin-1/2 nuclei or a spin-1/2-quadrupole spin pair is implemented. In what follows, all features of the software package SCFit will be described step-by-step. Each case consists of five similar steps in the analysis of the single-crystal NMR data as implemented through the *Load Data*, *Fit*, *Draw*, *Result*, and *Enter Initial Value* functions displayed in the left panel of Figure 6.3.3.

i) Input file format. The resonance frequencies determined from single-crystal NMR rotation experiments should be tabulated manually in a csv formatted file. The csv file should include the rotation angles in radians in the first column. Then the last three columns should contain the resonance frequency in Hz monitored during rotations about the three orthogonal X, Y, and Z cube axes, respectively. If there is no spin-spin coupling present, the frequency reported should be the corresponding peak resonance frequency in Hz. If there is spin-spin coupling present, the frequency listed should be the average resonance frequency of the two satellite peaks.

Figure 6.3.1. A screenshot of the main interface of the software before (a) and after (b) entering the spin-*I* and Larmor frequency.

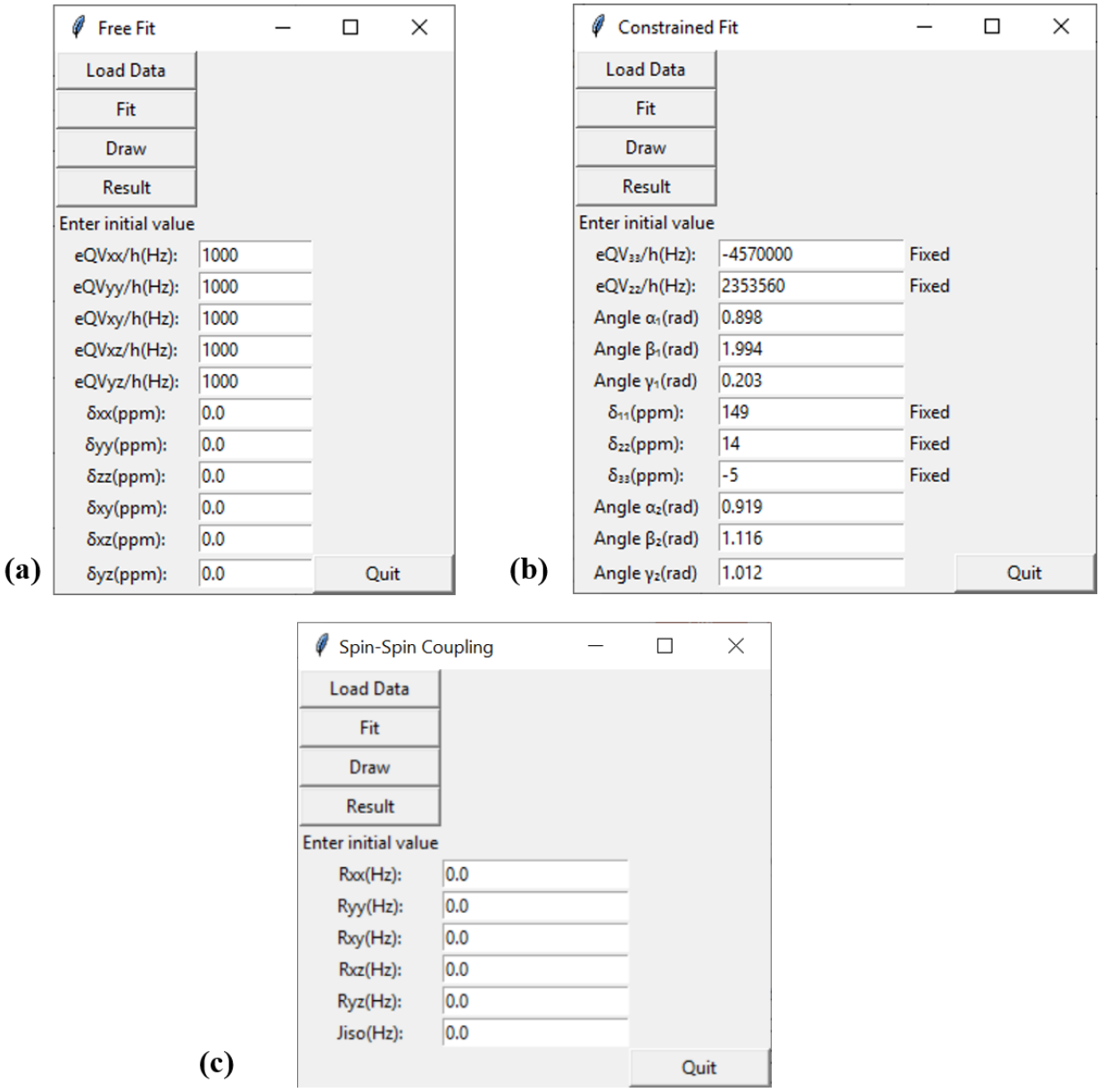

Figure 6.3.2. Image of the Input window of the software in three cases: *Free Fit* (a), *Constrained Fit* (b) and *Spin-Spin Coupling* (c).

ii) Analysis of CS and EFG tensors

1. Launch the software and click on either "*Free Fit*" or "*Constrained Fit*" after manually entering the spin-*I* number and Larmor frequency *ν*. The *q* value in Eq 6.2.1 will automatically calculated and an Input window (shown in Figure 6.3.2) will pop out.

Click '*Load Data*' and select an input file. The window then requires an initial guess of the tensor values. In *Free Fit,* the fitting process is so robust that the starting values of the parameters are not important. *Constrained Fit* allows the user to fix all the tensor magnitudes to known values; in this case also using a prior estimate of the Euler angles relating the CS and EFG tensors as initial guesses will help the solution easily converge.

2. By clicking "*Fit*", the spectral frequencies obtained from each rotation of the crystal are fitted using LMFIT code[22] with equation Eq 6.2.1 to obtain 11 parameters using the *Free Fit* module or 6 parameters with the *Constrained Fit* module. The complete fitting functions are provided in the Supporting Information.
3. The result windows provided from *Free Fit* and *Constrained Fit* are shown in Figure 6.3.3 and Figure 6.3.4, respectively. The *Draw* button will create a graph window (examples are given in Figure 6.3.3(a) and Figure 6.3.4(a)), which provides both the experimental data points and the solid lines corresponding to the best-fit values generated from the optimized parameters.
4. After the fitting, tensors corresponding to the anisotropic NMR interaction matrices (see left hand side of equations Eq 6.2.2 and Eq 6.2.3) are constructed with respect to the X, Y, and Z axes of the goniometer. The *Result* button will diagonalize these tensor matrices and generate the eigenvalues, which represent the magnitudes of the three principal components, as well as the eigenvectors, which provide the direction cosine values of the three components with respect to the cube axes (see Figure 6.3.3(b)). In Figure 6.3.4(b), the *Result* button will print out the fixed eigenvalues and the corresponding eigenvectors calculated from the optimized Euler angles in *Constrained Fit*, according to equation Eq 2.4.2.

5. Finally, by clicking "*Fit Report*", the parameters of the fit can be exported to a new workspace, including various fitting statistics and the final values of the optimized variables as shown in Figure 6.3.3(c) and Figure 6.3.4 (c). (Note: the Q_{ii} and FixQ_{ii} used as intermediate variables in the fitting functions were defined as: $Q_{ii}/FixQ_{ii} = \frac{1}{2I(2I-1)}\frac{eqV_{ii}}{h}$).

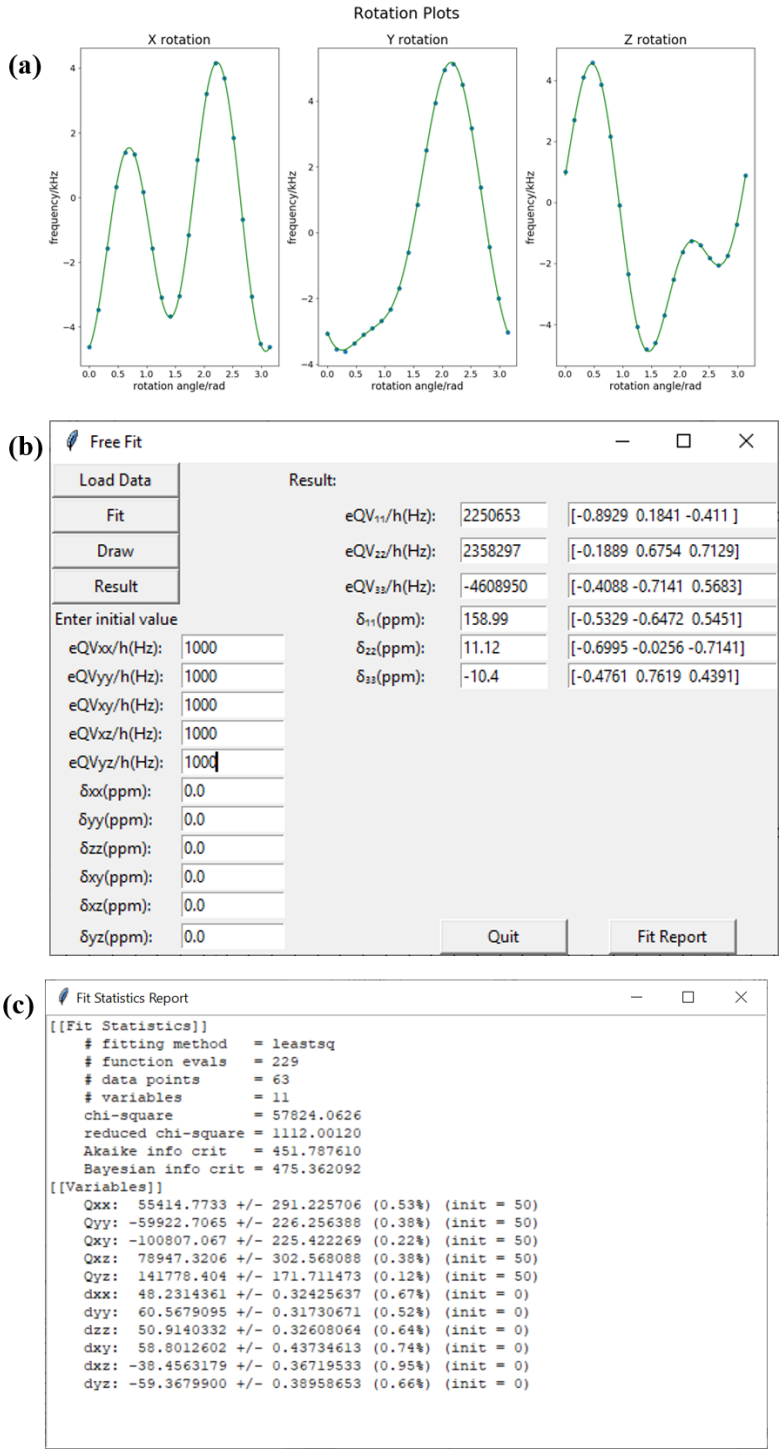

Figure 6.3.3. Screenshots of the *Plot* window (a) created by *Draw* button, *Result* window (b) created by *Result* button and *Fit Statistics* window (c) created by *Fit Report* button for *Free Fit* Analysis.

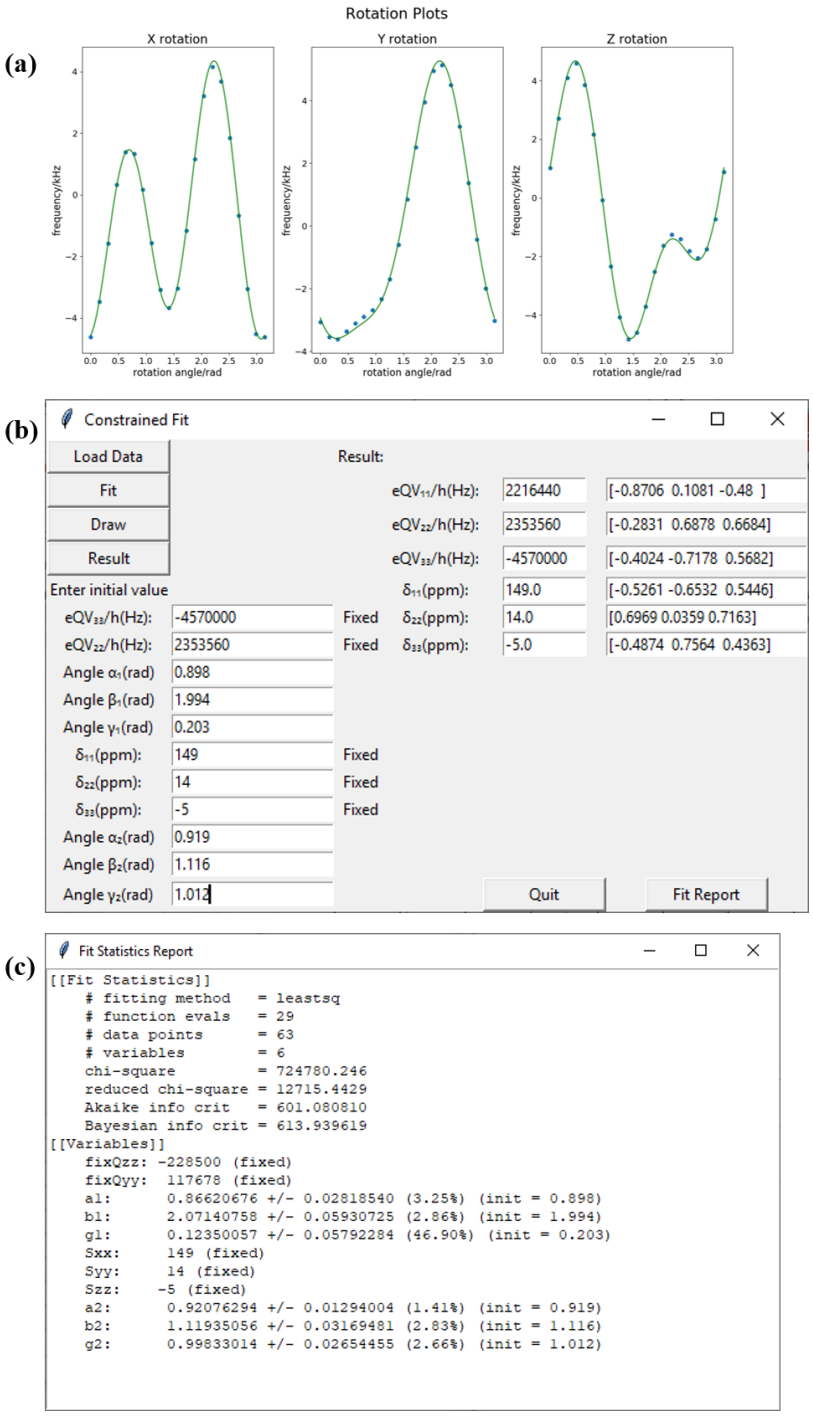

Figure 6.3.4. Screenshots of the *Plot* window (a) created by the *Draw* button, *Result* window (b) created by the *Result* button and the *Fit Statistics* window (c) created by the *Fit Report* button for *Constrained Fit* analysis.

iii) Analysis of spin-spin coupling

The procedure for the analysis of spin-spin coupling is similar to that for the *Free Fit* module, with a few variations as described below. The screenshots of the corresponding workflow are provided in Figure D1 in Appendix D.

1. The data should be loaded from a csv formatted file. The csv file should include the rotation angles in radians in the first column. However, when analyzing the spin-spin coupling, the last three columns should contain the variation of the splittings between the two peaks in Hz during rotations about the three orthogonal X, Y, and Z cube axes, respectively.
2. The fitting of the spin-spin coupling in equation Eq 2.4.10 eventually is simply a pure sine function. The fitting solution can easily converge even with zero initial guess. By clicking "*Fit*", the peak splittings obtained from each rotation of the crystal were fitted using equation Eq 2.4.10 to obtain J_{iso} and 5 elements corresponding to the effective dipolar coupling.
3. After the fitting is finished, the *Draw* button will create a graph window which again shows both the experimental data points and the solid lines corresponding to the best-fit values generated from the optimized parameters.
4. The *Result* button will diagonalize the effective dipolar coupling tensor matrix and generate the eigenvalues, which represent the magnitude of the three principal components, followed by the eigenvectors, which provide the cosine values of the three components with respect to the cube axes. By definition, $|R_{\text{eff},33}| \geq |R_{\text{eff},11}| \geq |R_{\text{eff},22}|$. *Fit Report* will open a new window with all the statistics generated from LMFIT.

A final note concerning the analysis of the quadrupolar coupling interaction and spin-spin coupling is necessary: the sign of neither the quadrupolar coupling tensor nor the effective dipolar coupling tensor can be determined from the central transition single-crystal NMR experiment. However, they can be determined either from ab initio or DFT calculation or from simulations of the polycrystalline NMR spectra, in favourable cases.

6.4 Experimental Demonstrations: Chemical Shift and Quadrupolar Coupling Tensors

The utility of the software will be illustrated by the analysis of the ^{17}O and ^{31}P single-crystal NMR spectra of $Ph_3P^{17}O$ and two halogen-bonded cocrystals. The systems are depicted in Figure 6.4.1. The experimental data and its interpretation in terms of the halogen bond has been provided in Chapter 5.[23] Presently, we use these data to demonstrate the chemical shift and quadrupolar coupling functionality of the SCFit software and to test the hypothesis that by constraining certain eigenvalues known independently of the SCNMR experiment, that the fitting process could be improved by increasing the precision of the final results.

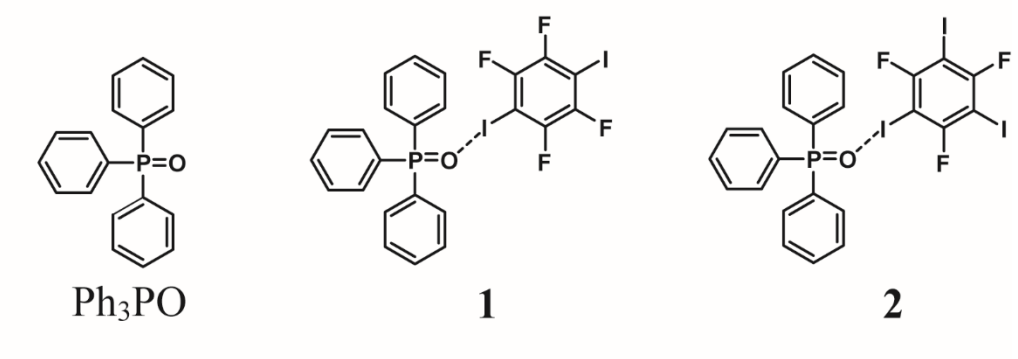

Figure 6.4.1. Chemical structures of compounds under investigation: triphenylphosphine oxide (Ph_3PO) and its halogen-bonded cocrystals: (Ph_3PO)(*p*-$C_6F_4I_2$) (**1**) and (Ph_3PO)(*sym*-$C_6F_3I_3$) (**2**).

The full single-crystal ^{17}O NMR spectra of $Ph_3P^{17}O$ and its halogen-bonded cocrystals **1** and **2** resulting from rotation about the X, Y, and Z axes have been provided previously (Figure C3 and Figure 5.3.7).[23] Here, we use both *Free Fit* and *Constrained Fit* modules to describe the orientation dependence of the chemical shift and quadrupolar coupling tensors (Figure 6.4.2; Table 6.4.1; Table 6.4.2). The orange and blue solid lines represent the best-fits obtained from regular free fitting with 11 parameters. The dark green and pink lines represent the best-fits obtained from fitting with known eigenvalues and six Euler angles. Goodness-of-fit is quantified using a reduced χ^2 parameter ($\chi^2 = \sum_{i=1}^{N} \frac{\left(\nu_i^{exp} - \nu_i^{calc}\right)^2}{\sigma_i (N - N_{var})}$, ν_i^{exp} and ν_i^{cal} are experimental and calculated data points respectively; N is the total number of data points; σ_i is the uncertainty in the measurement; N_{var} is number of optimized variables during the fitting) as shown in Table 6.4.3. Deviations between the two fitting functions can be noted visually in Figure 6.4.3.

Table 6.4.1. A Comparison of Principal Components (in ppm) and Direction Cosines of the Averaged ^{17}O Chemical Shift Tensors in the Crystal Axis Frame[a,b]

	compound		components / ppm	*a**	*b*	*c*
Constrained fit	Ph_3PO	δ_{11}	149	-0.43(2)	0.42(4)	-0.80(1)
		δ_{22}	14	-0.87(2)	0.06(2)	0.50(1)
		δ_{33}	-5	0.26(1)	0.90(1)	0.33(3)
	1	δ_{11}	121.8	-0.42(2)	-0.73(2)	-0.54(4)
		δ_{22}	13.2	-0.26(20)	0.66(9)	-0.70(14)
		δ_{33}	1.8	-0.87(10)	0.16(18)	0.47(18)
	2	δ_{11}	158.2	0.38(2)	0.30(4)	0.87(4)
		δ_{22}	19.9	0.92(20)	-0.13(9)	-0.36(14)
		δ_{33}	-0.79	-0.09(10)	-0.94(18)	0.33(18)
Free fit	Ph_3PO	δ_{11}	151(8)	-0.43(2)	0.41(3)	-0.81(1)
		δ_{22}	12(1)	-0.86(2)	0.05(5)	0.49(3)
		δ_{33}	-8(2)	0.24(3)	0.91(2)	0.33(6)
	1	δ_{11}	109(3)	-0.50(5)	-0.71(3)	-0.49(1)
		δ_{22}	19(2)	0.63(7)	0.08(7)	-0.78(7)
		δ_{33}	5(1)	0.59(6)	-0.70(3)	0.40(12)
	2	δ_{11}	152(8)	0.42(5)	0.29(3)	0.86(1)
		δ_{22}	33(2)	0.90(7)	-0.23(7)	-0.37(7)
		δ_{33}	-10(2)	-0.09(6)	-0.93(3)	0.36(12)

[a] The convention used for designating the three principal components of the CS tensor is $\delta_{11} \geq \delta_{22} \geq \delta_{33}$.

[b] For Ph_3PO and **1**, each with two magnetically non-equivalent sites, eigenvectors from the second site were transformed by a symmetry operation and then averaged with the eigenvectors from the first site in order to provide an error estimate. Errors for the eigenvectors for **2** were assumed to be similar.

Table 6.4.2. A Comparison of Principal Components (in MHz) and Direction Cosines of the ^{17}O Quadrupolar Coupling Tensors in the Crystal Axis Frame[a,b]

	compound		**components / MHz**	***a****	***b***	***c***
		eqV_{33}/h	4.570	0.32(2)	-0.51(1)	0.80(1)
Constrained	Ph_3PO	eqV_{22}/h	-2.354	0.20(10)	-0.79(4)	-0.58(1)
fit		eqV_{11}/h	-2.216	-0.92(3)	-0.34(10)	-0.15(5)
		eqV_{33}/h	5.030	0.44(2)	0.81(1)	0.38(4)
	1	eqV_{22}/h	-2.842	-0.59(8)	0.59 (1)	-0.56(10)
		eqV_{11}/h	-2.188	-0.67(7)	0.02(11)	0.73(6)
		eqV_{33}/h	4.810	0.20(2)	0.30(3)	0.93(4)
	2	eqV_{22}/h	-2.718	0.94(10)	0.21(4)	-0.27(10)
		eqV_{11}/h	-2.092	0.27(7)	-0.93(11)	0.24(6)
Free fit	Ph_3PO	eqV_{33}/h	4.57(4)	0.32(2)	-0.50(2)	0.80(1)
		eqV_{22}/h	-2.36(1)	0.22(6)	-0.78(2)	-0.58(1)
		eqV_{11}/h	-2.21(6)	-0.92(2)	-0.37(6)	-0.14(2)
	1	eqV_{33}/h	4.96(2)	0.46(3)	0.80(1)	0.37(1)
		eqV_{22}/h	-2.59(3)	-0.72(1)	0.58(2)	-0.37(4)
		eqV_{11}/h	-2.36(2)	-0.51(3)	-0.10(1)	0.85(1)
	2	eqV_{33}/h	4.80(4)	0.20(3)	0.28(2)	0.94(1)
		eqV_{22}/h	-2.64(3)	0.98(6)	0.01(2)	-0.21(4)
		eqV_{11}/h	-2.16(6)	0.06(3)	-0.96(6)	0.27(2)

[a] The convention used for designating the three principal components of the quadrupolar coupling tensor is $|\boldsymbol{eQV_{33}/h}| \geq |\boldsymbol{eQV_{22}/h}| \geq |\boldsymbol{eQV_{11}/h}|$.

[b] For Ph_3PO and **1**, each with two magnetically non-equivalent sites, eigenvectors from the second site were transformed by a symmetry operation and then averaged with the eigenvectors from the first site in order to provide an error estimate. Errors for the eigenvectors for **2** were assumed to be similar.

Table 6.4.3. The Reduced χ^2 Values in Hz Generated from Different Fitting Methods for ^{31}P and ^{17}O Single-Crystal NMR Data Analysis

		Free		Constrained	
		^{17}O	^{31}P	^{17}O	^{31}P
$Ph_3P^{17}O$	site 1	1112	24233	12715	39539
	site 2	6471	17432	11104	27738
1	site 1	9525	14312	95118	73382
	site 2	8956	17094	42724	47873
2		4591	33243	94502	35849

The eigenvectors of the two largest principal components (δ_{11} and eQV_{33}/h) obtained from the two fitting methods are in good agreement, where there is a deviation in direction cosines of less than 0.02 for both δ_{11} and eQV_{33}/h in all three crystals, except for δ_{11} in cocrystal **1** (a difference of ~0.08 along the crystallographic *a* axis). Larger deviations between the two methods are seen for the other tensor components, especially for the δ_{22} and δ_{33} components of compound **1**; however, these deviations become meaningless as the tensors approach axial symmetry.

For compound $Ph_3P^{17}O$ and **1**, in which there are two crystallographically equivalent but magnetically distinct molecules, these sites should be characterized by equivalent eigenvalues but different eigenvectors. As explained in previous chapter, oxygen atoms in these two compounds symmetric by a 2-fold rotation along

crystallographic b axis followed by translation, consequently the general NMR tensor matrix representing these two sites which are related by this symmetry is:[24]

$$\delta/Q_{\,site\,1} = \begin{bmatrix} a & b & c \\ d & e & f \\ g & h & i \end{bmatrix}, \delta/Q_{site\,2} = \begin{bmatrix} a & -b & c \\ -d & e & -f \\ g & -h & i \end{bmatrix} \qquad \text{Eq 6.4.1}$$

This symmetry information offers some redundancy to estimate the error in the tensor orientations. It is evident that there is significant difference between the eigenvectors of the two sites in compound **1**, represented by the substantial errors of about 0.20. The main reason for these large errors is that fixing the eigenvalues can force the data fit and may break the symmetry present in the molecule.

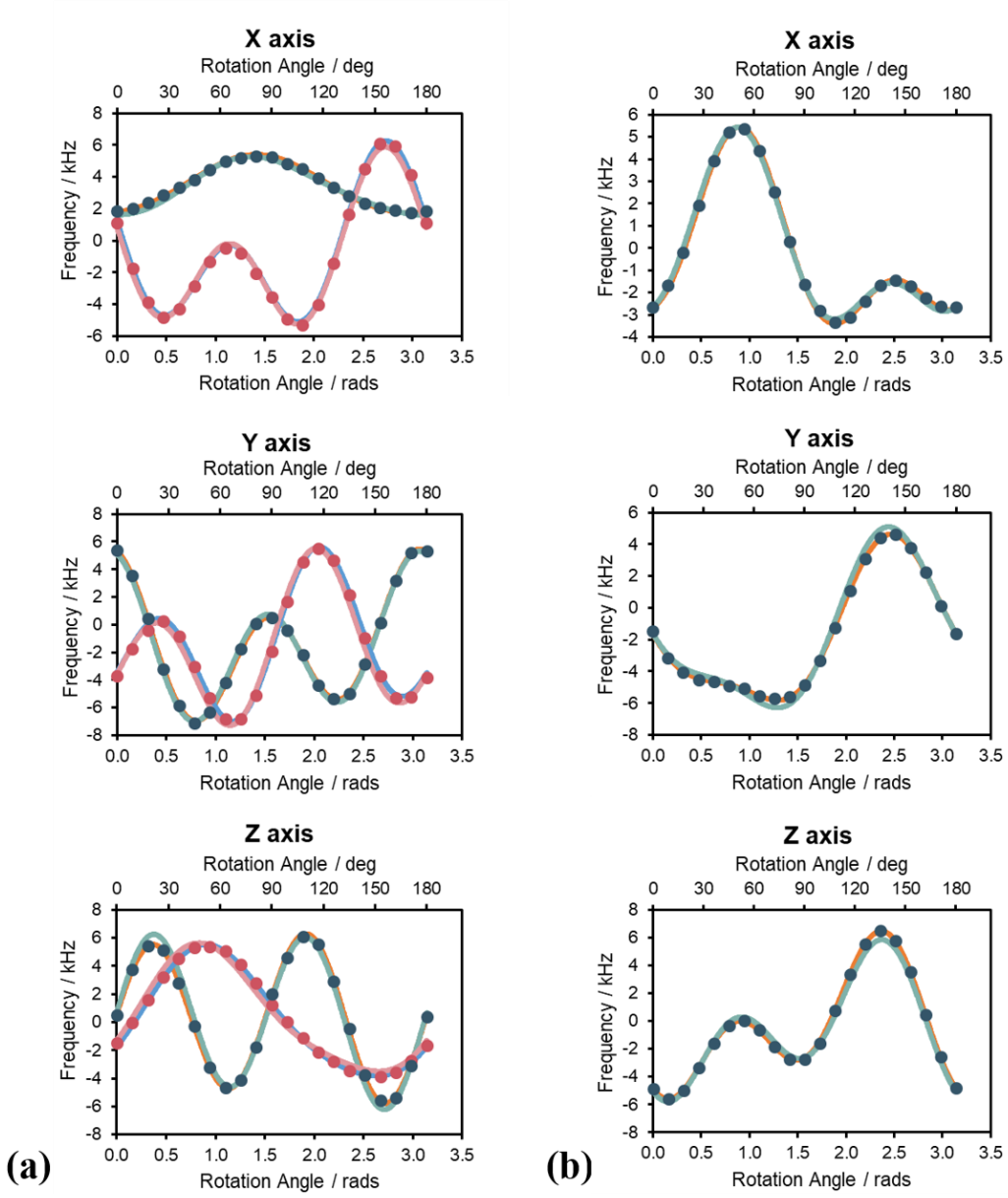

Figure 6.4.2. Rotation plots displaying the variation in the ^{17}O experimental frequency in kHz for rotations about the cube X, Y, Z axis for the halogen-bonded cocrystals: **1** (a) and **2** (b). Cocrystal **1** has two magnetically non-equivalent sites shown in dark green and pink. The solid lines correspond to the best-fit values generated from optimized parameters. The orange and blue solid lines represent the best-fits obtained from *Free Fit* with 11 parameters. The dark green and pink lines represent the best-fits obtained from *Constrained Fit* and 6 Euler angles. Experimental data were originally reported in reference [23]

^{17}O powder NMR experiments under static conditions for $Ph_3P^{17}O$ and for halogen-bonded compounds were present in Chapter 3.[25] Spectra are shown for Ph_3PO, **1** and **2** in Figure 6.4.3 along with three simulated traces. The first is the original best-fit to the powder spectrum (blue), the second uses the parameters obtained through the *Free Fit* to SCNMR data (yellow), and the third uses the parameters obtained through the *Constrained Fit* to SCNMR data (green). The procedure to convert the eigenvectors to three Euler angles was explained previously.[26] The *Free Fit* simulation is in excellent agreement with the experimental spectrum and with the original simulation. The *Constrained Fit* gives the worst visual agreement with experiment. Plots of experimental principal component values (Q_{ii} and δ_{ii}) versus values calculated using gauge-including projector-augmented wave density functional theory (GIPAW DFT) computations (Figure D2 in Appendix D) are in slightly better correlation with the *Free Fit* parameters ($R^2 = 0.9975$ for Q_{ii} and $R^2 = 0.9952$ for δ_{ii}) than with those obtained from the powder NMR experiments ($R^2 = 0.9967$ for Q_{ii} and $R^2 = 0.9756$ for δ_{ii}). Interestingly, the Euler angles obtained from the single-crystal NMR analysis have only a weak correlation with the calculated DFT results ($R^2 = 0.6796$); again, this is attributed in part to the near axial symmetry of the tensors.

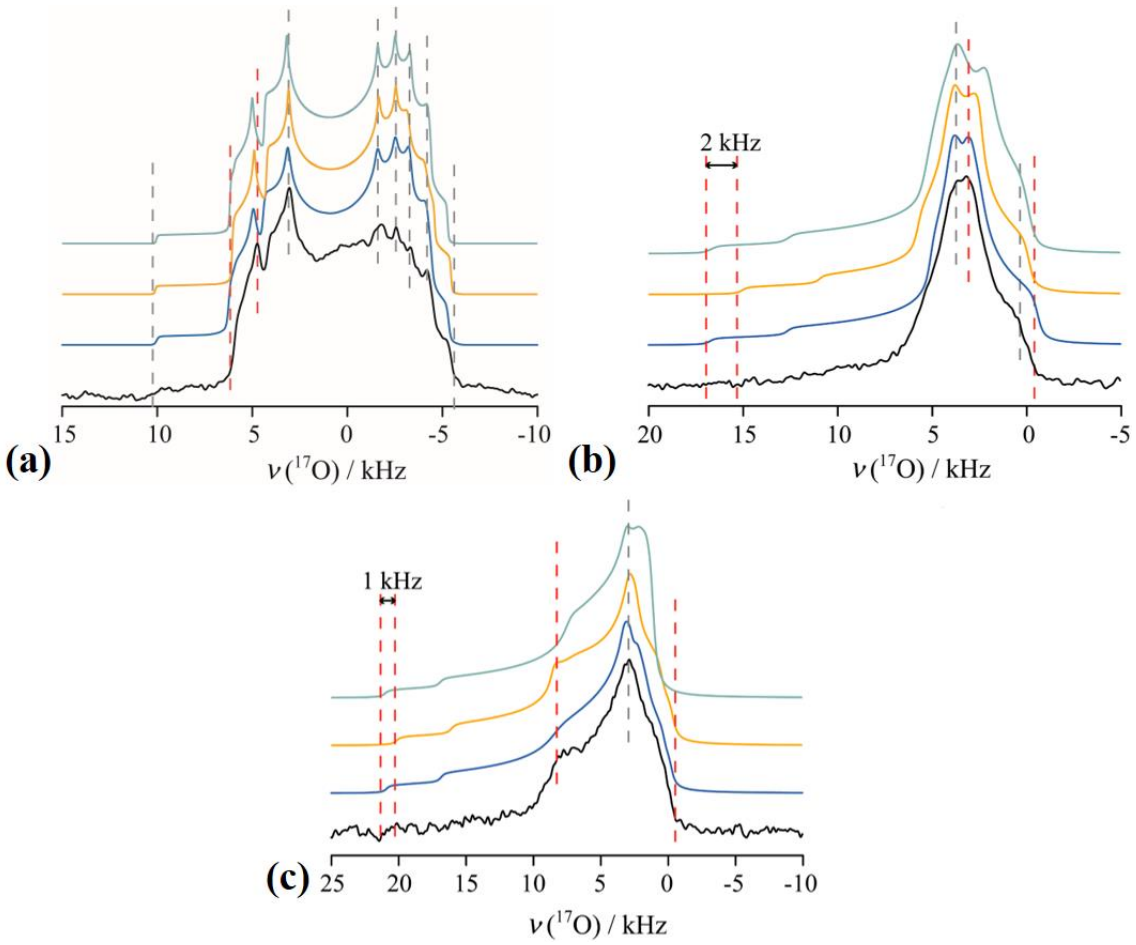

Figure 6.4.3. Experimental ^{17}O static NMR spectra (black) of $Ph_3P^{17}O$ (a) acquired at 9.4 T, and halogen-bonded cocrystals **1** (b) and **2** (c) acquired at 21.1 T. Experimental data were originally reported in reference 25. The corresponding simulated spectra are based on the parameters from powder NMR experiments (blue), regular *Free Fit* of single-crystal NMR data (yellow), and a *Constrained Fit* of single-crystal NMR data (green). Dashed lines denote points of comparison to aid the eye.

The eigenvectors, which describe the orientation of the ^{17}O NMR tensors with respect to the three cube axes, have been converted to express the orientation of ^{17}O NMR tensors with respect to the crystallographic axes using the rotation transformation matrix obtained from single crystal X-ray diffraction. Perspective drawings of the orientation of the ^{17}O intermediate quadrupolar coupling tensors and CS tensors determined by single-

crystal NMR analysis with *Free Fit* and with *Constrained Fit* for $Ph_3P^{17}O$ and cocrystal **1** and **2** in the molecular frame are shown in Figure D3.

The principal components of the CS tensor can often be determined with good accuracy and precision for an isolated spin-1/2 nucleus either by analyzing the powder pattern from a static sample or by analyzing a MAS NMR spectrum with a sufficiently large number of spinning sidebands.[27] Such is the case for the ^{31}P spins in the samples discussed in this study (prepared without ^{17}O enrichment). We therefore speculate that the ^{31}P chemical shift tensor eigenvalues determined from powder samples[25] could be as reliable as the values obtained from single-crystal NMR. If correct, then by fixing the eigenvalues to known values, the number of unknowns in the fitting function would be reduced, perhaps resulting in more precise eigenvectors. We have tested this hypothesis and the results are summarized in Table 6.4.4. The eigenvectors of the most shielded component obtained from the two different single-crystal fitting methods are identical (a cosine deviation smaller than 0.01). The other two components also agree well between the two methods. This consistency can be visualized in the perspective drawings of the orientation of the ^{31}P CS tensors for $Ph_3P^{17}O$ and cocrystal **1** and **2** in the molecular frame determined by the two single-crystal NMR analysis methods (shown in Figure D4). The precision of the ^{31}P chemical shift tensor orientations based constrained fitting is slightly improved in many cases, especially for Ph_3PO and **1**, where some of the direction cosine values are precise to three decimal places when using *Constrained Fitting* compared to two decimal places when using *Free Fitting*.

Table 6.4.4 Principal Components and Direction Cosines of the ^{31}P Chemical Shift Tensors in the Crystal Axis Frame[a,b]

	compound		components / ppm	*a**	*b*	*c*
Constrained fit	Ph_3PO	δ_{11}	96.6	-0.58(2)	0.55(1)	0.60(1)
		δ_{22}	83.7	0.752(4)	0.64(1)	0.14(4)
		δ_{33}	-101.4	0.31(3)	-0.54(2)	0.784(1)
	1	δ_{11}	92.3	-0.01(3)	-0.44(3)	0.896(6)
		δ_{22}	91.5	0.90(2)	-0.39(6)	-0.18(2)
		δ_{33}	-90.7	0.43(3)	0.81(2)	0.41(1)
	2	δ_{11}	97.5	0.10(3)	-0.95(3)	0.31(1)
		δ_{22}	82.3	-0.96(2)	-0.01(6)	0.27(4)
		δ_{33}	-92.5	0.26(3)	0.32(2)	0.91(1)
Free fit	Ph_3PO	δ_{11}	96.6(3)	-0.60(2)	0.53(1)	0.60(2)
		δ_{22}	83.3(6)	0.74(1)	0.65(2)	0.16(4)
		δ_{33}	-101.3(7)	0.31(4)	-0.54(2)	0.79(1)
	1	δ_{11}	93.9(1)	0.06(3)	-0.48(3)	0.88(3)
		δ_{22}	89.1(7)	0.90(2)	-0.35(3)	-0.25(5)
		δ_{33}	-92.0(2)	0.42(4)	0.81(3)	0.41(1)
	2	δ_{11}	96.4(3)	0.10(3)	-0.95(3)	0.31(2)
		δ_{22}	82.5(7)	-0.96(2)	-0.01(3)	0.28(5)
		δ_{33}	-92.0(7)	0.26(4)	0.32(3)	0.91(1)

[a] The convention used for designating the three principal components of the CS tensor is $\delta_{11} \geq \delta_{22} \geq \delta_{33}$.

[b] For Ph_3PO and **1**, each with two magnetically non-equivalent sites, eigenvectors from the second site were transformed by a symmetry operation and then averaged with the eigenvectors from the first site in order to provide an error estimate. Errors for the eigenvectors for **2** were assumed to be similar.

6.5 Conclusions

We have developed a graphical and user-friendly single-crystal NMR analysis program which includes four common anisotropic NMR interactions: chemical shift, quadrupole coupling, direct dipolar coupling, and indirect nuclear spin-spin coupling. The orientation of the chemical shift and quadrupolar coupling tensors can be determined through either a free or constrained fitting process. We have validated the applicability of the program with ^{17}O and ^{31}P single-crystal NMR data for $Ph_3P^{17}O$ and two of its halogen-bonded cocrystals. The free fitting protocol always provides better overall fits to the data (smaller reduced χ^2 values), confirming the conventional wisdom that single-crystal NMR is the gold standard, and disproving the hypothesis that fixing the eigenvalues consistently provides better results. However, fitting with known eigenvalues can narrow the error values generated for tensor orientations, in some cases, when the NMR results obtained from polycrystalline samples are known to be particularly accurate and precise. In any case, having access to both fitting methods in SCFit also provides an extra check on the quality and consistency of both powder and single-crystal NMR data.

6.6 References for Chapter 6

[1] Vosegaard, T.; Skibsted, J.; Bildsøe, H.; Jakobsen, H. J. *J. Magn. Reson. - Ser. A* **1996**, *122*, 111–119.

[2] Vosegaard, T.; Byriel, I. P.; Jakobsen, H. J. *J. Phys. Chem. B* **1997**, *101*, 8955–8958.

[3] Power, W. P.; Kirby, C. W.; Taylor, N. J. *J. Am. Chem. Soc.* **1998**, *120*, 9428–9434.

[4] Eichele, K.; Chan, J. C. C.; Wasylishen, R. E.; Britten, J. F. *J. Phys. Chem. A* **1997**, *101*, 5423–5430.

[5] Lumsden, M. D.; Eichele, K.; Wasylishen, R. E.; Cameron, T. S.; Britten, J. F. *J. Am. Chem. Soc.* **1994**, *116*, 11129–11136.

[6] Eichele, K.; Ossenkamp, G. C.; Wasylishen, R. E.; Cameron, T. S. *Inorg. Chem.* **1999**, *38*, 639–651.

[7] Vosegaard, T.; Hald, E.; Daugaard, P.; Jakobsen, H. J. *Rev. Sci. Instrum.* **1999**, *70*, 1771–1779.

[8] Vosegaard, T.; Daugaard, P.; Hald, E.; Jakobsen, H. J. *J. Magn. Reson.* **2000**, *142*, 379–381.

[9] Cvitanić, T.; Lukas, M.; Grbić, M. S. *Rev. Sci. Instrum.* **2019**, *90*, 043903.

[10] Szell, P. M. J.; Bryce, D. L. *Concepts Magn. Reson.* **2016**, *45A*, e21412.

[11] Medek, A.; Harwood, J. S.; Frydman, L. *J. Am. Chem. Soc.* **1995**, *117*, 12779-12787.

[12] Samoson, A.; Lippmaa, E.; Pines, A. *Mol. Phys.* **1988**, *65*, 1013–1018.

[13] Chmelka, B. F.; Mueller, K. T.; Pines, A.; Stebbins, J.; Wu, Y.; Zwanziger, J. W. *Nature* **1989**, *339*, 42–43.

[14] Hung, I.; Wong, A.; Howes, A. P.; Anupõld, T.; Past, J.; Samoson, A.; Mo, X.; Wu, G.; Smith, M. E.; Brown, S. P.; Dupree, R. *J. Magn. Reson.* **2007**, *188*, 246–259.

[15] Perras, F. A.; Bryce, D. L. *J. Magn. Reson.* **2011**, *213*, 82–89.

[16] Perras, F. A.; Korobkov, I.; Bryce, D. L. *Phys. Chem. Chem. Phys.* **2012**, *14*, 4677–4681.

[17] Perras, F. A.; Bryce, D. L. *J. Chem. Phys.* **2013**, *138*, 174202.

[18] Mueller, K. T.; Sun, B. Q.; Chingas, G. C.; Zwanziger, J. W.; Terao, T.; Pines, A. *J. Magn. Reson.* **1990**, *86*, 470–487.

[19] Grandinetti, P. J.; Baltisberger, J. H.; Llor, A.; Lee, Y. K.; Werner, U.; Eastman, M. A.; Pines, A. *J. Magn. Reson. - Ser. A* **1993**, *103*, 72–81.

[20] Vosegaard, T.; Hald, E.; Langer, V.; Skov, H. J.; Daugaard, P.; Bildsøe, H.; Jakobsen, H. J. *J. Magn. Reson.* **1998**, *135*, 126–132.

[21] Vinding, M. S.; Kessler, T. O.; Vosegaard, T. *J. Magn. Reson.* **2016**, *269*, 120–127.

[22] Newville, M.; Stensitzki, T.; Allen, D. B.; Ingargiola, A. LMFIT: Non-Linear Least-Square Minimization and Curve-Fitting for Python. September 2014. https://doi.org/10.5281/zenodo.11813.

[23] Xu, Y.; Gabidullin, B.; Bryce, D .L. *J. Phys. Chem. A* **2019**, *123*, 6194-6209.

[24] Kennedy, M. A.; Ellis, P. D. *Concepts Magn. Reson.* **1989**, 1, 35–47.

[25] Xu, Y.; Viger-Gravel, J.; Korobkov, I.; Bryce, D. L. *J. Phys. Chem. C* **2015**, *119*, 27104–27117.

[26] Adiga, S.; Aebi, D.; Bryce, D. L. *Can. J. Chem.* **2007**, *85*, 496–505.

[27] Hodgkinson, P.; Emsley, L. *J. Chem. Phys.* **1997**, *10*, 4808–4816.

PART 4 IN-SITU SOLID-STATE NMR

Chapter 7. A ^{31}P In Situ Solid-State NMR Study of Halogen Bond Formation

Permission: Chapter 7 was from: Y. Xu, L. Champion, B. Gabidullin and D. L. Bryce, *Chem. Commun.*, 2017, **53**, 9930(**DOI:** 10.1039/C7CC05051H). –Reproduced by permission of The Royal Society of Chemistry.

7.1 Introduction

Cocrystals contain two or more neutral solid molecular species that are present in definite stoichiometric amounts.[1] They are constructed by non-covalent interactions such as hydrogen bonding, π-stacking, halogen bonding, etc.[2] There continues to be marked interest in halogen bonding interactions[3] since halogen bonds (XB) can be comparable in strength to hydrogen bonds,[4] and highly directional as elucidated by the σ–hole model.[5] Methods of laboratory mechanochemical synthesis of various materials including cocrystals, such as liquid-assisted grinding (LAG) and ion and liquid-assisted grinding (ILAG), have attracted increased attention during last decade[6,7] due to the fact that chemical processes can be accelerated and the use of solvent can be minimised to decrease the generation of waste better than traditional solvent-based crystallization. However, the mechanistic details of such processes remain poorly understood. This relates to the practical reason that reactions involving milling are normally studied ex situ, whereby the milling process is periodically interrupted so that the mixture may be analysed by *e.g.*, X-ray diffraction or solid-state nuclear magnetic resonance (SSNMR) spectroscopy. However, it is known that chemical transformations can continue after the milling process,[8] which makes ex situ methods less reliable. Thus, it is expected that in situ monitoring will provide additional insight into the mechanochemical processes and the roles that liquid and salts play during the reaction. Recent in situ investigations of mechanochemical processes have been reported using Raman spectroscopy[9] and synchrotron X-ray diffraction.[10,11] Whereas diffraction based experiments perform poorly in samples with low

crystallinity and amorphous phases, SSNMR, which is able to directly report on amorphous components of a mixture, may provide some additional insights.[12] Even though previous *in-situ* SSNMR studies on crystallization and dehydration processes[13,14,15,16] or in electrochemical cells[17] have been reported, high-resolution in situ SSNMR monitoring of reactions requiring milling seems impractical because the standard ball milling apparatus is incompatible with the confined space and high magnetic fields used for magic-angle spinning (MAS) NMR, whereby the sample is sealed and packed into a small rotor, and highly stable spinning on the order of at least several kHz is required. We have probed the relation between various NMR parameters and the halogen bond in a series of solids featuring P=O···I–C motifs in the previous chapters.[18] However, in that ex situ study, we were only able to characterize the starting and final time points, but not the real-time mechanistic aspects of the actual crystallization process.

Mechanochemical reactions which occur in the absence of grinding have been documented previously.[19] Here, we report a real-time in situ study of the crystallization process that occurs between triphenylphosphine oxide (Ph_3PO) and *para*-diiodotetrafluorobenzene (*p*-$C_6F_4I_2$) without milling by ^{31}P cross-polarization magic-angle spinning (CP/MAS) SSNMR spectroscopy. This provides an opportunity to track the formation of halogen bonds in real time and observe the interconversion between two distinct halogen-bonded cocrystal products. More importantly, by carrying out multiple series of experiments under various conditions, the kinetic mechanism of halogen bond formation can be assessed. The roles that temperature, pressure, and added liquid play in the crystallization process

can be investigated, and the activation energy can be estimated based on the temperature-dependence of the kinetic rate.

7.2 **Experimental Section**

7.2.1 Sample Preparation

Triphenylphosphine oxide (Ph_3PO) and *para*-diiodotetrafluorobenzene (*p*-$C_6F_4I_2$) were purchased from Sigma Aldrich. *p*-$C_6F_4I_2$ was used without any further purification, but Ph_3PO was recrystallized from acetone to give a pure monoclinic polymorph. Equimolar amounts of these two starting materials were dissolved into a minimum volume of acetonitrile. Slow evaporation from acetonitrile at room temperature produced a pure crystal of **1**, and evaporation by boiling acetonitrile gave a crystal of **2**. The procedure to set up for an *in-situ* SSNMR experiment is adapted from previous literature.[20] The two starting materials were pre-ground into fine powders separately using a mortar and pestle. To initiate the reaction, 0.0661 g of pre-ground Ph_3PO was gently mixed with 0.0955 g of pre-ground *p*-$C_6F_4I_2$ followed immediately by the addition at time t = 0 of different volumes of acetonitrile (5 μL for temperature and spinning speed studies; and 0, 3, and 4 μL for liquid effect studies). The mixture was immediately vortexed for 10 seconds at top speed using a benchtop vortexer. Then the mixture of powders was immediately packed into a 4 mm o.d. zirconia rotor followed by normal sample spinning and NMR data acquisition. There was a 20 to 30 minute gap (t_0) between the initiation of the cocrystallization and the end of the acquisition of the first NMR spectrum.

7.2.2 In situ ^{31}P Solid-State NMR Spectroscopy

Data were acquired with a 9.4 T magnet, Bruker AVANCE III console, and a 4 mm Bruker HXY probe (University of Ottawa, Ottawa, Canada). ^{31}P chemical shifts were referenced to ammonium dihydrogen phosphate (δ_{iso} = 0.81 ppm with respect to 85% H_3PO_4). A standard cross-polarization pulse sequence was employed. The $\pi/2$ pulse length and contact time were 3.4 μs and 2 ms, respectively. The recycle delay was set to be 2 minutes and the number of scan was 8 for each spectrum. The sample temperature for all the experiments was calibrated using the ^{207}Pb resonance of lead nitrate.[21] The temperature was held constant where required by heating and cooling regulated by an FTS Systems TC-84 temperature controller. In order to study the effect of temperature on the reaction, a series of in situ ^{31}P CP/MAS experiments was performed at temperatures of 15, 25, and 35 ℃ at a spinning frequency of 10 kHz. In order to investigate the effect of pressure produced by MAS, experiments were carried out at constant temperature (25 ℃) and various MAS rates (8, 10, and 12 kHz). To observe the effect of different amounts of acetonitrile added, the reaction was started by adding 0, 3 (24 mol%), or 4 (32 mol%) μL of liquid and then monitored at 45 ℃ at a 10 kHz spinning speed. The relative CP efficiencies of different compounds were measured. Exactly 0.0850 g starting material (monoclinic Ph_3PO), 0.1571 g compound **1** and 0.0981 g **2** were packed separately into 4 mm o.d. zirconia rotors. The ^{31}P CP/MAS NMR spectra of three compounds were recorded using the same data collection parameters. The resulting isotropic peak integrals were measured to compare the different CP efficiencies.

7.2.3 Powder X-ray Diffraction

All PXRD patterns were obtained using a Rigaku Ultima IV powder diffractometer at room temperature (298 ± 1 K) with a copper source and one diffracted beam monochromator from 5° to 50° (2θ range) in increments of 0.02° with a scan rate of 1° per minute. Simulations were generated using Mercury 3.8 software from the Crystallographic Data Center.

7.2.4 CASTEP Calculations

The ^{31}P magnetic shielding tensors were calculated using CASTEP software version 4.4[22] on the Wooki cluster at the University of Ottawa. The input file generated from Materials Studio v. 4.4 (Accelrys) used the generalized gradient approximation (GGA) with the functional of Perdew Burke Ernzerhof (PBE)[23] and "on-the-fly" pseudopotentials to perform the geometry optimization of the hydrogen positions followed by NMR calculation. The cut-off energy of 610.0 eV and the *k*-point grid of 2×1×1 were used. Gauge-including projector-augmented wave density functional theory (GIPAW DFT)[24] calculations were applied to calculate all the NMR parameters, which were extracted from the CASTEP NMR output file using EFGShield version 4.2.[25]

7.2.5 Single-crystal X-ray diffraction

The crystal of **2** was mounted on a thin glass fiber using paraffin oil. Prior to data collection the crystal was cooled to 200 ± 2 K. Data was collected on Bruker AXS single crystal diffractometer equipped with a sealed Mo tube source (wavelength 0.71073 Å) and APEX II CCD detector. Raw data collection and processing were performed with Bruker APEX II software package.[26] Semi-empirical absorption corrections based on equivalent

reflections were applied.[27] Systematic absences in the diffraction dataset and unit cell parameters were consistent with triclinic $P\bar{1}$ (#2) space group. The structure was solved by direct methods and refined with a full-matrix least-squares procedure based on F^2, using SHELXL[28] and WinGX[29]. All non-hydrogen atoms were refined anisotropically. The positions of hydrogen atoms were calculated based on the geometry of related non-hydrogen atoms.

The compound crystallizes with 3 Ph_3PO and 2.5 *p*-$C_6F_4I_2$ molecules in the asymmetric unit. One of the *p*-$C_6F_4I_2$ molecules lies on an inversion centre. No additional restraints or constraints were applied during the refinement.

7.3 Results and Discussion

There are two distinct halogen-bonded cocrystals (**1** and **2**) formed from the same halogen bond donor (*p*-$C_6F_4I_2$) and acceptor (Ph_3PO) pair (see Figure 7.3.1(a)). Slow evaporation from acetonitrile at room temperature produced a pure crystal of **1**, and evaporation from boiling acetonitrile gave a crystal of **2**. Both structures are different from the previously reported zig-zag halogen-bonded chain.[30] Monoclinic **1** has been reported previously.[18] A new structure, **2**, packs in the triclinic crystal system ($P\bar{1}$ space group; Figure 7.3.1(b)). Crystallographic data for **2** and several selected intermolecular contact distances and angles are summarized in the Table E1 and Table E2. These data were used to characterize the XB geometry. This new cocrystal contains three crystallographically distinct halogen bonds in which one of the oxygens acts as a bifurcated halogen bond acceptor (**2_1**) interacting with two iodine atoms. Another iodine in one of these *p*-$C_6F_4I_2$ molecules forms a second halogen bond with a different Ph_3PO (**2_3**) molecule. The final Ph_3PO molecule

(**2_2**) has the shortest I···O contact with the third *p*-$C_6F_4I_2$. The phase purity of **2** was verified by X-ray powder diffraction (Figure E1).

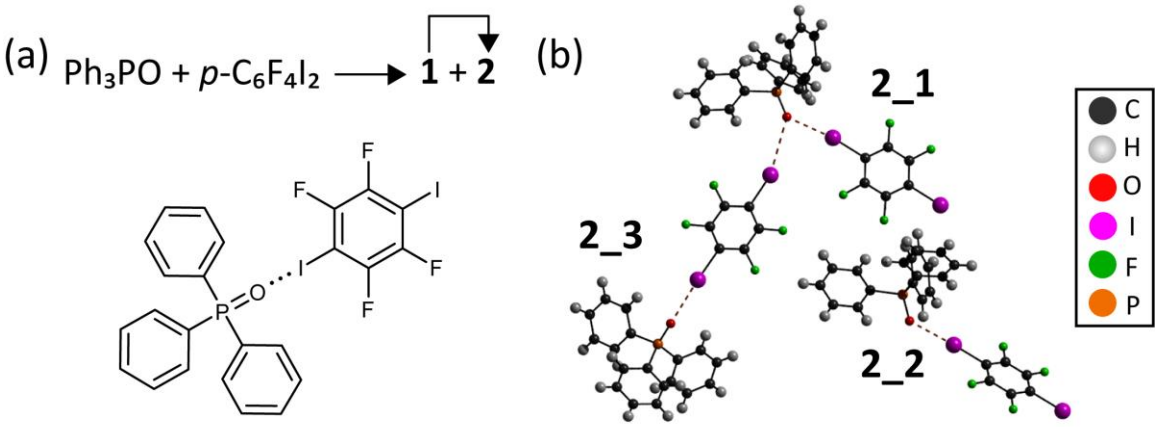

Figure 7.3.1 . (a) Formation of two XB cocrystals and the chemical structures of the XB acceptor and donor. (b) Crystallographic structure of **2** from SCXRD.

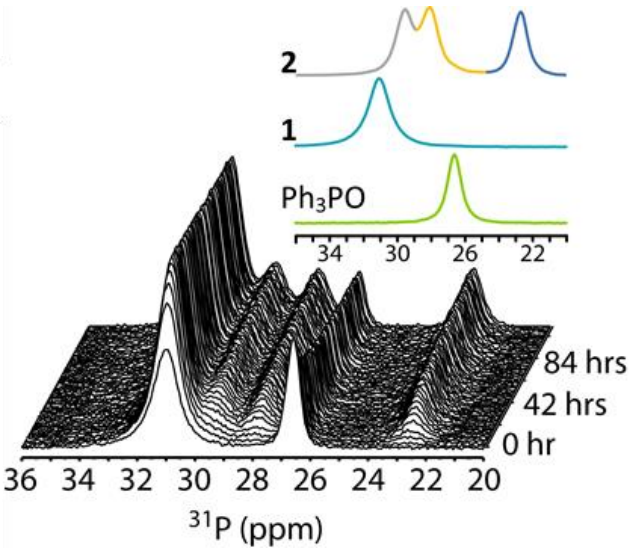

Figure 7.3.2. In situ ^{31}P CP/MAS SSNMR spectra of the reacting Ph_3PO and *p*-$C_6F_4I_2$ at 35 °C. B_0 = 9.4 T; ν_{MAS} = 10 kHz. 5 μL CH_3CN was added initially. The isotropic peaks

are shown. Inset: Experimental ^{31}P CP/MAS SSNMR spectra of monoclinic Ph_3PO (green), pure **1** (turquoise) and pure **2**.

The ^{31}P CP/MAS NMR spectra of the pure starting material (monoclinic Ph_3PO; δ_{iso} = 26.6 ppm) and the two pure halogen-bonded cocrystals obtained by slow evaporation from CH_3CN are presented in the inset in Figure 7.3.2. **1** has a δ_{iso} value of 30.7 ppm, consistent with the literature.[18] As shown in Figure 7.3.1, there are three crystallographically distinct Ph_3PO molecules involved in halogen bonds in **2**. This is further supported by the observation of three distinct ^{31}P chemical shifts (22.7 ppm (blue), 28.1 ppm (yellow) and 29.6 ppm (grey)). The resonances have been assigned to each phosphorus atom based on GIPAW DFT calculations.

Mechanochemical synthesis of **1** was attempted by ball milling equimolar amounts of Ph_3PO and *p*-$C_6F_4I_2$ with different liquids at 30 Hz in 25 mL stainless steel milling jars for 1 h. Under various conditions, the final product was consistently a mixture of **1** and **2** (see PXRD and ^{31}P CP/MAS data in Figure E2). We noted that the reaction producing these two cocrystals could be started under relatively mild conditions without any milling, and proceeded to directly monitor the formation of and the interconversion between these two cocrystals via in situ ^{31}P CP/MAS SSNMR. It is well known that fast MAS can increase the temperature inside the rotor; therefore, the true temperature of the sample was calibrated using the ^{207}Pb resonance of lead nitrate. Several reaction conditions were examined. Cocrystallization was initiated in the same way each time (dry powders were physically mixed then vortexed), but studied either at different sample temperatures (15, 25, and 35 ℃) with the same spinning speed (10 kHz) or at constant temperature

(25 ℃) with different MAS frequencies (8, 10, and 12 kHz). The 100% natural abundance of the ^{31}P isotope provides an intense signal, which allowed us to take a snapshot of the reacting mixture every 16 min with 8 scans. Each process under different conditions was monitored for at least 60 h. In situ three-dimensional plots of ^{31}P CP/MAS SSNMR spectra of the reacting mixture under different conditions are shown in Figure E3 in Appendix E. The result obtained at 35 ℃ at a spinning speed of 10 kHz is given as an example in Figure 7.3.2 and the corresponding plot of normalized peak integrals as a function of time is given in Figure 7.3.3(c). No detectable amorphous phase was present during the crystallization, as no broad peaks were identified and the sum of the peak integrals remained constant (see black trace in Figure 7.3.3(c)). The formation of **1** can be observed, and indeed this crystallization began even before the first spectrum was taken. Furthermore, the formation of **2** was seen after 2 h as evidenced by its corresponding three ^{31}P resonances.

Integrals of the deconvoluted peaks were normalized by multiplying the peak integration by a CP efficiency factor, as explained in Section 7.2.2. The normalized peak integrals from all in situ ^{31}P experiments were plotted as a function of time. As shown in Figure 7.3.3, the normalized peak integrals for Ph_3PO vary logarithmically with time under all conditions. The rate of formation of **1** and consumption of Ph_3PO increases when either the sample temperature or the MAS rate is increased. More interestingly, the formation of **2** can be observed after 128 minutes when the reaction temperature is increased to 35 ℃ (Figure 7.3.3 (c)). The slight decrease in the normalized integral of the signal for **1** and more significant increase for **2** after

around 16.5 h (Figure E4 in Appendix E) indicate that the formation of **2** arises from both the crystallization of the starting materials and the conversion from **1** (see Figure 7.3.1(a)). Furthermore, the effect from the amount of liquid added on the crystallization process was assessed by monitoring the spectra at 45 ℃ and a 10 kHz MAS rate with varying amounts of CH_3CN (0, 3, and 4 μL (Figure 7.3.3, liquid)). An increasing amount of liquid also results in more complete conversion. With the addition of 4 μL of CH_3CN, the formation of **2** can be observed after approximately 5 h.

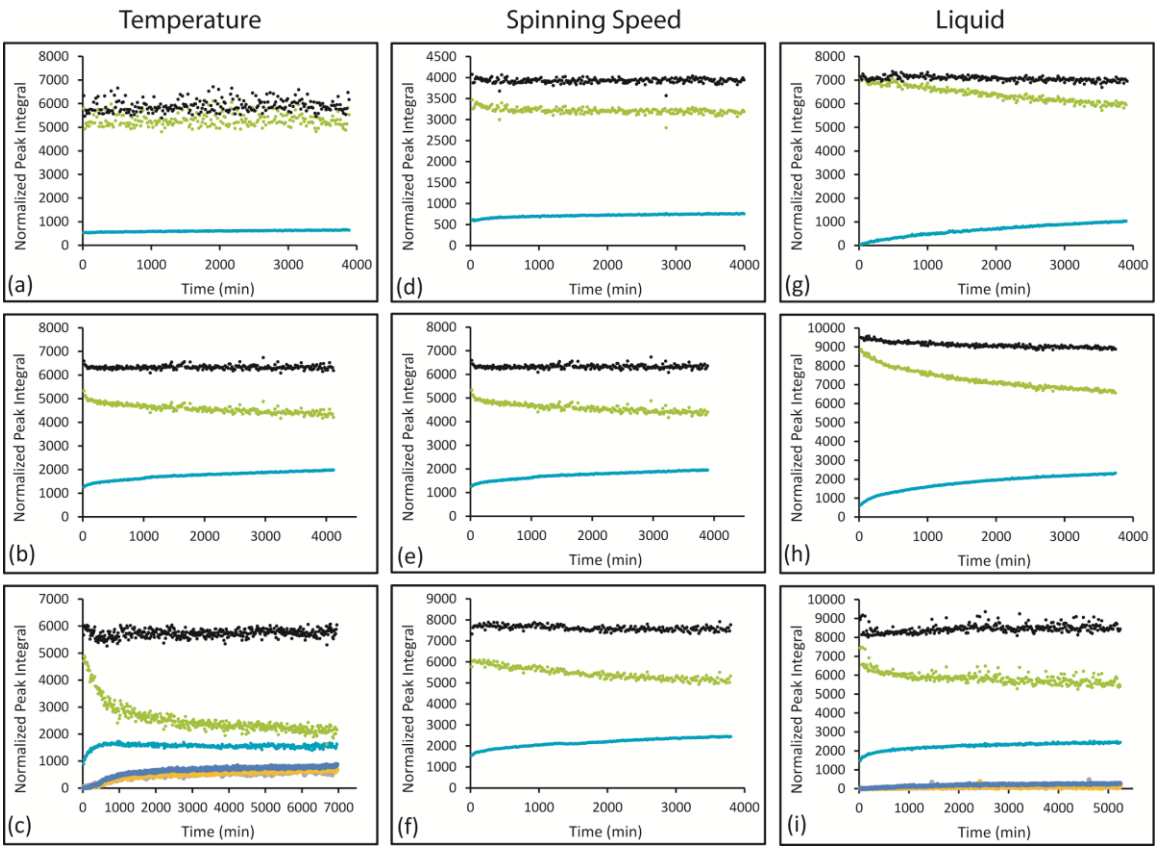

Figure 7.3.3. Time-resolved changes in the normalized peak integrals for the isotropic peaks of the starting material Ph_3PO (δ_{iso} = 26.6 ppm) shown in green, halogen-bonded cocrystal **1** (δ_{iso} = 30.7 ppm) shown in turquoise and **2** (δ_{iso} = 22.7 ppm, δ_{iso} = 28.1 ppm,

and δ_{iso} = 29.6 ppm) shown in blue, yellow, and grey, respectively, under different conditions: (a) at 15 ℃ with a 10 kHz spinning speed and an addition of 5 μL acetonitrile, (b) at 25 ℃ with a 10 kHz spinning speed and an addition of 5 μL acetonitrile, (c) at 35 ℃ with a 10 kHz spinning speed and an addition of 5 μL acetonitrile, (d) at 25 ℃ with a 8 kHz spinning speed and an addition of 5 μL acetonitrile, (e) at 25 ℃ with a 10 kHz spinning speed and an addition of 5 μL acetonitrile, (f) at 25 ℃ with a 12 kHz spinning speed and an addition of 5 μL acetonitrile, (g) at 45 ℃ with a 10 kHz spinning speed and no liquid, (h) at 45 ℃ with a 10 kHz spinning speed and an addition of 3 μL acetonitrile, and (i) at 45 ℃ with a 10 kHz spinning speed and an addition of 4 μL acetonitrile. The sum of all the peak integrals (black) remains constant, indicating the absence of amorphous intermediate.

Understanding the mechanisms that underlie mechanochemical reactions and whether varying the reaction conditions can change the mechanism can help one not only control the final product but also maximize the benefits of such reactions. Khawam and Flanagan classified and summarized solid-state reaction mechanism models into four categories:[31]: nucleation (A2 to A4), geometrical contraction (R2 and R3), diffusion (D1 to D4) and reaction order (F1 to F3) models. The reaction models are differentiated using the conversion fraction, α, which represents the fraction of complete conversion at a given time *t*, is defined by

$$\alpha = \frac{m_0 - m_t}{m_0 - m_\infty} \qquad \text{Eq 7.3.1}$$

where m_0 is initial weight, m_t is weight at time *t*, and m_∞ is final weight.

To account for the product formed before the first spectrum is recorded, the conversion fraction, α, is modified here as:

$$\alpha = \frac{I_0 - I_t}{I_0 - I_{max}} \qquad \text{Eq 7.3.2}$$

where I_0 is the initial normalized peak integral, I_t is the normalized peak integral at time *t*, and I_{max} is the maximum normalized peak integral. Also, a reduced time parameter is introduced, $t' = t - t_0$, where *t* is the experimental time starting from the point when the two starting materials were mixed together before vortexing, and t_0 is the time taken before the first spectrum was obtained. Determination of which model best fit the data was made by comparing the correlation coefficient (R^2) of the plot for each integrated rate equation (Table E3) as a function of *t'* for each model. Since the formation of **2** involves both direct cocrystallization as well as conversion from **1**, the formation of **2** cannot be explained simply by one mechanism. Therefore, only the α values for **1** have been linearized to 12 different kinetic models (Figure E5–Figure E12 in Appendix E). Although it is clear that a kinetic analysis alone cannot unequivocally provide a detailed reaction mechanism, this analysis revealed that the diffusion models, reaction order models, and contracting volume model R3 provided similarly high R^2 values. Especially in the cases of liquid effect analyses (Figure E10-Figure E12), large R^2 values for most of the diffusion, reaction order, and geometrical contraction models mean that it is difficult to unambiguously identify the main mechanism. Fortunately, the Sharp-Hancock (SH) plot, a plot of $\ln(-(\ln(1-\alpha)))$ as a function of $\ln(t')$, derived from the Johnson-Mehl-Avrami-Yerofeev-Kolmogrov (JMAYK) equation can provide distinct Avrami exponents, *n*, which differ greatly among different models.[31,32] Therefore, JMAYK analyses were also performed for each set of conditions to further assess the best mechanistic model (Figure 7.3.4(b), (d), (f)). All the *n* values, obtained from the slope of each SH plot, are summarized in Table 7.3.1. By

combining the R^2 values from the best fits and the slope values less than 1 obtained from JMAYK analysis, we conclude that the reaction mechanisms are predominantly diffusion-controlled.[32] When **2** starts forming, **1** undergoes two processes: formation from the crystallization process and consumption from conversion to **2**. Therefore, the analyses of **1** at 35 °C and 45 °C are treated with caution by only including the data before the formation of **2**. For the temperature study, the linearity of the plot and *n* values (ranging from 0.67 to 0.82) suggest that the mechanism remains one dimensional diffusion controlled (D1 model). The plot according to the D1 model at different temperatures is given in Figure 7.3.4 (a), where the rate constants can be determined from the slopes of the linear plots and are summarized in Table 7.3.1. The larger k value at higher temperature (increasing from 0.192×10^{-3} min^{-1} at 15 ℃ to 1.55×10^{-3} min^{-1} at 35 ℃) confirms that by increasing the temperature, the reaction rate can be accelerated. Given that one mechanism remains operative over this temperature range, it is valid to estimate the activation energy (E_a) for the formation of **1** based on the temperature dependence of the reaction rate, k. An Arrhenius plot of ln k versus $1/T$ is given in Figure 7.3.4 (h). The slope provides the value of $-E_a/R$, which gives an approximate E_a of 76 ± 38 kJ/mol, which may be compared to the apparent activation energy of the neat grinding synthesis of the ibuprofen:nicotinamide cocrystal in a ball mill (15 ± 6 kJ/mol).[33] It has been observed previously that mechanical milling can lower the apparent activation energy.[34] The large error on the reported activation energy follows from the linear regression algorithm used to fit the somewhat non-linear data. Limitations in the accuracy and precision of the value of the activation energy may arise from several factors. Two of the important factors presently are: (1) possible inherently non-linear (non-Arrhenius) behavior of the reaction, meaning that

fitting the data with a straight line necessarily results in significant error; (2) possible non-uniform particle size distribution (Our particles were prepared by simple grinding with a mortar and pestle, and the same batch was used for all experiments; however, there is likely a distribution of particle sizes (μm scale). Particle size was not investigated as a variable in this work, but we fully expect that the kinetics of the reaction may change as the particle size, and thus surface area, is changed).

Table 7.3.1. Kinetics Parameters for the Formation of **1**.

	Conditions	n[a]	k (10^{-3} min^{-1})[b]	E_a (kJ·mol^{-1})
Temperature effect[c]	15 ℃	0.82 ± 0.02	0.192 ± 0.004	76 ± 38
	25 ℃	0.67 ± 0.01	0.231 ± 0.002	
	35 ℃	0.70 ± 0.07	1.55 ± 0.25	
MAS rate[d]	8 kHz	0.75 ± 0.02	0.193 ± 0.003	---
	10 kHz	0.67 ± 0.01	0.231 ± 0.002	---
	12 kHz	0.64 ± 0.01	0.263 ± 0.002	---
Liquid effect[e]	0 μL	0.85 ± 0.03	0.142 ± 0.006[f]	---
	3 μL	0.75 ± 0.01	0.347 ± 0.006	---
	4 μL	0.57 ± 0.01	0.323 ± 0.002[g]	---

[a] Avrami exponent, obtained from the slope of Sharp-Hancock plots

[b] rate constant determined from the slope of the D1 model plots except where indicated.

[c] ν_{MAS} = 10 kHz. 5μL CH_3CN was added initially.

[d] T = 25 ℃, 5μL CH_3CN was added initially.

[e] ν_{MAS} = 10 kHz, T = 45 ℃,

[f] The F1 model provides an equally good fit and gives k = 0.62 ± 0.01; this suggest that nucleation plays a role when no liquid is added.

[g] k is determined from the slope of the D2 model; using the D4 model gives a value of 0.077 ± 0.002.

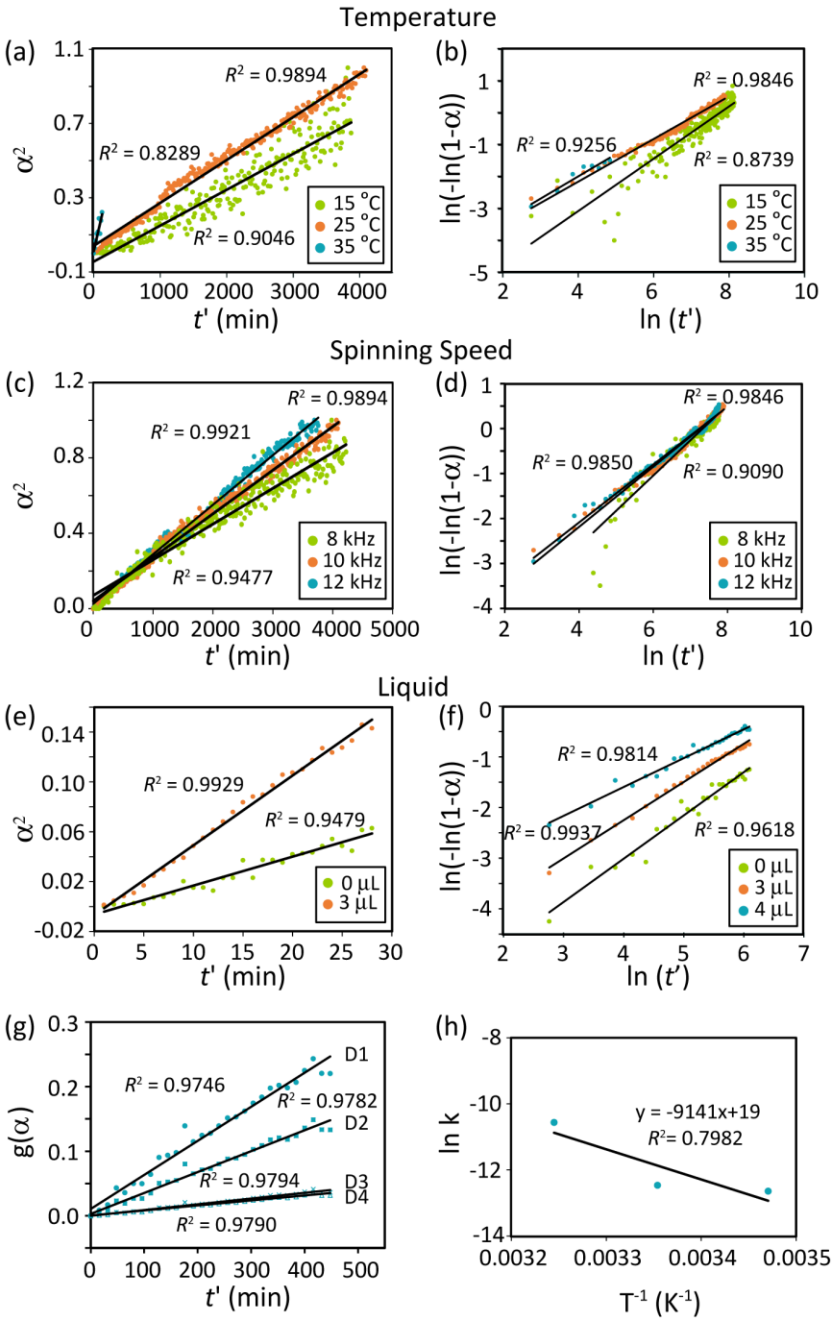

Figure 7.3.4. The fitting of α for the formation of **1** under different conditions: different temperatures (a), different spinning speeds (c), and different amounts of liquid added (e), after linearizing to the D1 model. The SH plots of JMAYK analyses for the formation of **1** under different conditions: different temperatures (b), different spinning speeds (d), and different amounts of liquid added (f). (g) Diffusion model plots for D1(•), D2(■), D3(×) and D4 (Δ) kinetics in the formation of **1** with an addition of 4 μL CH_3CN. $g(\alpha)$ is the

integral reaction model, varying for the various model (for example $g(\alpha) = \alpha^2$ for D1 model). $g(\alpha)$ functions for different models are summarized in Table E3. (h) Arrhenius plot to determine the activation energy for the cocrystallization of **1**. The k values are obtained from the slopes in plot (a).

The α values obtained from in situ ^{31}P CP/MAS experiments with different spinning speeds (8 kHz to 12 kHz), but constant temperature, have been linearized to 12 kinetic models. The $R^2 \sim 1$ values from the model plots (see Figure E6, Figure E8 and Figure E9) and *n* values ranging from 0.64 to 0.75, which are determined from the slopes of the corresponding SH plots (see Figure 7.3.4 (d)) support the notion that the mechanism is one-dimensional diffusion controlled. The plot of the 1D diffusion function for different MAS rates (8 kHz in green, 10 kHz in orange and 12 kHz in turquoise) is given in Figure 7.3.4 (c). Again, an increase in k with MAS rate (from 0.193×10^{-3} min^{-1} at 8 kHz spinning speed to 0.263×10^{-3} min^{-1} at 12 kHz) indicates that the pressure produced by MAS experiment can also speed up the reaction. The pressure at the rotor wall is estimated to be on the order of ~50 atm at 8 kHz and 100 atm at 12 kHz.[35]

Plots of the diffusion function for different amounts of liquid added (none, 3 μL (24 mol%), and 4 μL (32 mol%)) are given in Figure E10-Figure E12. The best fits for no liquid and an addition of 3 μL were both obtained with the D1 model (Figure 7.3.4 (e)), which is further confirmed by *n* values of 0.85 and 0.75, respectively, from the SH plots (Figure 7.3.4(f)). However, a change in kinetic model for the addition of 4 μL is evident in the lower *n* value of 0.57 and the better fit to a higher-dimensional diffusion model. As shown in Figure 7.3.4(g), it is difficult to distinguish which diffusion model dominates after 4 μL of CH_3CN was added based only on R^2 values. However, the *n* value suggests that the mechanism

is more likely to be D2 or D4.[32] All the changes in rate constant and Avrami exponents provide evidence that the amount of liquid added not only speeds up the reaction rate but also changes the kinetic mechanism from lower-dimensional diffusion to higher-dimensional diffusion. Increased orientational and conformational freedom introduced by liquid[36] allows diffusion to occur in higher dimensions instead of simply in a flat plane.

7.4 Conclusion

We have presented a real-time in situ SSNMR analysis of halogen bond formation resulting in two cocrystal products. By varying the sample temperature, the spinning rate, and the amount of liquid added, ^{31}P in situ SSNMR has provided information on the different formation rates of these two halogen-bonded cocrystals. The data are consistent with a reaction mechanism which is mainly diffusion controlled. This study provides a simple procedure for real-time monitoring of mechanochemical processes, as long as the rate and nature of the reaction is such that active milling is not required.

7.5 References for Chapter 7

[1] Aitipamula, S.; et al., *Cryst. Growth Des.* **2012**, *12*, 2147–2152.

[2] Aakeröy, C. B.; Salmon, D. J. *CrystEngComm* **2005**, *7*, 439–448.

[3] Gilday, L. C.; Robinson, S. W.; Barendt, T. A.; Langton, M. J.; Mullaney B. R.; Beer, P. D. *Chem. Rev.* **2015**, *115*, 7118–7195.

[4] Metrangolo, P.; Meyer, F.; Pilati, T.; Resnati, G.; Terraneo, G. *Angew. Chem., Int. Ed.* **2008**, *47*, 6114–6127.

[5] Clark, T.; Hennemann, M.; Murray, J. S.; Politzer, P. *J. Mol. Model* **2007**, *13*, 291–296.

[6] Friščić, T. *J. Mater. Chem.* **2010**, *20*, 7599–7605.

[7] Friščić, T. *Chem. Soc. Rev.* **2012**, *41*, 3493–3510.

[8] Ibrahim, A. Y.; Forbes, R. T.; Blagden, N. *CrystEngComm* **2011**, *13*, 1141–1152.

[9] Batzdorf, L.; Fischer, F.; Wilke, M.; Wenzel, K. -J.; Emmerling, F. *Angew. Chem., Int. Ed.* **2015**, *54*, 1799–1802.

[10] Friščić, T.; Halasz, I.; Beldon, P. J.; Belenguer, A. M.; Adams, F.; Kimber, S. A. J.; Honkimäki, V.; Dinnebier, R. E. *Nat. Chem.* **2013**, *5*, 66–73.

[11] Halasz, I.; Kimber, S. A. J.; Beldon, P. J.; Belenguer, A. M.; Adams, F.; Honkimäki, V.; Nightingale, R. C.; Dinnebier, R. E.; Friščić, T. *Nat. Protoc.* **2013**, *8*, 1718–1729.

[12] Xu, Y.; Southern, S. A.; Szell, P. M. J.; Bryce, D. L. *CrystEngComm* **2016**, *18*, 5236–5252.

[13] Hughes, C. E.; Williams, P. A.; Harris, K. D. M. *Angew. Chem., Int. Ed.* **2014**, *53*, 8939–8943.

[14] Harris, K. D. M.; Hughes, C. E.; Williams, P. A. *Solid State Nucl. Magn. Reson.* **2015**,

65, 107–113.

[15] Hughes, C. E.; Williams, P. A.; Peskett, T. R.; Harris, K. D. M. *J. Phys. Chem. Lett.* **2012**, *3*, 3176–3181.

[16] Xu, M.; Harris, K. D. M. *J. Am. Chem. Soc.* **2005**, *127*, 10832–10833.

[17] Blanc, F.; Leskes, M.; Grey, C. P. *Acc. Chem. Res.* **2013**, *46*, 1952–1963.

[18] Xu, Y.; Viger-Gravel, J.; Korobkov, I.; Bryce, D. L. *J. Phys. Chem. C* **2015**, *119*, 27104–27117.

[19] Chadwick, K.; Davey, R.; Cross, W. *CrystEngComm* **2007**, *9*, 732–734.

[20] Mandala, V. S.; Loewus, S. J.; Mehta, M. A. *J. Phys. Chem. Lett.* **2014**, *5*, 3340–3344.

[21] Neue, G.; Dybowski, C. *Solid State Nucl. Magn. Reson.* **1997**, *7*, 333–336.

[22] Segall, M. D.; Lindan, P. J. D.; Probert, M. J.; Pickard, C. J.; Hasnip, P. J.; Clark, S. J.; Payne, M. C. *J. Phys. Condens. Matter* **2002**, *14*, 2717–2744.

[23] Perdew, J. P.; Burke, K.; Ernzerhof, M. *Phys. Rev. Lett.* **1996**, *77*, 3865–3868.

[24] Bonhomme, C.; Gervais, C.; Babonneau, F.; Coelho, C.; Pourpoint, F.; Azaïs, T.; Ashbrook, S. E.; Griffin, J. M.; Yates, J. R.; Mauri, F.; Pickard, C. J. *Chem. Rev.* **2012**, *112*, 5733– 5779.

[25] Adiga, S.; Aebi, D.; Bryce, D. L. *Can. J. Chem.*, **2007**, *85*, 496–505.

[26] APEX 2, Bruker AXS Inc.: Madison, Wisconsin, USA, 2012.

[27] Sheldrick, G. M. SADABS, Program for empirical X-ray absorption correction, Bruker AXS Inc.: Madison, Wisconsin, USA, 2004.

[28] Sheldrick, G. M. *Acta Crystallogr. C* **2015**, *71*, 3–8.

[29] Farrugia, L. J. *J. Appl. Crystallogr.* **1999**, *32*, 837–838.

[30] Cinčić, D.; Friščić, T.; Jones, W. *CrystEngComm* **2011**, *13*, 3224–3231.

[31] Khawam, A.; Flanagan, D. R. *J. Phys. Chem. B* **2006**, *110*, 17315–17328.

[32] Hancock, J. D.; Sharp, J. H. *J. Am. Ceram. Soc.* **1972**, *55*, 74–77.

[33] Fischer, F.; Wenzel, K. -J.; Rademann, K.; Emmerling, F. *Phys. Chem. Chem. Phys.* **2016**, *18*, 23320–23325.

[34] Oliveira, P. F. M.; Baron, M.; Chamayou, A.; Baltas, M.; Guidetti, B.; Haruta, N.; Tanaka, K.; Sato, T. *ChemistrySelect* **2016**, *5*, 984–988.

[35] Hughes, C. E.; Williams, P. A.; Keast, V. L.; Charalampopoulos, V. G.; Edwards-Gau, G. R.; Harris, K. D. M. *Faraday Discuss.* **2015**, *179*, 115–140.

[36] Shan, N.; Toda, F.; Jones, W. *Chem. Commun.* **2002**, *1*, 2372–2373.

PART 5 CONCLUSIONS

Conclusions

Solid-state NMR has been used extensively to probe the formation and structure of halogen bonds. It has been a complementary tool combined with other methods, such as X-ray diffraction and quantum chemical calculations, to characterize the halogen bonding interaction. The solid-state NMR analyses have largely focused on effects of halogen bonding on various NMR parameters, including chemical shifts, quadrupolar coupling interaction, *J* coupling interaction, and relaxation times. The resulting effects either can be used to confirm the formation of halogen bonds or can elucidate several trends relating the NMR observables to the local molecular and electronic structure of the halogen bond.[1,2,3,4] All of these results have been obtained from the conventional polycrystalline NMR experiments. While these standard techniques can provide yield the magnitude of each NMR parameters, they are only able to characterize the starting and final time points of a reaction; also, the absolute orientation of each NMR tensor in the molecular frame is lost.

In this dissertation, three different solid-state NMR methods helped us understand the halogen bonding interaction from different perspectives. In addition to conventional polycrystalline NMR experiments, single-crystal NMR was employed to allow for the measurement of not only the magnitudes but also the orientations of various NMR interaction tensors relative to the halogen bonds. An in situ solid-state NMR was able to provide the real-time mechanistic characterization of the halogen bond cocrystallization process.

In Part 2, polycrystalline solid-state NMR experiments demonstrated how the magnitude of NMR observables respond upon the formation of halogen bonds. In Chapter 3, we have applied a combination of solid-state NMR, X-ray diffraction and DFT calculation to investigate the halogen-bonded cocrystal featuring P=O···I–C motifs. Five new halogen-bonded cocrystals were synthesized by simple mechanochemistry and solvent-based evaporation. The ^{31}P NMR experiments revealed a small increase in chemical shift and a small decrease in span upon halogen bond formation. Multinuclear (^{31}P and ^{17}O) magnetic resonance spectroscopies performed on ^{17}O-labeled compounds show a decrease in $J(^{31}P, ^{17}O)$ coupling and an increase in both ^{17}O quadrupolar coupling constant and asymmetry parameter in the presence of a halogen bonding interaction. A natural localized molecular orbital analysis revealed that the three main orbital contributions to $J(^{31}P, ^{17}O)$ coupling: the P=O bonding orbital, the oxygen lone pair orbital, and oxygen core orbitals, all together determined the overall trend observed experimentally for $J(^{31}P, ^{17}O)$ coupling. Further NLMO showed a linear correlation between the contribution of one oxygen lone pair orbital, which has lobes oriented towards the halogen bond, to the ^{17}O quadrupolar coupling constant and halogen bond distance. Chapter 4 provided a rare engineered cocrystal featuring phosphorus as a halogen bond acceptor and iodine as a halogen bond donor, which was characterized by single-crystal X-ray diffraction. A decrease in chemical shift in both ^{31}P solution- and solid-state NMR experiments and a reduction of ^{31}P span in solid-state NMR analysis indicated the presence of close P···I contact in both solution and solid states. Phosphine acting as a halogen bond donor can open up a new direction in crystal engineering.

Part 3 has established single-crystal NMR spectroscopy as a novel tool to characterize the halogen bond. Chapter 5 applied ^{31}P and ^{17}O single-crystal NMR experiments on the ^{17}O-labeled halogen bond formed between triphenylphosphine oxide and iodoperfluorobenzene derivatives. The absolute orientation of various NMR interaction tensor in the molecular frame, determined from single-crystal NMR experiments, revealed that the angular deviations in the directions of the unique components of the ^{31}P chemical shift tensors, the ^{17}O chemical shift tensors, and the ^{17}O quadrupolar coupling tensors from the direction of the oxygen–iodine halogen bond correlate with the P–O···I halogen bond angle. There is also a clear decrease in anisotropy and an increase in asymmetry of the $J(^{31}P,^{17}O)$ coupling tensors attributable to the formation of iodine–oxygen halogen bonds. Chapter 6 included the implementation of a software package for the analysis of single-crystal NMR data, SCFit. This software can analyze the NMR data resulting from various NMR interaction, including chemical shift tensor only, a combined effect from chemical shift tensor and quadrupolar coupling tensor, dipolar and indirect nuclear spin-spin coupling tensor, and all four interaction. It also can fit the chemical shift and quadrupolar coupling in two ways: (i) either through an unconstrained fitting process where all tensor parameters are freely optimized or (ii) through a constrained fitting process where the principal components of the tensors may be fixed to values previously known via the analysis of polycrystalline NMR experiments. A comparison between these two fitting strategies improved the precision of the resulting tensor orientations in some cases.

Part 4 provided a real-time in situ observation of the crystallization process that occurred to form a halogen bonding interaction by varying the sample temperature, the

spinning rate, and the amount of liquid added to initiate reaction. In situ ^{31}P solid-state NMR studies, present in Chapter 7, have provided information on the different formation rates of the halogen-bonded cocrystals formed between triphenylphosphine oxide and *para*-diiodotetrafluorobenzene, Fitting data to different kinetic models suggested the reaction mechanism is mainly diffusion controlled. The temperature dependence of the reaction rate allowed for the estimation of the activation energy (76 ± 38 kJ mol^{-1}).

Future Works

Recent years have seen the concept of the σ-hole extended to additional classes of element-based non-covalent interactions. The elements from group 14, 15, and 16 of the periodic table can also act as electrophilic sites and form attractive interactions with electron-rich moieties, giving rise to tetrel,[5,6] pnictogen,[7] and chalcogen bonds,[8,9,10] respectively. An official IUPAC definition to describe chalcogen, pnictogen, and tetrel bonds, and other interactions involving group 14-16 elements, is currently under discussion.[10,11] The highly directional nature and tunability present in these interactions have led to them experience an increasing application in supramolecular chemistry[12,13,14,15], molecular recognition[16,17,18], and organocatalysis[19,20,21,22], for example. Our group has previously explored the NMR response upon the formation of tetrel bonds,[23,24] pnictogen bonds,[25] and chalcogen bonds,[26,27,28] in polycrystalline samples via multinuclear magnetic resonance spectroscopy.

Part 3 of this dissertation has provided the first single-crystal NMR study of the electronic structure of halogen bond donor in the halogen-bonded cocrystal featuring P=O···I–C motifs. This approach could also be applied to various systems involving other σ-hole interactions. For example, a series of chalcogen-bonded cocrystals featuring

dicyanoselenadiazole as a chalcogen bond donor has been characterized by ^{77}Se solid-state NMR.[26,28] Various single crystals containing chalcogen-bonded systems can be grown, and ^{77}Se single-crystal NMR can be a direct probe of the chalcogen bond donor. Applying this method to different systems can provide various novel insights into the connection between the NMR observables and the nature of all sorts of interactions.

Part 4 of this dissertation provided a real-time in situ observation of the crystallization process that occurred to form a halogen bonding interaction under different conditions. This approach could also be employed to other σ-hole interactions. Pyridine derivatives, such as pyridine, 4,4'-dipyridyl, and 4,4'-vinylenedipyridine, have been reported as promising halogen bond acceptors. ^{15}N-labeled pyridine derivatives can be synthesized and act as electron-rich moieties (bond acceptors) in tetrel, pnictogen, and chalcogen bonds. Therefore, in situ ^{15}N solid-state NMR analyses can allow for the real-time monitoring of different cocrystallization processes. Moreover, it will be even more promising if a milling apparatus is designed to be compatible with MAS probe used for solid-state NMR. The reaction rate and mechanism of a wide range of reactions under various conditions (*i.e.*, different temperatures, different milling frequencies, different amounts of liquid added, materials of milling balls, etc.) can be investigated to provide an optimal condition for the desired product.

References for Part 5

[1] Bryce, D. L.; Viger-Gravel, J. *Top. Curr. Chem.* **2015**, *358*, 183–204.

[2] Szell, P. M. J.; Bryce, D. L. *Modern Magn. Reson.* **2016**, 1–18.

[3] Cerreia Vioglio, P.; Chierotti, M. R.; Gobetto, R. *CrystEngComm* **2016**, ***18***, 9173–9184.

[4] Xu, Y.; Szell, P. M. J.; Kumar, V. Bryce, D. L. *Coord. Chem. Rev.* **2020**, *411*, 213237.

[5] Bauzá, A.; Mooibroek, T. J.; Frontera, A. *Angew. Chem., Int. Ed.* **2013**, *52*, 12317–12321.

[6] Bauzá, A.; Seth, S. K.; Frontera, A. *Coord. Chem. Rev.* **2019**, *384*, 107–125

[7] Scilabra, P.; Terraneo, G.; Resnati, G. *J. Fluorine Chem.* **2017**, *203*, 62–74.

[8] Pascoe, D. J.; Ling, K. B.; Cockroft, S. L. *J. Am. Chem. Soc.* **2017**, *139*, 15160–15167.

[9] Vogel, L.; Wonner, P.; Huber, S. M. *Angew. Chem., Int. Ed.* **2019**, *58*, 1880–1891.

[10] Aakeroy, C. B.; Bryce, D. L.; Desiraju, G. R.; Frontera, A.; Legon, A. C.; Nicotra, F.; Rissanen, K.; Scheiner, S.; Terraneo, G.; Metrangolo, P.; Resnati, G. *Pure Appl. Chem.* **2019**, *91*, 1889–1892.

[11] Bryce, D. L.; Desiraju, G. R.; Frontera, A.; Krossing, I; Legon, A. C.; Nicotra, F.; Rissanen, K.; Scheiner, S.; Terraneo, G.; Metrangolo, P.; Resnati, G. Categorizing Chalcogen, Pnictogen, and Tetrel Bonds, And Other Interactions Involving Groups 14–16 Elements. IUPAC Project No.: 2016-001-2-300. https://iupac.org/projects/project-details/?project_nr=2016-001-2-300.

[12] Ho, P. C.; Szydlowski, P.; Sinclair, J.; Elder, P. J. W.; Kübel, J.; Gendy, C.; Lee, L. M.; Jenkins, H.; Britten, J. F.; Morim, D. R.; Vargas-Baca, I. *Nat. Commun.*, **2016**, *7*, 1–10.

[13] Zeng, R.; Gong, Z.; Yan, Q. *J. Org. Chem.* **2020**, *85*, 8397–8404.

[14] Moaven, S.; Andrews, M. C.; Polaske, T. J.; Karl, B. M.; Unruh, D. K.; Bosch, E.; Bowling, N. P.; Cozzolino, A. F. *Inorg. Chem.* **2019**, *58*, 16227–16235.

[15] Gleiter, R.; Haberhauer, G.; Werz, D. B.; Rominger, F.; Bleiholder, C. *Chem. Rev.* **2018**, *118*, 2010–2041.

[16] Lim, J. Y. C.; Beer, P. D. *Chem* **2018**, *4*, 731–783.

[17] Garrett, G. E.; Carrera, E. I.; Seferos, D. S.; Taylor, M. S. *Chem. Commun.* **2016**, *52*, 9881–9884.

[18] Gropp, C.; Quigley, B. L.; Diederich F. *J. Am. Chem. Soc.* **2018**, *140*, 2705–2717.

[19] Benz, S.; López-Andarias, J.; Mareda, J.; Sakai, N.; Matile, S. *Angew. Chem., Int. Ed.* **2017**, *56*, 812–815.

[20] Benz, S.; Poblador-Bahamonde, A. I.; Low-Ders, N.; Matile, S. *Angew. Chem., Int. Ed.* **2018**, *57*, 5408–5412.

[21] Wonner, P.; Vogel, L.; Düser, M.; Gomes, L.; Kniep, F.; Mallick, B.; Werz, D. B.; Huber, S. M. *Angew. Chem., Int. Ed.* **2017**, *56*, 12009–12012.

[22] Wonner, P.; Vogel, L.; Kniep, F.; Huber, S. M. *Chem. -Eur. J.* **2017**, *23*, 16972–16975.

[23] Southern, S. A.; Bryce, D. L. *J. Phys. Chem. A* **2015**, *119*, 11891–11899.

[24] Southern, S. A.; Errulat, D.; Frost, J. M.; Gabidullin, B.; Bryce, D. L. *Faraday Discuss.* **2017**, *203*, 165–186.

[25] Leroy, C.; Johannson, R.; Bryce, D. L. *J. Phys. Chem. A* **2019**, *123*, 1030–1043.

[26] Kumar, V.; Xu, Y.; Bryce, D. L. *Chem. -Eur. J.* **2020**, *26*, 3275–3286.

[27] Kumar, V.; Xu, Y.; Leroy C.; Bryce, D. L. *Phys. Chem. Chem. Phys.* **2020**, *22*, 3817–3824.

[28] Xu, Y.; Kumar, V.; Bradshaw, M. J. Z.; Bryce, D. L. *Cryst. Growth Des.* **2020**, in press.

APPENDICES

Appendix A: Supporting Information for Chapter 3

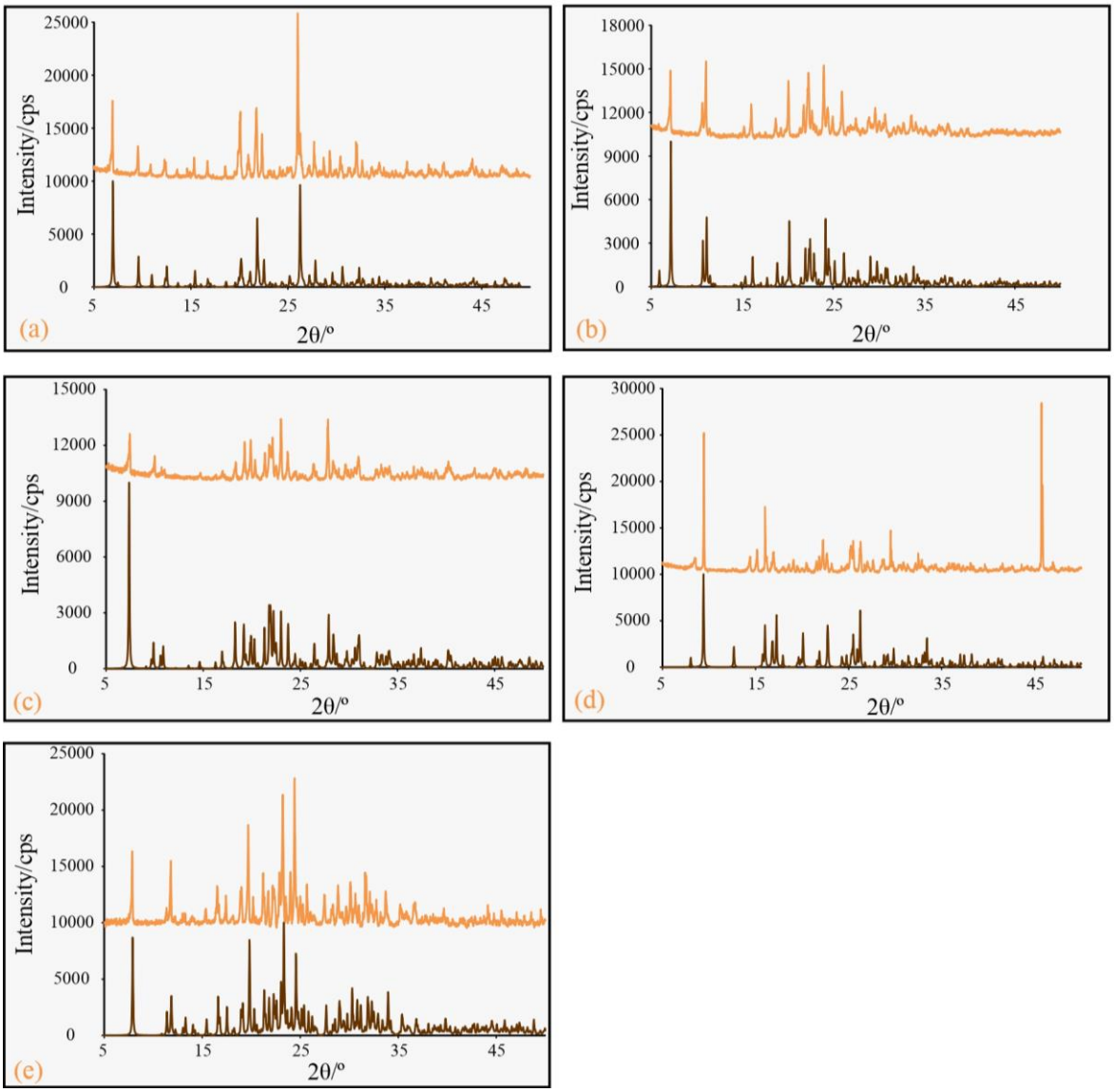

Figure A1. Experimental powder X-ray diffraction patterns (shown in orange) for halogen-bonded samples (a) **A1**, (b) **A2**, (c) **A3**, (d) **B1** and (e) **B3**. The calculated powder X-ray diffraction patterns from single crystal structure data are present in brown at the bottom. Simulations were generated using Mercury 3.6 software from the Crystallographic Data Center. The powder pattern for compound **B1** (d) is inconsistent with the simulation from the single crystal.

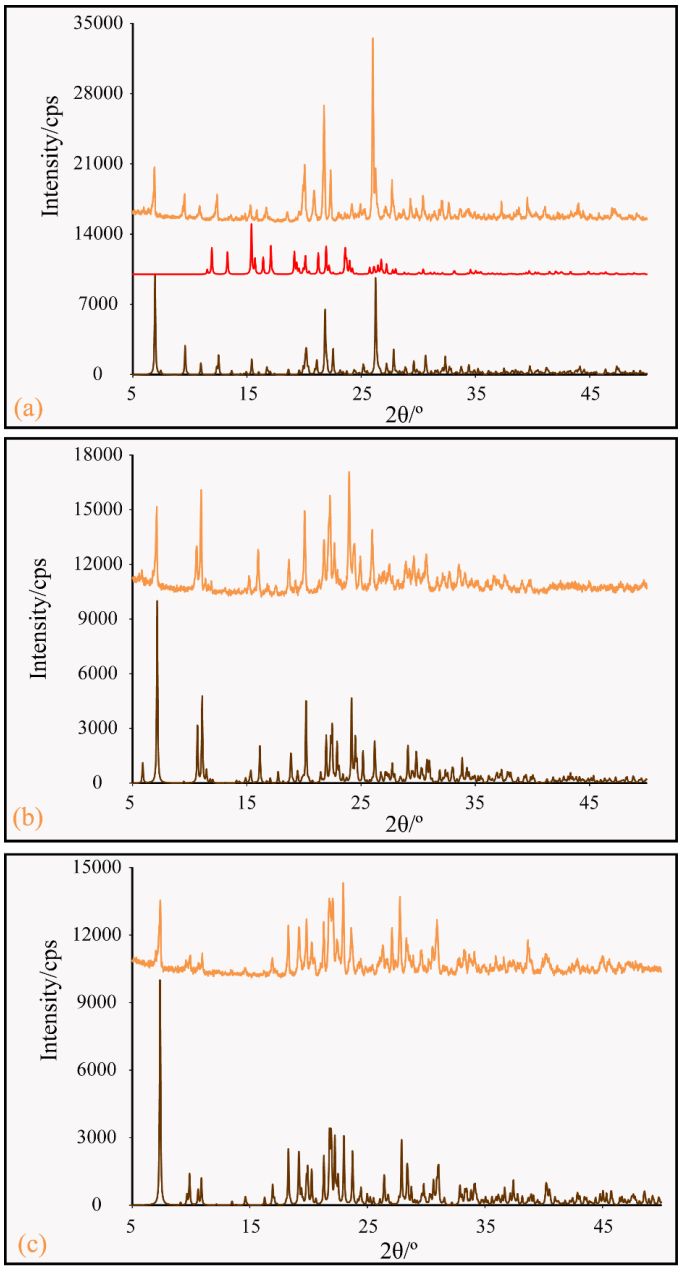

Figure A2. Experimental powder X-ray diffraction patterns (shown in orange) for ^{17}O-labeled halogen-bonded samples (a) **A1**, (b) **A2**, (c) **A3**. The calculated powder X-ray diffraction patterns from single crystal structure data are present in brown at the bottom. Simulations were generated using Mercury 3.6 software from the Crystallographic Data Center. Compound **A1** may contain a small amount of the starting material Ph_3PO, whose calculated PXRD pattern is shown in red.

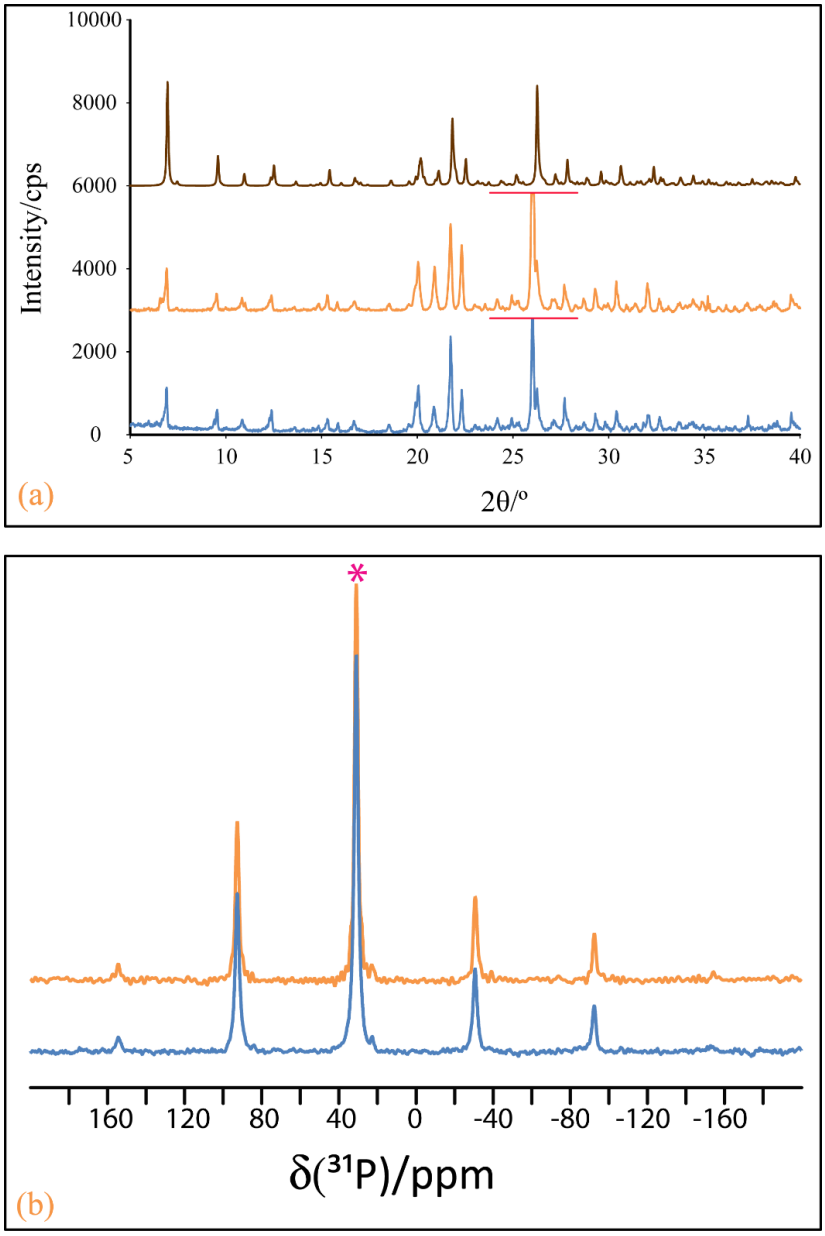

Figure A3. (a) Experimental powder X-ray diffraction patterns for compound **A1** produced by slow evaporation (shown in blue) and LAG (shown in orange). The calculated powder X-ray diffraction pattern from single crystal structure data are shown in brown. Simulations were generated using Mercury 3.6 software from the Crystallographic Data Center. (b) Representative experimental ^{31}P CP/MAS SSNMR spectra obtained at 4.7 T with a spinning speed of 5 kHz for compound **A1** synthesized from slow evaporation (shown in blue) and LAG (shown in orange). The isotropic peak is indicated by pink asterisks.

(a)

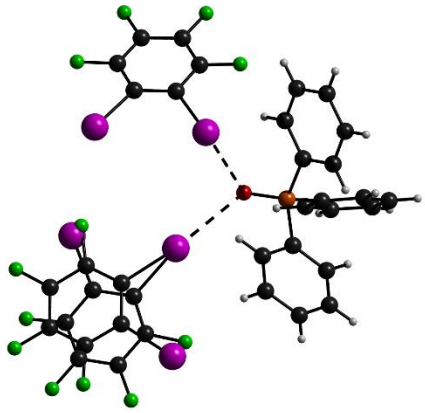

(b)

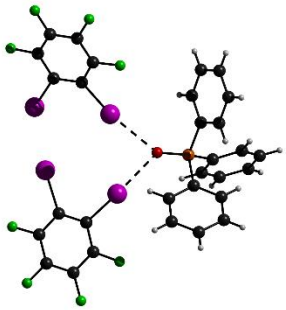

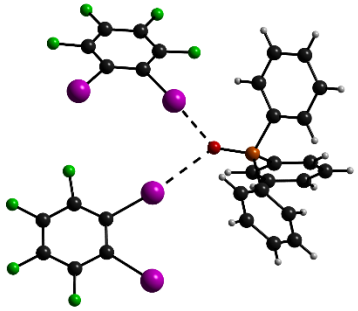

Figure A4. (a) Intermolecular geometries for halogen-bonded compound **A2** from single crystal X-ray diffraction. (b) Each of the two orientations for the lower diiodotetrafluorobenzene ring for compound **A2**.

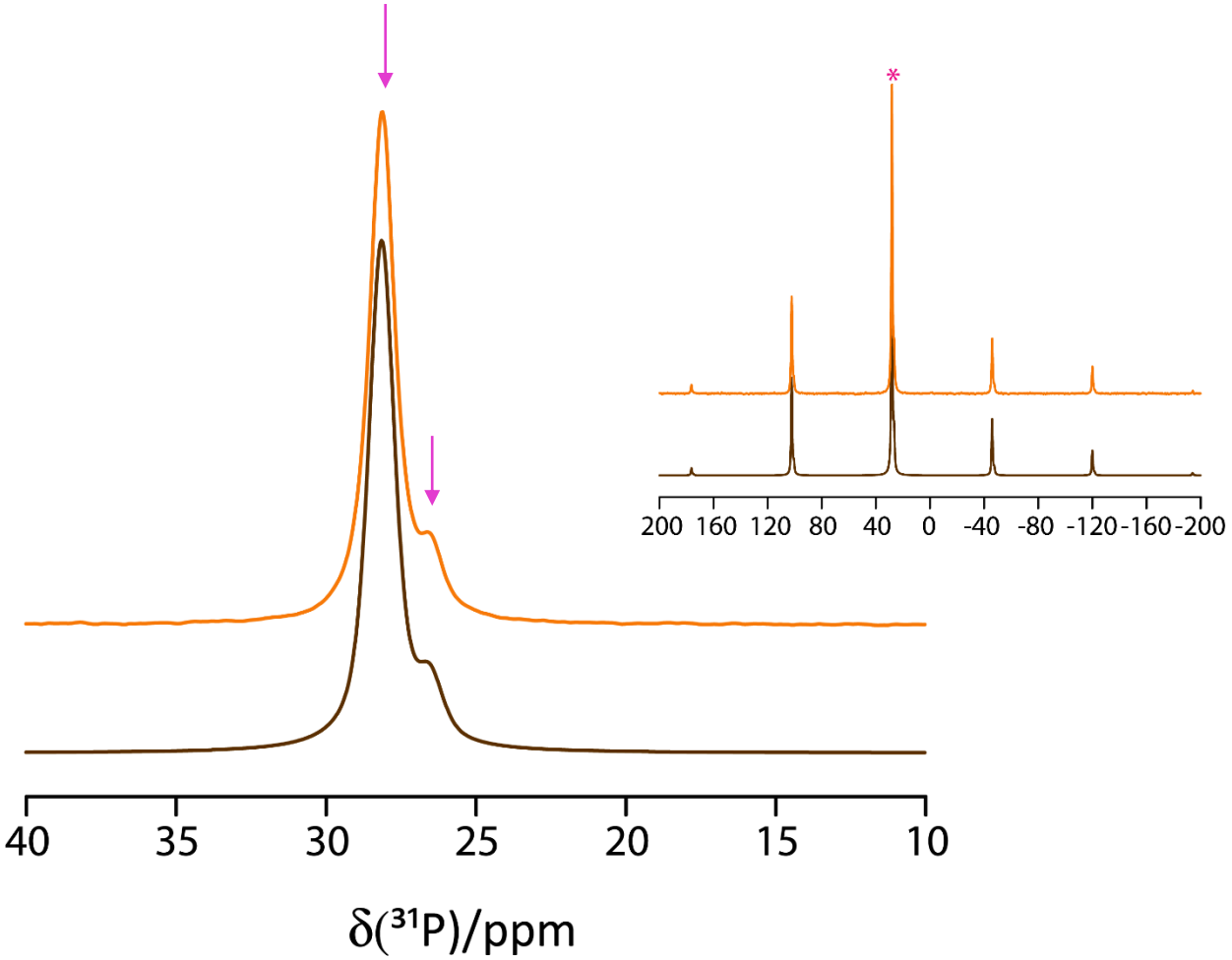

Figure A5. ^{31}P CP/MAS centerband (orange) of purchased Ph_3PO without any further crystallization at 4.7 T. The purchased Ph_3PO is a mixture of two polymorphs (shown with pink arrows): monoclinic (δ_{iso} = 26.4 ppm) and orthorhombic (δ_{iso} = 28.1 ppm). The simulation is shown in brown. The top inset presents the ^{31}P CP/MAS spectra of purchased Ph_3PO with all spinning sidebands. The spinning speed was 6 kHz. The isotropic peaks are shown with a pink asterisk.

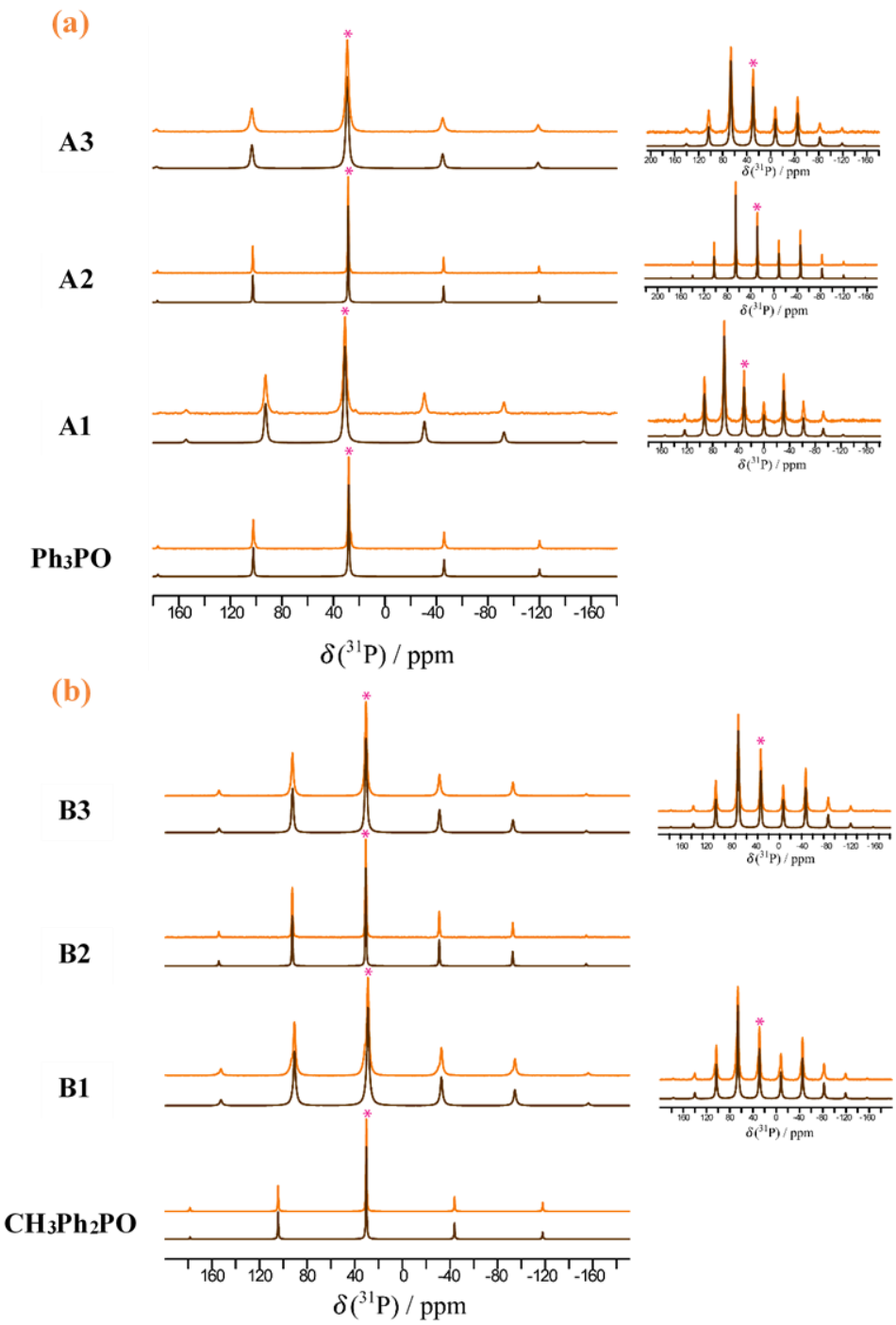

Figure A6. Experimental ^{31}P CP/MAS SSNMR spectra (orange) obtained at 4.7 T for Ph_3PO and its halogen-bonded compounds (a), CH_3Ph_2PO and its halogen-bonded compounds (b). The corresponding simulated spectra are shown at the bottom (brown). The isotropic peaks are indicated by pink asterisks. The spectra on the left were acquired at faster spinning speeds, varying from 5 kHz to 6 kHz. The spectra on the right were acquired at slower spinning speed, varying from 2.5 kHz to 4 kHz.

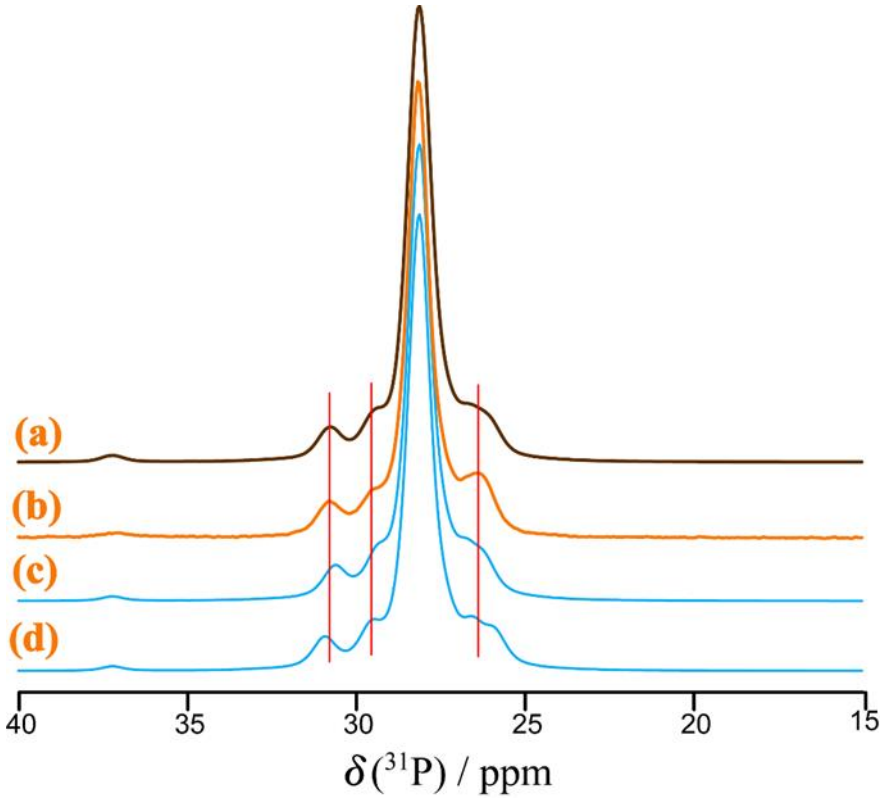

Figure A7. ^{31}P CP/MAS SSNMR spectra of ^{17}O-labeled compound **A2**. (a) Simulation where the $J(^{31}P, ^{17}O)$ value used in this best fit is 154 Hz. (b) The experimental spectrum for ^{17}O-labeled compound **A2** acquired at 9.4 T. Two additional simulations with the value of $J(^{31}P, ^{17}O)$ adjusted to 150 Hz (c) and 158 Hz (d) are shown for comparison. Vertical red lines denote points of comparison to aid the eye.

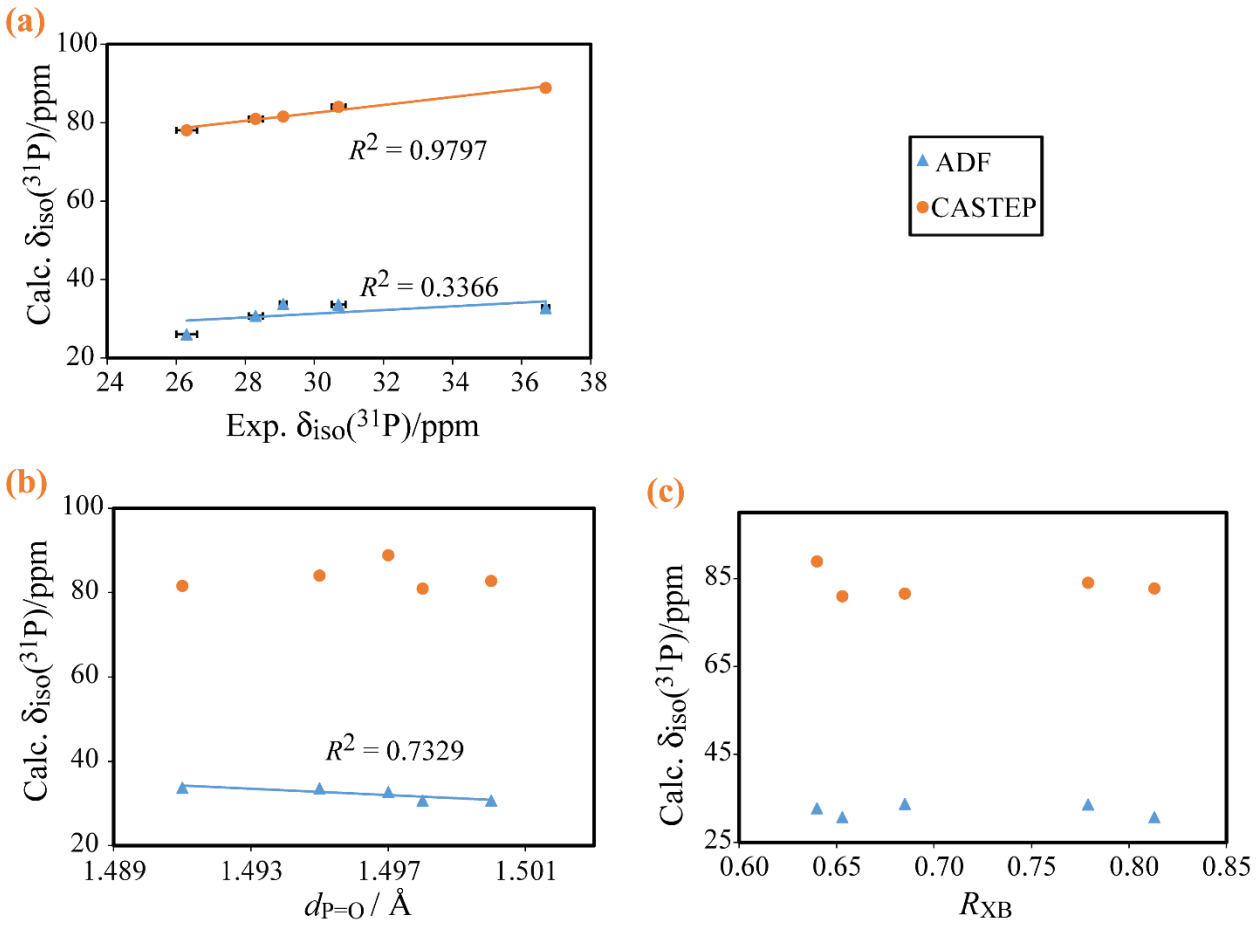

Figure A8. (a) Calculated versus experimental δ_{iso} (^{31}P) for the compounds in Table 3.3.1. (b) A plot of calculated δ_{iso} (^{31}P) vs the phosphorus-oxygen distance for the halogen-bonded compounds in Table 3.3.1 (c) A plot of calculated δ_{iso} (^{31}P) vs R_{XB} values for the halogen-bonded compounds **A1**, **A2**, **A3**, **B1** and **B3**. Two different types of DFT calculation were performed: GIPAW DFT calculation using CASTEP (shown in orange circle), and ZORA DFT using ADF (shown in blue triangle). Lines represent the best linear fit. The best linear fit are as follows: (a) CASTEP: calc. δ_{iso} (^{31}P) = 1.0132 exp.δ_{iso} (^{31}P) + 52.092, ADF: calc. δ_{iso} (^{31}P) = 0.4725 exp.δ_{iso} (^{31}P) + 17.091; (b) ADF: calc.δ_{iso} (^{31}P) = -375.77 $d_{P=O}$ + 594.53, R^2 = 0.7329.

Table A1. Amounts of Starting Materials for Synthesis

compound		MM (g/mol)	quantity (g)	mmol	yield (g)	melting point (℃)
A1	Ph_3PO	278.28	0.139	0.4977	0.1516	114
	p-$C_6F_4I_2$	401.87	0.200	0.4977		
A2	Ph_3PO	278.28	0.139	0.4977	0.1324	58
	o-$C_6F_4I_2$	401.87	0.200	0.4977		
A3	Ph_3PO	278.28	0.109	0.3923	0.0995	110
	sym-$C_6F_3I_3$	509.77	0.200	0.3923		
B1	CH_3Ph_2PO	216.22	0.108	0.4977	0.1040	58
	p-$C_6F_4I_2$	401.87	0.200	0.4977		
B2	CH_3Ph_2PO	216.22	0.108	0.4977	0.2711	39
	o-$C_6F_4I_2$	401.87	0.200	0.4977		
B3	CH_3Ph_2PO	216.22	0.128	0.5885	0.2697	102
	sym-$C_6F_3I_3$	509.77	0.300	0.5885		

Table A2. Crystallographic Data and Selected Data Collection Parameters for Halogen-Bonded Compounds

	A1	**A2**	**A3**	**B1**	**B3**
Empirical formula	$C_{30}H_{15}F_8I_4OP$	$C_{30}H_{15}F_8I_4OP$	$C_{24}H_{15}F_3I_3OP$	$C_{21}H_{16}F_4I_2NOP$	$C_{25}H_{13}F_6I_6OP$
Formula wt.	1081.99	1081.99	788.03	659.12	1235.72
Cryst size, mm^3	0.290 x 0.220 x 0.160	0.260 x 0.070 x 0.050	0.220 x 0.220 x 0.160	0.360 x 0.260 x 0.230	0.230 x 0.210 x 0.180
Cryst system	monoclinic	triclinic	triclinic	orthorhombic	monoclinic
Space group	$P2_1/c$	$P\bar{1}$	$P\bar{1}$	*Pnma*	$P2_1/n$
Z	4	2	2	4	4
a, Å	9.3190(6)	8.6823(2)	9.7436(2)	21.9816(16)	8.4758(3)
b, Å	25.4268(18)	12.8395(2)	10.7585(2)	18.0739(14)	44.7106(15)
c, Å	13.8063(9)	15.1270(3)	13.5453(3)	5.8075(4)	9.2023(3)
α, deg	90	90.4885(10)	113.1738(10)	90	90
β, deg	103.9422(17)	97.5416(10)	96.9048(10)	90	115.9700(15)
γ, deg	90	105.8860(11)	107.4200(11)	90	90
Volume, $Å^3$	3175.1 (4)	1606.12(6)	1198.74(4)	2307.3(3)	3135.15(19)
Calculated density, Mg m^{-3}	2.264	2.237	2.183	1.897	2.618
Absorption coefficient, mm^{-1}	4.048	4.001	4.016	2.84	6.051
F (000)	2008	1004	736	1256	2232
θ range for data collection,°	1.718 to 28.316	2.089 to 30.600	1.699 to 28.382	2.169 to 28.300	2.504 to 28.311
Limiting indices	-12≤h≤12, -33≤k≤33, -18≤I≤18	-12≤h≤11, -18≤k≤18, -21≤I≤21	-12≤h≤13, -14≤k≤14, -18≤I≤17	-29≤h≤20, -24≤k≤24, -5≤I≤7	-11≤h≤11, -57≤k≤59, -12≤I≤10
Reflections collected/ unique	43139/7858	20879/9517	13769/5836	24781/2874	27270/7712
R_{int}	0.0455	0.0218	0.0162	0.0184	0.026
Completeness to θ=25.242,%	99.1	99	98.4	97.7	98.9
Max and min transmission	0.7457 and 0.3303	0.7461 and 0.5116	0.7457 and 0.5613	0.7457 and 0.5469	0.7457 and 0.4902
Data/ restraints/ parameters	7858/0/398	9517/390/505	5836/0/290	2874/0/146	7712/0/352
Goodness-of-fit on F^2	1.044	1.034	1.017	1.022	1.348
Final R indices [I>2α(I)]	R_1=0.0339, wR_2=0.0850	R_1=0.0408, wR_2=0.1019	R_1=0.0198, wR_2=0.0519	R_1=0.0182, wR_2=0.0492	R_1=0.0492, wR_2=0.1072
R indices (all data)	R_1=0.0353, wR_2=0.0864	R_1=0.0520, wR_2=0.1092	R_1=0.0216, wR_2=0.0530	R_1=0.0192, wR_2=0.0497	R_1=0.0503, wR_2=0.1077
largest diff. peak and hole, e.$Å^{-3}$	2.944 and -2.057	1.510 and -2.708	1.289 and -1.045	0.318 and -1.016	1.212 and -1.442

Table A3. Cut-off Energies and *k*-point Grids Used for GIPAW DFT Calculation in CASTEP

Compounds	energy cut-off (eV)	*k*-point grids
monoclinic Ph_3PO	500	2×2×1
A1	500	2×1×1
A2	500	2×2×1
A3	500	2×2×2
B1	500	1×1×3
B3	500	3×1×2

Table A4. Analysis of Three Main NLMO Contributions to J (^{31}P, ^{17}O) in All Compounds.

Compound	P=O bonding	O lone pair	O core	sum[a]	$K(^{31}P, ^{17}O)$ / $10^{19}kg{\cdot}m^{-2}{\cdot}s^{-2}{\cdot}A^{-2}$
monoclinic Ph_3PO	139.72	-315.35	-97.65	-273.29	-317.81
CH_3Ph_2PO	142.84	-319.65	-99.06	-275.86	-319.17
A1	149.45	-309.68	-81.64	-241.87	-301.65
A2	149.42	-299.09	-74.80	-224.47	-286.23
A3	146.39	-300.33	-80.64	-234.58	-292.75
B1	147.64	-294.49	-75.24	-222.09	-286.31
B3	140.31	-287.84	-77.03	-224.57	-284.78

[a] Sum of three main contributions is different from total calculated $K(^{31}P, ^{17}O)$ because not all of the contributions are included here.

Table A5. Analysis of Three Main NLMO Contributions to the Largest Principal Component of the ^{17}O EFG Tensor (V_{33}) in All Compounds

Compound	P=O bonding	O lone pair *x*	O lone pair *y*	O lone pair *z*	sum[a]	V_{33} / au
Ph_3PO	-3.290	2.974	-1.909	2.953	0.728	0.8869
CH_3Ph_2PO	-3.275	2.985	-1.907	2.967	0.770	0.9131
A1	-3.243	2.982	-1.843	2.869	0.765	0.9634
A2	-3.239	3.002	-1.969	2.943	0.737	0.9510
A3	-3.244	2.955	-1.972	2.929	0.668	0.8907
B1	-3.251	2.941	-1.922	2.959	0.727	0.9355
B3	-3.267	2.912	-1.897	2.930	0.678	0.8877

[a] Sum of three main contributions is different from total calculated V_{33} because not all of the contributions are included here.

Table A6. ZORA-DFT Calculations of ^{31}P Chemical Shift Tensors[a] and $J(^{31}P, ^{17}O)$ Coupling[b] Values.

	compound	δ_{iso} / ppm[a]	Ω / ppm[a]	κ[a]	$J_{iso}(^{31}P, ^{17}O)$ / Hz
	monoclinic Ph_3PO	26.03	231.1	-0.840	210
A1	$(Ph_3PO)(p\text{-}C_6F_4I_2)_2$	33.61	204.4	-0.920	199
A2	$(Ph_3PO)(o\text{-}C_6F_4I_2)_2$	30.72	208.6	-0.931	191
A3	$(Ph_3PO)(sym\text{-}C_6F_3I_3)$	33.74	196.3	-0.821	193
B1	$(CH_3Ph_2PO)(p\text{-}C_6F_4I_2)(CH_3CN)$	30.71	238.8	-0.647	189
B3	$(CH_3Ph_2PO)(sym\text{-}C_6F_3I_3)_2$	32.75	181.7	-0.950	188

[a] The ^{31}P chemical shift tensors were obtained from GGA revPBE calculations with scalar relativistic effects via the zeroth-order regular approximation (ZORA) in ADF. The basis set was ZORA/TZP.

[b] The $J(^{31}P, ^{17}O)$ coupling values were determined using ADF with scalar relativistic effects via ZORA with meta-GGA, the TPSS functional, and the ZORA/DZP basis set.

Table A7. ZORA-DFT calculations of ^{17}O CS and EFG Tensor Parameters[a].

	compound	δ_{iso} / ppm[a]	Ω / ppm[a]	κ[a]	$\lvert C_Q(^{17}O)\rvert$ / MHz[b]	η_Q[b]
	monoclinic Ph_3PO	62.33	206.4	0.754	5.33	0.060
A1	$(Ph_3PO)(p\text{-}C_6F_4I_2)_2$	52.07	114.1	0.759	5.79	0.050
A2	$(Ph_3PO)(o\text{-}C_6F_4I_2)_2$	39.26	136.9	0.568	5.72	0.178
A3	$(Ph_3PO)(sym\text{-}C_6F_3I_3)$	67.48	185.0	0.394	5.41	0.103
B1	$(CH_3Ph_2PO)(p\text{-}C_6F_4I_2)(CH_3CN)$	50.67	160.3	0.419	5.62	0.120
B3	$(CH_3Ph_2PO)(sym\text{-}C_6F_3I_3)_2$	86.69	163.0	0.827	5.34	0.058

[a.] The ^{17}O CS and EFG tensors were obtained from GGA revPBE calculations including scalar relativistic effects via ZORA in ADF. The basis set was ZORA/TZP.

Table A8. GIPAW-DFT Calculations of ^{31}P Chemical Shift Tensors[a]

	compound	δ_{iso} / ppm[a]	Ω / ppm[a]	κ[a]
	monoclinic Ph_3PO	78.08	222.3	-0.829
A1	$(Ph_3PO)(p\text{-}C_6F_4I_2)_2$	84.03	208.2	-0.925
A2	$(Ph_3PO)(o\text{-}C_6F_4I_2)_2$	80.98	212.2	-0.945
A3	$(Ph_3PO)(sym\text{-}C_6F_3I_3)$	81.58	210.3	-0.811
B1	$(CH_3Ph_2PO)(p\text{-}C_6F_4I_2)(CH_3CN)$	82.76	251.5	-0.577
B3	$(CH_3Ph_2PO)(sym\text{-}C_6F_3I_3)_2$	88.88	182.7	-0.941

[a] The ^{31}P chemical shift tensors were obtained from GIPAW calculations with the PBE functional in CASTEP. The settings are listed in Table A2.

Table A 9. GIPAW-DFT Calculations of ^{17}O CS and EFG Tensor Parameters[a]

	compound	δ_{iso} / ppm[a]	Ω / ppm[a]	κ[a]	$\lvert C_Q(^{17}O)\rvert$ / MHz[b]	η_Q[b]
	monoclinic Ph_3PO	76.30	200.8	0.730	4.80	0.045
A1	$(Ph_3PO)(p\text{-}C_6F_4I_2)_2$	68.01	113.8	0.678	5.37	0.078
A2	$(Ph_3PO)(o\text{-}C_6F_4I_2)_2$	51.39	141.6	0.727	5.20	0.215
A3	$(Ph_3PO)(sym\text{-}C_6F_3I_3)$	82.39	186.8	0.529	4.94	0.182
B1	$(CH_3Ph_2PO)(p\text{-}C_6F_4I_2)(CH_3CN)$	60.33	163.1	0.426	5.12	0.188
B3	$(CH_3Ph_2PO)(sym\text{-}C_6F_3I_3)_2$	98.87	156.8	0.866	4.86	0.085

[a] The ^{17}O CS and EFG tensors were obtained from GIPAW calculation with PBE functional in CASTEP. The settings were listed in Table A2.

Appendix B: Supporting Information for Chapter 4

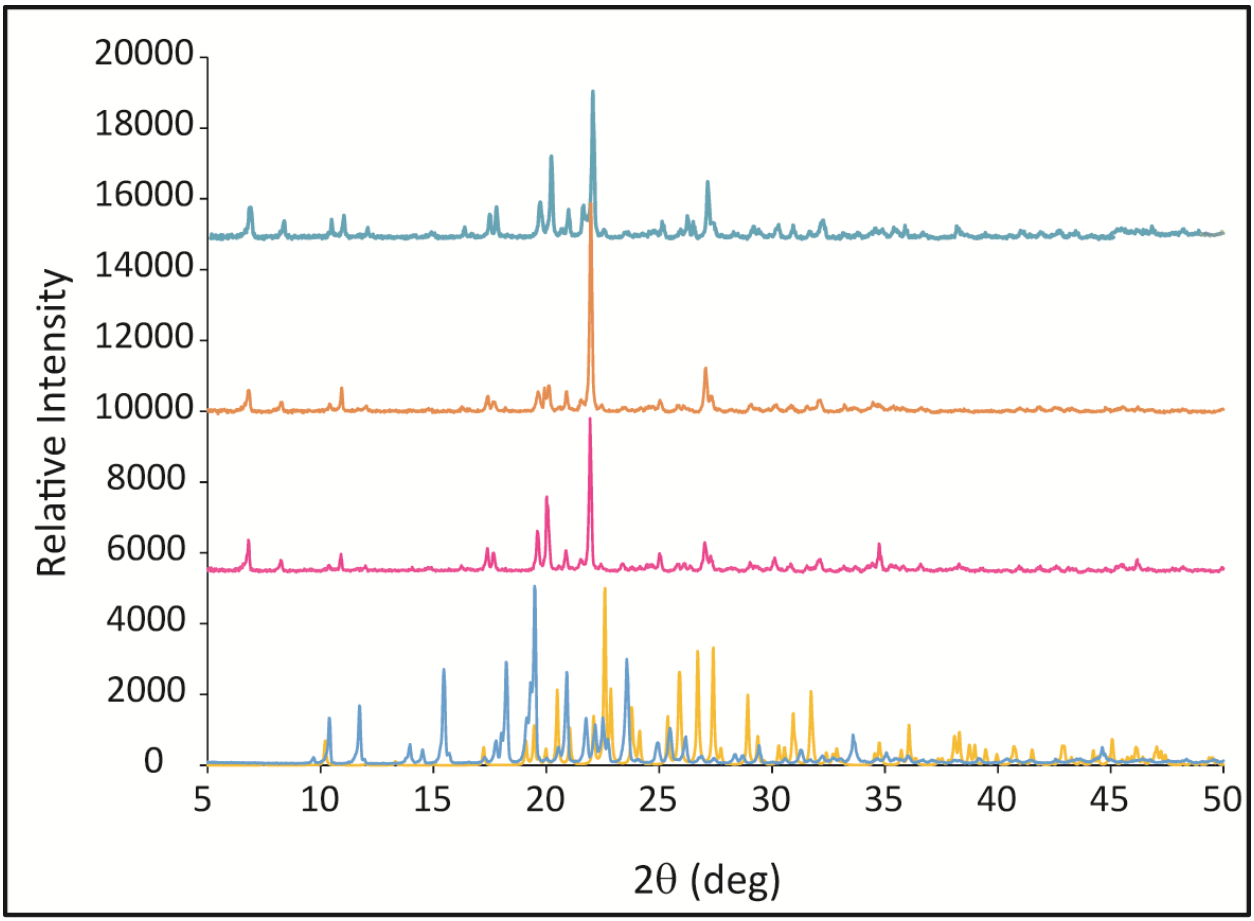

Figure B1. Experimental powder X-ray diffraction patterns for Ph_3P (blue), *sym*-$C_6F_3I_3$ (yellow) and halogen-bonded cocrystal **1** obtained by slow evaporation from diethyl ether at room temperature with different molar ratios of Ph_3P to *sym*-$C_6F_3I_3$: 2 (pink), 1 (orange) and 0.5 (dark green). All data were acquired using a Rigaku Ultima IV diffractometer with 2θ ranging from 5º to 50º at a rate of 1º per minute. The PXRD results indicate that different molar ratios of the starting materials always produced the same cocrystal.

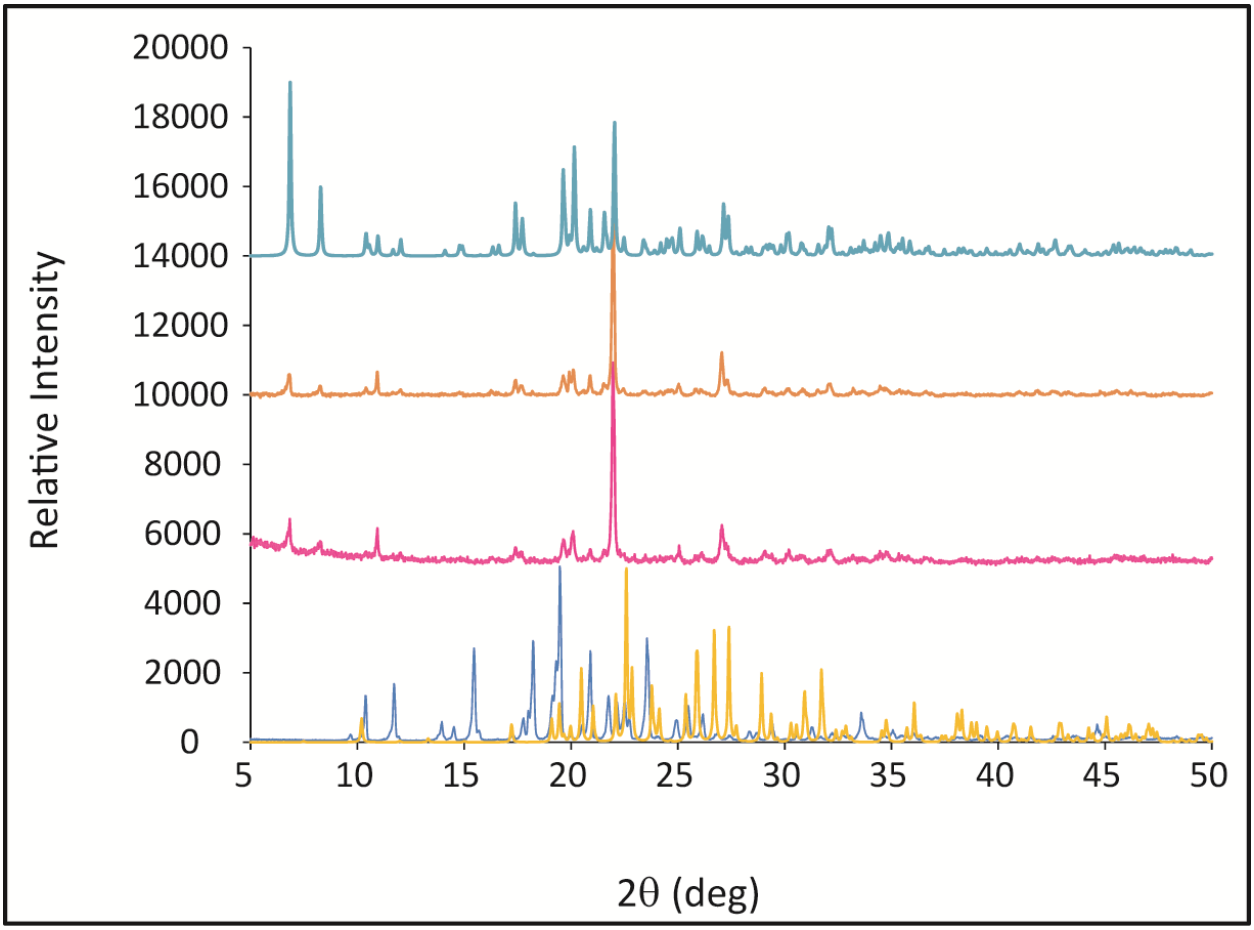

Figure B2. Experimental powder X-ray diffraction patterns for Ph_3P (blue), *sym*-$C_6F_3I_3$ (yellow) and halogen-bonded cocrystal **1** obtained by slow evaporation from different solvents at room temperature: chloroform (pink) and diethyl ether (orange). All data were acquired using a Rigaku Ultima IV diffractometer with 2θ ranging from 5º to 50º at a rate of 1º per minute. The simulated PXRD pattern from SCXRD structure generated by Mercury 3.10.2 is shown in dark green at top.

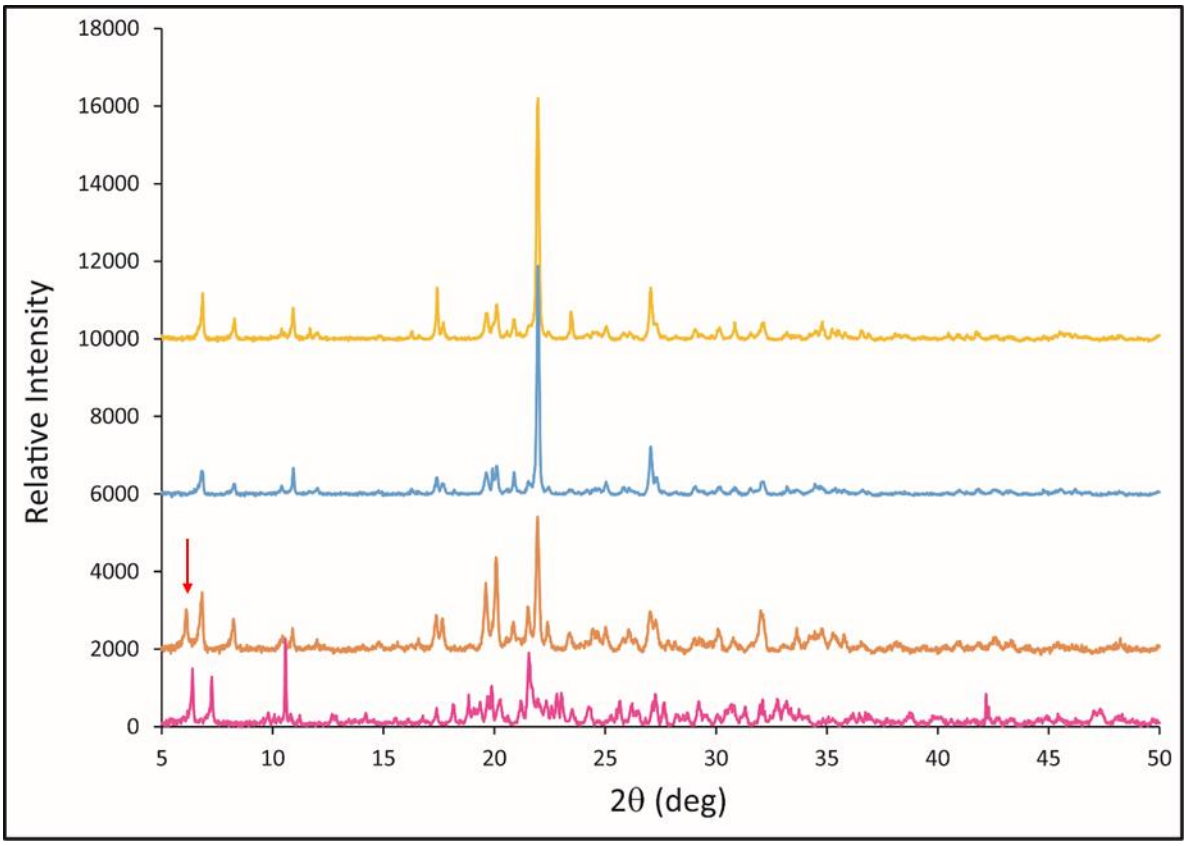

Figure B3. Experimental powder X-ray diffraction pattern for halogen-bonded cocrystal **1** obtained from different methods: ball milling with 50 μL acetonitrile (orange), cooling down a saturated diethyl ether solution (blue), and slow evaporation from diethyl ether at room temperature (yellow). All data were acquired using a Rigaku Ultima IV diffractometer with 2θ ranging from 5º to 50º at a rate of 1º per minute. The red arrow an impurity, which could be due to cocrystal **2** (shown in pink) or due to another impurity.

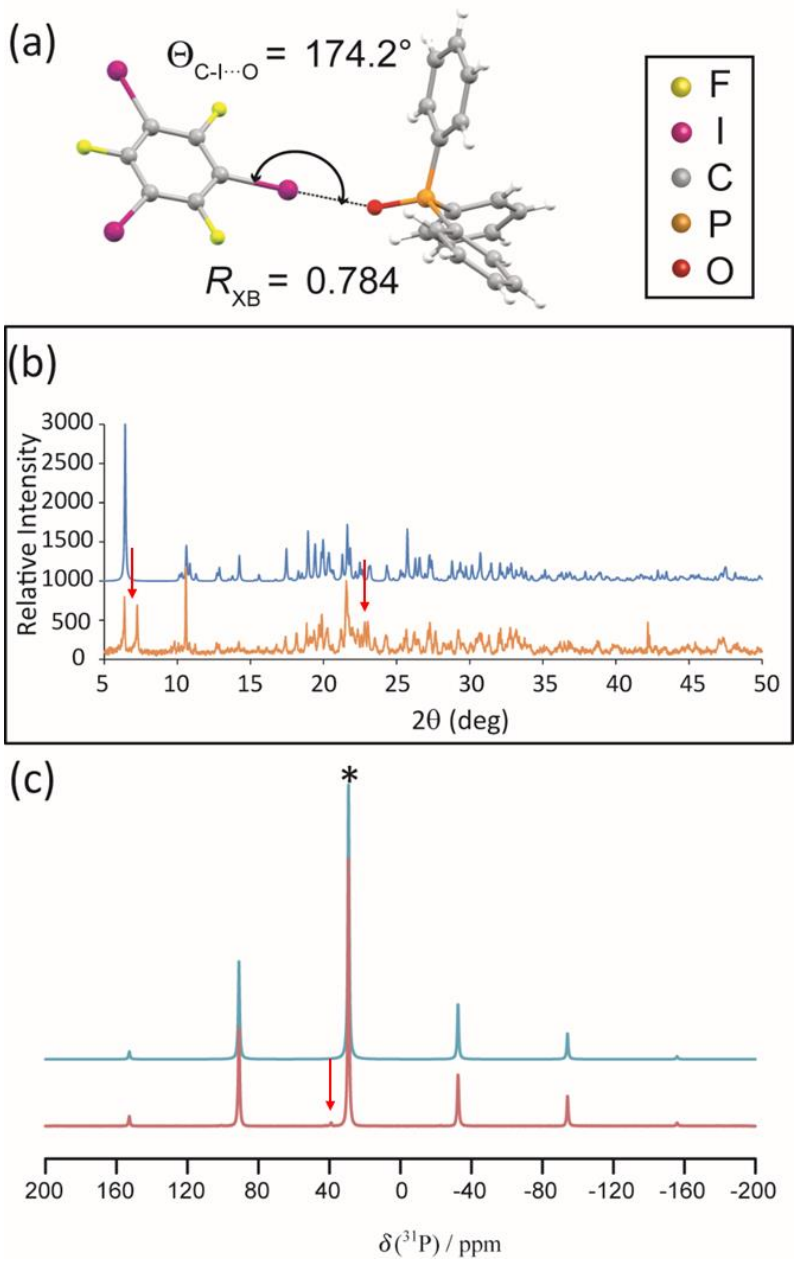

Figure B4. (a) Intermolecular geometry for halogen-bonded cocrystal **2** obtained from single-crystal X-ray diffraction. (b) Experimental (orange) and simulated (blue) powder X-ray diffraction patterns for the cocrystal **2** obtained from slow evaporation of acetonitrile at room temperature. All data were acquired using a Rigaku Ultima IV diffractometer with 2θ ranging from 5º to 50º at a rate of 1º per minute. Simulations were generated using Mercury 3.10.2 software. (c) Experimental (pink) and simulated (dark green) ^{31}P CP/MAS SSNMR spectra obtained at 9.4 T for the cocrystal **2** with MAS spinning speed of 10 kHz. The arrows in the PXRD and SSNMR spectra indicate a decomposition product.

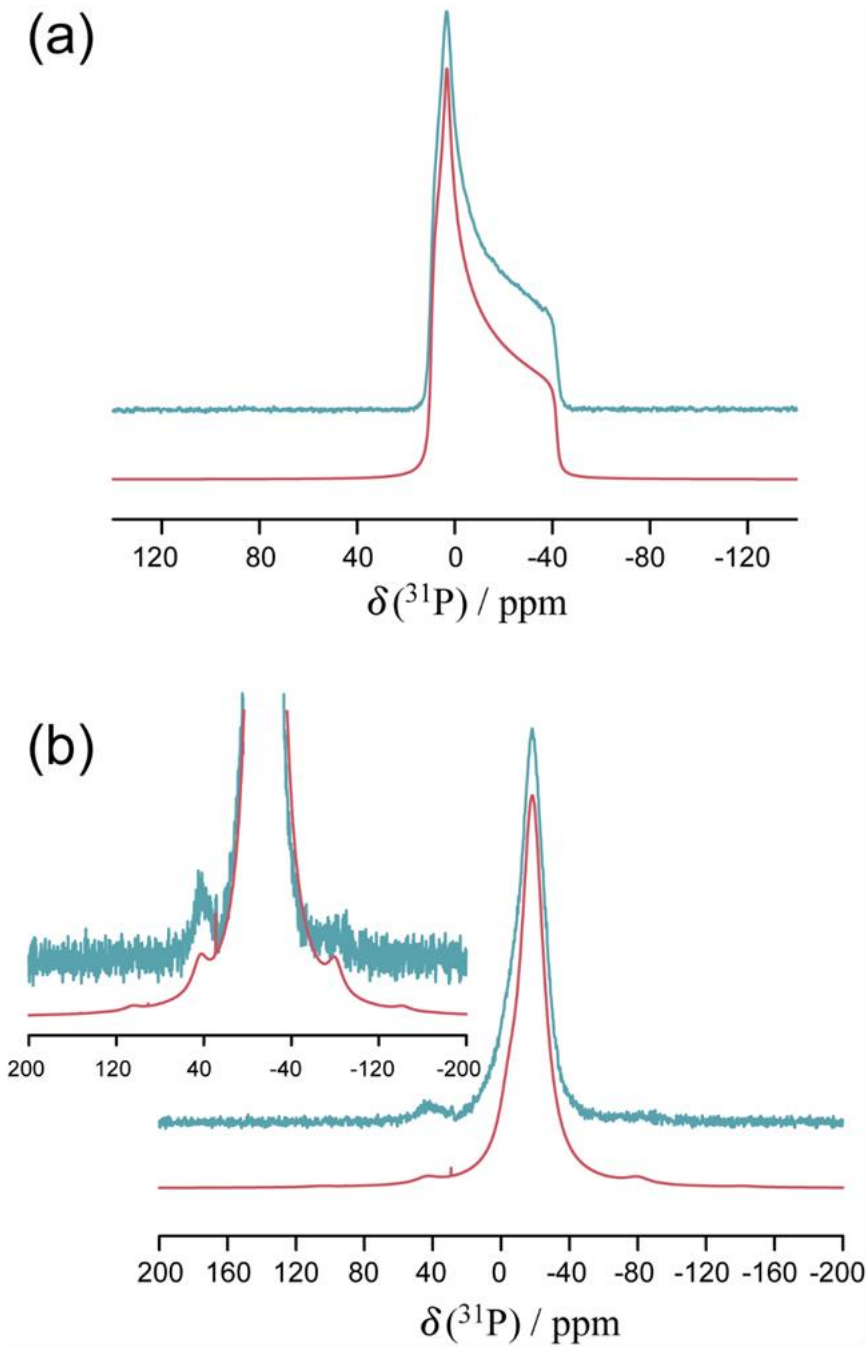

Figure B5. (a) Experimental static ^{31}P CP SSNMR spectra (dark green) obtained at 9.4 T for Ph_3P. (b) Experimental ^{31}P CP/MAS SSNMR spectra (dark green) obtained at 4.7 T for halogen-bonded cocrystal **1** with a spinning speed of 5 kHz. The isotropic peaks are indicated by asterisks. The corresponding simulated spectra are shown in pink. Shown in the inset is a magnified region of the spectrum.

Table B1. CSD Entries Featuring Phosphorus-Halogen Contacts Shorter Than the Sum of Their van der Waals' Radii (but significantly longer than the sum of their covalent radii)[a]

	compound	**CCDC entry**	**XB donor**
self	3,5,7,9-Tetra-t-butyl-4,4-di-iodo-4-sila-1,2,6,8,10,11-hexaphosphapentacyclo(4.3.2.$0^{2,5}$.$0^{3,10}$.$0^{7,11}$)undec-8-ene	DOQQOP	I
	((8-Iodo-1-naphthyl)methyl)(phenyl)phosphine	EGOVOM	I
	(η^2-1,2-bis(diphenylphosphino)ethyne)-carbonyl-(hydridotris(3,4,5-trimethylpyrazol-1-yl)borate)-iodo-tungsten(iii) hexafluorophosphate dichloromethane solvate	HAXYIR	I
	1,3-bis(Iodo)-2,4-bis(tri-t-butylsilyl)tetraphosphetane	HOVHUW	I
	3,6,8,10-Tetra-t-butyl-1,4-di-iodo-1,2,4,5,7,9-hexaphosphahexacyclo(4.4.0.02,5.03,9.04,8.07,10)decane	HUKBUL	I
	bis(7-iodo-2,3-dihydrothieno[3,4-b][1,4]dioxin-5-yl)(phenyl)phosphine	XIZCEQ	I
	tris(2-Bromo-5-thienyl)phosphine	COJWUU	Br
	1-Bromo-8-(diethoxyphosphino)naphthalene	OJEJET	Br
	1,8-bis(Dichlorophosphino)naphthalene	GUTJEK	Cl
	(C_{14} H_{10} Ag Mo_2 O_4 P_6 $^+$)$_n$,n(C H_2 Cl_2),n(C_{16} Al F_{36} O_4 $^-$)	LUJKOR	Cl
	6,6,7,7-Tetrachloro-2,4-dimethyl-2,4-diaza-1,5-diphosphabicyclo(3.1.1)heptan-3-one	XOMMOB	Cl
cocrystal	1-Diphenylphosphino-2-methyl-1,2-dicarbadodecaborane(10) hemikis(iodine)	ECISIT	I
solvate	(E)-1-(2,4-dinitrophenyl)-2-(2-(diphenylphosphino)benzylidene)hydrazine chloroform solvate	BUWXUO	Cl
	hexakis(μ-phosphido)-pentakis(η^5-cyclopentadienyl)-penta-molybdenum dichloromethane solvate	HAHHAC	Cl
	1,4-(Biphenyl-2,2'-diyl)-2,3-diethyl-1,1,4,4-tetraphenyl-1,2,3,4-tetraphosphy-[4]catenium hemikis(hexacloro-tin) pentachloro-tin chloroform solvate	NIDREY	Cl

[a] For a survey of phosphines interacting with molecular iodine at much shorter distances, see also Pennington, W. T.; Hanks, T. W.; Arman, H. D. Halogen Bonding with Dihalogens and Interhalogens. In *Halogen Bonding. Structure and Bonding;* Metrangolo P., Resnati G., Eds; Springer: Heidelberg, 2007; Vol 126, pp 65-104.

Table B2. Crystallographic Data and Selected Data Collection Parameters for Halogen-Bonded Cocrystals

	1	**2**
Empirical Formula	$C_{24}H_{15}F_3I_3P$	$C_{24}H_{15}F_3I_3OP$
Formula Weight	772.03	788.03
Crystal Size, mm^3	0.460 × 0.320 × 0.190	0.900 × 0.320 × 0.190
Crystal System	Triclinic	Monoclinic
Space Group	$P\bar{1}$	$P2_{1/C}$
Z	2	4
Volume, Å	1258.6 (2)	2469.7 (6)
Calculated density, Mg m^{-3}	2.037	2.119
a, Å	9.1640 (9)	14.230 (2)
b, Å	10.9788 (11)	10.1079 (14)
c, Å	13.5101 (13)	17.790 (2)
α, deg	87.9470 (10)	90
β, deg	72.5210 (10)	105.164 (2)
γ, deg	76.2900 (10)	90
Absorption coefficient, mm^{-1}	3.820	3.899
$F(000)$	720	1472
θ range for data collection, °	1.571 to 28.201	2.338 to 30.459
Limiting indices	$-12 \le h \le 12$, $-14 \le k \le 14$, $-17 \le l \le 17$	$-19 \le h \le 19$, $-13 \le k \le 13$, $-23 \le l \le 24$
Reflections collected/ unique	21984 / 5727	29024 / 6464
R_{int}	0.0214	0.0291
Completeness to θ = 25.242°, %	99.9	100.0
Max and min transmission	0.746 and 0.581	0.746 and 0.504
Data/ restraints/ parameters	5727 / 0 / 280	6464 / 0 / 289
Goodness-of-fit on F^2	1.026	1.012
Final R indices [$I > 2\alpha(I)$]	R_1 = 0.0281, wR_2 = 0.0568	R_1 = 0.0264, wR_2 = 0.0573
R indices (all data)	R_1 = 0.0373, wR_2 = 0.0607	R_1 = 0.0386, wR_2 = 0.0624
largest diff. peak and hole, e·$Å^{-3}$	1.166 and -1.017	0.814 and -1.071

Appendix C: Supporting Information for Chapter 5

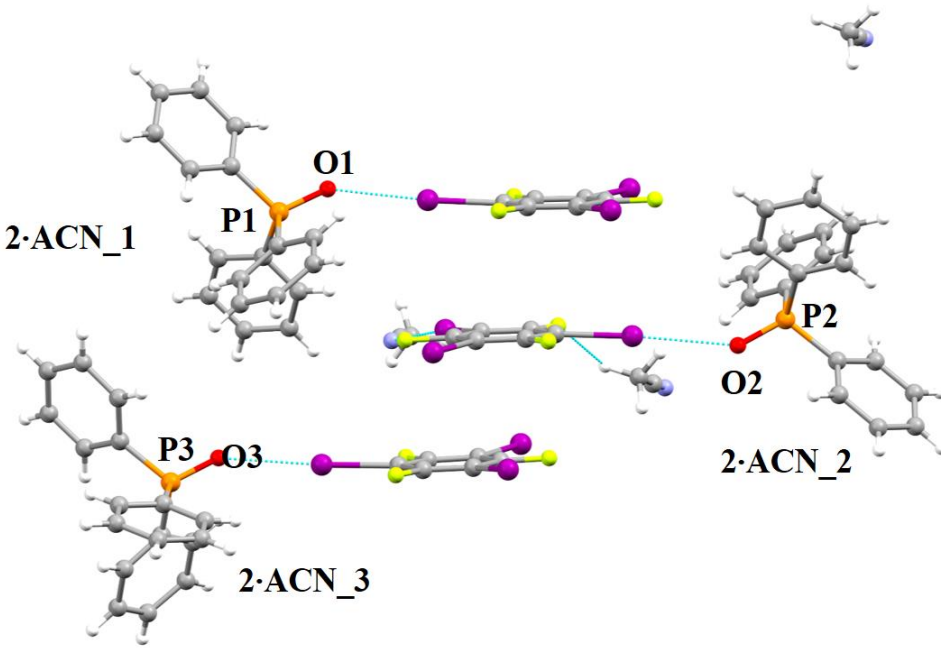

Figure C1. Halogen bond geometry in one unit cell of cocrystal **2·ACN** from single-crystal X-ray diffraction. The three crystallographically distinct sites are shown with labels consistent with the main text. Molecules **2·ACN_1** and **_3** share similar environments and orientation whereas **2·ACN_2** faces in the opposite direction.

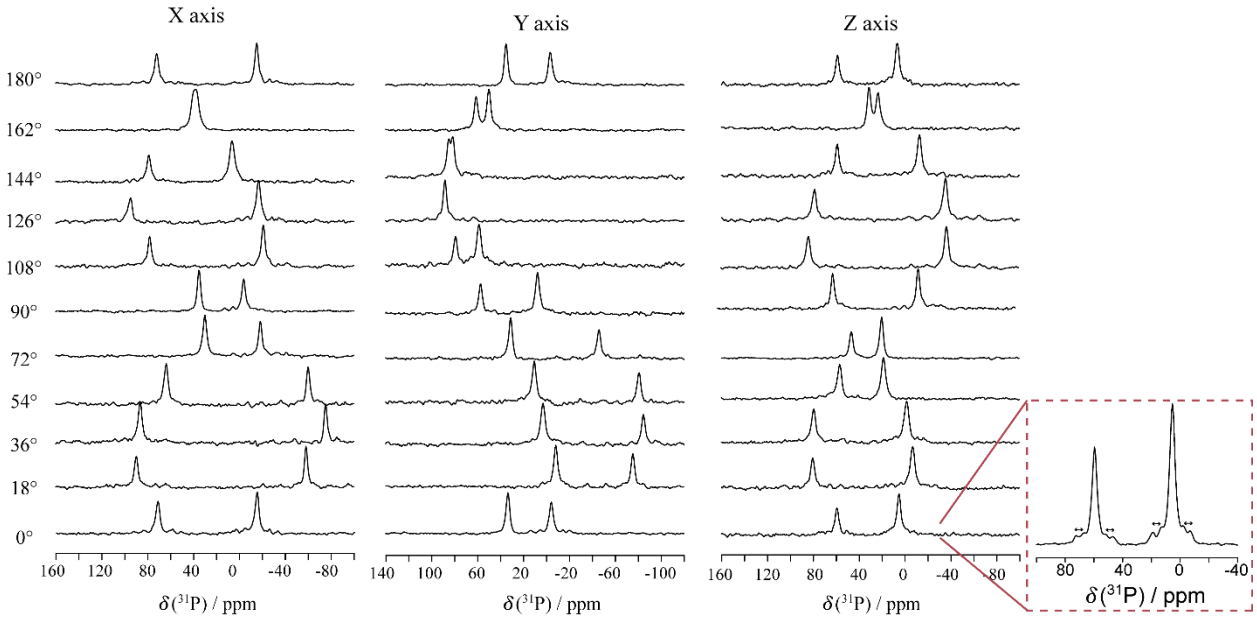

Figure C2. Single-crystal ^{31}P NMR spectra (B_0 = 9.4 T) for $Ph_3P^{17}O$. Spectra were obtained at 9° rotational increments about the X, Y, and Z axes. Here only every second spectrum is shown. Shown in the inset is a magnification of the spectra to show the presence of spin-spin coupling between ^{17}O and ^{31}P.

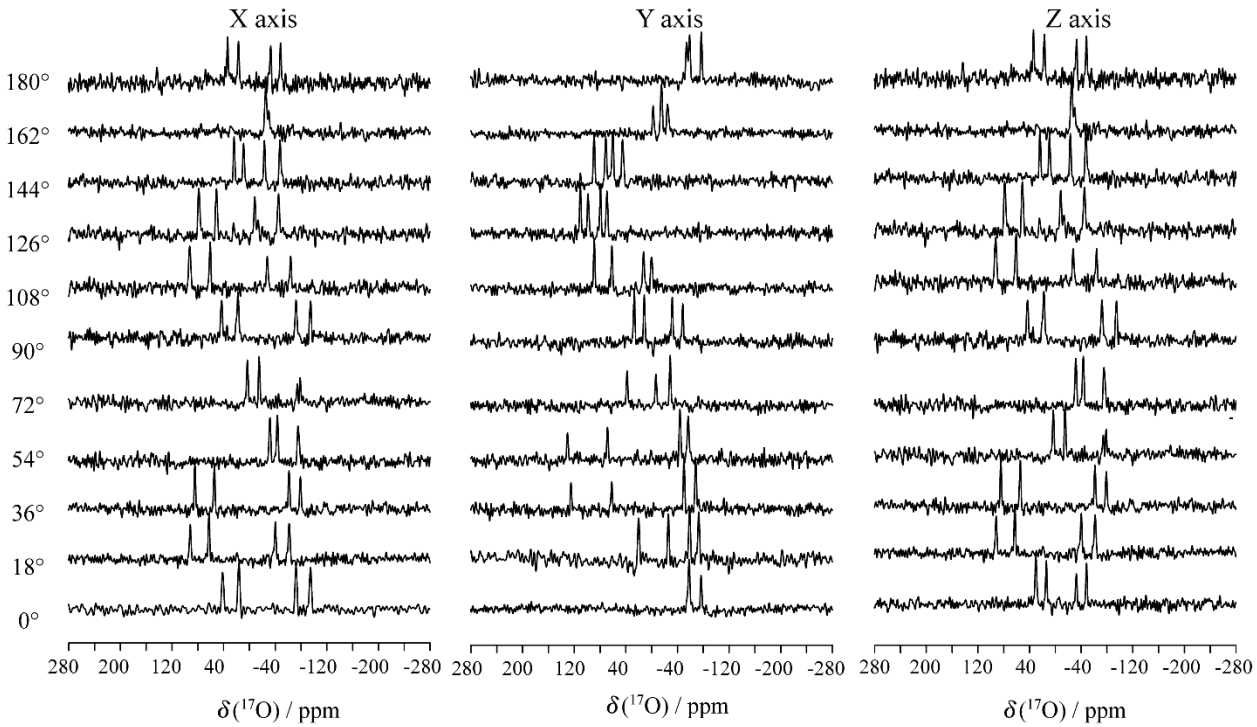

Figure C3. Single-crystal ^{17}O NMR spectra (B_0 = 9.4 T) for monoclinic $Ph_3P^{17}O$. Spectra were obtained at 9° rotational increments about the X, Y, and Z axes. Here only every second spectrum is shown.

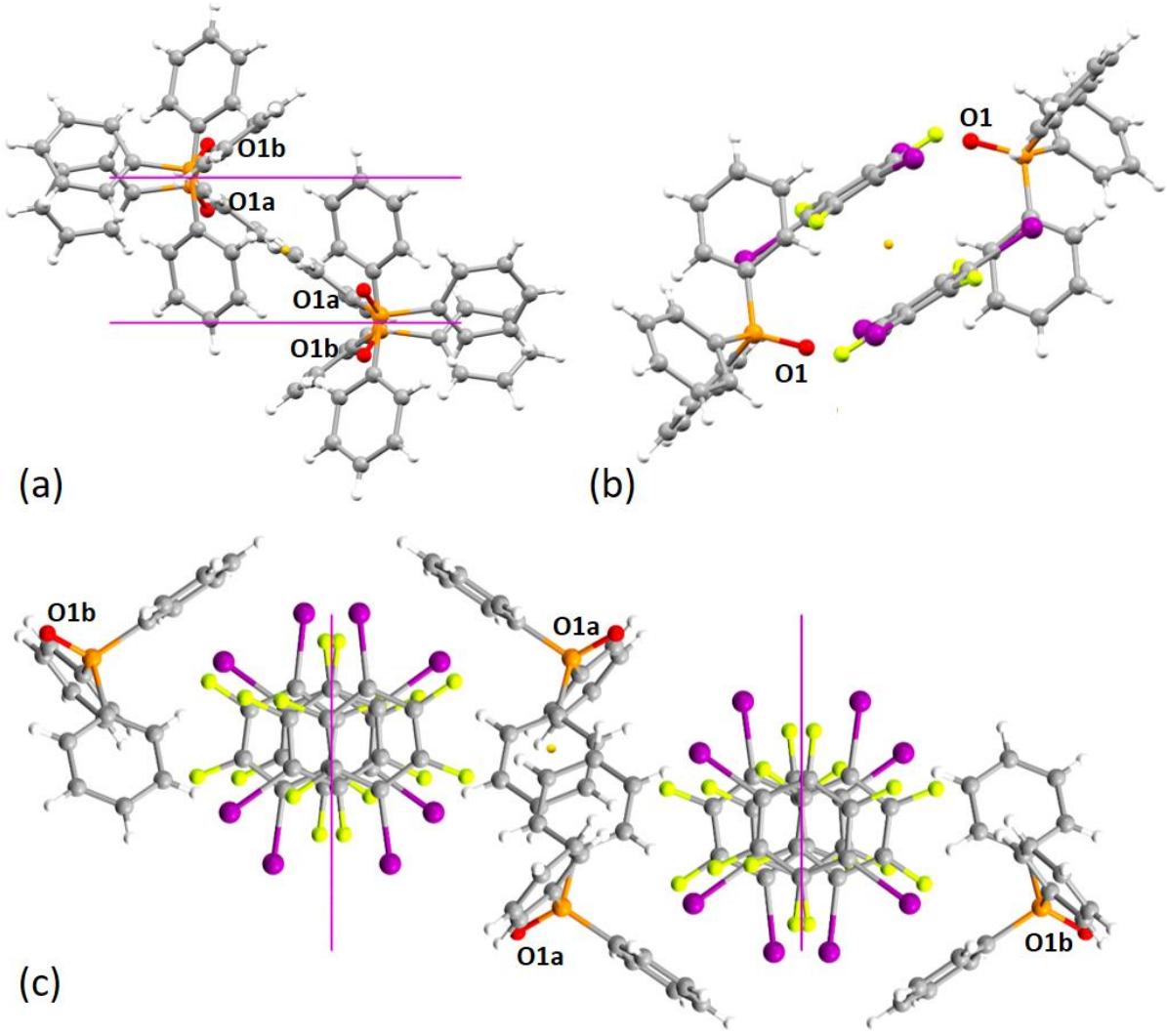

Figure C4. Representation of one unit cell of Ph_3PO (a) and its halogen-bonded cocrystal **2**(b) and **1**(c) from single-crystal X-ray diffraction. The small yellow-orange spheres indicate the inversion centers, resulting in two magnetically equivalent oxygen atoms represent by same label. The pink lines indicate the glide planes, generating two magnetically non-equivalent oxygen atoms represent by different letters.

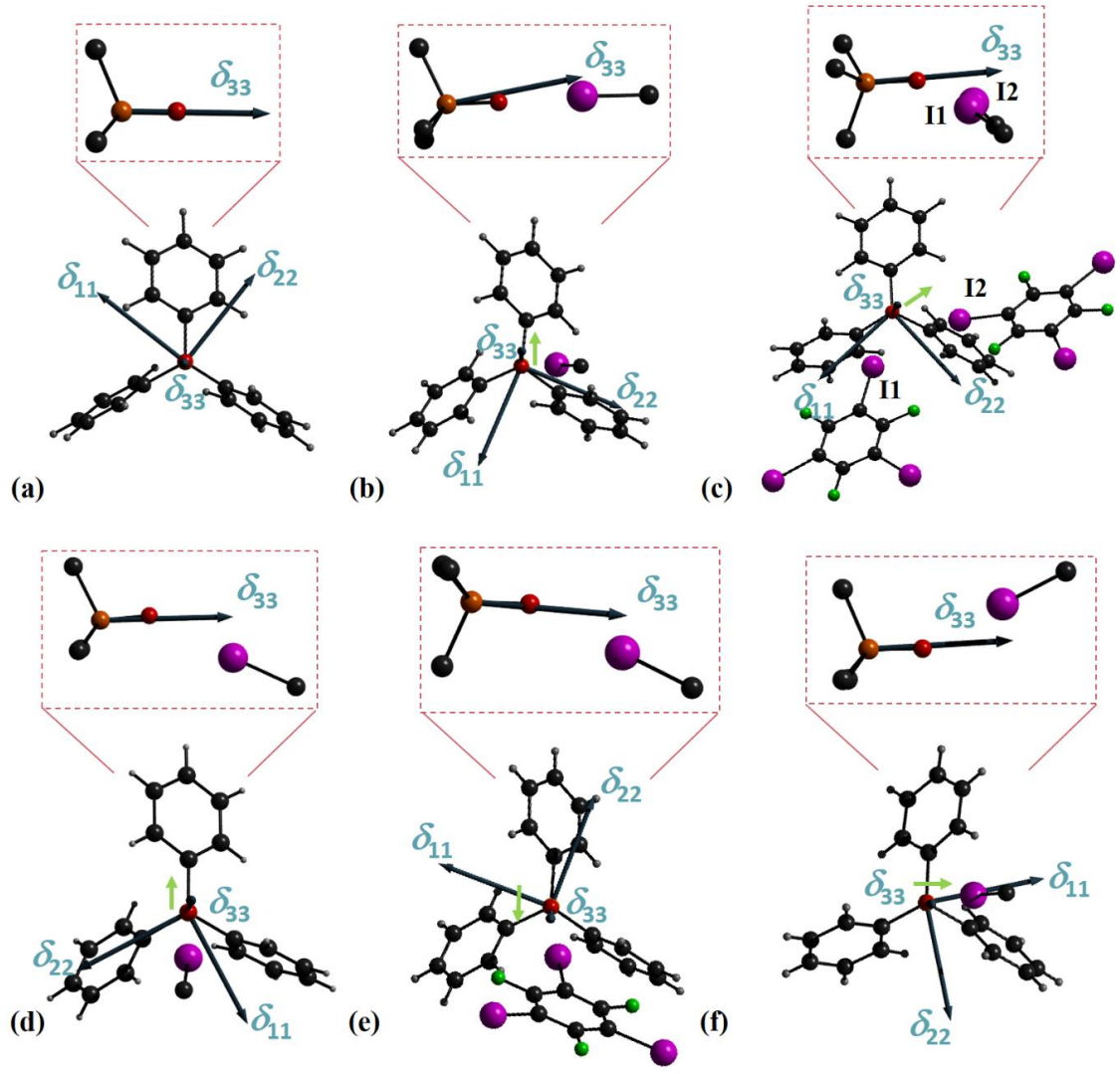

Figure C5. Depictions of the crystal structure of the starting material $Ph_3P^{17}O$ (a), and its halogen-bonded cocrystals: **1** (b), **2** (c) and **2·ACN_1** (d), **2·ACN_2** (e) and **2·ACN_3** (f) where the P=O bond is perpendicular to the plane for illustration of the orientation of ^{31}P CS tensors (indicated by dark green arrows) in the molecular frame. The light green arrows indicate the direction of δ_{33} movement upon halogen bond formation. In **1**, **2·ACN_1**, and **2·ACN_3**, only iodine-carbon fragments are shown; the rest of the molecules are omitted to more clearly show the vectors. Shown in the insets are the truncated projections of the structures when the P=O bond is within the plane to illustrate the change in direction of δ_{33}.

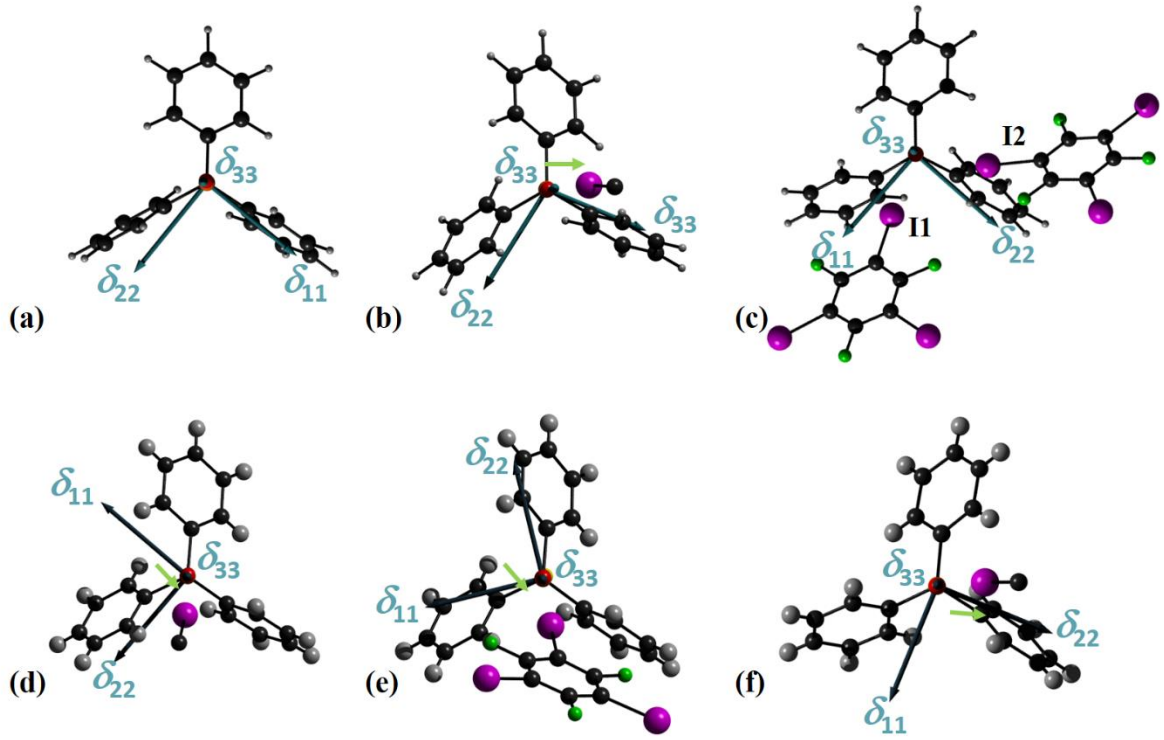

Figure C6. Projection of the crystal structures of the starting material $Ph_3P^{17}O$ (a), and its halogen-bonded cocrystals: **1** (b), **2** (c), and **2·ACN _1** (d), **2·ACN _2** (e) and **2·ACN _3** (f) where the P=O bond is perpendicular to the plane for illustration of the GIPAW DFT-calculated orientations of ^{31}P the CS tensors (indicated as dark green arrows) in the molecular frame. The light green arrows indicate the direction of δ_{33} movement upon halogen bonding. In **1, 2·ACN _1**, and **2·ACN _3**, only iodine-carbon fragments are shown and the rest of the molecules are omitted to more clearly show the vectors.

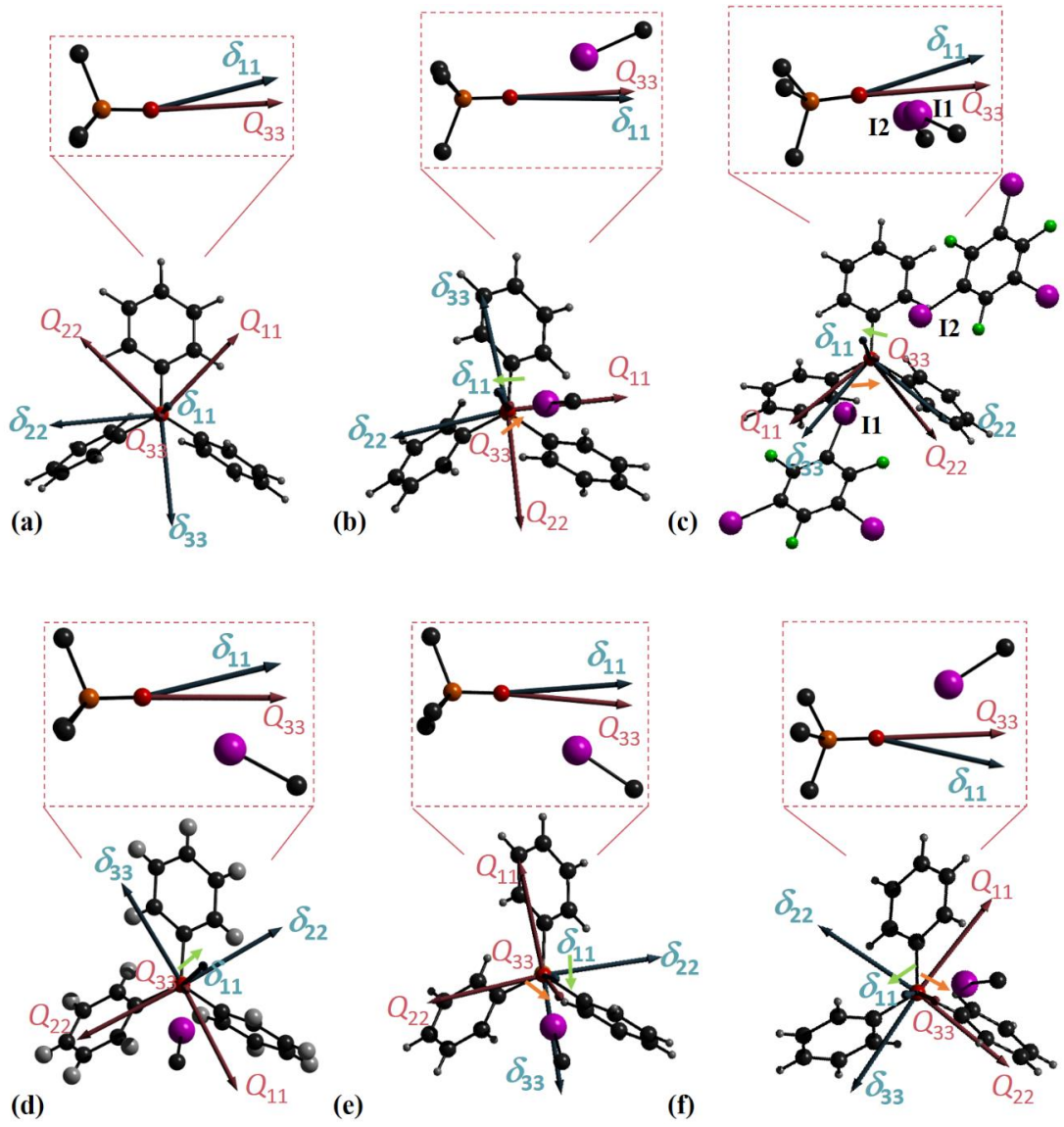

Figure C7. Projection of the crystal structure of the starting material $Ph_3P^{17}O$ (a), and its halogen-bonded cocrystals: **1** (b), **2** (c) and **2·ACN_1** (d), **2·ACN_2** (e), and **2·ACN_3** (f) where the P=O bond is perpendicular to the plane to illustrate the orientation of the principal components of the ^{17}O CS (dark green arrows) and quadrupolar coupling tensors (pink arrows) in the molecular frame. The light green arrows and orange arrows, respectively, indicate the direction of δ_{11} and Q_{33} movement upon halogen bonding. In **1** and **2·ACN**, only iodine-carbon fragments are shown and the rest of the molecules are omitted to more clearly show the vectors. Shown in the insets are the simplified projections of the structures when the P=O bond is within the plane to illustrate the change of the direction of δ_{11} and Q_{33}.

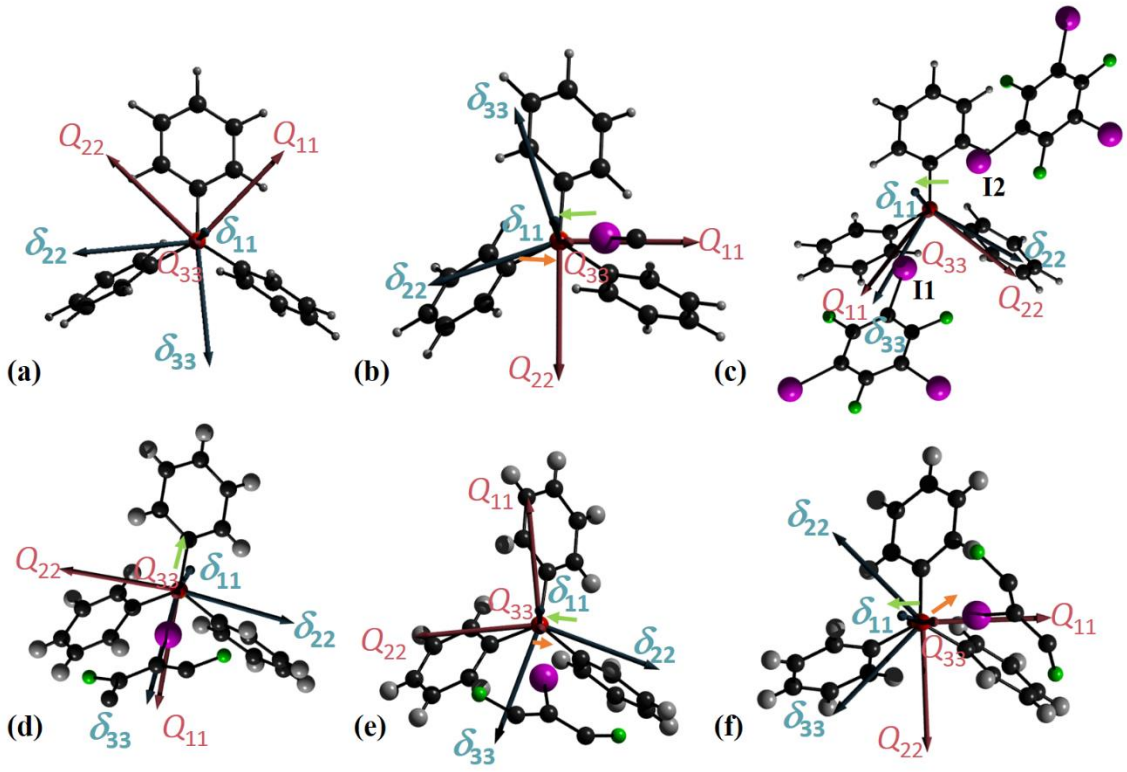

Figure C8. Projection of the crystal structure of the starting material $Ph_3P^{17}O$ (a), and its halogen-bonded cocrystals: **1** (b), **2** (c) and **2·ACN_1** (d), **2·ACN _2** (e), and **2·ACN _3** (f) where the P=O bond is perpendicular to the plane to illustrate the GIPAW DFT-calculated orientation of the principal components of ^{17}O CS (dark green arrows) and quadrupolar coupling tensors (pink arrows) in the molecular frame. The green arrows and orange arrows, respectively, indicate the direction of δ_{11} and Q_{33} movement upon halogen bonding. In **1** and **2·ACN**, only iodine-carbon fragments are shown and the rest of the molecules are omitted to more clearly show the vectors.

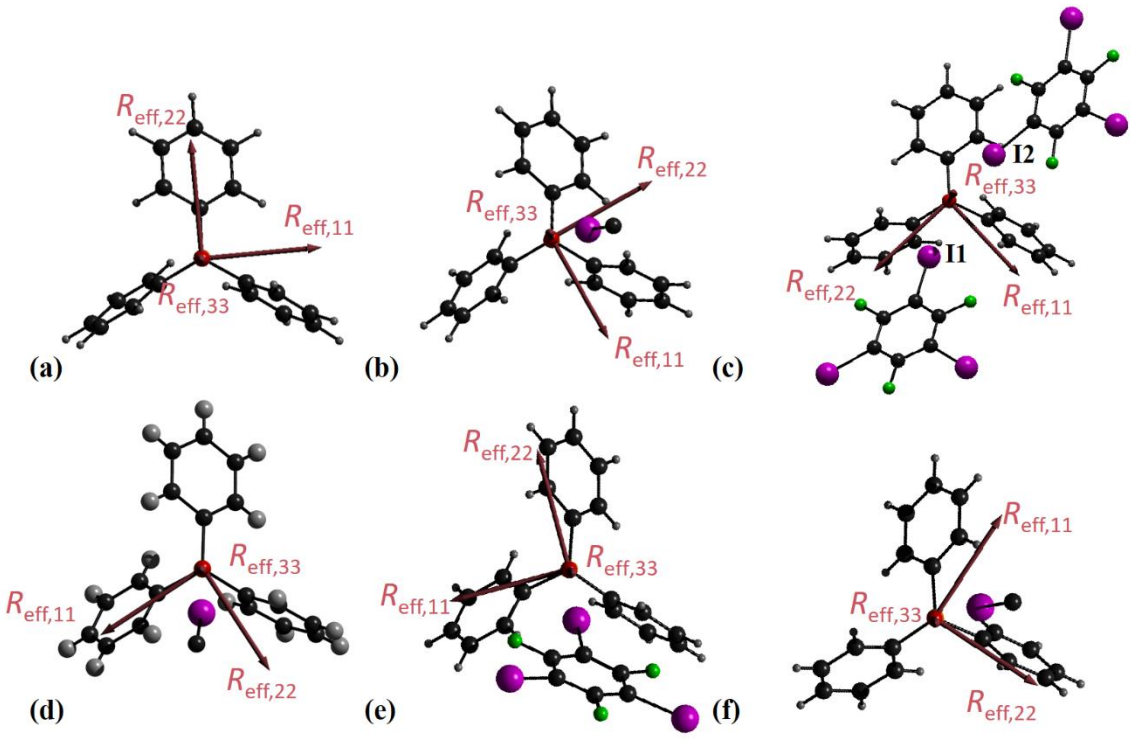

Figure C9. Projection of the crystal structures of the starting material $Ph_3P^{17}O$ (a), and its halogen-bonded cocrystals: **1** (b), **2** (c) and **2·ACN _1** (d), **2·ACN _2** (e), and **2·ACN _3** (f) where the P=O bond is perpendicular to the plane for illustration of the experimental orientations of ^{31}P-^{17}O effective dipolar coupling principal components (indicated as pink arrows) in the molecular frame. In **1**, **2·ACN _1**, and **2·ACN _3**, only iodine-carbon fragments are shown and the rest of the molecules are omitted to more clearly show the vectors.

Table C1. Single-Crystal X-Ray Data and Selected Data Collection Parameters for **2·ACN**

	2·ACN
Empirical Formula	$C_{26}H_{18}F_3I_3NOP$
Formula Weight	829.08
Crystal Size, mm^3	0.722 × 0.404 × 0.353
Crystal System	Triclinic
Space Group	$P\bar{1}$
Z	6
Volume, Å	4229.61(13)
Calculated density, Mg m^{-3}	1.953
a, Å	13.6994 (2)
b, Å	18.2829 (4)
c, Å	20.3552 (3)
α, deg	115.9880 (10)
β, deg	92.9510 (10)
γ, deg	108.6840 (10)
Absorption coefficient, mm^{-1}	3.421
F(000)	2340
θ range for data collection, °	1.845 to 26.500
Limiting indices	$-15 \le h \le 17$, $-22 \le k \le 18$, $-24 \le l \le 25$
Reflections collected/ unique	33791 / 17404
R_{int}	0.0298
Completeness to θ = 25.242°, %	99.3
Max and min transmission	0.746 and 0.534
Data/ restraints/ parameters	17404 / 0 / 949
Goodness-of-fit on F^2	0.975
Final *R* indices [$I > 2\alpha(I)$]	R_1 = 0.0427, wR_2 = 0.0904
R indices (all data)	R_1 = 0.0983, wR_2 = 0.1179
largest diff. peak and hole, e·$Å^{-3}$	0.669 and -1.145

Table C2. Principal Components and Direction Cosines of the ^{31}P Chemical Shift Tensors in the Crystal Axis Frame[a]

compound		components / ppm	a*	b	c
	δ_{11}	96.6(3)	-0.60(2)	0.53(1)	0.60(2)
Ph_3PO	δ_{22}	83.3(6)	0.74(1)	0.65(2)	0.16(4)
	δ_{33}	-101.3(7)	0.31(4)	-0.54(2)	0.79(1)
	δ_{11}	93.9(1)	0.06(3)	-0.48(3)	0.88(3)
1	δ_{22}	89.1(7)	0.90(2)	-0.35(3)	-0.25(5)
	δ_{33}	-92.0(2)	0.42(4)	0.81(3)	0.41(1)
	δ_{11}	96.4(3)	0.10(3)	-0.95(3)	0.31(2)
2[b]	δ_{22}	82.5(7)	-0.96(2)	-0.01(3)	0.28(5)
	δ_{33}	-92.0(7)	0.26(4)	0.32(3)	0.91(1)
2·ACN	δ_{11}	92 (1)	-0.93(2)	0.37(5)	0.07(1)
	δ_{22}	87(2)	-0.37(4)	-0.83(2)	-0.43(2)
	δ_{33}	-94(6)	0.10(2)	0.42(3)	-0.90(1)
	δ_{11}	93(1)	-0.98(2)	-0.10(1)	-0.17(1)
	δ_{22}	87(2)	-0.16(2)	0.92(2)	0.37(2)
	δ_{33}	-96(6)	0.12(2)	0.39(3)	-0.91(1)
	δ_{11}	92(1)	-0.92(2)	0.38(5)	0.06(1)
	δ_{22}	87(2)	-0.37(4)	-0.83(2)	-0.42(2)
	δ_{33}	-98(6)	0.11(2)	0.41(3)	-0.90(2)

[a] The convention used for designating the three principal components of the CS tensor is $\delta_{11} \geq \delta_{22} \geq \delta_{33}$.

[b] Compound **2** cannot provide error estimates generated from comparison between two crystallographic equivalent but magnetically distinct sites like Ph_3PO and **1**. Uncertainties from single-crystal NMR data fitting are only on the order of 0.1 ppm. Therefore, we estimate the error to be similar to the largest error present in analysis of Ph_3PO and **1**.

Table C3. Principal Components and Direction Cosines of the ^{17}O Chemical Shift Tensors in the Crystal Axis Frame[a]

compound		components / ppm	a*	b	c
Ph_3PO	δ_{11}	151(8)	-0.43(2)	0.41(3)	-0.81(1)
	δ_{22}	12(1)	-0.86(2)	0.05(5)	0.49(3)
	δ_{33}	-8(2)	0.24(3)	0.91(2)	0.33(6)
1	δ_{11}	109(3)	-0.50(5)	-0.71(3)	-0.49(1)
	δ_{22}	19(2)	0.63(7)	0.08(7)	-0.78(7)
	δ_{33}	5(1)	0.59(6)	-0.70(3)	0.40(12)
2[b]	δ_{11}	152(8)	0.42(5)	0.29(3)	0.86(1)
	δ_{22}	33(2)	0.90(7)	-0.23(7)	-0.37(7)
	δ_{33}	-10(2)	-0.09(6)	-0.93(3)	0.36(12)
2·ACN[b]	δ_{11}	125(8)	0.19(5)	0.56(3)	-0.81(1)
	δ_{22}	29(2)	-0.92(7)	0.38(7)	0.05(7)
	δ_{33}	-11(2)	-0.34(6)	-0.74(3)	-0.58(12)
	δ_{11}	133(8)	0.33(5)	0.57(3)	-0.75(1)
	δ_{22}	41(2)	-0.89(7)	-0.08(7)	-0.46(7)
	δ_{33}	-30(2)	0.32(6)	-0.82(3)	-0.47(12)

[a] The convention used for designating the three principal components of the CS tensor is $\delta_{11} \geq \delta_{22} \geq \delta_{33}$.

[b] Compounds **2** and **2·ACN** cannot provide error estimates generated from comparison between two crystallographic equivalent but magnetically distinct sites like Ph_3PO and **1**. Uncertainties from single-crystal NMR data fitting are only on the order of 0.1 ppm for CS tensors. Therefore, we estimate the error to be similar to the largest error present in analysis of Ph_3PO and **1**.

Table C4. Principal Components (in MHz) and Direction Cosines of the ^{17}O Intermediate Quadrupolar Coupling Tensors in the Crystal Axis Frame[a]

compound		components / MHz	a*	b	c
Ph_3PO	Q_{33}	-0.228(2)	0.32(2)	-0.50(2)	0.80(1)
	Q_{22}	0.118(1)	0.22(6)	-0.78(2)	-0.58(1)
	Q_{11}	0.110(3)	-0.92(2)	-0.37(6)	-0.14(2)
1	Q_{33}	-0.248(1)	0.46(3)	0.80(1)	0.37(1)
	Q_{22}	0.130(2)	-0.72(1)	0.58(2)	-0.37(4)
	Q_{11}	0.118(1)	-0.51(3)	-0.10(1)	0.85(1)
2[b]	Q_{33}	-0.240(2)	0.20(3)	0.28(2)	0.94(1)
	Q_{22}	0.132(1)	0.98(6)	0.01(2)	-0.21(4)
	Q_{11}	0.108(3)	0.06(3)	-0.96(6)	0.27(2)
2·ACN[b]	Q_{33}	-0.247(2)	0.11(3)	0.43(2)	-0.90(1)
	Q_{22}	0.135(1)	0.89(6)	-0.44(2)	-0.10(4)
	Q_{11}	0.112(3)	-0.43(3)	-0.79(6)	-0.43(2)
	Q_{33}	-0.241(2)	0.13(3)	0.44(2)	-0.89(1)
	Q_{22}	0.133(1)	-0.97(6)	-0.13(2)	-0.21(4)
	Q_{11}	0.107(3)	-0.21(3)	0.89(6)	0.40(2)

[a] The convention used for designating the three principal components of the quadrupolar coupling tensor is $|Q_{33}| \geq |Q_{22}| \geq |Q_{11}|$.

[b] Compounds **2** and **2·ACN** cannot provide error values estimated from comparison between two crystallographic equivalent but magnetically distinct sites like Ph_3PO and **1**. Uncertainties from single-crystal NMR data fitting are only on the order of 0.001 MHz for EFG tensors. Therefore, we estimate the error to be similar to the largest error present in analysis of Ph_3PO and **1**.

Table C5. Principal Components (in Hz) and Direction Cosines of the Averaged Effective ^{17}O-^{31}P Dipolar Coupling Tensors in the Crystal Axis Frame[a]

compound		components / Hz	a*	b	c
Ph_3PO	$R_{eff,33}$	3715(42)	-0.33(3)	0.51(2)	-0.80(1)
	$R_{eff,22}$	-1832(32)	0.22(11)	0.86(2)	0.46(4)
	$R_{eff,11}$	-1883(10)	-0.92(3)	0.03(11)	0.39(4)
1	$R_{eff,33}$	3734(20)	-0.45(3)	-0.80(3)	-0.40(2)
	$R_{eff,22}$	-1821(10)	0.74(2)	-0.09(5)	-0.67(3)
	$R_{eff,11}$	-1913(30)	-0.50(5)	0.59(3)	-0.63(2)
2[b]	$R_{eff,33}$	3795(42)	0.26(3)	0.32(3)	0.91(3)
	$R_{eff,22}$	-1853(32)	0.10(11)	-0.95(5)	0.31(4)
	$R_{eff,11}$	-1942(30)	-0.96(5)	-0.01(11)	0.28(4)
2·ACN[b]	$R_{eff,33}$	3883(42)	0.11(3)	0.46(3)	-0.88(3)
	$R_{eff,22}$	-1870(32)	-0.44(11)	-0.77(5)	-0.46(4)
	$R_{eff,11}$	-2014(30)	0.89(5)	-0.44(11)	-0.12(4)
	$R_{eff,33}$	3944(42)	0.12(3)	0.44(3)	-0.89(3)
	$R_{eff,22}$	-1900(32)	-0.30(11)	0.87(5)	0.39(4)
	$R_{eff,11}$	-2044(30)	-0.95(5)	-0.22(11)	-0.23(4)

[a] The convention used for designating the three principal components of the effective ^{31}P-^{17}O dipolar coupling tensor is $|R_{eff,33}| \geq |R_{eff,11}| \geq |R_{eff,22}|$.

[b] Compounds **2** and **2·ACN** cannot provide error values estimated from comparison between two crystallographic equivalent but magnetically distinct sites like Ph_3PO and **1**. Uncertainties from single-crystal NMR data fitting are only on the order of 10 Hz. Therefore, we estimate the error to be similar to the largest error present in analysis of Ph_3PO and **1**.

Appendix D: Supporting Information for Chapter 6

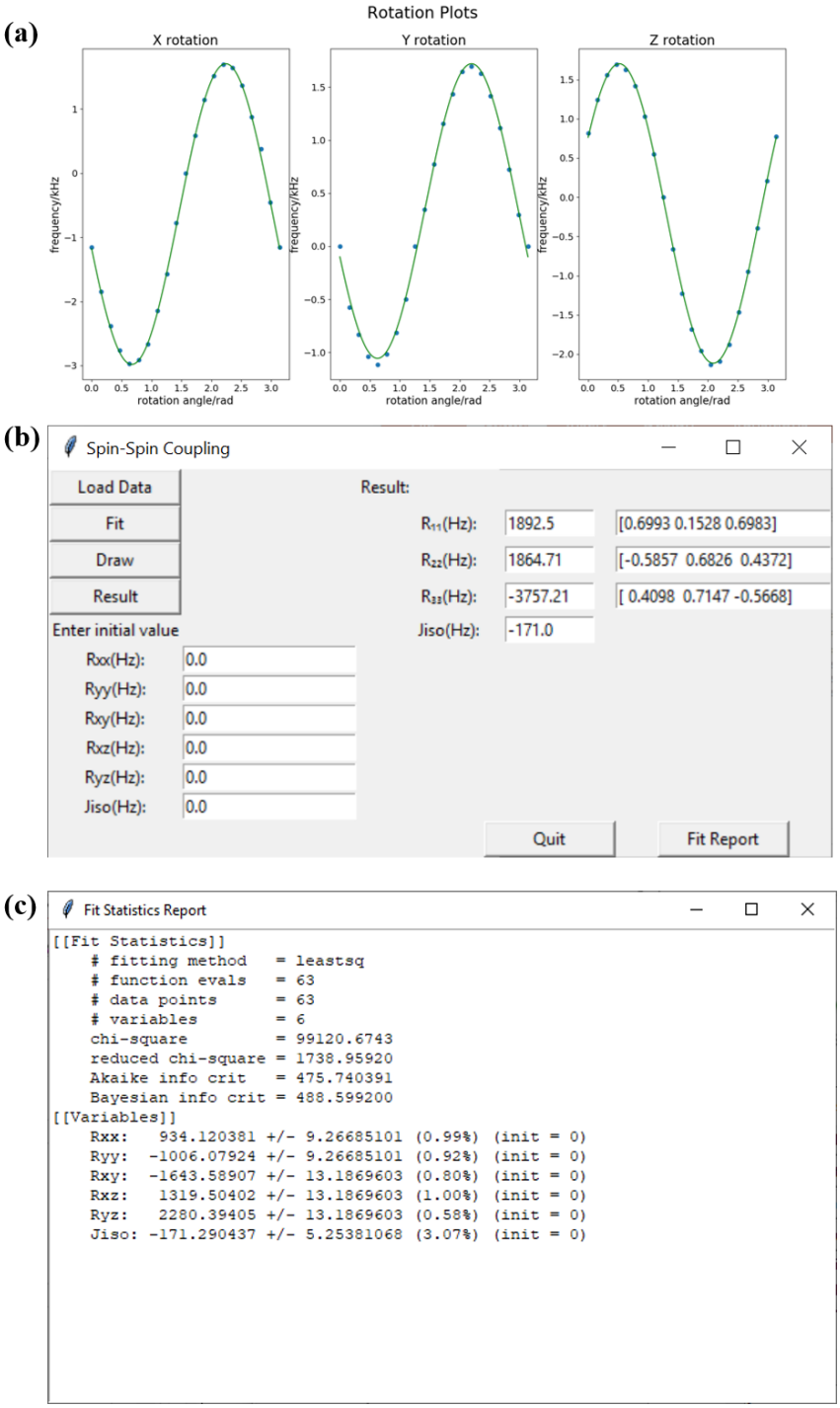

Figure D1. Screenshots of the *Plot* window (a) created by the *Draw* button, *Result* window (b) created by the *Result* button and *Fit* Statistics window (c) created by the *Fit Report* button for *Spin-Spin Coupling* analysis.

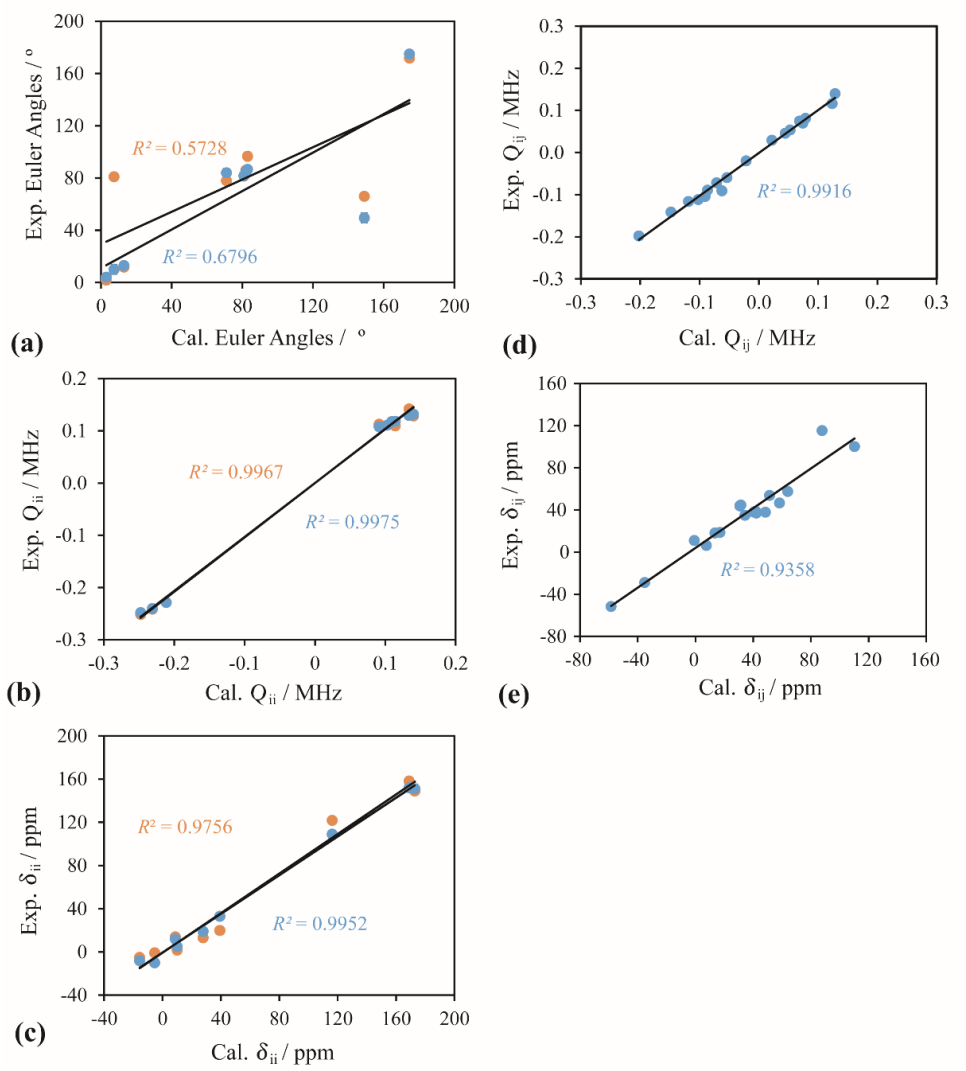

Figure D2. Plots of experimental versus calculated Euler angles (a), ^{17}O intermediate quadrupolar coupling principal components (Q_{ii}) (b), ^{17}O chemical shift principal components (δ_{ii}) (c), the complete ^{17}O intermediate quadrupolar coupling tensors (Q_{ij}) (d), and the complete ^{17}O chemical shift tensors (δ_{ij}) (e) for $Ph_3P^{17}O$ and cocrystals 1 and 2. Results generated from the simulation of powder patterns (orange) and *Free Fit* single-crystal NMR analysis (blue) are presented here. Lines represent the best linear fits: *Powder:* $Exp.Euler = 0.619Cal.Euler + 29.358$; *Free Fit:* $Exp.Euler = 0.737Cal.Euler + 11.084$; *Powder:* $Exp.Q_{ii} = 1.0403Cal.Q_{ii} - 3 \times 10^{-18}$; *Free Fit:* $Exp.Q_{ii} = 1.0328Cal.Q_{ii} - 6 \times 10^{-8}$; *Powder:* $Exp.\delta_{ii} = 0.9156Cal.\delta_{ii} - 0.7532$; *Free Fit:* $Exp.\delta_{ii} = 0.8959Cal.\delta_{ii} - 0.6192$; *Free Fit* : $Exp.Q_{ij} = 1.0175Cal.Q_{ij} - 0.001$; *Free Fit:* $Exp.\delta_{ii} = 0.9431Cal.\delta_{ii} + 3.9424$.

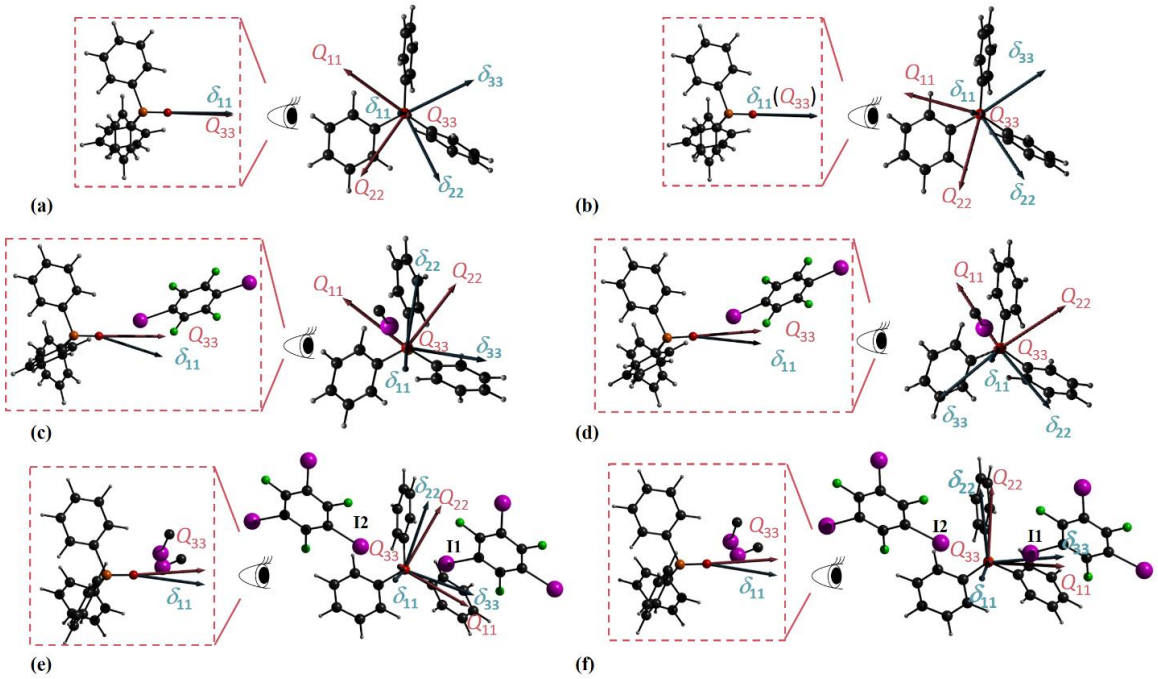

Figure D3. Projection of the crystal structure of $Ph_3P^{17}O$ (top), and its halogen-bonded cocrystals: **1** (middle) and **2** (bottom) where the P=O bond is perpendicular to the plane of the page for ^{17}O CS (dark green vectors) and intermediate quadrupolar coupling tensors (pink vectors) in the molecular frame. Left column ((a), (c), and (e)) contains the tensor orientations obtained from a constrained SCNMR fit and right column ((b), (d), and (f)) contains the tensor orientations obtained from a free fit of the SCNMR data. Shown in the insets are projections of the structures when the P=O bond is within the plane to illustrate the change of the direction of all the vectors.

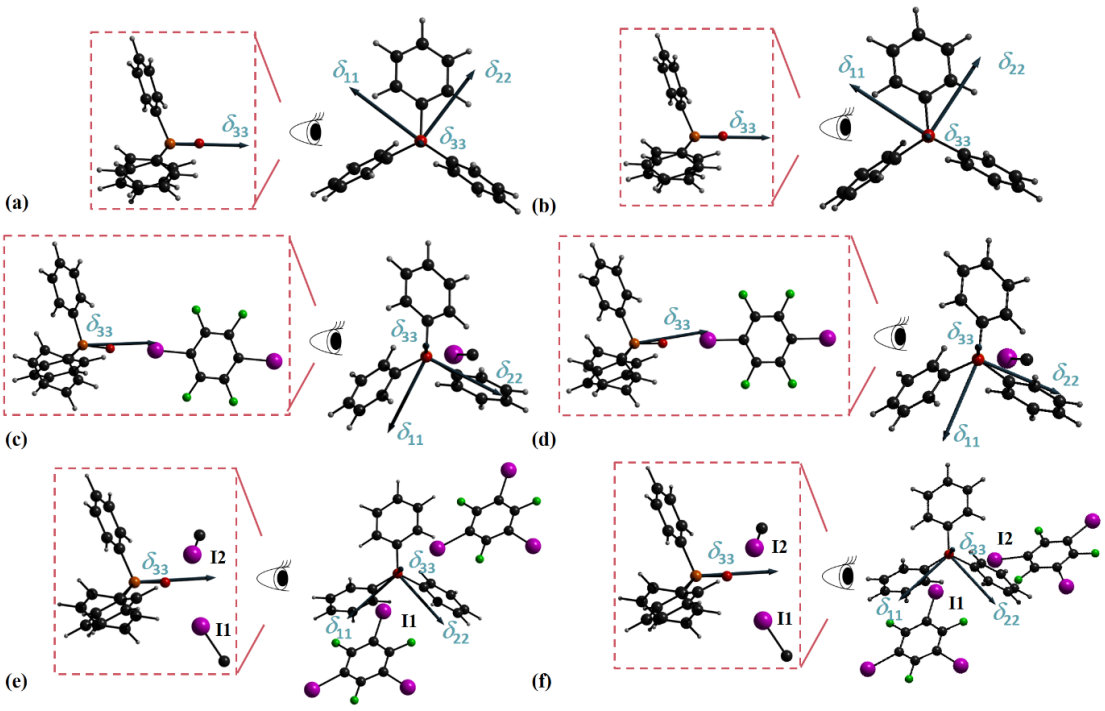

Figure D4. Projection of the crystal structure of Ph_3PO (top), and its halogen-bonded cocrystals: **1** (middle) and **2** (bottom) when the P=O bond is perpendicular to the plane of the page for ^{31}P CS tensors in the molecular frame. The left column ((a), (c), and (e)) contains the tensor orientations obtained from a constrained SCNMR fit and the right column ((b), (d), and (f)) contains the tensor orientations obtained from a free fit of the SCNMR data. Shown in the insets are the projections of the structures when the P=O bond is within the plane to illustrate the change of the direction of δ_{33}.

Equations input in the software

Free Fit:

```
x=((q/8)*((-11)*(Qyy*Qyy+(-Qxx-Qyy)*(-Qxx-Qyy))-50*Qyy*(-Qxx-
Qyy)+28*Qyz*Qyz+16*(Qxy*Qxy+Qxz*Qxz))+(dyy+dzz)*v/2000000)+((3*q/
2)*(Qyy*Qyy-(-Qxx-Qyy)*(-Qxx-Qyy)+4*Qxy*Qxy-4*Qxz*Qxz)+(dyy-
dzz)*v/2000000)*np.cos(2*t1)+((-3*q)*((Qyy+(-Qyy-
Qxx))*Qyz+4*Qxy*Qxz)-dyz*v/1000000)*np.sin(2*t1)+((-9*q/8)*((Qyy-
(-Qyy-Qxx))*(Qyy-(-Qyy-Qxx))-
4*Qyz*Qyz))*np.cos(4*t1)+((9*q/2)*(Qyy-(-Qyy-
Qxx))*Qyz)*np.sin(4*t1);

y=((q/8)*((-11)*(Qxx*Qxx+(-Qxx-Qyy)*(-Qxx-Qyy))-50*Qxx*(-Qxx-
Qyy)+28*Qxz*Qxz+16*(Qyz*Qyz+Qxy*Qxy))+(dxx+dzz)*v/2000000)+((3*q/
2)*((-Qxx-Qyy)*(-Qxx-Qyy)-Qxx*Qxx+4*Qyz*Qyz-4*Qxy*Qxy)+(dzz-
dxx)*v/2000000)*np.cos(2*t1)+((-3*q)*((Qxx+(-Qyy-
Qxx))*Qxz+4*Qxy*Qyz)-dxz*v/1000000)*np.sin(2*t1)+((-9*q/8)*(((-
Qyy-Qxx)-Qxx)*((-Qyy-Qxx)-Qxx)-
4*Qxz*Qxz))*np.cos(4*t1)+((9*q/2)*((-Qyy-Qxx)-
Qxx)*Qxz)*np.sin(4*t1);

z=((q/8)*((-11)*(Qxx*Qxx+Qyy*Qyy)-
50*Qxx*Qyy+28*Qxy*Qxy+16*(Qxz*Qxz+Qyz*Qyz))+(dxx+dyy)*v/2000000)+
((3*q/2)*(Qxx*Qxx-Qyy*Qyy+4*Qxz*Qxz-4*Qyz*Qyz)+(dxx-
dyy)*v/2000000)*np.cos(2*t1)+((-3*q)*((Qxx+Qyy)*Qxy+4*Qyz*Qxz)-
dxy*v/1000000)*np.sin(2*t1)+((-9*q/8)*((Qxx-Qyy)*(Qxx-Qyy)-
4*Qxy*Qxy))*np.cos(4*t1)+((9*q/2)*((Qxx-Qyy)*Qxy))*np.sin(4*t1)
```

Constrained Fit:

```
x=((q/8)*((-11)*((fixQzz*(-np.cos(a1)*np.cos(b1)*np.sin(g1)-
np.sin(a1)*np.cos(g1))**2+fixQyy*(-
np.sin(a1)*np.cos(b1)*np.sin(g1)+np.cos(a1)*np.cos(g1))**2+(-
fixQzz-fixQyy)*(np.sin(b1)*np.sin(g1))**2)*(fixQzz*(-
np.cos(a1)*np.cos(b1)*np.sin(g1)-
np.sin(a1)*np.cos(g1))**2+fixQyy*(-
np.sin(a1)*np.cos(b1)*np.sin(g1)+np.cos(a1)*np.cos(g1))**2+(-
fixQzz-
fixQyy)*(np.sin(b1)*np.sin(g1))**2)+((fixQzz*(np.cos(a1)*np.sin(b
1))**2+fixQyy*(np.sin(a1)*np.sin(b1))**2+(-fixQzz-
fixQyy)*(np.cos(b1))**2))*((fixQzz*(np.cos(a1)*np.sin(b1))**2+fix
Qyy*(np.sin(a1)*np.sin(b1))**2+(-fixQzz-
```

```
fixQyy)*(np.cos(b1))**2)))-50*(fixQzz*(-
np.cos(a1)*np.cos(b1)*np.sin(g1)-
np.sin(a1)*np.cos(g1))**2+fixQyy*(-
np.sin(a1)*np.cos(b1)*np.sin(g1)+np.cos(a1)*np.cos(g1))**2+(-
fixQzz-
fixQyy)*(np.sin(b1)*np.sin(g1))**2)*((fixQzz*(np.cos(a1)*np.sin(b
1))**2+fixQyy*(np.sin(a1)*np.sin(b1))**2+(-fixQzz-
fixQyy)*(np.cos(b1))**2))+28*(fixQzz*(-
np.cos(a1)*np.cos(b1)*np.sin(g1)-
np.sin(a1)*np.cos(g1))*(np.cos(a1)*np.sin(b1))+fixQyy*(-
np.sin(a1)*np.cos(b1)*np.sin(g1)+np.cos(a1)*np.cos(g1))*(np.sin(a
1)*np.sin(b1))+(-fixQzz-
fixQyy)*(np.cos(b1))*(np.sin(b1)*np.sin(g1)))*(fixQzz*(-
np.cos(a1)*np.cos(b1)*np.sin(g1)-
np.sin(a1)*np.cos(g1))*(np.cos(a1)*np.sin(b1))+fixQyy*(-
np.sin(a1)*np.cos(b1)*np.sin(g1)+np.cos(a1)*np.cos(g1))*(np.sin(a
1)*np.sin(b1))+(-fixQzz-
fixQyy)*(np.cos(b1))*(np.sin(b1)*np.sin(g1)))+16*((fixQzz*(np.cos
(a1)*np.cos(b1)*np.cos(g1)-np.sin(a1)*np.sin(g1))*(-
np.cos(a1)*np.cos(b1)*np.sin(g1)-
np.sin(a1)*np.cos(g1))+fixQyy*(np.sin(a1)*np.cos(b1)*np.cos(g1)+n
p.cos(a1)*np.sin(g1))*(-
np.sin(a1)*np.cos(b1)*np.sin(g1)+np.cos(a1)*np.cos(g1))+(-fixQzz-
fixQyy)*(-
np.sin(b1)*np.cos(g1))*(np.sin(b1)*np.sin(g1)))*(fixQzz*(np.cos(a
1)*np.cos(b1)*np.cos(g1)-np.sin(a1)*np.sin(g1))*(-
np.cos(a1)*np.cos(b1)*np.sin(g1)-
np.sin(a1)*np.cos(g1))+fixQyy*(np.sin(a1)*np.cos(b1)*np.cos(g1)+n
p.cos(a1)*np.sin(g1))*(-
np.sin(a1)*np.cos(b1)*np.sin(g1)+np.cos(a1)*np.cos(g1))+(-fixQzz-
fixQyy)*(-
np.sin(b1)*np.cos(g1))*(np.sin(b1)*np.sin(g1)))+(fixQzz*(np.cos(a
1)*np.cos(b1)*np.cos(g1)-
np.sin(a1)*np.sin(g1))*(np.cos(a1)*np.sin(b1))+fixQyy*(np.sin(a1)
*np.cos(b1)*np.cos(g1)+np.cos(a1)*np.sin(g1))*(np.sin(a1)*np.sin(
b1))+(-fixQzz-fixQyy)*(-
np.sin(b1)*np.cos(g1))*(np.cos(b1)))*(fixQzz*(np.cos(a1)*np.cos(b
1)*np.cos(g1)-
np.sin(a1)*np.sin(g1))*(np.cos(a1)*np.sin(b1))+fixQyy*(np.sin(a1)
*np.cos(b1)*np.cos(g1)+np.cos(a1)*np.sin(g1))*(np.sin(a1)*np.sin(
b1))+(-fixQzz-fixQyy)*(-
np.sin(b1)*np.cos(g1))*(np.cos(b1)))))+((Sxx/1000000*(-
np.cos(a2)*np.cos(b2)*np.sin(g2)-
np.sin(a2)*np.cos(g2))**2+Syy/1000000*(-
np.sin(a2)*np.cos(b2)*np.sin(g2)+np.cos(a2)*np.cos(g2))**2+Szz/10
00000*(np.sin(b2)*np.sin(g2))**2)+(Sxx/1000000*(np.cos(a2)*np.sin
(b2))**2+Syy/1000000*(np.sin(a2)*np.sin(b2))**2+Szz/1000000*(np.c
os(b2))**2))*v/2)+((3*q/2)*((fixQzz*(-
np.cos(a1)*np.cos(b1)*np.sin(g1)-
np.sin(a1)*np.cos(g1))**2+fixQyy*(-
np.sin(a1)*np.cos(b1)*np.sin(g1)+np.cos(a1)*np.cos(g1))**2+(-
fixQzz-fixQyy)*(np.sin(b1)*np.sin(g1))**2)*(fixQzz*(-
```

```
np.cos(a1)*np.cos(b1)*np.sin(g1)-
np.sin(a1)*np.cos(g1))**2+fixQyy*(-
np.sin(a1)*np.cos(b1)*np.sin(g1)+np.cos(a1)*np.cos(g1))**2+(-
fixQzz-fixQyy)*(np.sin(b1)*np.sin(g1))**2)-
((fixQzz*(np.cos(a1)*np.sin(b1))**2+fixQyy*(np.sin(a1)*np.sin(b1)
)**2+(-fixQzz-
fixQyy)*(np.cos(b1))**2))*((fixQzz*(np.cos(a1)*np.sin(b1))**2+fix
Qyy*(np.sin(a1)*np.sin(b1))**2+(-fixQzz-
fixQyy)*(np.cos(b1))**2))+4*(fixQzz*(np.cos(a1)*np.cos(b1)*np.cos
(g1)-np.sin(a1)*np.sin(g1))*(-np.cos(a1)*np.cos(b1)*np.sin(g1)-
np.sin(a1)*np.cos(g1))+fixQyy*(np.sin(a1)*np.cos(b1)*np.cos(g1)+n
p.cos(a1)*np.sin(g1))*(-
np.sin(a1)*np.cos(b1)*np.sin(g1)+np.cos(a1)*np.cos(g1))+(-fixQzz-
fixQyy)*(-
np.sin(b1)*np.cos(g1))*(np.sin(b1)*np.sin(g1)))*(fixQzz*(np.cos(a
1)*np.cos(b1)*np.cos(g1)-np.sin(a1)*np.sin(g1))*(-
np.cos(a1)*np.cos(b1)*np.sin(g1)-
np.sin(a1)*np.cos(g1))+fixQyy*(np.sin(a1)*np.cos(b1)*np.cos(g1)+n
p.cos(a1)*np.sin(g1))*(-
np.sin(a1)*np.cos(b1)*np.sin(g1)+np.cos(a1)*np.cos(g1))+(-fixQzz-
fixQyy)*(-np.sin(b1)*np.cos(g1))*(np.sin(b1)*np.sin(g1)))-
4*(fixQzz*(np.cos(a1)*np.cos(b1)*np.cos(g1)-
np.sin(a1)*np.sin(g1))*(np.cos(a1)*np.sin(b1))+fixQyy*(np.sin(a1)
*np.cos(b1)*np.cos(g1)+np.cos(a1)*np.sin(g1))*(np.sin(a1)*np.sin(
b1))+(-fixQzz-fixQyy)*(-
np.sin(b1)*np.cos(g1))*(np.cos(b1)))*(fixQzz*(np.cos(a1)*np.cos(b
1)*np.cos(g1)-
np.sin(a1)*np.sin(g1))*(np.cos(a1)*np.sin(b1))+fixQyy*(np.sin(a1)
*np.cos(b1)*np.cos(g1)+np.cos(a1)*np.sin(g1))*(np.sin(a1)*np.sin(
b1))+(-fixQzz-fixQyy)*(-
np.sin(b1)*np.cos(g1))*(np.cos(b1))))+((Sxx/1000000*(-
np.cos(a2)*np.cos(b2)*np.sin(g2)-
np.sin(a2)*np.cos(g2))**2+Syy/1000000*(-
np.sin(a2)*np.cos(b2)*np.sin(g2)+np.cos(a2)*np.cos(g2))**2+Szz/10
00000*(np.sin(b2)*np.sin(g2))**2)-
(Sxx/1000000*(np.cos(a2)*np.sin(b2))**2+Syy/1000000*(np.sin(a2)*n
p.sin(b2))**2+Szz/1000000*(np.cos(b2))**2))*v/2)*np.cos(2*t1)+((-
3*q)*(((fixQzz*(-np.cos(a1)*np.cos(b1)*np.sin(g1)-
np.sin(a1)*np.cos(g1))**2+fixQyy*(-
np.sin(a1)*np.cos(b1)*np.sin(g1)+np.cos(a1)*np.cos(g1))**2+(-
fixQzz-
fixQyy)*(np.sin(b1)*np.sin(g1))**2)+((fixQzz*(np.cos(a1)*np.sin(b
1))**2+fixQyy*(np.sin(a1)*np.sin(b1))**2+(-fixQzz-
fixQyy)*(np.cos(b1))**2)))*(fixQzz*(-
np.cos(a1)*np.cos(b1)*np.sin(g1)-
np.sin(a1)*np.cos(g1))*(np.cos(a1)*np.sin(b1))+fixQyy*(-
np.sin(a1)*np.cos(b1)*np.sin(g1)+np.cos(a1)*np.cos(g1))*(np.sin(a
1)*np.sin(b1))+(-fixQzz-
fixQyy)*(np.cos(b1))*(np.sin(b1)*np.sin(g1)))+4*(fixQzz*(np.cos(a
1)*np.cos(b1)*np.cos(g1)-np.sin(a1)*np.sin(g1))*(-
np.cos(a1)*np.cos(b1)*np.sin(g1)-
np.sin(a1)*np.cos(g1))+fixQyy*(np.sin(a1)*np.cos(b1)*np.cos(g1)+n
```

```
p.cos(a1)*np.sin(g1))*(-
np.sin(a1)*np.cos(b1)*np.sin(g1)+np.cos(a1)*np.cos(g1))+(-fixQzz-
fixQyy)*(-
np.sin(b1)*np.cos(g1))*(np.sin(b1)*np.sin(g1)))*(fixQzz*(np.cos(a
1)*np.cos(b1)*np.cos(g1)-
np.sin(a1)*np.sin(g1))*(np.cos(a1)*np.sin(b1))+fixQyy*(np.sin(a1)
*np.cos(b1)*np.cos(g1)+np.cos(a1)*np.sin(g1))*(np.sin(a1)*np.sin(
b1))+(-fixQzz-fixQyy)*(-np.sin(b1)*np.cos(g1))*(np.cos(b1))))-
(Sxx/1000000*(-np.cos(a2)*np.cos(b2)*np.sin(g2)-
np.sin(a2)*np.cos(g2))*(np.cos(a2)*np.sin(b2))+Syy/1000000*(-
np.sin(a2)*np.cos(b2)*np.sin(g2)+np.cos(a2)*np.cos(g2))*(np.sin(a
2)*np.sin(b2))+Szz/1000000*(np.cos(b2))*(np.sin(b2)*np.sin(g2)))*
v)*np.sin(2*t1)+((-9*q/8)*(((fixQzz*(-
np.cos(a1)*np.cos(b1)*np.sin(g1)-
np.sin(a1)*np.cos(g1))**2+fixQyy*(-
np.sin(a1)*np.cos(b1)*np.sin(g1)+np.cos(a1)*np.cos(g1))**2+(-
fixQzz-fixQyy)*(np.sin(b1)*np.sin(g1))**2)-
((fixQzz*(np.cos(a1)*np.sin(b1))**2+fixQyy*(np.sin(a1)*np.sin(b1)
)**2+(-fixQzz-fixQyy)*(np.cos(b1))**2)))*((fixQzz*(-
np.cos(a1)*np.cos(b1)*np.sin(g1)-
np.sin(a1)*np.cos(g1))**2+fixQyy*(-
np.sin(a1)*np.cos(b1)*np.sin(g1)+np.cos(a1)*np.cos(g1))**2+(-
fixQzz-fixQyy)*(np.sin(b1)*np.sin(g1))**2)-
((fixQzz*(np.cos(a1)*np.sin(b1))**2+fixQyy*(np.sin(a1)*np.sin(b1)
)**2+(-fixQzz-fixQyy)*(np.cos(b1))**2)))-4*(fixQzz*(-
np.cos(a1)*np.cos(b1)*np.sin(g1)-
np.sin(a1)*np.cos(g1))*(np.cos(a1)*np.sin(b1))+fixQyy*(-
np.sin(a1)*np.cos(b1)*np.sin(g1)+np.cos(a1)*np.cos(g1))*(np.sin(a
1)*np.sin(b1))+(-fixQzz-
fixQyy)*(np.cos(b1))*(np.sin(b1)*np.sin(g1)))*(fixQzz*(-
np.cos(a1)*np.cos(b1)*np.sin(g1)-
np.sin(a1)*np.cos(g1))*(np.cos(a1)*np.sin(b1))+fixQyy*(-
np.sin(a1)*np.cos(b1)*np.sin(g1)+np.cos(a1)*np.cos(g1))*(np.sin(a
1)*np.sin(b1))+(-fixQzz-
fixQyy)*(np.cos(b1))*(np.sin(b1)*np.sin(g1))))*np.cos(4*t1)+((9*
q/2)*((fixQzz*(-np.cos(a1)*np.cos(b1)*np.sin(g1)-
np.sin(a1)*np.cos(g1))**2+fixQyy*(-
np.sin(a1)*np.cos(b1)*np.sin(g1)+np.cos(a1)*np.cos(g1))**2+(-
fixQzz-fixQyy)*(np.sin(b1)*np.sin(g1))**2)-
((fixQzz*(np.cos(a1)*np.sin(b1))**2+fixQyy*(np.sin(a1)*np.sin(b1)
)**2+(-fixQzz-fixQyy)*(np.cos(b1))**2)))*(fixQzz*(-
np.cos(a1)*np.cos(b1)*np.sin(g1)-
np.sin(a1)*np.cos(g1))*(np.cos(a1)*np.sin(b1))+fixQyy*(-
np.sin(a1)*np.cos(b1)*np.sin(g1)+np.cos(a1)*np.cos(g1))*(np.sin(a
1)*np.sin(b1))+(-fixQzz-
fixQyy)*(np.cos(b1))*(np.sin(b1)*np.sin(g1))))*np.sin(4*t1);



y=((q/8)*((-11)*((fixQzz*(np.cos(a1)*np.cos(b1)*np.cos(g1)-
np.sin(a1)*np.sin(g1))**2+fixQyy*(np.sin(a1)*np.cos(b1)*np.cos(g1
```

```
)+np.cos(a1)*np.sin(g1))**2+(-fixQzz-fixQyy)*(-
np.sin(b1)*np.cos(g1))**2)*(fixQzz*(np.cos(a1)*np.cos(b1)*np.cos(
g1)-
np.sin(a1)*np.sin(g1))**2+fixQyy*(np.sin(a1)*np.cos(b1)*np.cos(g1
)+np.cos(a1)*np.sin(g1))**2+(-fixQzz-fixQyy)*(-
np.sin(b1)*np.cos(g1))**2)+((fixQzz*(np.cos(a1)*np.sin(b1))**2+fi
xQyy*(np.sin(a1)*np.sin(b1))**2+(-fixQzz-
fixQyy)*(np.cos(b1))**2))*((fixQzz*(np.cos(a1)*np.sin(b1))**2+fix
Qyy*(np.sin(a1)*np.sin(b1))**2+(-fixQzz-
fixQyy)*(np.cos(b1))**2)))-
50*(fixQzz*(np.cos(a1)*np.cos(b1)*np.cos(g1)-
np.sin(a1)*np.sin(g1))**2+fixQyy*(np.sin(a1)*np.cos(b1)*np.cos(g1
)+np.cos(a1)*np.sin(g1))**2+(-fixQzz-fixQyy)*(-
np.sin(b1)*np.cos(g1))**2)*((fixQzz*(np.cos(a1)*np.sin(b1))**2+fi
xQyy*(np.sin(a1)*np.sin(b1))**2+(-fixQzz-
fixQyy)*(np.cos(b1))**2))+28*(fixQzz*(np.cos(a1)*np.cos(b1)*np.co
s(g1)-
np.sin(a1)*np.sin(g1))*(np.cos(a1)*np.sin(b1))+fixQyy*(np.sin(a1)
*np.cos(b1)*np.cos(g1)+np.cos(a1)*np.sin(g1))*(np.sin(a1)*np.sin(
b1))+(-fixQzz-fixQyy)*(-
np.sin(b1)*np.cos(g1))*(np.cos(b1)))*(fixQzz*(np.cos(a1)*np.cos(b
1)*np.cos(g1)-
np.sin(a1)*np.sin(g1))*(np.cos(a1)*np.sin(b1))+fixQyy*(np.sin(a1)
*np.cos(b1)*np.cos(g1)+np.cos(a1)*np.sin(g1))*(np.sin(a1)*np.sin(
b1))+(-fixQzz-fixQyy)*(-
np.sin(b1)*np.cos(g1))*(np.cos(b1)))+16*((fixQzz*(-
np.cos(a1)*np.cos(b1)*np.sin(g1)-
np.sin(a1)*np.cos(g1))*(np.cos(a1)*np.sin(b1))+fixQyy*(-
np.sin(a1)*np.cos(b1)*np.sin(g1)+np.cos(a1)*np.cos(g1))*(np.sin(a
1)*np.sin(b1))+(-fixQzz-
fixQyy)*(np.cos(b1))*(np.sin(b1)*np.sin(g1)))*(fixQzz*(-
np.cos(a1)*np.cos(b1)*np.sin(g1)-
np.sin(a1)*np.cos(g1))*(np.cos(a1)*np.sin(b1))+fixQyy*(-
np.sin(a1)*np.cos(b1)*np.sin(g1)+np.cos(a1)*np.cos(g1))*(np.sin(a
1)*np.sin(b1))+(-fixQzz-
fixQyy)*(np.cos(b1))*(np.sin(b1)*np.sin(g1)))+(fixQzz*(np.cos(a1)
*np.cos(b1)*np.cos(g1)-np.sin(a1)*np.sin(g1))*(-
np.cos(a1)*np.cos(b1)*np.sin(g1)-
np.sin(a1)*np.cos(g1))+fixQyy*(np.sin(a1)*np.cos(b1)*np.cos(g1)+n
p.cos(a1)*np.sin(g1))*(-
np.sin(a1)*np.cos(b1)*np.sin(g1)+np.cos(a1)*np.cos(g1))+(-fixQzz-
fixQyy)*(-
np.sin(b1)*np.cos(g1))*(np.sin(b1)*np.sin(g1)))*(fixQzz*(np.cos(a
1)*np.cos(b1)*np.cos(g1)-np.sin(a1)*np.sin(g1))*(-
np.cos(a1)*np.cos(b1)*np.sin(g1)-
np.sin(a1)*np.cos(g1))+fixQyy*(np.sin(a1)*np.cos(b1)*np.cos(g1)+n
p.cos(a1)*np.sin(g1))*(-
np.sin(a1)*np.cos(b1)*np.sin(g1)+np.cos(a1)*np.cos(g1))+(-fixQzz-
fixQyy)*(-
np.sin(b1)*np.cos(g1))*(np.sin(b1)*np.sin(g1)))))+((Sxx/1000000*(
np.cos(a2)*np.cos(b2)*np.cos(g2)-
np.sin(a2)*np.sin(g2))**2+Syy/1000000*(np.sin(a2)*np.cos(b2)*np.c
```

```
os(g2)+np.cos(a2)*np.sin(g2))**2+Szz/1000000*(-
np.sin(b2)*np.cos(g2))**2)+(Sxx/1000000*(np.cos(a2)*np.sin(b2))**
2+Syy/1000000*(np.sin(a2)*np.sin(b2))**2+Szz/1000000*(np.cos(b2))
**2))*v/2)+((3*q/2)*(((fixQzz*(np.cos(a1)*np.sin(b1))**2+fixQyy*(
np.sin(a1)*np.sin(b1))**2+(-fixQzz-
fixQyy)*(np.cos(b1))**2))*((fixQzz*(np.cos(a1)*np.sin(b1))**2+fix
Qyy*(np.sin(a1)*np.sin(b1))**2+(-fixQzz-
fixQyy)*(np.cos(b1))**2))-
(fixQzz*(np.cos(a1)*np.cos(b1)*np.cos(g1)-
np.sin(a1)*np.sin(g1))**2+fixQyy*(np.sin(a1)*np.cos(b1)*np.cos(g1
)+np.cos(a1)*np.sin(g1))**2+(-fixQzz-fixQyy)*(-
np.sin(b1)*np.cos(g1))**2)*(fixQzz*(np.cos(a1)*np.cos(b1)*np.cos(
g1)-
np.sin(a1)*np.sin(g1))**2+fixQyy*(np.sin(a1)*np.cos(b1)*np.cos(g1
)+np.cos(a1)*np.sin(g1))**2+(-fixQzz-fixQyy)*(-
np.sin(b1)*np.cos(g1))**2)+4*(fixQzz*(-
np.cos(a1)*np.cos(b1)*np.sin(g1)-
np.sin(a1)*np.cos(g1))*(np.cos(a1)*np.sin(b1))+fixQyy*(-
np.sin(a1)*np.cos(b1)*np.sin(g1)+np.cos(a1)*np.cos(g1))*(np.sin(a
1)*np.sin(b1))+(-fixQzz-
fixQyy)*(np.cos(b1))*(np.sin(b1)*np.sin(g1)))*(fixQzz*(-
np.cos(a1)*np.cos(b1)*np.sin(g1)-
np.sin(a1)*np.cos(g1))*(np.cos(a1)*np.sin(b1))+fixQyy*(-
np.sin(a1)*np.cos(b1)*np.sin(g1)+np.cos(a1)*np.cos(g1))*(np.sin(a
1)*np.sin(b1))+(-fixQzz-
fixQyy)*(np.cos(b1))*(np.sin(b1)*np.sin(g1)))-
4*(fixQzz*(np.cos(a1)*np.cos(b1)*np.cos(g1)-
np.sin(a1)*np.sin(g1))*(-np.cos(a1)*np.cos(b1)*np.sin(g1)-
np.sin(a1)*np.cos(g1))+fixQyy*(np.sin(a1)*np.cos(b1)*np.cos(g1)+n
p.cos(a1)*np.sin(g1))*(-
np.sin(a1)*np.cos(b1)*np.sin(g1)+np.cos(a1)*np.cos(g1))+(-fixQzz-
fixQyy)*(-
np.sin(b1)*np.cos(g1))*(np.sin(b1)*np.sin(g1)))*(fixQzz*(np.cos(a
1)*np.cos(b1)*np.cos(g1)-np.sin(a1)*np.sin(g1))*(-
np.cos(a1)*np.cos(b1)*np.sin(g1)-
np.sin(a1)*np.cos(g1))+fixQyy*(np.sin(a1)*np.cos(b1)*np.cos(g1)+n
p.cos(a1)*np.sin(g1))*(-
np.sin(a1)*np.cos(b1)*np.sin(g1)+np.cos(a1)*np.cos(g1))+(-fixQzz-
fixQyy)*(-
np.sin(b1)*np.cos(g1))*(np.sin(b1)*np.sin(g1))))+((Sxx/1000000*(n
p.cos(a2)*np.sin(b2))**2+Syy/1000000*(np.sin(a2)*np.sin(b2))**2+S
zz/1000000*(np.cos(b2))**2)-
(Sxx/1000000*(np.cos(a2)*np.cos(b2)*np.cos(g2)-
np.sin(a2)*np.sin(g2))**2+Syy/1000000*(np.sin(a2)*np.cos(b2)*np.c
os(g2)+np.cos(a2)*np.sin(g2))**2+Szz/1000000*(-
np.sin(b2)*np.cos(g2))**2))*v/2)*np.cos(2*t1)+((-
3*q)*(((fixQzz*(np.cos(a1)*np.cos(b1)*np.cos(g1)-
np.sin(a1)*np.sin(g1))**2+fixQyy*(np.sin(a1)*np.cos(b1)*np.cos(g1
)+np.cos(a1)*np.sin(g1))**2+(-fixQzz-fixQyy)*(-
np.sin(b1)*np.cos(g1))**2)+((fixQzz*(np.cos(a1)*np.sin(b1))**2+fi
xQyy*(np.sin(a1)*np.sin(b1))**2+(-fixQzz-
fixQyy)*(np.cos(b1))**2)))*(fixQzz*(np.cos(a1)*np.cos(b1)*np.cos(
```

```
g1)-
np.sin(a1)*np.sin(g1))*(np.cos(a1)*np.sin(b1))+fixQyy*(np.sin(a1)
*np.cos(b1)*np.cos(g1)+np.cos(a1)*np.sin(g1))*(np.sin(a1)*np.sin(
b1))+(-fixQzz-fixQyy)*(-
np.sin(b1)*np.cos(g1))*(np.cos(b1)))+4*(fixQzz*(np.cos(a1)*np.cos
(b1)*np.cos(g1)-np.sin(a1)*np.sin(g1))*(-
np.cos(a1)*np.cos(b1)*np.sin(g1)-
np.sin(a1)*np.cos(g1))+fixQyy*(np.sin(a1)*np.cos(b1)*np.cos(g1)+n
p.cos(a1)*np.sin(g1))*(-
np.sin(a1)*np.cos(b1)*np.sin(g1)+np.cos(a1)*np.cos(g1))+(-fixQzz-
fixQyy)*(-
np.sin(b1)*np.cos(g1))*(np.sin(b1)*np.sin(g1)))*(fixQzz*(-
np.cos(a1)*np.cos(b1)*np.sin(g1)-
np.sin(a1)*np.cos(g1))*(np.cos(a1)*np.sin(b1))+fixQyy*(-
np.sin(a1)*np.cos(b1)*np.sin(g1)+np.cos(a1)*np.cos(g1))*(np.sin(a
1)*np.sin(b1))+(-fixQzz-
fixQyy)*(np.cos(b1))*(np.sin(b1)*np.sin(g1))))-
(Sxx/1000000*(np.cos(a2)*np.cos(b2)*np.cos(g2)-
np.sin(a2)*np.sin(g2))*(np.cos(a2)*np.sin(b2))+Syy/1000000*(np.si
n(a2)*np.cos(b2)*np.cos(g2)+np.cos(a2)*np.sin(g2))*(np.sin(a2)*np
.sin(b2))+Szz/1000000*(-
np.sin(b2)*np.cos(g2))*(np.cos(b2)))*v)*np.sin(2*t1)+((-
9*q/8)*((((fixQzz*(np.cos(a1)*np.sin(b1))**2+fixQyy*(np.sin(a1)*n
p.sin(b1))**2+(-fixQzz-fixQyy)*(np.cos(b1))**2))-
(fixQzz*(np.cos(a1)*np.cos(b1)*np.cos(g1)-
np.sin(a1)*np.sin(g1))**2+fixQyy*(np.sin(a1)*np.cos(b1)*np.cos(g1
)+np.cos(a1)*np.sin(g1))**2+(-fixQzz-fixQyy)*(-
np.sin(b1)*np.cos(g1))**2))*(((fixQzz*(np.cos(a1)*np.sin(b1))**2+
fixQyy*(np.sin(a1)*np.sin(b1))**2+(-fixQzz-
fixQyy)*(np.cos(b1))**2))-
(fixQzz*(np.cos(a1)*np.cos(b1)*np.cos(g1)-
np.sin(a1)*np.sin(g1))**2+fixQyy*(np.sin(a1)*np.cos(b1)*np.cos(g1
)+np.cos(a1)*np.sin(g1))**2+(-fixQzz-fixQyy)*(-
np.sin(b1)*np.cos(g1))**2))-
4*(fixQzz*(np.cos(a1)*np.cos(b1)*np.cos(g1)-
np.sin(a1)*np.sin(g1))*(np.cos(a1)*np.sin(b1))+fixQyy*(np.sin(a1)
*np.cos(b1)*np.cos(g1)+np.cos(a1)*np.sin(g1))*(np.sin(a1)*np.sin(
b1))+(-fixQzz-fixQyy)*(-
np.sin(b1)*np.cos(g1))*(np.cos(b1)))*(fixQzz*(np.cos(a1)*np.cos(b
1)*np.cos(g1)-
np.sin(a1)*np.sin(g1))*(np.cos(a1)*np.sin(b1))+fixQyy*(np.sin(a1)
*np.cos(b1)*np.cos(g1)+np.cos(a1)*np.sin(g1))*(np.sin(a1)*np.sin(
b1))+(-fixQzz-fixQyy)*(-
np.sin(b1)*np.cos(g1))*(np.cos(b1)))))*np.cos(4*t1)+((9*q/2)*(((f
ixQzz*(np.cos(a1)*np.sin(b1))**2+fixQyy*(np.sin(a1)*np.sin(b1))**
2+(-fixQzz-fixQyy)*(np.cos(b1))**2))-
(fixQzz*(np.cos(a1)*np.cos(b1)*np.cos(g1)-
np.sin(a1)*np.sin(g1))**2+fixQyy*(np.sin(a1)*np.cos(b1)*np.cos(g1
)+np.cos(a1)*np.sin(g1))**2+(-fixQzz-fixQyy)*(-
np.sin(b1)*np.cos(g1))**2))*(fixQzz*(np.cos(a1)*np.cos(b1)*np.cos
(g1)-
np.sin(a1)*np.sin(g1))*(np.cos(a1)*np.sin(b1))+fixQyy*(np.sin(a1)
```

```
*np.cos(b1)*np.cos(g1)+np.cos(a1)*np.sin(g1))*(np.sin(a1)*np.sin(
b1))+(-fixQzz-fixQyy)*(-
np.sin(b1)*np.cos(g1))*(np.cos(b1))))*np.sin(4*t1);



z=((q/8)*((-11)*((fixQzz*(np.cos(a1)*np.cos(b1)*np.cos(g1)-
np.sin(a1)*np.sin(g1))**2+fixQyy*(np.sin(a1)*np.cos(b1)*np.cos(g1
)+np.cos(a1)*np.sin(g1))**2+(-fixQzz-fixQyy)*(-
np.sin(b1)*np.cos(g1))**2)*(fixQzz*(np.cos(a1)*np.cos(b1)*np.cos(
g1)-
np.sin(a1)*np.sin(g1))**2+fixQyy*(np.sin(a1)*np.cos(b1)*np.cos(g1
)+np.cos(a1)*np.sin(g1))**2+(-fixQzz-fixQyy)*(-
np.sin(b1)*np.cos(g1))**2)+(fixQzz*(-
np.cos(a1)*np.cos(b1)*np.sin(g1)-
np.sin(a1)*np.cos(g1))**2+fixQyy*(-
np.sin(a1)*np.cos(b1)*np.sin(g1)+np.cos(a1)*np.cos(g1))**2+(-
fixQzz-fixQyy)*(np.sin(b1)*np.sin(g1))**2)*(fixQzz*(-
np.cos(a1)*np.cos(b1)*np.sin(g1)-
np.sin(a1)*np.cos(g1))**2+fixQyy*(-
np.sin(a1)*np.cos(b1)*np.sin(g1)+np.cos(a1)*np.cos(g1))**2+(-
fixQzz-fixQyy)*(np.sin(b1)*np.sin(g1))**2))-
50*(fixQzz*(np.cos(a1)*np.cos(b1)*np.cos(g1)-
np.sin(a1)*np.sin(g1))**2+fixQyy*(np.sin(a1)*np.cos(b1)*np.cos(g1
)+np.cos(a1)*np.sin(g1))**2+(-fixQzz-fixQyy)*(-
np.sin(b1)*np.cos(g1))**2)*(fixQzz*(-
np.cos(a1)*np.cos(b1)*np.sin(g1)-
np.sin(a1)*np.cos(g1))**2+fixQyy*(-
np.sin(a1)*np.cos(b1)*np.sin(g1)+np.cos(a1)*np.cos(g1))**2+(-
fixQzz-
fixQyy)*(np.sin(b1)*np.sin(g1))**2)+28*(fixQzz*(np.cos(a1)*np.cos
(b1)*np.cos(g1)-np.sin(a1)*np.sin(g1))*(-
np.cos(a1)*np.cos(b1)*np.sin(g1)-
np.sin(a1)*np.cos(g1))+fixQyy*(np.sin(a1)*np.cos(b1)*np.cos(g1)+n
p.cos(a1)*np.sin(g1))*(-
np.sin(a1)*np.cos(b1)*np.sin(g1)+np.cos(a1)*np.cos(g1))+(-fixQzz-
fixQyy)*(-
np.sin(b1)*np.cos(g1))*(np.sin(b1)*np.sin(g1)))*(fixQzz*(np.cos(a
1)*np.cos(b1)*np.cos(g1)-np.sin(a1)*np.sin(g1))*(-
np.cos(a1)*np.cos(b1)*np.sin(g1)-
np.sin(a1)*np.cos(g1))+fixQyy*(np.sin(a1)*np.cos(b1)*np.cos(g1)+n
p.cos(a1)*np.sin(g1))*(-
np.sin(a1)*np.cos(b1)*np.sin(g1)+np.cos(a1)*np.cos(g1))+(-fixQzz-
fixQyy)*(-
np.sin(b1)*np.cos(g1))*(np.sin(b1)*np.sin(g1)))+16*((fixQzz*(np.c
os(a1)*np.cos(b1)*np.cos(g1)-
np.sin(a1)*np.sin(g1))*(np.cos(a1)*np.sin(b1))+fixQyy*(np.sin(a1)
*np.cos(b1)*np.cos(g1)+np.cos(a1)*np.sin(g1))*(np.sin(a1)*np.sin(
b1))+(-fixQzz-fixQyy)*(-
np.sin(b1)*np.cos(g1))*(np.cos(b1)))*(fixQzz*(np.cos(a1)*np.cos(b
1)*np.cos(g1)-
```

```
np.sin(a1)*np.sin(g1))*(np.cos(a1)*np.sin(b1))+fixQyy*(np.sin(a1)
*np.cos(b1)*np.cos(g1)+np.cos(a1)*np.sin(g1))*(np.sin(a1)*np.sin(
b1))+(-fixQzz-fixQyy)*(-
np.sin(b1)*np.cos(g1))*(np.cos(b1)))+(fixQzz*(-
np.cos(a1)*np.cos(b1)*np.sin(g1)-
np.sin(a1)*np.cos(g1))*(np.cos(a1)*np.sin(b1))+fixQyy*(-
np.sin(a1)*np.cos(b1)*np.sin(g1)+np.cos(a1)*np.cos(g1))*(np.sin(a
1)*np.sin(b1))+(-fixQzz-
fixQyy)*(np.cos(b1))*(np.sin(b1)*np.sin(g1)))*(fixQzz*(-
np.cos(a1)*np.cos(b1)*np.sin(g1)-
np.sin(a1)*np.cos(g1))*(np.cos(a1)*np.sin(b1))+fixQyy*(-
np.sin(a1)*np.cos(b1)*np.sin(g1)+np.cos(a1)*np.cos(g1))*(np.sin(a
1)*np.sin(b1))+(-fixQzz-
fixQyy)*(np.cos(b1))*(np.sin(b1)*np.sin(g1)))))+((Sxx/1000000*(np
.cos(a2)*np.cos(b2)*np.cos(g2)-
np.sin(a2)*np.sin(g2))**2+Syy/1000000*(np.sin(a2)*np.cos(b2)*np.c
os(g2)+np.cos(a2)*np.sin(g2))**2+Szz/1000000*(-
np.sin(b2)*np.cos(g2))**2)+(Sxx/1000000*(-
np.cos(a2)*np.cos(b2)*np.sin(g2)-
np.sin(a2)*np.cos(g2))**2+Syy/1000000*(-
np.sin(a2)*np.cos(b2)*np.sin(g2)+np.cos(a2)*np.cos(g2))**2+Szz/10
00000*(np.sin(b2)*np.sin(g2))**2))*v/2)+((3*q/2)*((fixQzz*(np.cos
(a1)*np.cos(b1)*np.cos(g1)-
np.sin(a1)*np.sin(g1))**2+fixQyy*(np.sin(a1)*np.cos(b1)*np.cos(g1
)+np.cos(a1)*np.sin(g1))**2+(-fixQzz-fixQyy)*(-
np.sin(b1)*np.cos(g1))**2)*(fixQzz*(np.cos(a1)*np.cos(b1)*np.cos(
g1)-
np.sin(a1)*np.sin(g1))**2+fixQyy*(np.sin(a1)*np.cos(b1)*np.cos(g1
)+np.cos(a1)*np.sin(g1))**2+(-fixQzz-fixQyy)*(-
np.sin(b1)*np.cos(g1))**2)-(fixQzz*(-
np.cos(a1)*np.cos(b1)*np.sin(g1)-
np.sin(a1)*np.cos(g1))**2+fixQyy*(-
np.sin(a1)*np.cos(b1)*np.sin(g1)+np.cos(a1)*np.cos(g1))**2+(-
fixQzz-fixQyy)*(np.sin(b1)*np.sin(g1))**2)*(fixQzz*(-
np.cos(a1)*np.cos(b1)*np.sin(g1)-
np.sin(a1)*np.cos(g1))**2+fixQyy*(-
np.sin(a1)*np.cos(b1)*np.sin(g1)+np.cos(a1)*np.cos(g1))**2+(-
fixQzz-
fixQyy)*(np.sin(b1)*np.sin(g1))**2)+4*(fixQzz*(np.cos(a1)*np.cos(
b1)*np.cos(g1)-
np.sin(a1)*np.sin(g1))*(np.cos(a1)*np.sin(b1))+fixQyy*(np.sin(a1)
*np.cos(b1)*np.cos(g1)+np.cos(a1)*np.sin(g1))*(np.sin(a1)*np.sin(
b1))+(-fixQzz-fixQyy)*(-
np.sin(b1)*np.cos(g1))*(np.cos(b1)))*(fixQzz*(np.cos(a1)*np.cos(b
1)*np.cos(g1)-
np.sin(a1)*np.sin(g1))*(np.cos(a1)*np.sin(b1))+fixQyy*(np.sin(a1)
*np.cos(b1)*np.cos(g1)+np.cos(a1)*np.sin(g1))*(np.sin(a1)*np.sin(
b1))+(-fixQzz-fixQyy)*(-np.sin(b1)*np.cos(g1))*(np.cos(b1)))-
4*(fixQzz*(-np.cos(a1)*np.cos(b1)*np.sin(g1)-
np.sin(a1)*np.cos(g1))*(np.cos(a1)*np.sin(b1))+fixQyy*(-
np.sin(a1)*np.cos(b1)*np.sin(g1)+np.cos(a1)*np.cos(g1))*(np.sin(a
1)*np.sin(b1))+(-fixQzz-
```

```
fixQyy)*(np.cos(b1))*(np.sin(b1)*np.sin(g1)))*(fixQzz*(-
np.cos(a1)*np.cos(b1)*np.sin(g1)-
np.sin(a1)*np.cos(g1))*(np.cos(a1)*np.sin(b1))+fixQyy*(-
np.sin(a1)*np.cos(b1)*np.sin(g1)+np.cos(a1)*np.cos(g1))*(np.sin(a
1)*np.sin(b1))+(-fixQzz-
fixQyy)*(np.cos(b1))*(np.sin(b1)*np.sin(g1))))+((Sxx/1000000*(np.
cos(a2)*np.cos(b2)*np.cos(g2)-
np.sin(a2)*np.sin(g2))**2+Syy/1000000*(np.sin(a2)*np.cos(b2)*np.c
os(g2)+np.cos(a2)*np.sin(g2))**2+Szz/1000000*(-
np.sin(b2)*np.cos(g2))**2)-(Sxx/1000000*(-
np.cos(a2)*np.cos(b2)*np.sin(g2)-
np.sin(a2)*np.cos(g2))**2+Syy/1000000*(-
np.sin(a2)*np.cos(b2)*np.sin(g2)+np.cos(a2)*np.cos(g2))**2+Szz/10
00000*(np.sin(b2)*np.sin(g2))**2))*v/2)*np.cos(2*t1)+((-
3*q)*(((fixQzz*(np.cos(a1)*np.cos(b1)*np.cos(g1)-
np.sin(a1)*np.sin(g1))**2+fixQyy*(np.sin(a1)*np.cos(b1)*np.cos(g1
)+np.cos(a1)*np.sin(g1))**2+(-fixQzz-fixQyy)*(-
np.sin(b1)*np.cos(g1))**2)+(fixQzz*(-
np.cos(a1)*np.cos(b1)*np.sin(g1)-
np.sin(a1)*np.cos(g1))**2+fixQyy*(-
np.sin(a1)*np.cos(b1)*np.sin(g1)+np.cos(a1)*np.cos(g1))**2+(-
fixQzz-
fixQyy)*(np.sin(b1)*np.sin(g1))**2))*(fixQzz*(np.cos(a1)*np.cos(b
1)*np.cos(g1)-np.sin(a1)*np.sin(g1))*(-
np.cos(a1)*np.cos(b1)*np.sin(g1)-
np.sin(a1)*np.cos(g1))+fixQyy*(np.sin(a1)*np.cos(b1)*np.cos(g1)+n
p.cos(a1)*np.sin(g1))*(-
np.sin(a1)*np.cos(b1)*np.sin(g1)+np.cos(a1)*np.cos(g1))+(-fixQzz-
fixQyy)*(-
np.sin(b1)*np.cos(g1))*(np.sin(b1)*np.sin(g1)))+4*(fixQzz*(-
np.cos(a1)*np.cos(b1)*np.sin(g1)-
np.sin(a1)*np.cos(g1))*(np.cos(a1)*np.sin(b1))+fixQyy*(-
np.sin(a1)*np.cos(b1)*np.sin(g1)+np.cos(a1)*np.cos(g1))*(np.sin(a
1)*np.sin(b1))+(-fixQzz-
fixQyy)*(np.cos(b1))*(np.sin(b1)*np.sin(g1)))*(fixQzz*(np.cos(a1)
*np.cos(b1)*np.cos(g1)-
np.sin(a1)*np.sin(g1))*(np.cos(a1)*np.sin(b1))+fixQyy*(np.sin(a1)
*np.cos(b1)*np.cos(g1)+np.cos(a1)*np.sin(g1))*(np.sin(a1)*np.sin(
b1))+(-fixQzz-fixQyy)*(-np.sin(b1)*np.cos(g1))*(np.cos(b1))))-
(Sxx/1000000*(np.cos(a2)*np.cos(b2)*np.cos(g2)-
np.sin(a2)*np.sin(g2))*(-np.cos(a2)*np.cos(b2)*np.sin(g2)-
np.sin(a2)*np.cos(g2))+Syy/1000000*(np.sin(a2)*np.cos(b2)*np.cos(
g2)+np.cos(a2)*np.sin(g2))*(-
np.sin(a2)*np.cos(b2)*np.sin(g2)+np.cos(a2)*np.cos(g2))+Szz/10000
00*(-
np.sin(b2)*np.cos(g2))*(np.sin(b2)*np.sin(g2)))*v)*np.sin(2*t1)+(
(-9*q/8)*(((fixQzz*(np.cos(a1)*np.cos(b1)*np.cos(g1)-
np.sin(a1)*np.sin(g1))**2+fixQyy*(np.sin(a1)*np.cos(b1)*np.cos(g1
)+np.cos(a1)*np.sin(g1))**2+(-fixQzz-fixQyy)*(-
np.sin(b1)*np.cos(g1))**2)-(fixQzz*(-
np.cos(a1)*np.cos(b1)*np.sin(g1)-
np.sin(a1)*np.cos(g1))**2+fixQyy*(-
```

```
np.sin(a1)*np.cos(b1)*np.sin(g1)+np.cos(a1)*np.cos(g1))**2+(-
fixQzz-
fixQyy)*(np.sin(b1)*np.sin(g1))**2))*((fixQzz*(np.cos(a1)*np.cos(
b1)*np.cos(g1)-
np.sin(a1)*np.sin(g1))**2+fixQyy*(np.sin(a1)*np.cos(b1)*np.cos(g1
)+np.cos(a1)*np.sin(g1))**2+(-fixQzz-fixQyy)*(-
np.sin(b1)*np.cos(g1))**2)-(fixQzz*(-
np.cos(a1)*np.cos(b1)*np.sin(g1)-
np.sin(a1)*np.cos(g1))**2+fixQyy*(-
np.sin(a1)*np.cos(b1)*np.sin(g1)+np.cos(a1)*np.cos(g1))**2+(-
fixQzz-fixQyy)*(np.sin(b1)*np.sin(g1))**2))-
4*(fixQzz*(np.cos(a1)*np.cos(b1)*np.cos(g1)-
np.sin(a1)*np.sin(g1))*(-np.cos(a1)*np.cos(b1)*np.sin(g1)-
np.sin(a1)*np.cos(g1))+fixQyy*(np.sin(a1)*np.cos(b1)*np.cos(g1)+n
p.cos(a1)*np.sin(g1))*(-
np.sin(a1)*np.cos(b1)*np.sin(g1)+np.cos(a1)*np.cos(g1))+(-fixQzz-
fixQyy)*(-
np.sin(b1)*np.cos(g1))*(np.sin(b1)*np.sin(g1)))*(fixQzz*(np.cos(a
1)*np.cos(b1)*np.cos(g1)-np.sin(a1)*np.sin(g1))*(-
np.cos(a1)*np.cos(b1)*np.sin(g1)-
np.sin(a1)*np.cos(g1))+fixQyy*(np.sin(a1)*np.cos(b1)*np.cos(g1)+n
p.cos(a1)*np.sin(g1))*(-
np.sin(a1)*np.cos(b1)*np.sin(g1)+np.cos(a1)*np.cos(g1))+(-fixQzz-
fixQyy)*(-
np.sin(b1)*np.cos(g1))*(np.sin(b1)*np.sin(g1)))))*np.cos(4*t1)+((
9*q/2)*(((fixQzz*(np.cos(a1)*np.cos(b1)*np.cos(g1)-
np.sin(a1)*np.sin(g1))**2+fixQyy*(np.sin(a1)*np.cos(b1)*np.cos(g1
)+np.cos(a1)*np.sin(g1))**2+(-fixQzz-fixQyy)*(-
np.sin(b1)*np.cos(g1))**2)-(fixQzz*(-
np.cos(a1)*np.cos(b1)*np.sin(g1)-
np.sin(a1)*np.cos(g1))**2+fixQyy*(-
np.sin(a1)*np.cos(b1)*np.sin(g1)+np.cos(a1)*np.cos(g1))**2+(-
fixQzz-
fixQyy)*(np.sin(b1)*np.sin(g1))**2))*(fixQzz*(np.cos(a1)*np.cos(b
1)*np.cos(g1)-np.sin(a1)*np.sin(g1))*(-
np.cos(a1)*np.cos(b1)*np.sin(g1)-
np.sin(a1)*np.cos(g1))+fixQyy*(np.sin(a1)*np.cos(b1)*np.cos(g1)+n
p.cos(a1)*np.sin(g1))*(-
np.sin(a1)*np.cos(b1)*np.sin(g1)+np.cos(a1)*np.cos(g1))+(-fixQzz-
fixQyy)*(-
np.sin(b1)*np.cos(g1))*(np.sin(b1)*np.sin(g1)))))*np.sin(4*t1)
```

Spin-Spin Coupling:

```
x=Jiso+0.5*(Ryy+(-Rxx-Ryy))+1/2*(Ryy-(-Rxx-Ryy))*np.cos(2*(t1))-
1*Ryz*np.sin(2*(t1));

y=Jiso+0.5*((-Rxx-Ryy)+Rxx)+1/2*((-Rxx-Ryy)-Rxx)*np.cos(2*(t1))-
1*Rxz*np.sin(2*(t1));

z=Jiso+0.5*(Rxx+Ryy)+1/2*(Rxx-Ryy)*np.cos(2*(t1))-
1*Rxy*np.sin(2*(t1)).
```

Appendix E: Supporting Information for Chapter 7

Table E1. Crystallographic Data and Selected Data Collection Parameters for **2**.

Empirical formula	$C_{69}H_{45}F_{10}I_5O_3P_3$
Formula weight	1839.46
Crystal size, mm^3	0.955 x 0.786 x 0.548
Crystal system	triclinic
Space group	$P\overline{1}$
Z	2
a, Å	8.4755(8)
b, Å	18.6290(18)
c, Å	21.907(2)
α, °	82.080(1)
β, °	78.944(1)
γ, °	80.992(1)
Volume, $Å^3$	3332.1(6)
Calculated density, Mg m^{-3}	1.833
Absorption coefficient, mm^{-1}	2.480
F(000)	1766
θ range for data collection, °	2.098 to 28.213
Limiting indices	$-11 \leq h \leq 10$, $-24 \leq k \leq 24$, $-29 \leq l \leq 28$
Reflections collected/ unique	39918 / 15885
R_{int}	0.0231
Completeness to θ = 25.242°, %	99.6
Max and min transmission	0.7457 and 0.4061
Data/ restraints/ parameters	15885 / 0 / 811
Goodness-of-fit on F^2	1.076
Final *R* indices [$I > 2\alpha(I)$]	R_1 = 0.0261, wR_2 = 0.0609
R indices (all data)	R_1 = 0.0311, wR_2 = 0.0632
largest diff. peak and hole, e·$Å^{-3}$	0.699 and -1.332

Table E2. Compound Numbering and Local Halogen Bonding Geometrical Information from Single-Crystal X-ray Diffraction

Compound	P site	#I	$d_{I\cdots O}$/Å	$d_{P=O}$/Å	R_{XB}[a]	$\theta_{O\cdots I\text{-}C}$/deg	$\theta_{P=O\cdots I}$/deg	$\theta_{I..O\cdots I}$/deg
1[b]		1	2.725	1.495	0.779	175.7	152.1	
2	**2_1**	1	2.766	1.493	0.790	172.4	136.5	81.4
	2_1	2a	3.304	1.493	0.944	160.3	140.4	
	2_3	2b	2.856	1.491	0.816	175.6	142.3	
	2_2	3	2.759	1.496	0.788	176.6	132.8	

[a] R_{XB} is the normalized distance parameter, $R_{XB} = d_{I\cdots O} / \sum d_{VDW}$, where $d_{I\cdots O}$ is the shortest distance between the oxygen and iodine and $\sum d_{VDW}$ is the sum of their van der Waals radii (1.52 Å for O and 1.98 Å for I).

[b] Contains one extra *p*-$C_6F_4I_2$, which is not involved in halogen bonding. The crystallographic information has been reported previously.[11]

Table E3. Solid-State Rate and Integral Expressions for 12 Different Reaction Models[a]

Model	Differential Form $f(\alpha) = 1/k\frac{d\alpha}{dt'}$	Integral Form $g(\alpha) = kt'$
Nucleation Models		
Avrami-Erofeyev (A2)	$2(1-\alpha)[-\ln(1-\alpha)]^{1/2}$	$[-\ln(1-\alpha)]^{1/2}$
Avrami-Erofeyev (A3)	$3(1-\alpha)[-\ln(1-\alpha)]^{2/3}$	$[-\ln(1-\alpha)]^{1/3}$
Avrami-Erofeyev (A4)	$4(1-\alpha)[-\ln(1-\alpha)]^{3/4}$	$[-\ln(1-\alpha)]^{1/4}$
Geometrical contraction Models		
Contracting Area (R2)	$2(1-\alpha)^{1/2}$	$1-(1-\alpha)^{1/2}$
Contracting Volume (R3)	$3(1-\alpha)^{2/3}$	$1-(1-\alpha)^{1/3}$
Diffusion Models		
One Dimensional Diffusion (D1)	$1/(2\alpha)$	α^2
Two Dimensional Diffusion (D2)	$-[1/\ln(1-\alpha)]$	$(1-\alpha)\ln(1-\alpha)+\alpha$
Three Dimensional Diffusion (D3)	$[3(1-\alpha)^{2/3}]/\{2[1-(1-\alpha)^{1/3}]\}$	$[1-(1-\alpha)^{1/3}]^2$
Ginstling-Brounshtein (D4)	$3/\{2[(1-\alpha)^{-1/3}-1]\}$	$1-(\frac{2}{3})\alpha-(1-\alpha)^{2/3}$
Reaction Order Models		
First-Order (F1)	$(1-\alpha)$	$-\ln(1-\alpha)$
Second-Order (F2)	$(1-\alpha)^2$	$1/(1-\alpha)-1$
Third-Order (F3)	$(1-\alpha)^3$	$(1/2)[(1-\alpha)^{-2}-1]$

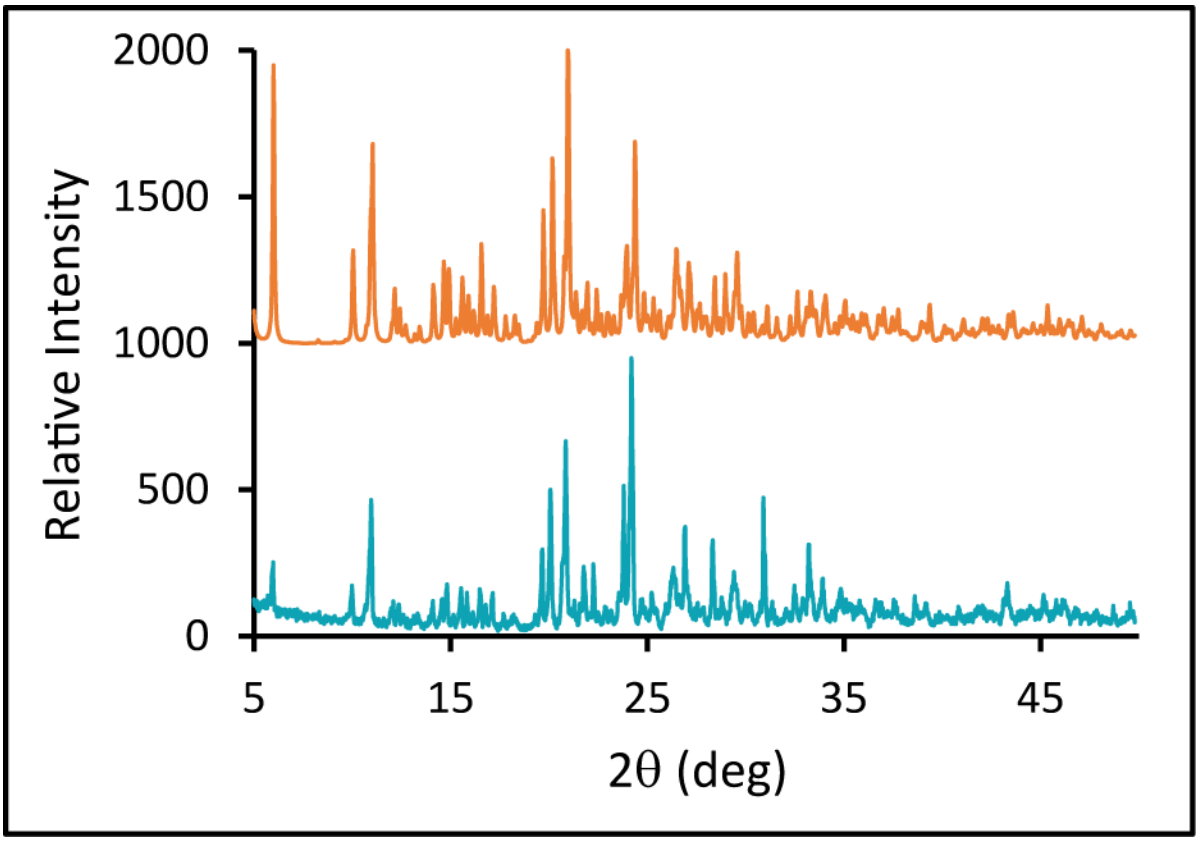

Figure E1. Experimental powder X-ray diffraction pattern (shown in turquoise) for halogen-bonded cocrystal **2**. All data were acquired using a Rigaku Ultima IV diffractometer with 2θ ranging from 5º to 50º at a rate of 1º per minute. The calculated powder X-ray diffraction pattern from single crystal structure data is presented in orange at the top. Simulations were generated using Mercury 3.8 software from the Crystallographic Data Center.

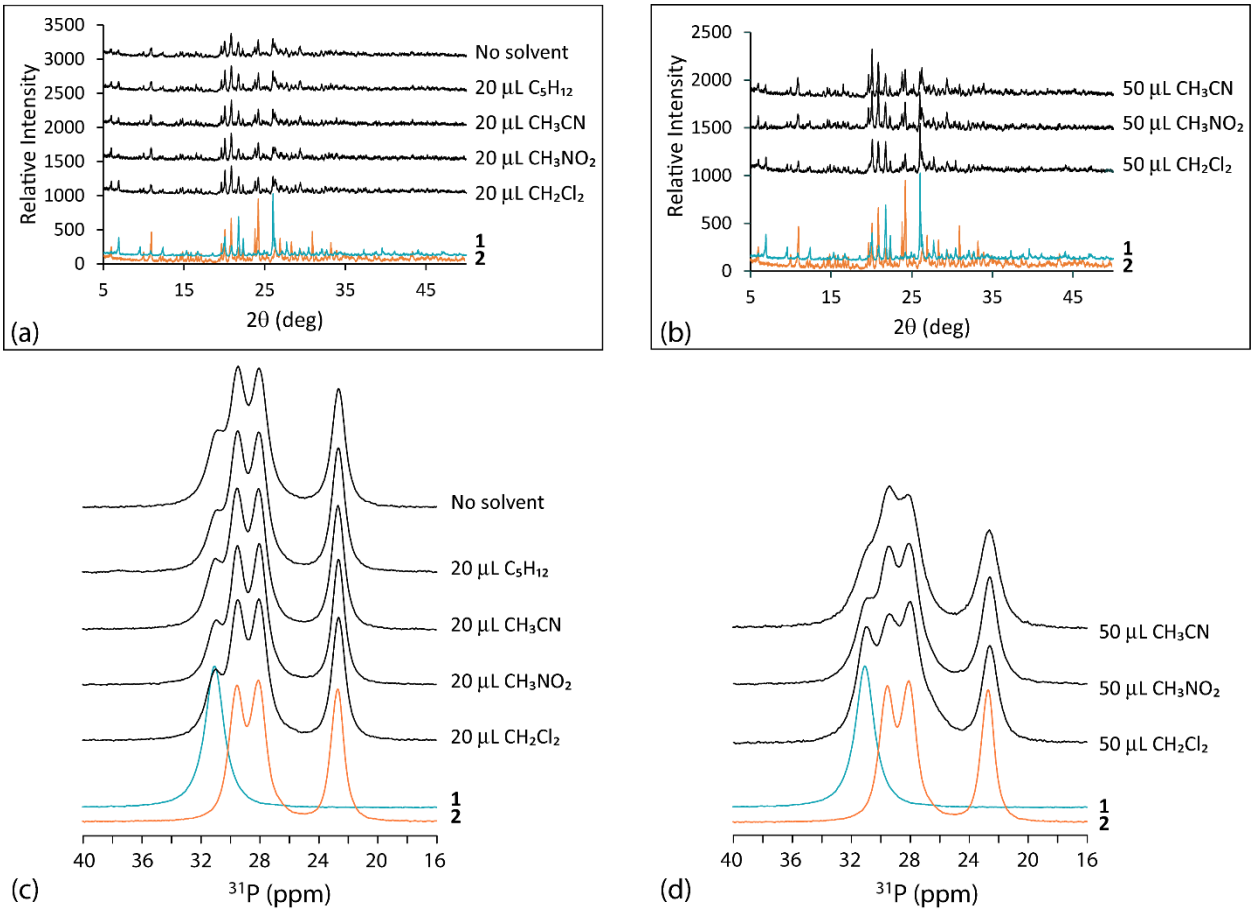

Figure E2. Experimental powder X-ray diffraction pattern for the final product (black) from ball milling with 20 μL (a) and 50 μL (b) of different liquids at 30 Hz for 1 h and halogen-bonded cocrystals from slow evaporation: **1** (turquoise) and **2** (orange). All data were acquired using a Rigaku Ultima IV diffractometer with 2θ ranging from 5º to 50º at a rate of 1º per minute. The MAS spinning speed for the ball milled product is 8 kHz and for the halogen-bonded cocrystals from slow evaporation is 10 kHz. Here mechanochemical synthesis of **1** was attempted by ball milling equimolar amounts of Ph_3PO and *p*-$C_6F_4I_2$ with different liquids at 30 Hz in 25 mL stainless steel milling jars for 1 h. However, as shown in PXRD and ^{31}P CP/MAS spectra, the final product was a mixture of **1** and **2**.

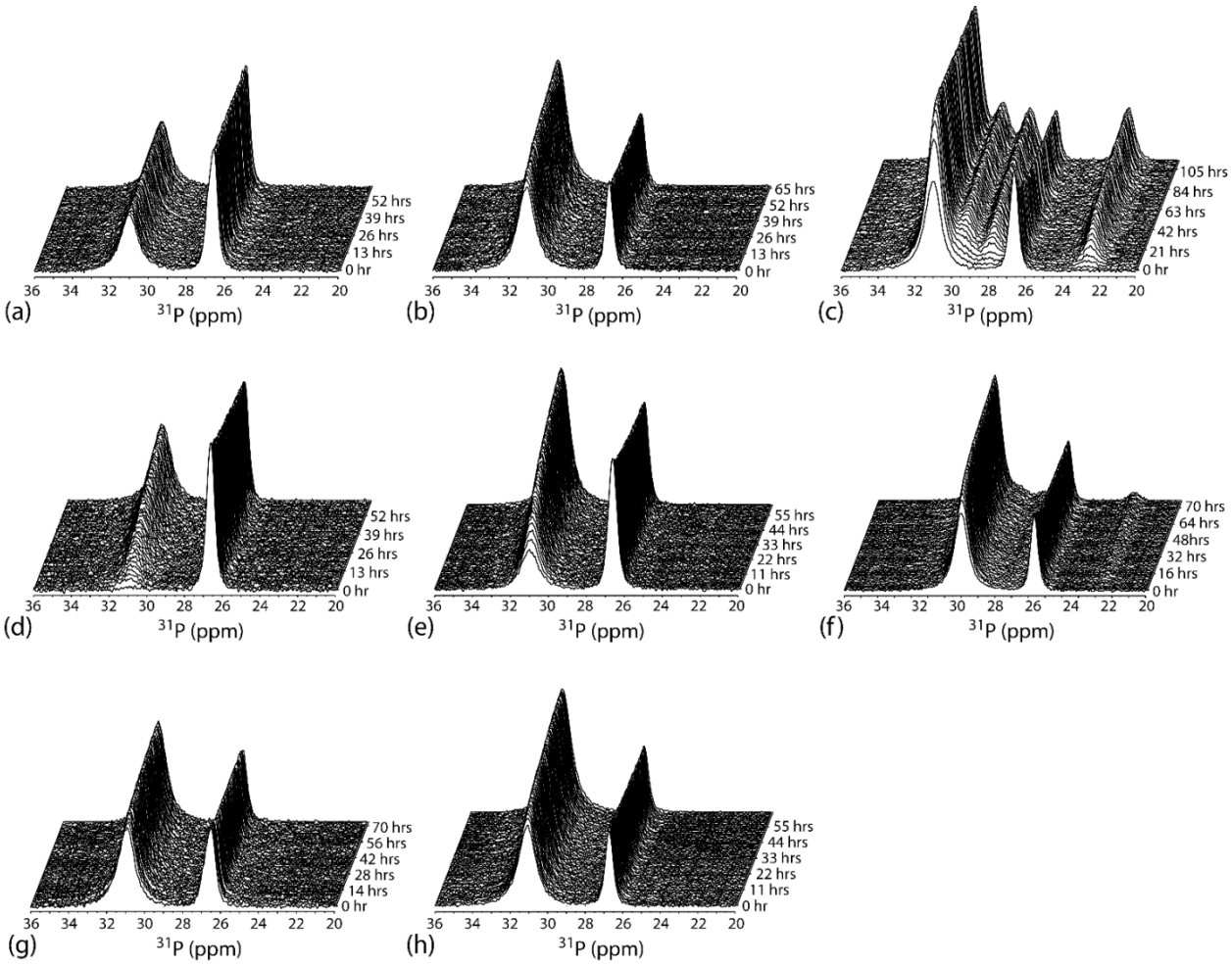

Figure E3. In situ ^{31}P CP/MAS SSNMR spectra of the reacting Ph_3PO and *p*-$C_6F_4I_2$ obtained at 9.4 T under different conditions: (a) at 15 ℃ with a 10 kHz spinning speed and an addition of 5 μL acetonitrile, (b) at 25 ℃ with a 10 kHz spinning speed and an addition of 5 μL acetonitrile, (c) at 35 ℃ with a 10 kHz spinning speed and an addition of 5 μL acetonitrile, (d) at 45 ℃ with a 10 kHz spinning speed and no liquid, (e) at 45 ℃ with a 10 kHz spinning speed and an addition of 3 μL acetonitrile, and (f) at 45 ℃ with a 10 kHz spinning speed and an addition of 4 μL acetonitrile, (g) at 25 ℃ with a 8 kHz spinning speed and an addition of 5 μL acetonitrile, (h) at 25 ℃ with a 12 kHz spinning speed and an addition of 5 μL acetonitrile. Each spectrum was collected for 16 min (8 scans, 2 min recycle delay). Only the isotropic peaks are shown here.

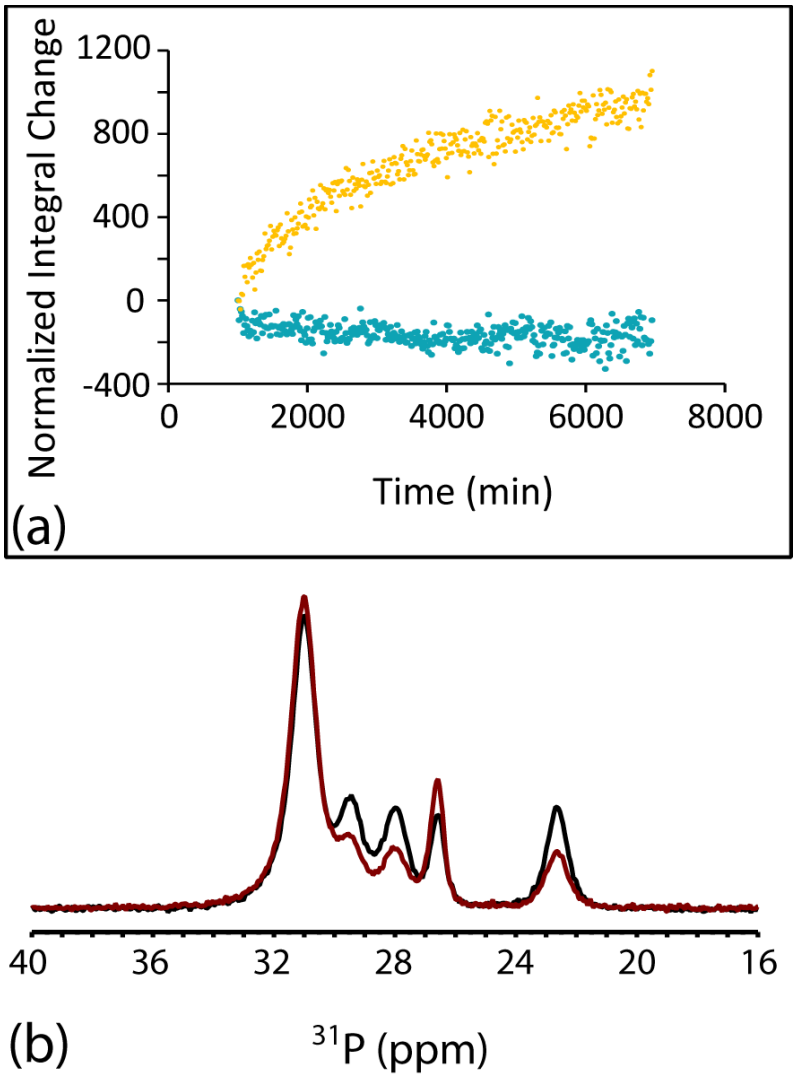

Figure E4. (a) Normalized peak integral change ($I_t - I_{t=16.5h}$) of **1**(turquoise) and the sum of three peaks in **2**(yellow) after around 16.5 h. More significant increase for **2** indicate that the formation of **2** is mainly from crystallization between two starting materials. (b) Comparison between the experimental ^{31}P CP/MAS SSNMR spectra of the mixture at t = 16.5 h (red) and the mixture at end time point (black). The slight decrease in peak intensity of **1** indicates the conversion from **1** to **2**.

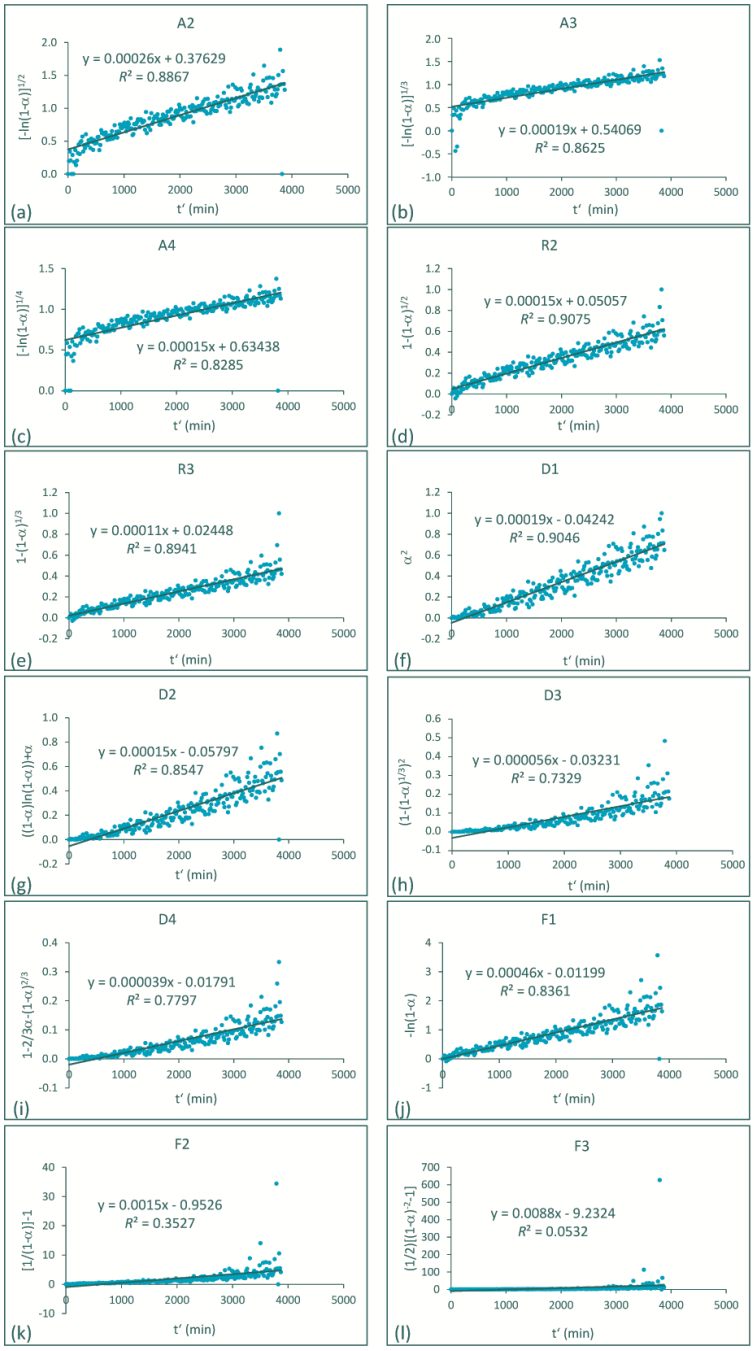

Figure E5. The fitting of conversion fraction α for the MAS in situ formation of **1** (15 ℃, 10 kHz MAS, 5 μL acetonitrile), after linearization α to 12 different models of solid-state reactivity: (a) the A2 model; (b) the A3 model; (c) the A4 model (d) the R2 model; (e) the R3 model; (f) the D1 model; (g) the D2 model; (h) the D3 model; (i) the D4 model; (j) the F1 model; (k) the F2 model; (l) the F3 model. The integrated rate functions g(α), varying for the different models, are given on the y-axis and also summarized in Table E3.

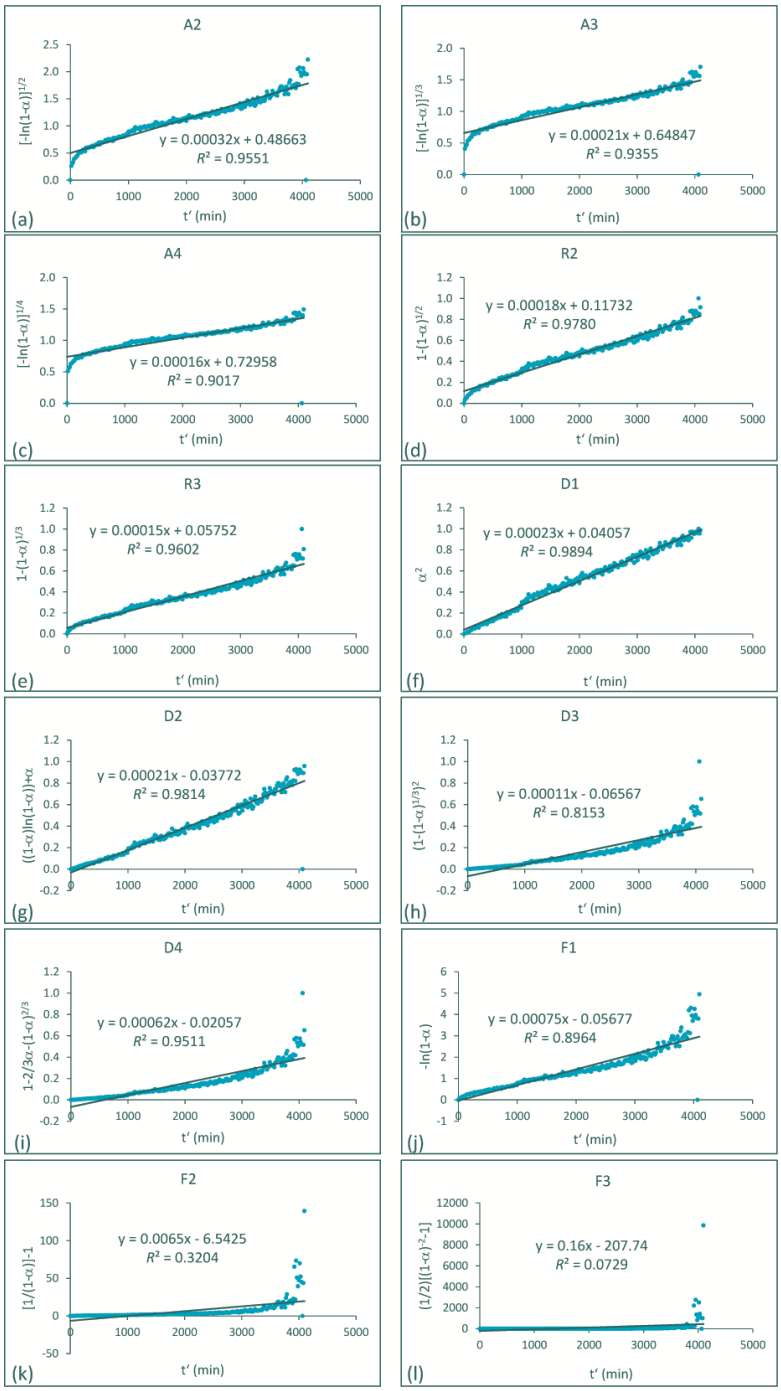

Figure E6. The fitting of conversion fraction α for the MAS in situ formation of **1** (25 ℃, 10 kHz MAS, 5 μL acetonitrile), after linearization α to 12 different models of solid-state reactivity: (a) the A2 model; (b) the A3 model; (c) the A4 model (d) the R2 model; (e) the R3 model; (f) the D1 model; (g) the D2 model; (h) the D3 model; (i) the D4 model; (j) the F1 model; (k) the F2 model; (l) the F3 model. The integrated rate functions g(α), varying for the different models, are given on the y-axis and also summarized in Table E3.

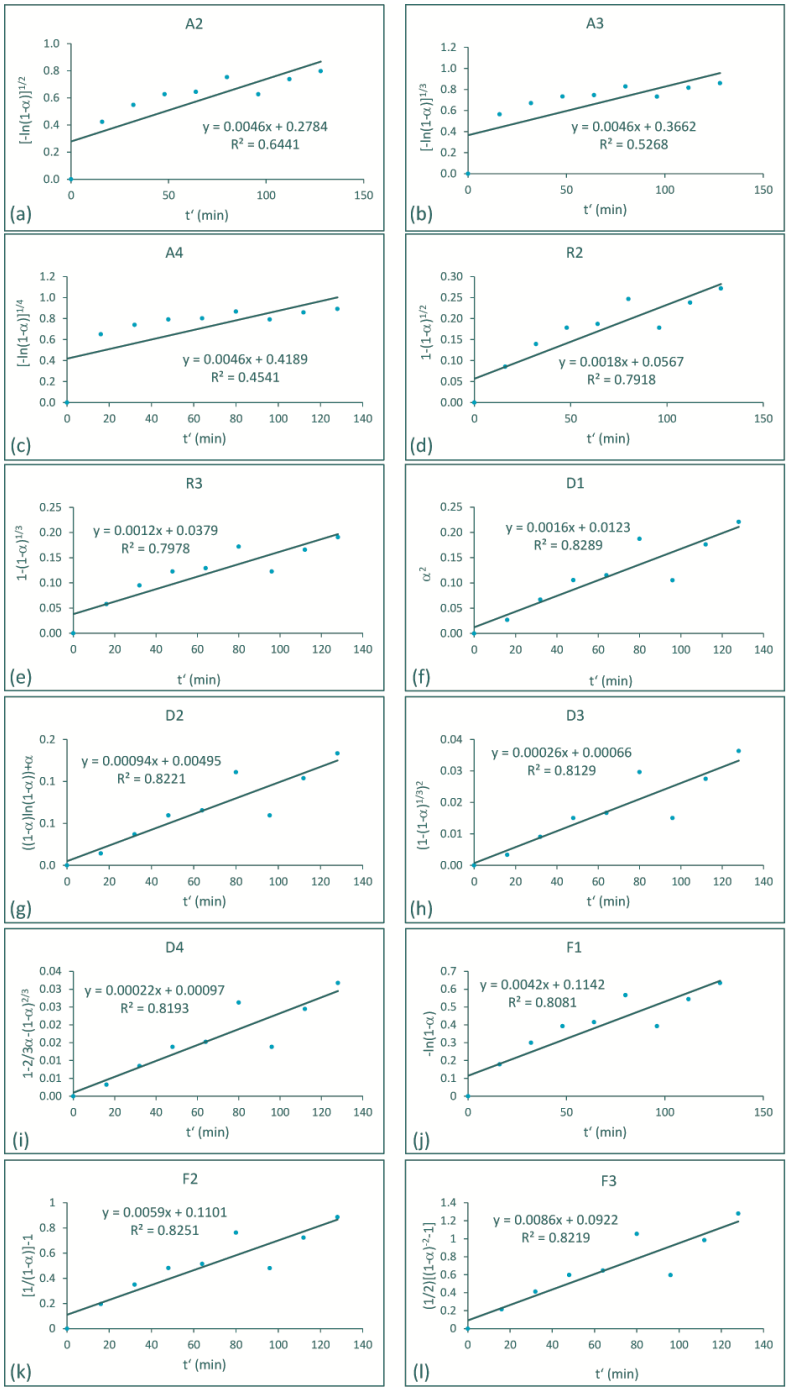

Figure E7. The fitting of conversion fraction α for the MAS in situ formation of **1** (35 ℃, 10 kHz MAS, 5 μL acetonitrile**),** after linearization α to 12 different models of solid-state reactivity: (a) the A2 model; (b) the A3 model; (c) the A4 model (d) the R2 model; (e) the R3 model; (f) the D1 model; (g) the D2 model; (h) the D3 model; (i) the D4 model; (j) the F1 model; (k) the F2 model; (l) the F3 model. The integrated rate functions g(α), varying for the different models, are given on the y-axis and also summarized in Table E3.

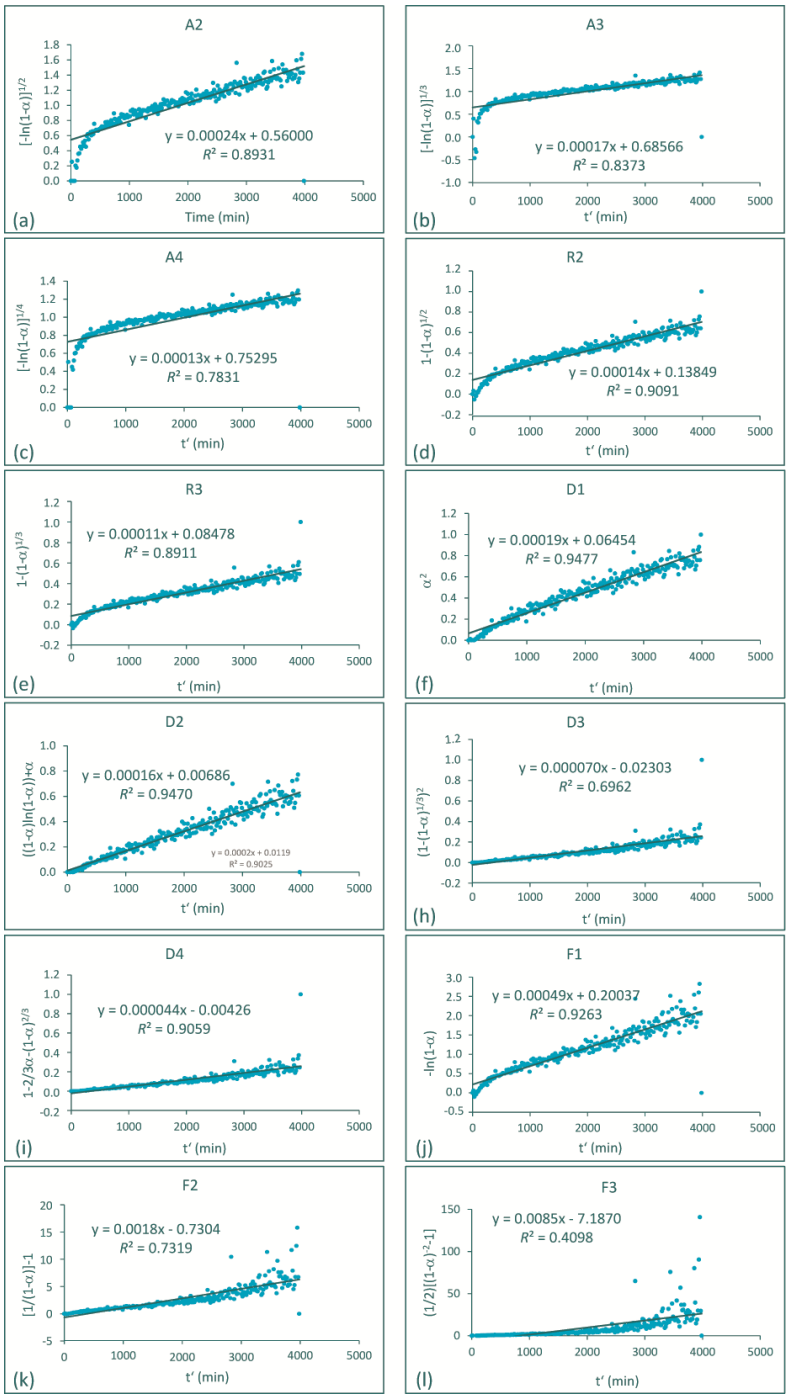

Figure E8. The fitting of conversion fraction α for the MAS in situ formation of **1** (25 ℃, 8 kHz MAS, 5 μL acetonitrile), after linearization α to 12 different models of solid-state reactivity: (a) the A2 model; (b) the A3 model; (c) the A4 model (d) the R2 model; (e) the R3 model; (f) the D1 model; (g) the D2 model; (h) the D3 model; (i) the D4 model; (j) the F1 model; (k) the F2 model; (l) the F3 model. The integrated rate functions g(α), varying for the different models, are given on the y-axis and also summarized in Table E3.

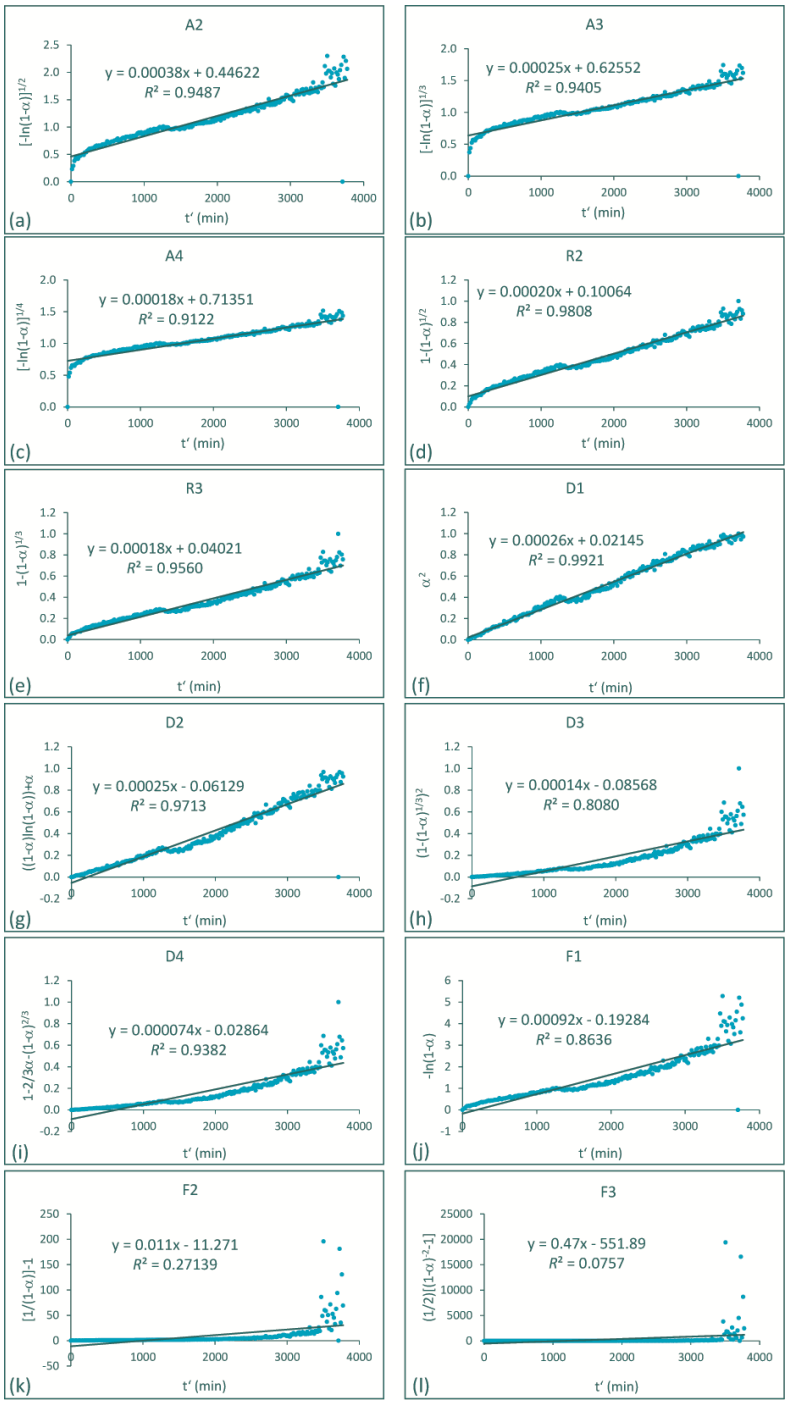

Figure E9. The fitting of conversion fraction α for the MAS in situ formation of **1** (25 ℃, 12 kHz MAS, 5 μL acetonitrile), after linearization α to 12 different models of solid-state reactivity: (a) the A2 model; (b) the A3 model; (c) the A4 model (d) the R2 model; (e) the R3 model; (f) the D1 model; (g) the D2 model; (h) the D3 model; (i) the D4 model; (j) the F1 model; (k) the F2 model; (l) the F3 model. The integrated rate functions g(α), varying for the different models, are given on the y-axis and also summarized in Table E3.

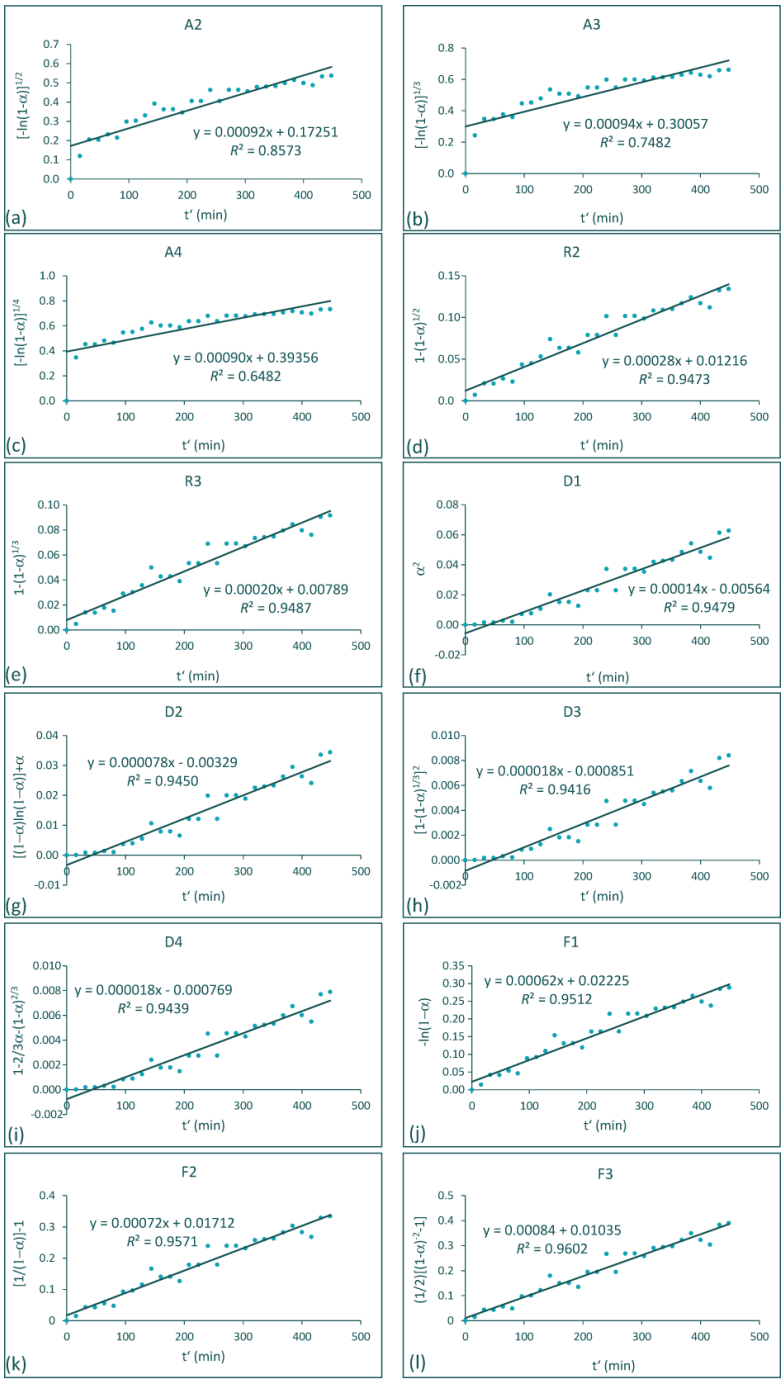

Figure E10. The fitting of conversion fraction α for the MAS in situ formation of **1** (45 ℃, 10 kHz MAS, 0 μL acetonitrile), after linearization α to 12 different models of solid-state reactivity: (a) the A2 model; (b) the A3 model; (c) the A4 model (d) the R2 model; (e) the R3 model; (f) the D1 model; (g) the D2 model; (h) the D3 model; (i) the D4 model; (j) the F1 model; (k) the F2 model; (l) the F3 model. The integrated rate functions g(α), varying for the different models, are given on the y-axis and also summarized in Table E3.

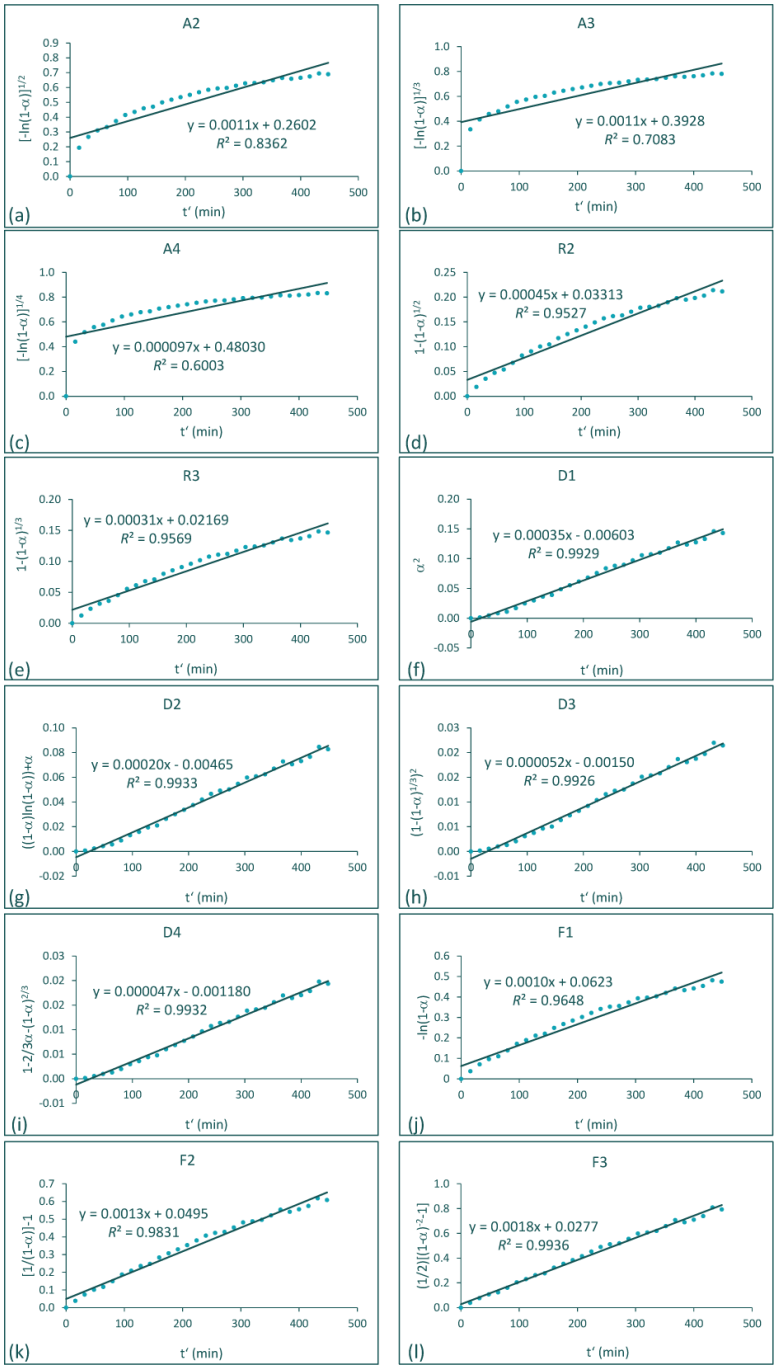

Figure E11. The fitting of conversion fraction α for the MAS in situ formation of **1** (45 ℃, 10 kHz MAS, 3 μL acetonitrile), after linearization α to 12 different models of solid-state reactivity: (a) the A2 model; (b) the A3 model; (c) the A4 model (d) the R2 model; (e) the R3 model; (f) the D1 model; (g) the D2 model; (h) the D3 model; (i) the D4 model; (j) the F1 model; (k) the F2 model; (l) the F3 model. The integrated rate functions g(α), varying for the different models, are given on the y-axis and also summarized in Table E3.

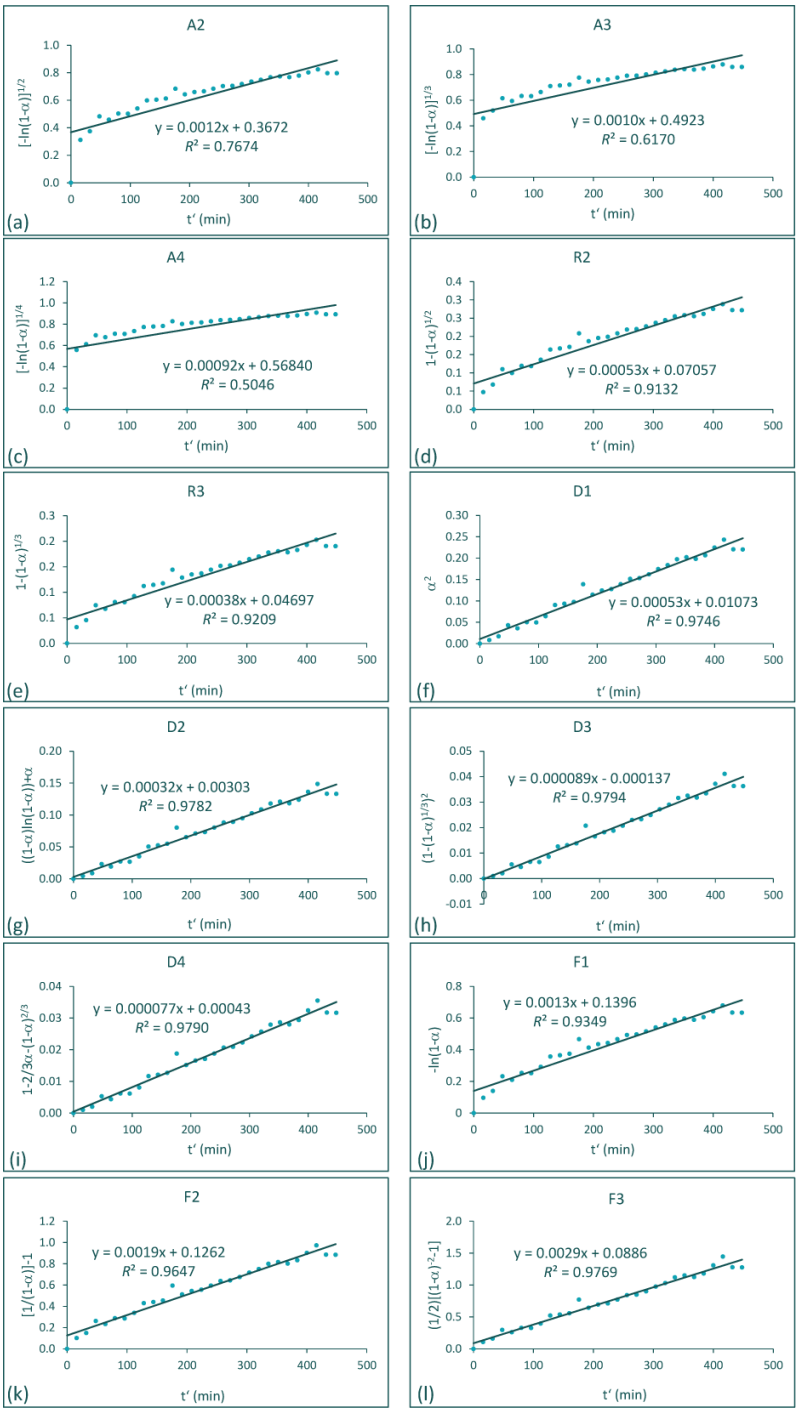

Figure E12. The fitting of conversion fraction α for the MAS in situ formation of **1** (45 ℃, 10 kHz MAS, 4 μL acetonitrile), after linearization α to 12 different models of solid-state reactivity: (a) the A2 model; (b) the A3 model; (c) the A4 model (d) the R2 model; (e) the R3 model; (f) the D1 model; (g) the D2 model; (h) the D3 model; (i) the D4 model; (j) the F1 model; (k) the F2 model; (l) the F3 model. The integrated rate functions g(α), varying for the different models, are given on the y-axis and also summarized in Table E3.

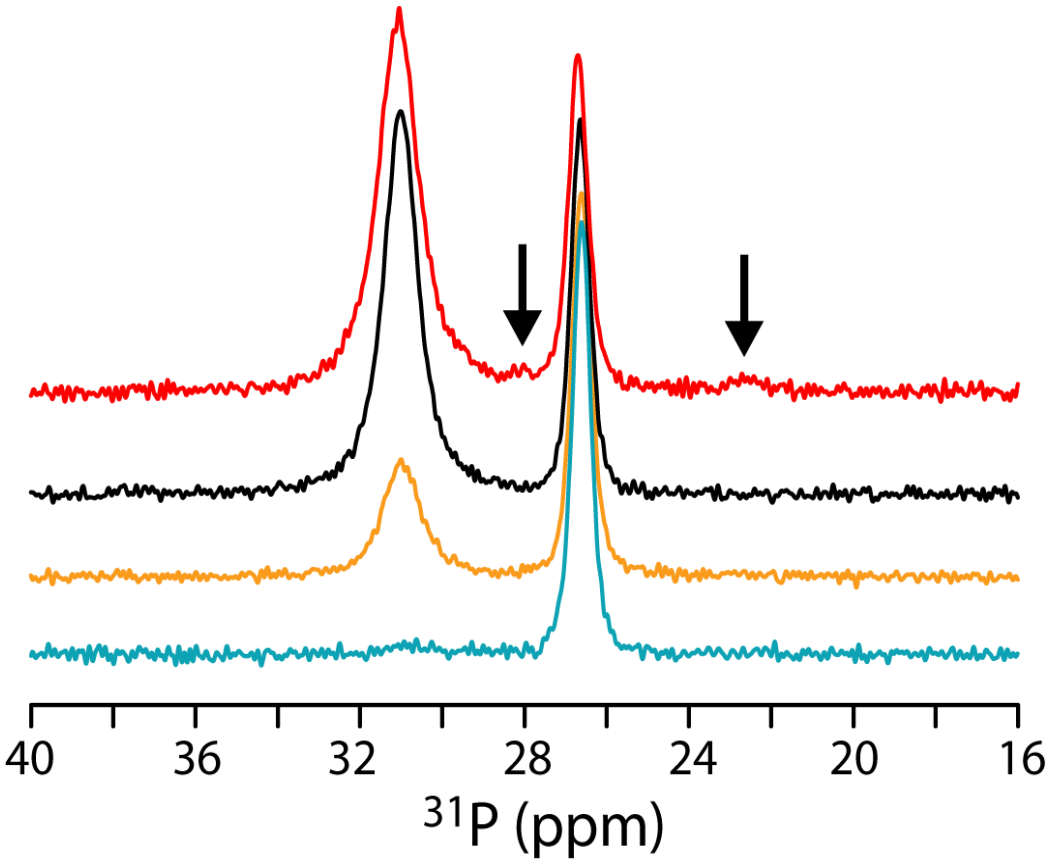

Figure E13. The in situ ^{31}P CP/MAS SSNMR spectra obtained at 9.4 T at 45 ℃ with a 10 kHz spinning speed at $t = t_0$ after adding different amounts of acetonitrile: 0 μL (turquoise), 3 μL (orange), 4 μL (black) and 5 μL (red). In the last case, the arrows show the presence of a trace amount of **2**, which indicates the formation of **2** before the first spectrum was taken.

Appendix F: List of Contributions of Yijue Xu

Publications

Xu, Y.; Kumar, V.; Bradshaw, M. J. Z.; Bryce, D. L. Chalcogen-Bonded Cocrystals of Substituted Pyridine *N*-oxides and Chalcogenodiazoles: An X-ray Diffraction and Solid-State NMR Investigation. *Cryst. Growth Des.* **2020**, in press.

Kumar, V.; **Xu, Y.**; Leroy, C.; Bryce, D. L. Direct Investigation of Chalcogen Bonds by Multinuclear Solid-State Magnetic Resonance and Vibrational Spectroscopy. *Phys. Chem. Chem. Phys.* **2020**, *22*, 3817–3824.

Xu, Y.; Szell, P. M.; Kumar, V.; Bryce, D. L. Solid-State NMR Spectroscopy for the Analysis of Element-Based Non-Covalent Interactions. *Coord. Chem. Rev.* **2020**, *411*, 213237.

Kumar, V.; **Xu, Y.**; Bryce, D. L. Double Chalcogen Bonds: Crystal Engineering Stratagems via Diffraction and Multinuclear Solid-State Magnetic Resonance Spectroscopy. *Chem. -Eur. J.* **2020**, *26*, 1–13. Featured frontispiece article.

Xu, Y.; Bryce, D. L. SCFit: Software for Single-Crystal NMR Analysis. Free vs Constrained Fitting. *Solid State Nucl. Magn. Reson.* **2019**, *102*, 53–62.

Xu, Y.; Gabidullin, B.; Bryce, D. L. Single-Crystal NMR Characterization of Halogen Bonds. *J. Phys. Chem. A* **2019**, *123*, 6194–6209.

Xu, Y.; Huang, J.; Gabidullin, B.; Bryce, D. L. A Rare Example of a Phosphine as a Halogen Bond Acceptor. *Chem Commun.* **2018**, *54*, 11041–11043.

Xu, Y.; Champion, L.; Gabidullin, B.; Bryce, D. L. A Kinetic Study of Mechanochemical Halogen Bond Formation by In-situ ^{31}P Solid-State NMR Spectroscopy. *Chem Commun.* **2017**, *53*, 9930–9933.

Xu, Y.; Southern, S. A.; Szell, P. M. J.; Bryce, D. L. The Role of Solid-State Nuclear Magnetic Resonance in Crystal Engineering. *CrystEngComm*, **2016**, *18*, 5236–5252.

Xu, Y.; Viger-Gravel, J.; Korobkov I.; Bryce, D. L. Mechanochemical Production of Halogen-Bonded Solids Featuring P=O···I-C Motifs and Characterization via X-ray Diffraction, Solid-State Multinuclear Magnetic Resonance, and Density Functional Theory. *J. Phys. Chem. C* **2015**, *119*, 27104–27117.

Burgess, K. M. N.; Perras, F. A.; Moudrakovski, I.; **Xu, Y.**; Bryce, D. L. High Sensitivity and Resolution in ^{43}Ca Solid-State NMR Experiments. *Can. J. Chem.* **2015**, *93*, 799–807.

Conference Presentations

Xu, Y.; Gabidullin, B.; Bryce, D. L. Single-Crystal NMR Characterization of Halogen Bonds. Poster presentation at MOOT NMR Mini-symposium, Ottawa, ON, October 2019.

Xu, Y.; Gabidullin, B.; Bryce, D. L. Single-Crystal NMR Characterization of Halogen Bonds. round-table oral presentation at Alpine Conference on Magnetic Resonance in Solids, Chamonix-Mont-Blanc, France, September 2019.

Xu, Y.; Gabidullin, B.; Bryce, D. L. Single-Crystal NMR Characterization of Halogen Bonds. Poster presentation at Ampere NMR School, Zakopane, Poland, June 2019. (winner of the best poster)

Xu, Y.; Gabidullin, B.; Bryce, D. L. Insights into the Effect of Halogen Bonding Interaction on NMR Tensor Orientations by ^{31}P and ^{17}O Single-Crystal NMR. Oral presentation at Canadian Chemistry Conference and Exhibition, Quebec City, QC, June 2019. (winner of the best talk prize in the solid-state NMR symposium)

Xu, Y.; Gabidullin, B.; Bryce, D. L. Insights into the Effect of Halogen Bonding Interaction on NMR Tensor Orientations by ^{31}P and ^{17}O Single-Crystal NMR. Oral presentation at Ottawa-Carleton Chemistry Institute Research Day, Ottawa, ON, May 2019.

Xu, Y.; Gabidullin, B.; Bryce, D. L. ^{31}P and ^{17}O Single-Crystal NMR Characterization of Halogen-Bonded Cocrystals. Poster presentation at Rocky Mountain Conference on Magnetic Resonance, Snowbird, Utah, July 2018.

Xu, Y.; Bryce, D. L. In-Situ Monitoring of Halogen Bonding Formation by ^{31}P Solid-State NMR. Poster presentation at International Society of Magnetic Resonance Conference (ISMAR), Quebec City, QC, July 2017.

Xu, Y.; Bryce, D. L. In-Situ Monitoring of Halogen Bonding Formation by ^{31}P Solid-State NMR. Poster presentation and flash presentation at Halogen Bonding in Supramolecular and Solid State Chemistry - Faraday Discussion, Ottawa, ON, July 2017.

Xu, Y.; Bryce, D. L. In-Situ Monitoring of Halogen Bonding Formation by ^{31}P Solid-State NMR. Poster presentation at Canadian Chemistry Conference and Exhibition, Toronto, ON, May 2017.

Xu, Y.; Viger-Gravel, J.; Bryce, D. L. A Combined Solid-State Multinuclear Magnetic Resonance and Molecular Orbital Study of P=O···I-C Halogen Bonding. Poster presentation at International Symposium on Halogen Bonding (ISXB II), Gothenburg, Sweden, June 2016.

Xu, Y.; Viger-Gravel, J.; Bryce, D. L. Mechanochemical Production of Halogen-Bonded P=O···I-C Solids and Characterization by Solid-State Multinuclear Magnetic Resonance and Molecular Orbital Study. Poster presentation at Crystal Engineering and Emerging Materials Workshop of Ontario and Quebec (CEMWOQ-3), Windsor, ON, May 2016.

Xu, Y.; Viger-Gravel, J.; Bryce, D. L. A Study of P=O···I-C Halogen Bonding via Solid-State Multinuclear Magnetic Resonance and Molecular Orbital Analysis. Poster presentation at MOOT XXVII NMR Symposium, Hamilton, ON, October 2015. (winner of a poster prize)

Xu, Y.; Viger-Gravel, J.; Bryce, D. L. Direct Study of Halogen-Bonded P=O···I-C Motifs by ^{17}O Solid-State NMR and X-ray Diffraction. Poster presentation at Canadian Chemistry Conference and Exhibition, Ottawa, ON, June 2015. (winner of a poster prize)

Xu, Y.; Viger-Gravel, J.; Bryce, D. L. Solid-State NMR Study of Halogen-Bonded P=O···I-C Motifs. Poster presentation. 27th MOOT NMR symposium, Montreal, QC, 2014.